NIST Technical Note 2169

Seismic Behavior and Design of Deep, Slender Wide-Flange Structural Steel Beam-Columns

Piyachai Chansuk
Gulen Ozkula
Chia-Ming Uang
John L. Harris III

This publication is available free of charge from:
https://doi.org/10.6028/NIST.TN.2169

National Institute of Standards and Technology
U.S. Department of Commerce

Disclaimers

Any opinions, recommendations, and conclusions contained within this report are solely those of the authors, and do not necessarily reflect the views or policies of the project sponsors. This report does not constitute a standard, specification, or regulation.

Certain commercial software, equipment, instruments, or materials may have been used in the preparation of information contributing to this report. Identification in this report is not intended to imply recommendation or endorsement by NIST, nor is it intended to imply that such software, equipment, instruments, or materials are necessarily the best available for the purpose.

NIST policy is to use the International System of Units (metric units) in all its publications. In this report, however, information is presented in U.S. Customary Units (inch-pound), as this is the preferred system of units in the U.S. earthquake engineering industry.

National Institute of Standards and Technology Technical Note 2169
Natl. Inst. Stand. Technol. Tech Note 2169, 320 pages (July 2021)
CODEN: NTNOEF

This publication is available free for charge from:
https://doi.org/10.6028/NIST.TN.2169

NIST Technical Note 2169

Seismic Behavior and Design of Deep, Slender Wide-Flange Structural Steel Beam-Columns

Piyachai Chansuk
Gulen Ozkula
Chia-Ming Uang
John L. Harris III

This publication is available free of charge from:
https://doi.org/10.6028/NIST.TN.2169

July 2021

U.S. Department of Commerce
Gina M. Raimondo, *Secretary*

National Institute of Standards and Technology
James K. Olthoff, *Performing the Non-Exclusive Functions and Duties of the Under Secretary of Commerce for Standards and Technology & Director, National Institute of Standards and Technology*

This page intentionally left blank.

ACKNOWLEDGEMENTS

Support for this research was provided by the National Institute of Standards and Technology (NIST) to the NEHRP Consultants Joint Venture (NCJV), a joint venture between the Applied Technology Council (ATC) and Consortium of Universities for Research in Earthquake Engineering (CUREE). Dr. J. Harris was the Contracting Officer's Technical Representative for NIST. Ms. A. Hortacsu from ATC served as the project manager and Mr. J. Malley from Degenkolb Engineers chaired the Project Technical Committee for the NCJV. Further, Dr. G. Mosqueda and Dr. A. Sarebanha assisted in developing a closed-loop control algorithm for the testing facility. Considerable support was received from the American Institute of Steel Construction who provided steel materials and from the Herrick Cooperation who provided fabrication of Phase 1 test specimens.

This page intentionally left blank.

TABLE OF CONTENTS

This page intentionally left blank.

LIST OF FIGURES

LIST OF TABLES

This page intentionally left blank.

EXECUTIVE SUMMARY

Design engineers prefer to use deep wide-flange columns for Steel Special Moment Frames (SMF) in high seismic regions in the U.S to achieve architectural flexibility, construction economy, and to satisfy story drift limits prescribed in the applicable code. In an SMF, plastic hinges are expected to develop at frame beam ends, but also at the base of frame columns. However, the understanding of the seismic behavior of deep wide-flange columns with plastic hinges is limited, which corresponds to a dearth of full-scale tests. Forty-four full-scale isolated columns were cyclically tested as part of a research program lead by the National Institute of Standards and Technology to fill the knowledge gap in seismic behavior, design, and modeling of deep wide-flange columns. Critical to this knowledge is understanding the effects of their relatively large cross-sectional slenderness parameters for the web and flange (h/t_w and $b_f/2t_f$, respectively) and high member slenderness parameter (L/r_y).

Twenty-one W24 hot-rolled columns of ASTM A992 steel with five different sections were tested in Phase 1 of this research program to investigate the effects of slenderness parameters, constant axial load levels, lateral drift loading sequences, and weak-axis bending on the column base responses. The 'W' denotes 'wide-flange' and 24 is the nominal depth of the section (in inches). It was observed from these tests that the webs of these sections with much higher h/t_w ratios were not as effective in restraining and delaying flange local buckling as those of shallow, stocky columns (e.g., W12 or W14). Specimens with sections that satisfied the 'highly ductile' requirement in the AISC Seismic Provisions experienced significant buckling and axial shortening due to the interaction between flange and web local buckling. For the first time, an unusual failure mode with local buckling coupled with lateral-torsional buckling was observed. Based on these tests results, observed buckling modes were classified, and a simplified procedure to predict the governing buckling mode was proposed.

An additional twenty-three columns, including W14, W18, W24, and W30 sections, were subsequently tested in Phase 2 to further evaluate the effects due to variations in section depth, boundary condition, and axial load. Phase 2 consisted of twelve tests identified as Phase 2A and eleven tests identified as Phase 2B. Test results revealed that

findings from Phase 1 could be extrapolated to deeper and shallower sections than W24; the proposed buckling mode prediction procedure in Phase 1 predicted very well the buckling mode of the specimens in Phase 2. Allowing the column top end to rotate increased the story drift capacity but did not change the buckling mode. Results from tests that cycled the axial load higher and lower around an initial constant value showed that exterior frame columns (columns located at the outermost ends of the frame) behave very differently from interior frame columns that generally support a constant axial load. W14 column test results showed that classifying a column as deep or shallow simply based on the nominal depth of the section may be inappropriate as significant interaction between flange and web local buckling could develop in shallow columns with relatively slender web and flanges.

1. INTRODUCTION

1.1 General

Moment-resisting frames are one of the most common seismic force-resisting systems used in high seismic regions due to their high energy-dissipation capacity and architectural versatility. Unexpected non-ductile failure of seismically designed welded steel moment connections that was observed after the 1994 Northridge, California Earthquake had triggered extensive studies on the behavior of Steel Special Moment Frames (SMFs). Extensive studies, including those completed by the SAC Joint Venture (FEMA 2000), have been conducted to evaluate the cyclic behavior and design of beam-to-column moment connections. As such, cyclic behavior of the plastic hinge in a beam has been thoroughly researched and is well understood, but research on the behavior of the supporting column is extremely limited.

Before the Northridge Earthquake, shallow wide-flange columns (e.g., W14 or W12 sections) were commonly used in moment-resisting frames because of their comparable strong- and weak-axis radii of gyration. However, it became challenging to continue designing with shallow sections after the earthquake since frames were required to have a large lateral stiffness to satisfy new code-enforced story drift limits, as that prescribed currently in ASCE 7 (ASCE 2016). To overcome this challenge, engineers turned to using deeper steel columns, which were more economical in providing adequate lateral stiffness due to their in-plane strong-axis moment of inertia. For instance, Figure 1.1 and Table 1.1 compare the properties of a shallow and a deep section that have similar strong-axis moments of inertia, I_x. The benefit of using the deep W30×148 section is clear; the weight of the column is reduced from 426 lb/ft to 148 lb/ft [634 kg/m to 220 kg/m]. However, the section slenderness parameters related to flange local buckling (FLB) and, particularly, web local buckling (WLB) controls (i.e., $b_f/2t_f$ and h/t_w, respectively, as identified in Figure 1.1) are much larger for the deep section. In addition, the deep column is also prone to out-of-plane, global-type member buckling like flexural buckling (FB) and lateral-torsional buckling (LTB) since its radius of gyration about the weak-axis (r_y) is much smaller than that about the strong-axis (r_x).

Because columns in moment frames are subjected to both bending and axial loads during a seismic event, they are commonly referred to as 'beam-columns' in design. Unfortunately, little experimental research on cyclic behavior of beam-columns is available to expansively support the seismic design or assessment provisions in AISC 341 (AISC 2016a) and ASCE 41 (ASCE 2017). Newell and Uang (2008) conducted full-scale testing of W14 columns (W14×132 to W14×370) subjected to variable axial load and cyclic bending. It was concluded that this type of shallow columns, even under high axial loads, had a ductility capacity that was much higher than that specified in ASCE 41 (ASCE 2013) mainly because of their compact sections that are common for shallow columns. On the contrary, the behavior of deep columns is not well understood and extrapolation from shallow columns may not be appropriate. To fill this knowledge gap, the National Institute of Standards and Technology (NIST) developed a comprehensive research plan to study the seismic behavior and design of deep, slender wide-flange structural steel beam-columns (NIST 2011). The plan included studies at the member, subassemblage, and system levels.

1.2 Research Objective

The objective of this research was to experimentally study the cyclic response of deep, slender wide-flange beam-columns for use in moment frames. Test data generated from this test program are to be used in the next phase of the NIST research plan to (1) calibrate analytical models, (2) evaluate the adequacy of design provisions for seismic design of new construction in AISC 341, and (3) evaluate the adequacy of design provisions for seismic evaluation of existing construction in ASCE 41.

1.3 Scope

This research focused on column behavior at the member level; it initiated with full-scale testing of twenty-one wide-flange (W24) specimens under various levels of constant axial compression, lateral drift loading protocols (including both cyclic and monotonic types), and bending directions (strong- and weak-axis) to investigate each associated effect on column behavior. An unexpected out-of-plane, lateral-torsional buckling type failure was observed in some specimens, which motivated additional testing. Testing of the first twenty-one W24 columns was referred to as Phase 1 study. The subsequent Phase 2 study encompassed testing of additional twenty-three specimens with further diversified wide-

flange sections (W14 to W30); all were subjected to strong-axis bending. Twelve specimens with seven different sections were tested in the first part of Phase 2 study, i.e., Phase 2A. All Phase 2A specimens were subjected to cyclic bending, except for one that was tested monotonically. Phase 2B included testing of eleven specimens with six additional sections to further investigate the objectives of Phase 2A study. A number of specimens from both Phases 2A and 2B were subjected to varying axial load sequences, which simulated the loading condition of first-story exterior columns in an SMF, or cyclic end rotation at the moving end, which simulated the rotation at the top end of the first-story columns that resulted from beam flexibility.

1.4 Uncertainty and Error Quantification for Full-Scale Testing

All full-scale tests of the column specimens presented in this report were conducted using the California Department of Transportation (CALTRANS) Seismic Response Modification Device (SRMD) located at the University of California, San Diego. This device was calibrated in January through February of 2017. A complete report of the calibration of the device and its instrumentation, displacement devices, and data acquisition system, including accuracy quantification, can be found in SRMD2017-05: *SRMD System Calibration Conducted Jan.-Feb. 2017* (Benzoni and Innamorato 2017).

All column specimens were fabricated in accordance with AISC 303-10: *Code of Standard Practice for Structural Steel Buildings and Bridges* (AISC 2010).

No formal investigation was included as part of this testing program to evaluate all potential sources of uncertainty or error in the testing or analysis systems, or whether multiple sources are correlated. Repeat tests for a few selected columns were included to evaluate the uncertainty in observed behavior (repeatability). The question of uncertainty and error created by the test apparatus, analytical model calibrations, solution algorithms, material properties and even potential as-built dimensions and positions of specimens are beyond the scope of this testing.

1.5 International System of Units Conversion

NIST policy is to use the International System (SI) of Units (modern standard form for metric units) in all its publications. In this report, however, information is presented in U.S. Customary Units (inch-pound), as this is the preferred system of units in the U.S.

earthquake engineering industry. In some areas, a direct conversion is provided in the text. For figures and tables, the following can be used to convert U.S. Customary Unites to SI:

1 inch (in.) = 25.4 mm (length)

1 foot (ft.) = 304.8 mm (length)

1 kip (k) = 1000 pounds (lbs.) = 4.448 kN (force)

1 kip/in (k/in) = 175.1 N/mm (stiffness)

1 ksi (k/in^2) = 6.895 MPa (stress)

1 kip-foot (k-ft) = 1.356 kN-mm (moment)

Table 1.1 Comparison of Two Sample Wide-Flange Column Sections

Section	Weight (lb/ft)	r_x (in.)	r_y (in.)	I_x (in.^{4})	I_y (in.^{4})	$\frac{b_f}{2t_f}$	$\frac{h}{t_w}$
W14×426	426	7.26	4.34	6600	2360	2.75	6.08
W30×148	148	12.4	2.28	6680	227	4.44	41.6

Notes: Parameters are defined in AISC 360 (AISC 2016b) and some are shown in Figure 1.1.
r_x and r_y = radius of gyration about the x (strong) and y (weak) axis, respectively;
I_x and I_y = moment inertia about the x (strong) and y (weak) axis, respectively;
b_f = flange width; t_f = flange thickness; t_w = web thickness; and
h = clear distance between flanges less the fillet or corner radius at each flange.

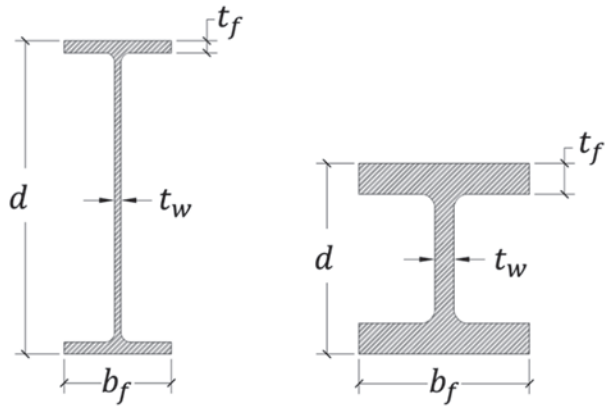

Figure 1.1 Cross-Section Comparison of a Deep Column and a Shallow Column

2. TEST PROGRAM: PHASE 1

2.1 Introduction

Phase 1 encompassed testing of twenty-one W24 columns under various levels of constant axial load and inelastic cyclic drifts. They were intended to represent interior first-story columns in an SMF. The normalized parameter C_a was used to indicate the levels of axial load being applied to the specimens (AISC 2010):

$$C_a = \frac{P_u}{\phi_c P_n} \tag{2.1}$$

where P_u = targeted axial load magnitude (positive for compression), $P_n = A_g F_{yn}$, A_g = gross area, F_{yn} = nominal yield stress, and ϕ_c = resistance factor (0.9). With a few exceptions, low, medium, or high levels of axial compression, i.e., C_a = 0.2, 0.4, or 0.6, respectively, were used in testing to investigate the effect of constant axial load on column ductility capacity and axial shortening. Fixed-fixed boundary conditions were imposed to all specimens.

Five W24 sections (ranging from W24×55 to W24×176) were tested in Phase 1 as shown in Table 2.1; their section slenderness encompasses both highly and moderately ductile web and flanges, as specified in AISC 341 (2016a), to investigate the effect of section slenderness. While Group 1 to 5 specimens were subjected to strong-axis bending, Group 6 and 7 specimens with W24×131 section (same as Group 2 specimens) were subjected to weak-axis and biaxial bending, respectively, to investigate column responses associated with other bending directions. Except for Specimens 2L-P and 6L-P that were subjected to monotonic pushover tests, and Specimen 2M-NF that was subjected to the near-fault loading protocol, all other specimens underwent the AISC cyclic loading protocol (see Section 2.5). This was intended to examine the effect of lateral-drift sequences.

2.2 Test Setup

Testing was conducted in the Seismic Response Modification Device (SRMD) Test Facility at the University of California, San Diego with the test setup as shown in Figure

2.1. Specimens were tested in a horizontal position; L indicates their clear lengths (see Table 2.1). The west end of the specimens was connected to a reaction fixture that was fixed to a strong wall. The east or moving end was connected to a reaction fixture that was tied down to the SRMD moving platen, simulating a column top end that swayed (and rotated for the fixed-rotating loading case) during a seismic event.

To achieve fully-restrained moment connections at both ends, bolted end-plate connections (ASTM A572 Gr. 50 steel) were used in this test program as shown in Figure 2.2(b) and Figure 2.3(b). The end plates were fastened to the reaction fixtures with 1½-in. [38 mm] diameter high-strength pre-tensioned threaded rods (ASTM A354 Gr. BD). The weld access hole profile specified in AISC 360 (AISC 2016b) was used for welding detail.

With this test setup, longitudinal movements of the platen, which were force-controlled, imposed a targeted axial force, P, to the specimen. A force-control algorithm was employed to either maintain a constant axial load or apply varying axial load; the latter was utilized in varying axial load tests in Phase 2 program. Applied (i.e., measured) cyclic lateral displacement, Δ_m, of the platen in the horizontal plane imposed double-curvature, strong- or weak-axis bending to the specimens, depending on the specimen longitudinal orientations as shown in Figure 2.2 and Figure 2.3. For a biaxial test, the platen was prescribed both lateral and vertical displacements to apply both strong- and weak-axis bending simultaneously. Cyclic rotations, θ_m, of the platen about the member strong-axis simulated top end rotation of the first-story columns in an SMF. The platen was in a displacement-control mode for the lateral, vertical, and strong-axis rotational movements.

2.3 Design of Test Specimens

Table 2.1 summarizes slenderness parameters of each specimen. To investigate the effect of section slenderness on column behavior, five W24 sections were included in Phase 1 testing to cover a wide range of h/t_w and $b_f/2t_f$. Figure 2.4 shows the distribution of the width-to-thickness ratios with respect to the seismic compactness limits specified in AISC 341 (AISC 2016a), i.e., the highly and moderately ductile limits (λ_{hd} and λ_{md}, respectively):

- For flange local buckling,

$$\lambda_{hd} = 0.32\sqrt{\frac{E}{R_y F_{yn}}} \tag{2.2}$$

$$\lambda_{md} = 0.40\sqrt{\frac{E}{R_y F_{yn}}} \tag{2.3}$$

- For web local buckling with $C_a > 0.114$,

$$\lambda_{hd} = 0.88\sqrt{\frac{E}{R_y F_{yn}}}(2.68 - C_a) \geq 1.57\sqrt{\frac{E}{R_y F_{yn}}} \tag{2.4}$$

$$\lambda_{md} = 1.29\sqrt{\frac{E}{R_y F_{yn}}}(2.12 - C_a) \geq 1.57\sqrt{\frac{E}{R_y F_{yn}}} \tag{2.5}$$

where $E = 29{,}000$ ksi [200 GPa], and $R_y = 1.1$ for A992 steel.

Wide-flange sections were selected such that the member slenderness parameter, L/r_y, fell within a targeted and practical range. The use of lighter sections (W24×55 and W24×84) in this program also widened the range of L/r_y. Figure 2.5 shows distribution of the L/r_y ratios. AISC 341 does not specify limiting L/r_y ratios for highly and moderately ductile beam-columns. For comparison purpose, those for highly and moderately ductile beams are shown in the figure:

$$\lambda_{hd} = \frac{L_{hd}}{r_y} = \frac{0.095E}{R_y F_{yn}} \tag{2.6}$$

$$\lambda_{md} = \frac{L_{md}}{r_y} = \frac{0.19E}{R_y F_{yn}} \tag{2.7}$$

R

egarding specimen designation, letters “L”, “M”, and “H” represent low ($C_a = 0.2$), medium ($C_a = 0.4$), and high ($C_a = 0.6$) constant axial loads applied to the specimens,

respectively. Most specimen groups comprised columns subjected to each level of axial compression to investigate the axial load effect. Group 2 also included Specimen 2Z, which was tested without an axial load to obtain a beam response.

To examine the effect of lateral-drift sequences, various loading protocols discussed in Section 2.5 were used. The AISC cyclic loading protocol was imposed on all specimens except: (1) Specimens 2L-P and 6L-P ("P" for "Pushover"), which underwent a large monotonic drift initially and the reversed AISC cyclic loading protocol successively, and (2) Specimen 2M-NF ("NF" for "Near-fault"), which underwent the near-fault loading protocol.

Group 1 to 5 specimens were subjected to strong-axis bending. To examine column responses associated with other bending directions, Group 6 and 7 specimens with W24×131 section (same as Group 2 specimens) were subjected to weak-axis and biaxial bending, respectively.

2.4 Steel Material Properties

ASTM A992 was specified for all beam-column specimens, and A572 Gr. 50 steel was specified for the end plates. Table 2.2 summarizes mechanical properties of the specimens; coupons were taken from both webs and flanges for material testing. The engineering stress versus engineering strain relationships are shown in Figure 2.6.

The sectioning method described in the SSRC Technical Memorandum No. 6 (Ziemian 2010) was used to establish the residual stress pattern of a W24×131 column section. As shown in Figure 2.7, a 12-in. portion of the member was selected; each web and flange of this portion was then subdivided into 12 strips. Two holes were drilled on each strip 10 in. apart. Then, the whole portion was saw-cut from the member and further sliced into each strip using waterjet; a Whittemore gage was used to measure changes in distance between the two holes after both cutting processes. The measurement was then used to determine residual stress inherent in each strip and establish the residual stress profile in the section. Although this research focuses on deep columns, residual stresses in a shallow W14×176 column were also measured for comparison purposes. Figure 2.8 shows that the commonly assumed residual stress pattern with compressive stresses at flange tips (Ziemian 2010) is consistent with the pattern measured in the W14×176 section

as shown in Figure 2.9(a). However, Figure 2.9(b) shows an opposite trend in the flanges of the W24×131 section.

2.5 Testing Procedure and Loading Protocols

For constant axial load tests, axial loads were applied first and maintained at a constant level throughout the test. Then, cyclic lateral drifts were imposed at the moving end of the columns (see Figure 2.1). Since the objective of this research was to evaluate the cyclic response of steel columns in moment frames, the standard loading protocol for qualifying cyclic tests of beam-to-column moment connections in Special and Intermediate Moment Frames specified in Section K2.4b of AISC 341-16 was applied to most cyclically loaded specimens. Figure 2.10(a) shows the typical story drift angle (*SDA*) sequence of the AISC loading protocol.

To investigate the effect of loading protocols on column response, pushover and near-fault loading tests were also conducted in Phase 1 program. Specimens 2L-P and 6L-P were subjected to the pushover tests. They were displaced monotonically up to 0.04 radians [see Figure 2.10(b)] and 0.07 rad *SDA*, respectively. The intent was to compare their monotonic responses against the backbone curves of the cyclic responses of Specimens 2L and 6L, respectively. Because both pushover specimens did not exhibit significant damage after the monotonic drifts, the reversed AISC loading protocol [points A to B in Figure 2.10(b) for Specimen 2L-P] was applied sequentially to examine their failure behavior. Subjected to weak-axis bending, Specimen 6L-P sustained both the monotonic and reversed cyclic drifts without showing significant damage and strength degradation. As a result, it was subjected to an additional drift cycle at 0.10 rad *SDA*. Specimen 2M-NF was tested with the near-fault loading protocol shown in Figure 2.10(d). This loading protocol was characterized by its initial large displacements that was followed by smaller-amplitude cycles oscillating about a level of residual drift (Krawinkler et al. 2000). The near-fault column responses were compared to the cyclic responses of Specimen 2M; the latter corresponded to the AISC loading protocol, which resembled a far-field drift characteristic.

Specimen 7M was tested to investigate the effect of biaxial bending. AISC 341 did not provide any guidance on biaxial loading protocol. Thus, the AISC loading protocol was

also used in this biaxial test. The intent was to facilitate direct result comparisons to uniaxial (i.e., strong- or weak-axis bending only) AISC tests. In the biaxial test, 100 % and 30 % of the AISC cyclic drift magnitudes were simultaneously applied in the strong- and weak-axis directions, respectively [see Figure 2.10(c)].

The effects of varying axial load and fixed-rotating boundary conditions were investigated in Phase 2 testing. Loading protocols for these cases will be described in Section 4.5.

2.6 Instrumentation

Displacement transducers, inclinometers, strain gauge rosettes, and uniaxial strain gauges were used to measure global and local responses. Figure 2.11 shows displacement transducer and inclinometer layout. Figure 2.12 shows rosette and uniaxial strain gauge locations. Movements of the platen and their associated forces in six degrees of freedom were also recorded.

2.7 Data Reduction

2.7.1 Introduction

In this test program, the specimens had either fixed-fixed or fixed-rotating boundary conditions; the latter were tested in Phase 2. For both cases, it was observed that the measured beam-column responses, especially in the elastic range, were sensitive to flexibility of the fully-restrained moment connections that fixed the specimen ends. Correspondingly, this connection flexibility became another unintended variable that influenced the test responses, hindering investigation of parameters of interest in this research. Thus, a data correction procedure is needed to eliminate the effect of connection flexibility from the measured beam-column responses and enables meaningful response investigations.

The first part of this section discusses the challenges in analyzing test data that arise from the effects of connection flexibility. Subsequently, a data correction procedure is presented to overcome the challenges. Finally, the methodology used to extract lateral drifts and moments at member ends from raw test data, as well as the implementation of the data correction procedure to eliminate the effect of connection flexibility, are discussed for each testing condition encountered in both Phases 1 and 2.

2.7.2 Effects of Connection Flexibility and Challenges

The use of bolted end-plate connections to fix the specimens to reaction fixtures did not constitute ideal rigid boundary conditions. Due to out-of-plane flexibility of the end plates and elongation of the fastening rods, some relative rotations between the specimen ends and the reaction fixtures, i.e., connection rotations, were observed during the cyclic testing. Although Figure 2.13(a) was the targeted fixed-fixed boundary conditions, end connection flexibility caused rigid-body rotation of the specimens as shown in Figure 2.13(b). Since the measured column lateral drift, Δ_m, included a drift component contributed from the rigid-body movement due to the connection flexibility, the measured elastic lateral stiffness, K_{me}, obtained from linear regression of the elastic portion of the lateral force-story drift response could be significantly lower than a theoretical prediction, K_e, considering ideal rigid boundary conditions as shown in Figure 2.13(a). Taking Specimen 13M for example, K_{me} is 23.1 % smaller than K_e as shown in Figure 2.15.

For specimens with the fixed-rotating boundary conditions, not only the imposed lateral drifts but also the imposed end rotations included a component contributed from connection rotations [see Figure 2.14(b)]. Again, this caused the measured elastic responses to deviate from theoretical elastic responses of a beam-column with rigid end connections [see Figure 2.14(a)]. For Specimen 11H-BC, K_{me} is 13.4 % smaller than K_e as shown in Figure 2.16.

For specimens subjected to weak-axis bending (only in Phase 1 testing), connection rotations were negligible because the member weak-axis flexural stiffness was small in magnitudes relative to the rotational stiffness of the end connections. As a result, K_{me} and K_e of Specimen 6L (Phase 1 specimen), for example, are comparable as shown in Figure 2.17. Thus, only the effect of connection flexibility on beam-column tests with strong-axis bending needs to be considered. A procedure that removes the deformation component due to connection flexibility from the measured test responses is presented in the next section.

2.7.3 Drift Correction Procedure

Considering the flexibility of the end moment connections that causes rigid-body rotation of the specimens, the imposed (or measured) lateral drift at the moving end of the specimens, Δ_m, can be expressed as

$$\Delta_m = \Delta_{me} + \Delta_{mc} + \Delta_{mp} \tag{2.8}$$

where Δ_{me} and Δ_{mp} represent the elastic and plastic components of the measured lateral drift due to column straining, respectively, and Δ_{mc} is the component resulting from rigid-body rotation of the column due to connection flexibility at member ends. Removing Δ_{mc} from Δ_m gives the corrected story drift corresponding to ideal boundary conditions. Since it is difficult to measure Δ_{mc} experimentally due to the complex out-of-plane deformation of the end plates, this component was removed using the following procedure.

Assuming that Δ_{mc} remains elastic, Δ_{me}+Δ_{mc} collectively represents the elastic component of Δ_m. Accordingly, the plastic component of Δ_m can be extracted as follows:

$$\Delta_{mp} = \Delta_m - \frac{V}{K_{me}} \tag{2.9}$$

where V is the measured column shear (i.e., lateral force), and K_{me} is the experimentally determined elastic stiffness (i.e., the initial slope of the Δ_m versus V response). Corrected lateral drift due to the column deformation only is then the sum of the theoretical elastic drift, Δ_e, and the experimentally determined Δ_{mp}:

$$\Delta = \Delta_e + \Delta_{mp} \tag{2.10}$$

where

$$\Delta_e = \frac{V}{K_e} \tag{2.11}$$

K_e is the best estimate of the elastic lateral stiffness and is represented by the theoretical lateral stiffness of a beam-column with ideal boundary conditions, i.e., rigid end connections. Chansuk et al. (2019) present a literature review of classical beam-column stiffness formulas and derive internal force and stiffness formulas for Timoshenko beam-columns with rotationally flexible end connections. These expressions are used in the calculation of K_e.

Substituting Eqs. (2.9) and (2.11) into Eq. (2.10) yields the final formula used to determine the corrected story drifts:

$$\Delta = \Delta_e + \Delta_{mp} = \frac{V}{K_e} + \left(\Delta_m - \frac{V}{K_{me}}\right) \tag{2.12}$$

The corrected story drift can also be expressed in terms of a story drift angle (SDA) as

$$SDA = \frac{\Delta}{L} \tag{2.13}$$

The following sections present methods used to extract lateral drifts and moments at specimen ends from test data, and formulas used to calculate K_e in Eq. (2.12) for each testing condition.

2.7.4 Beam-Column Tests with Fixed-Fixed Boundary Conditions and Constant Axial Compression

Member Lateral Drift and End Moment Calculation

In fixed-fixed boundary condition tests, the lateral movement measured at the center of the SRMD platen, Δ_T, reflects the lateral drift at the moving (or east) end of the column [see Figure 2.18(a)]. Thus,

$$\Delta_m = \Delta_T \tag{2.14}$$

This drift includes the rigid-body translation due to connection flexibility.

Assuming an inflection point remains at the midspan of the specimens throughout the test [see Figure 2.13(b)], west and east end moments, including *P*-Δ effect, are computed as follows:

$$M_W = M_E = \frac{1}{2}[V(L - \Delta_s) + P\Delta_m] \tag{2.15}$$

where $\Delta_s =$ axial shortening, and $P =$ applied axial load (see Figure 2.19 for sign conventions). The calculated end moment can be normalized by either the plastic moment, M_p, or the reduced plastic moment, M_{pc}, of the section (ASCE-WRC 1971):

(i) for $P/P_y \geq 0.15$,

$$M_{pc} = 1.18\left(1 - \frac{P}{P_y}\right)M_p \tag{2.16a}$$

(ii) for $P/P_y < 0.15$,

$$M_{pc} = M_p \tag{2.16b}$$

The measured yield stresses from tensile coupon testing (see Table 2.2) are used to compute P_y and M_p.

Lateral Drift Correction

Due to the symmetry of the fixed-fixed boundary conditions and the test setup, it was observed that the yielding and buckling patterns at both ends of the columns were very similar. Therefore, the inflection point can reasonably be assumed to remain at the midspan [see Figure 2.13(b)]. With this assumption [see Figure 2.13(a)], K_e for calculating the corrected story drift in Eq. (2.12) follows (Chugh 1977).

$$K_e = K'_{11} = \frac{EIk^3\left[\sin kL - \frac{2P}{kLGA_s}(1 - \cos kL)\right]}{2\left(1 + \frac{P}{GA_s}\right)(1 - \cos kL) - kL\sin kL} \tag{2.17}$$

where $k = \sqrt{P/EI}$, $P =$ axial load magnitude (i.e., absolute value of P), $E =$ elastic modulus, $I =$ moment of inertia about the bending axis, $G =$ shear modulus, and A_s for strong-axis bending is simplified as

$$A_s = \left(d - 2t_f\right)t_w \tag{2.18}$$

An example correction of the lateral force-story drift response of Specimen 13M is shown in Figure 2.20. The last column in Table 2.3 shows that the connection flexibility can reduce the lateral stiffness by 32.0 % for the largest member (W30×261) tested. The stiffness reduction is lower for shallower and lighter members (e.g., W14×53 and W24×55).

Although the corrected story drift can be computed based on the above procedure, the equivalent rotational flexibility (or stiffness) of the end connections is still unknown. Idealizing the connection flexibility at both column ends as end rotational springs with an equivalent spring stiffness of [see Figure 2.13(b)].

$$K_\theta = \beta\left(\frac{EI}{L}\right) \tag{2.19}$$

where β is the normalized rotational spring constant, connection stiffness (K_θ) can be quantified using the lateral stiffness relationship of the Timoshenko beam-column with end rotational springs. Including the effect of connection stiffness, the relationship between the column shear and the measured lateral drift in the elastic range can be expressed as follows:

$$V = K_{11}\Delta_m \tag{2.20}$$

where

$$K_{11} = \frac{EIk^3}{\Psi}\left\{2kL\left(\sqrt{1-\mu}\right)\beta c - [(kL)^2 - (1-\mu)\beta^2]s\right\} \tag{2.21}$$

In the above expression, $\mu = P/GA_s$, $c = \cos\frac{kL}{\sqrt{1-\mu}}$, $s = \sin\frac{kL}{\sqrt{1-\mu}}$, and

$$\begin{aligned}\Psi = {} & 2\left(\sqrt{1-\mu}\right)\beta^2\left\{1 - \left[1 + \frac{(kL)^2}{\beta}\right]c\right\} \\ & -kL[(1-\mu)\beta^2 - 2\beta - (kL)^2]s\end{aligned} \tag{2.22}$$

Eq. (2.20) can be calibrated with the elastic portion of the measured lateral force-story drift test responses to determine β and the associated K_θ.

The calculated values of β for the fixed-fixed boundary condition test specimens are listed in Table 2.3. Note that it is difficult to achieve a rigid connection, i.e., $\beta \to \infty$, in real steel construction. Commentary of AISC 360 (AISC 2016b) states that it is acceptable to consider a connection to be fully restrained, i.e., able to maintain the angle between two members, when $\beta \geq 20$. A connection is considered simple and can be modeled as a hinge, i.e., it rotates without developing moment, when $\beta \leq 2$. Considering the β values listed in Table 2.3, the test end moment connections behaved in a more flexible manner when a low level of axial compression was applied to the specimen: β values associated with low-axial load specimens were lower than those associated with medium- and high-axial load specimens.

2.7.5 Beam-Column Tests with Fixed-Rotating Boundary Conditions and Constant Axial Compression

Member Lateral Drift and End Moment Calculation

Forces, moments, displacements, and rotations applied in all three primary directions of interest at the center of the SRMD platen were recorded [see Figure 2.18(b)]. For fixed-rotating boundary condition tests, a cyclic rotation in-phase with and proportional to the applied cyclic lateral drift was prescribed to the platen, resulting in strong-axis rotation at the column east end. The strong-axis rotation measured at the center of the platen, θ_E, reflects the strong-axis rotation at the moving (or east) end of the column, θ_m [see Figure 2.18(b)]. Thus,

$$\theta_m = \xi_m \left(\frac{\Delta_m}{L} \right) = \theta_E \tag{2.23}$$

where further discussion of the cyclic rotation loading sequence and the values of ξ_m are presented in Section 4.5.

The east (i.e., moving) end of column was connected to the SRMD platen a distance L_T away from this reference point. As a result of this setup, rotating the SRMD platen with respect to its center also displaced the east end of the specimens. To maintain a consistent loading protocol, this translation was accounted for in the prescribed lateral displacement

of the platen for testing. Accordingly, the lateral drift at the column moving end can be obtained from the following relationship.

$$\Delta_m = \Delta_T - \theta_E L_T \tag{2.24}$$

Figure 2.14(b) shows the inflection point of the fixed-rotating column, which locates closer to the rotating end depending on the magnitude of the end rotation that is applied in proportion to the lateral drift. Due to the unsymmetrical nature of the fixed-rotating boundary condition tests, the inflection point location also moves once the column exhibits inelastic behavior. Therefore, the approach described in Section 2.7.4 cannot be used to determine end moments. Instead, using the recorded strong-axis moment applied by the SRMD platen, M_T, a moment equilibrium can be applied to the entire system, and the moment at the column west end can be calculated. Figure 2.18(b) demonstrates this free body diagram. Thus, west (i.e., fixed) end moment becomes

$$M_W = V(L + L_T - \Delta_s) + P\Delta_T - M_T \tag{2.25}$$

Enforcing moment equilibrium in the column, the following equation calculates east end moment:

$$M_E = V(L - \Delta_s) + P\Delta_m - M_W \tag{2.26a}$$

which can be simplified to

$$M_E = M_T - P\theta_E L_T - VL_T \tag{2.26b}$$

The accuracy of the calculated moments [i.e., Eqs. (2.25) and (2.26)] was confirmed by comparing them with the end moments computed using strain gauge data when the column responded in the elastic range (results not shown).

Lateral Drift Correction

Because the end moments at the fixed and rotating ends were not the same in magnitude, connection rotation at each column end also differed in magnitude. Consequently, in addition to the applied end rotation at the moving end, connection flexibility also influenced the location of inflection point in the specimens. The following steps determine K_e for fixed-rotating specimens, which is needed in Eq. (2.12) to remove the effect of connection flexibility from the lateral drift responses:

(1) Determine the equivalent end rotational spring stiffness and locate the inflection point in the specimens.

(2) Based on the determined inflection point location, calculate an equivalent moving-end rotation assuming both column-end connections are rigid.

(3) Calculate K_e based on the equivalent moving-end rotation determined in (2).

Step 1: Determine the end rotational spring stiffness and inflection point location

By idealizing the connection flexibility at both ends of the specimens as rotational springs with an identical equivalent stiffness, $\beta(EI/L)$, Eq. (2.27) expresses the theoretical elastic lateral stiffness relationship of a fixed-rotating beam-column with rotationally flexible ends:

$$V = K_{11}\Delta_m - K_{12}\theta_m = \left(K_{11} - \frac{\xi_m}{L}K_{12}\right)\Delta_m \tag{2.27}$$

where K_{11} is as defined in Eq. (2.21) and

$$K_{12} = \frac{EIk^2\beta}{\Psi}\left[kLs + \left(\sqrt{1-\mu}\right)\beta(1-c)\right] \tag{2.28}$$

Eq. (2.27) is then calibrated with the measured lateral force-story drift elastic response to back-calculate β. Once β is determined, internal moment along the member can be expressed using the superposition principle:

$$M(x) = M_{\Delta_1}(x)\Delta_m - M_{\theta_1}(x)\theta_m = \left[M_{\Delta_1}(x) - \frac{\xi_m}{L}M_{\theta_1}(x)\right]\Delta_m \tag{2.29}$$

where

$$M_{\Delta_1}(x) = -\frac{2EIk^2\beta}{\Psi}\left[kL\cos\frac{kL}{2\sqrt{1-\mu}} + \left(\sqrt{1-\mu}\right)\beta\sin\frac{kL}{2\sqrt{1-\mu}}\right]\sin\frac{k(L-2x)}{2\sqrt{1-\mu}} \tag{2.30}$$

$$M_{\theta_1}(x) = \frac{EIk\beta}{\Psi}\left\{kL\left(\sqrt{1-\mu}\right)\beta\cos\frac{k(L-x)}{\sqrt{1-\mu}} - [(kL)^2+\beta]\sin\frac{k(L-x)}{\sqrt{1-\mu}} - \beta\sin\frac{kx}{\sqrt{1-\mu}}\right\} \tag{2.31}$$

and x is measured from the moving end. Setting Eq. (2.29) to zero and solving for x give the inflection point location, x_{IP}, in the specimen. See Table 2.4 for the calculated x_{IP} values for the three test specimens.

Step 2: Determine an equivalent moving-end rotation

To eliminate the effect of rigid-body rotation caused by connection flexibility that contributed to both the measured lateral drift (Δ_m) and end rotation (θ_m) as shown in Figure 2.14(b), the specimen is assumed to have ideal fixed-rotating boundary conditions, i.e., rigid end connections as shown in Figure 2.14(a), and sustain an equivalent moving-end rotation of

$$\theta = \xi\left(\frac{\Delta}{L}\right) \tag{2.32}$$

Essentially, if the specimen sustained θ and Δ at the moving end with ideal boundary conditions, it would have the same inflection point location as if it sustained θ_m and Δ_{m} with flexible end connections; both the ideal and real configurations are equivalent. The equivalent moving end rotation, θ, is determined as follows.

Similar to Eq. (2.29), Eq. (2.33) expresses the theoretical internal moment along a beam-column with ideal fixed-rotating boundary conditions:

$$M'(x) = \left[M'_{\Delta_1}(x) - \frac{\xi}{L}M'_{\theta_1}(x)\right]\Delta \tag{2.33}$$

where

$$M'_{\Delta_1}(x) = \frac{-2EIk^2\left(\sqrt{1-\mu}\right)\sin\frac{kL}{2\sqrt{1-\mu}}\sin\frac{k(L-2x)}{2\sqrt{1-\mu}}}{2\sqrt{1-\mu}(1-c) - kL(1-\mu)s} \tag{2.34}$$

$$M'_{\theta_1}(x) = \frac{EIk\left\{kL\left(\sqrt{1-\mu}\right)\cos\frac{k(L-x)}{\sqrt{1-\mu}} - \sin\frac{k(L-x)}{\sqrt{1-\mu}} - \sin\frac{kx}{\sqrt{1-\mu}}\right.}{2\sqrt{1-\mu}(1-c) - kL(1-\mu)s} \tag{2.35}$$

Eqs. (2.34) and (2.35) are obtained by setting $\beta \to \infty$ in Eqs. (2.30) and (2.31) for $M_{\boldsymbol{\Delta_1}}(x)$ and $M_{\boldsymbol{\theta_1}}(x)$.

Substituting x_{IP} determined in Step 1 into Eq. (2.33) gives

$$M'(x_{IP}) = \left[M'_{\Delta_1}(x_{IP}) - \frac{\xi}{L}M'_{\theta_1}(x_{IP})\right]\Delta \tag{2.36}$$

Accordingly, ξ can be calculated such that $M'(x_{IP}) = 0$ to make the inflection point location of the ideal configuration identical to that of the actual configuration. The value of θ is then calculated per Eq. (2.32). See Table 2.4 for the calculated ξ values.

Step 3: Calculate K_e

Eq. (2.37) expresses the theoretical lateral force-story drift relationship of the specimens with equivalent ideal fixed-rotating boundary conditions.

$$V = \left(K'_{11} - \frac{\xi}{L}K'_{12}\right)\Delta \tag{2.37}$$

Thus, K_e based on the Timoshenko theory considering both shearing and second-order effects becomes

$$K_e = K'_{11} - \frac{\xi}{L} K'_{12} \tag{2.38}$$

where K'_{11} is calculated as in Eq. (2.17) and K'_{12} is (Chugh 1977)

$$K'_{12} = \frac{EIk^2(1 - \cos kL)}{2\left(1 + \frac{P}{GA_s}\right)(1 - \cos kL) - kL \sin kL} \tag{2.39}$$

The calculated K_e is then used in Eq. (2.12) to compute the corrected drift.

An example correction of the lateral force-story drift response of Specimen 11H-BC is shown in Figure 2.21. Note that the calculated values of K_{me} and K_e are 55.70 and 64.00 kips/in., respectively, showing that the connection flexibility reduces the lateral stiffness by 13 %. Table 2.4 summarizes key variables associated with this drift correction procedure for each fixed-rotating specimen.

2.7.6 Beam-Column Tests with Fixed-Fixed Boundary Conditions and Varying Axial Load Sequences

Member Lateral Drift and End Moment Calculation

This process is the same as that described in Section 2.7.4.

Lateral Drift Correction

The difference in the second-order effect due to varying axial loads can be small for the wide-flange beam-column specimens tested in this program with strong-axis bending. Therefore, the simplified drift correction approach described in Section 2.7.4 is used for this testing condition. The average value of the axial load range is used for P.

2.7.7 Beam-Column Tests with Fixed-Rotating Boundary Conditions and Varying Axial Load Sequences

Member Lateral Drift and End Moment Calculation

This process is the same as that described in Section 2.7.5.

Lateral Drift Correction

The difference in the second-order effect due to varying axial loads can be small for the wide-flange beam-column specimens tested in this program with strong-axis

bending. Therefore, the simplified drift correction approach described in Section 2.7.5 is used for this testing condition. The average value of the axial load range is used for P.

2.8 Characterization of Failure Modes

Testing of deep, slender columns in this study and shallow, stocky (W14) columns by Newell and Uang (2008) has shown that beam-column buckling mode characterizes the column hysteretic response. Within a certain limit of L/r_y, a parameter based on section slenderness properties was proposed to predict the governing buckling mode (or failure mode), which are categorized into: (1) Symmetric Flange Local Buckling (SFB) mode, (2) Anti-symmetric Local Buckling (ALB) mode, and (3) Coupled Buckling (CB) mode (Ozkula et al. 2017). The buckled configuration and hysteretic feature of each failure mode are briefly summarized herein. Failure mode classifications and certain phenomena discussed in this section are referenced in Chapters 3, 5, and 7 to help explain the column behaviors observed during testing.

2.8.1 Symmetric Flange Local Buckling (SFB) Mode

For highly ductile sections with relatively low web and flange slenderness ratios (mostly shallow columns, e.g., W12 and W14 columns), SFB is the common governing failure mode. It involves in-plane plastic hinging at the column ends (or only at the bottom end of first-story columns in an SMF in real application) without out-of-plane, global-type member buckling. In the plastic hinge regions, at least a half-wave local buckle is observed at each half-width flange in a *symmetric* (or 'mirrored') configuration with respect to the web plane as shown in Figure 2.22. For example, both top and bottom half-width flanges of the northeast flange in Figure 2.22(a) buckle outward locally, and their respective apexes are aligned. In addition, web local buckling, if occurs, is limited for this failure mode. Figure 2.23 illustrates the cross-sectional view of the SFB configuration. The corresponding column response exhibits large ductility capacity and limited axial shortening even under high axial compression (Newell and Uang 2008). In fact, strength degradation is moderate and happens gradually for columns with SFB mode.

2.8.2 Anti-symmetric Local Buckling (ALB) Mode

As the section slenderness ratios increase, both flange and web local buckling modes occur simultaneously as the web cannot provide sufficient rotational restraint to maintain

fix-ended boundary condition for the half-width, unstiffened flange elements. Figure 2.25 shows this combined local buckling mode, which features at least a half-wave local buckle at each half-width flange in an *anti-symmetric* (or 'opposite') configuration with respect to the web plane. Considering the northeast flange in Figure 2.25(a) for example, the top and bottom half-width flanges of the same flange buckle outward and inward, respectively, and their respective apexes are not aligned; the apex of the outward flange local buckle usually locates closer to the end plate compared to that of the inward one. In addition, as the web tries to remain perpendicular to the flanges at the web-flange junctions, it buckles locally in the direction that complies with the flange local buckling configuration; Figure 2.24 demonstrates the cross-sectional view of this phenomenon. Ultimately, ALB refers to the in-plane, plastic hinging failure mode with this combined local buckling configuration. Once ALB occurs, drastic strength degradation prevails, accompanied by significant column axial shortening. As a result, the column ductility capacity is relatively limited compared to the SFB case. The ductility capacity associated with this failure mode is sensitive to the axial force level.

For specimens with ALB failure mode that sustain the AISC loading protocol in strong-axis bending, the ALB sequence initiates with one *half-wave buckle set* (i.e., one half-wave buckle at each unstiffen flange and stiffened web element) as shown in Figure 2.25(a). At higher drifts, some ALB specimens also develop an additional half-wave buckle set, making a full-wave buckle set, as shown in Figure 2.25(b). This full-wave ALB configuration usually results in severely deformed column ends, which initiates an out-of-plane, rigid-body translation of the column portion between the buckled regions; this movement should not be confused with lateral-torsional buckling or flexural buckling.

2.8.3 Coupled Buckling (CB) Mode

Coupled Buckling (CB) mode involves both local buckling and global-type, lateral-torsional buckling (LTB). The sequence of these local and global instabilities may not be obvious for all specimens since the two reciprocal phenomena are *coupled*. In apparent cases, two observations include: (1) local buckling at column proceeds LTB, and (2) LTB proceeds local buckling. Figure 2.26(a) shows the buckled configuration of the former sequence of which local buckling usually exhibits the ALB pattern as shown. The latter buckled configuration shown in Figure 2.26(b) is similar to the former one regarding the

out-of-plane, LTB-type buckling behavior. However, local buckling pattern of the latter case as shown in Figure 2.27(a) only exhibits half-wave local buckles in either the top or bottom half-width flanges, not both like the SFB or ALB pattern; therefore, this type of flange local buckling should not be confused with the conventional local buckling as in SFB or ALB mode. Instead, it was triggered by LTB, which induces nonuniform stress distribution across the flange width because each flange bends about its strong axis (explained in the following paragraph). In this report, LTB-induced flange local buckling refers to this phenomenon.

Twisting and out-of-plane bending associated with the LTB movements caused stress distribution to be nonuniform across the flange width. To demonstrate this phenomenon, strains at the upper and lower flange edges are plotted against each other in Figure 2.28 [see West End of Figure 2.26(b) for the strain gauge locations in the specimen under consideration]. Both strains are initially the same in magnitude (data points move along the 1:1 or 45° line), indicating a uniform bending stress distribution across the flange width due to in-plane bending of the specimen. Tendency of LTB then can be observed in the plot as the strains started to deviate from the 1:1 line, which initiates at *SDA* = 0.015 rad. Physically, flaking of the whitewash as shown in Figure 2.29(a) also illustrates this nonuniform stress distribution due to LTB; it exhibits a *sloped* flaking pattern as the upper flange portion experiences more compression and flakes off more mill scale compared to the lower portion. As twisting and out-of-plane movements become more visually observable at higher *SDA* levels, the out-of-plane, torsional, and warping stresses induced by LTB increase drastically. As a result, the strains become more nonuniform and the sloped flaking pattern grows drastically as shown in Figure 2.29(b) and Figure 2.29(c). In this case, the conventional way of defining the plastic hinge zone or length becomes difficult and may not be meaningful.

Furthermore, LTB buckling configuration can be further subdivided into two cases: single and reverse curvatures; Figure 2.26(a) and Figure 2.26(b) refer to the former case, while Figure 2.26(c) refers to the latter case. The terms “single curvature” and “reverse curvature” refer to the deformed column profile between inflection points near member ends annotated as point a and b in Figure 2.30.

Table 2.1 Test Matrix for Phase 1 Testing

Group No.	Section	Specimen Designation	L (ft)	Slenderness			Column Axial Load		Bending Direction
				$\frac{b_f}{2t_f}$	$\frac{h}{t_w}$	$\frac{L}{r_y}$	C_a	P_u (kips)	
1	W24×176	1L 1M 1H	18	4.81	28.7	71.1	0.2 0.4 0.6	465 931 1396	Strong-axis
2	W24×131	2Z 2L 2L-P 2M 2M-NF 2H	18	6.70	35.6	72..7	0.0 0.2 0.2 0.4 0.4 0.6	0 347 347 695 695 1042	
3	W24×104	3L 3M 3H	18	8.50	43.1	74.2	0.2 0.4 0.6	276 553 829	
4	W24×84	4L 4M	18	5.86	45.9	110.8	0.2 0.4	222 445	
5	W24×55	5L 5LM 5M	18	6.94	54.6	161.2	0.2 0.3 0.4	146 219 292	
6	W24×131	6L 6L-P 6H	18	6.70	35.6	72..7	0.2 0.2 0.6	347 347 1042	Weak-axis
7	W24×131	7M	18	6.70	35.6	72..7	0.4	695	Biaxial

Table 2.2 Steel Mechanical Properties for Phase 1 Testing

Group No.	Section	Comp.	Yield Stress (ksi)	Tensile Strength (ksi)	Elong.[a] (%)
1	W24×176	Flange	52.5	81.8	38.1
		Web	58.5	82.5	38.0
2, 6, 7	W24×131	Flange	50.8	75.9	38.4
		Web	55.4	77.7	35.4
3	W24×104	Flange	51.5	78	36.5
		Web	58.1	80.6	31.3
4	W24×84	Flange	51.3	77.6	36.2
		Web	58.8	80.2	31.0
5	W24×55	Flange	53.7	71.5	38.0
		Web	59.8	74.3	32.4

[a] Elongations are based on a 2-in. gauge length.

Table 2.3 Data Reduction Parameters: Test Specimens with Fixed-Fixed Boundary Conditions

Specimen No.	Shape	L (in.)	P (kips)	μ ($\times 10^{-3}$)	K_e (kips/in.)	K_{me} (kips/in.)	β	K_θ ($\times 10^6$ kip·in/rad)	Stiffness reduction[a] (%)
1L	W24×176	216	464	2.46	157.69	114.02	13.00	9.92	27.7
1M	W24×176	216	929	4.93	155.25	123.63	19.75	15.06	20.4
1H	W24×176	216	1,395	7.40	152.81	125.06	22.84	17.42	18.2
2Z	W24×131	216	28	0.18	115.84	85.02	13.82	7.46	26.6
2L	W24×131	216	347	2.28	114.16	81.48	12.72	6.86	28.6
2L-P	W24×131	216	345	2.26	114.17	86.45	21.74	11.74	24.3
2M	W24×131	216	697	4.57	112.31	92.34	23.94	12.92	17.8
2M-NF	W24×131	216	693	4.55	112.33	88.27	14.94	8.07	21.4
2H	W24×131	216	1,038	6.81	110.51	87.67	19.92	10.75	20.7
3L	W24×104	216	273	2.17	89.01	71.95	21.78	9.07	19.2
3M	W24×104	216	548	4.35	87.55	74.28	29.32	12.20	15.2
3H	W24×104	216	823	6.53	86.10	72.95	29.31	12.20	15.3
4L	W24×84	216	219	1.85	70.03	60.46	33.44	10.64	13.7
4M	W24×84	216	443	3.75	68.84	61.43	44.59	14.19	10.8
5L	W24×55	216	143	1.44	41.56	37.84	56.36	10.22	8.9
5LM	W24×55	216	220	2.21	41.15	38.53	85.17	15.44	6.4
5M	W24×55	216	254	2.55	40.96	39.02	82.88	15.02	4.7
6L	W24×131	216	354	-	-	9.60	-	-	-
6L-P	W24×131	216	348	-	-	9.46	-	-	-
6H	W24×131	216	1,043	-	-	6.14	-	-	-
7M	W24×131	216	687	4.51	112.37	89.93	20.73	11.19	20.0

[a] Stiffness reduction $= (K_e - K_{me})/K$.

Table 2.3 Data Reduction Parameters: Test Specimens with Fixed-Fixed Boundary Conditions (continued)

Specimen No.	Shape	L (in.)	P (kips)	μ ($\times 10^{-3}$)	K_e (kips/in.)	K_{me} (kips/in.)	β	K_θ ($\times 10^6$ kip·in/rad)	Stiffness reduction[a] (%)
11H-VAU	W24×176	210	1033	5.48	166.85	134.59	20.88	16.38	19.3
12LM	W30×261	210	1,037	3.53	358.58	243.79	9.61	17.39	32.0
12LM-P	W30×261	210	1032	3.52	358.61	236.60	12.82	23.19	34.0
13M	W30×173	210	914	4.43	230.40	177.18	15.71	17.86	23.1
14L	W30×90	212	237	1.60	109.66	96.65	37.71	18.62	11.9
15L	W18×192	212	505	2.79	118.53	97.09	23.75	12.57	18.1
16M	W18×130	212	684	5.42	74.36	63.91	33.20	11.17	14.0
17L	W18×76	212	197	2.47	41.95	39.24	78.66	14.31	6.5
21M-VAU	W18×130	212	167	1.32	77.17	66.78	34.10	11.48	13.5
21M-NF	W18×130	212	686	5.43	74.35	58.25	26.70	8.99	21.7
21M-VAM	W18×130	212	679	5.38	74.38	64.74	36.89	12.41	13.0
22L	W30×148	216	389	1.89	183.62	143.67	17.63	15.81	21.8
23L	W18×60	168	155	1.99	61.42	55.84	52.34	8.89	9.1
24L	W14×82	168	213	2.97	54.68	46.90	32.14	4.89	14.2
25L	W14×53	168	137	2.64	34.24	32.06	79.69	7.44	6.4
26LM	W14×132	168	520	5.72	89.48	76.71	30.81	8.14	14.3
26LM-VAM	W14×132	168	529	5.82	89.42	79.44	41.20	10.88	11.2
27L	W24×84	216	219	1.85	70.03	61.03	35.90	11.42	12.9

[a] Stiffness reduction $= (K_e - K_{me})/K_e$.

Table 2.4 Data Reduction Parameters: Test Specimens with Fixed-Rotating Boundary Conditions

Specimen No.	Shape	L (in.)	ξ_m	P (kips)	μ ($\times 10^{-3}$)	β	K_θ ($\times 10^6$ kip·in/rad)	x_{IP} (in.)	ξ	K_e (kips/in.)	K_{me} (kips/in.)	Stiffness reduction[a] (%)
11H-BC	W24×176	210	1.12	1,393	7.40	23.49	18.42	43.5	1.18	64.00	55.70	13.0
13M-BC	W30×173	210	1.00	914	4.43	17.20	19.55	52.9	1.06	105.62	88.45	16.3
16M-BC	W18×130	212	1.00	688	5.45	33.56	11.29	61.6	1.04	33.84	30.38	10.2
21M-VAU-BC	W18×130	212	1.00	174	1.38	37.42	12.59	62.0	1.04	36.62	33.40	8.8

[a] Stiffness reduction $= (K_e - K_{me})/K_e$.

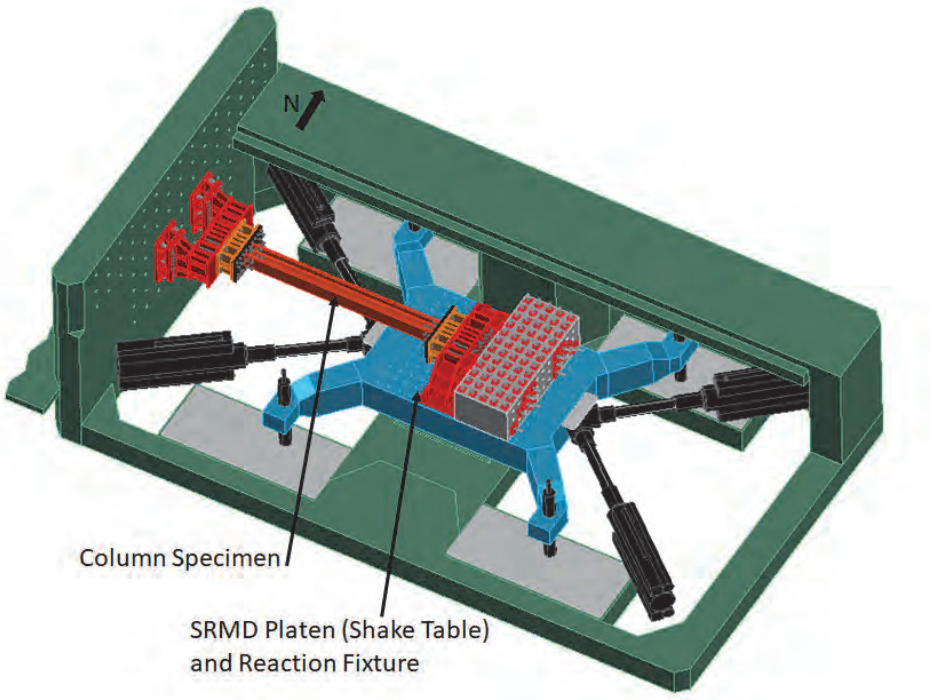

(a) Specimen Orientation in the SRMD

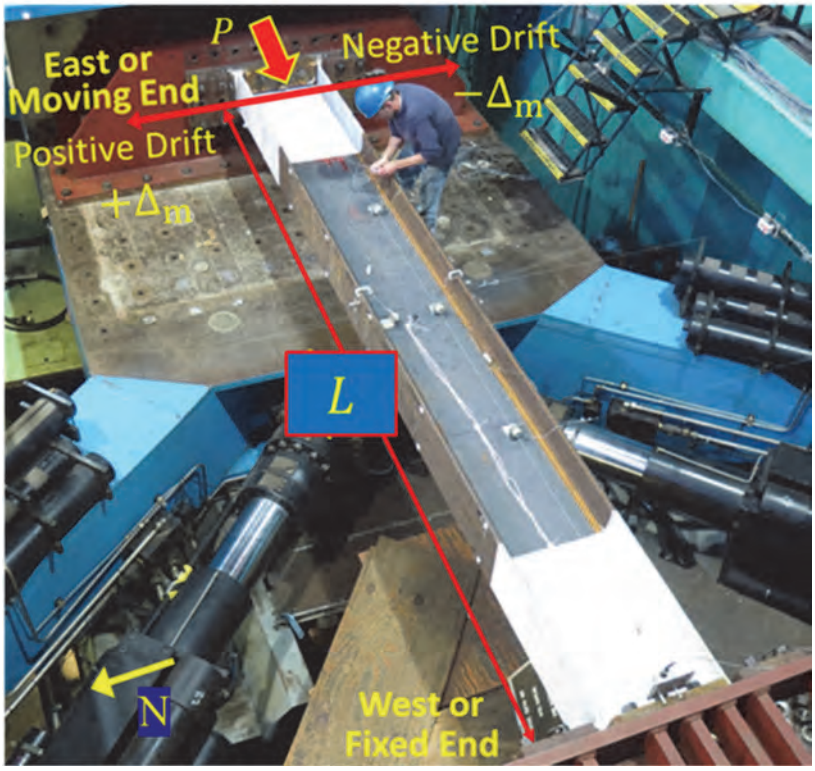

(b) Test Setup Overview

Figure 2.1 Test Setup in the Seismic Response Modification Device (SRMD)

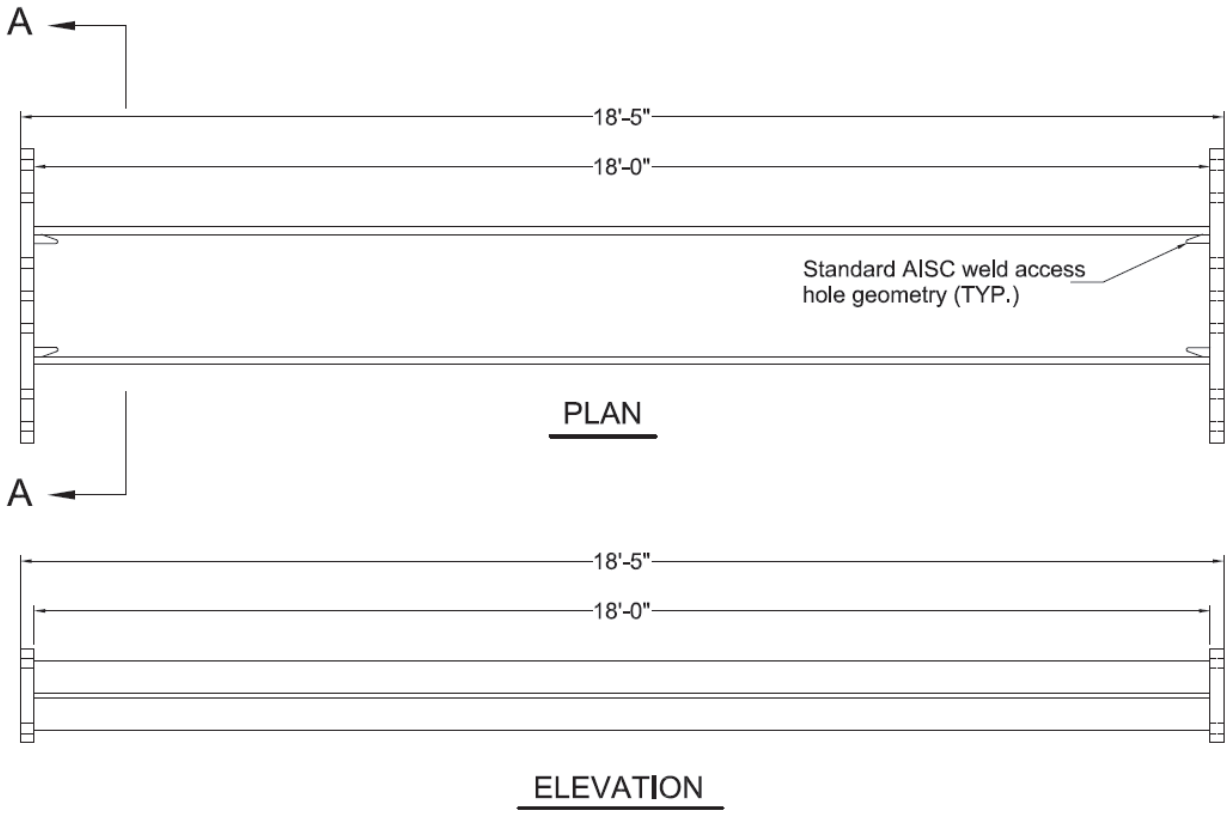

(a) Overall Dimentions

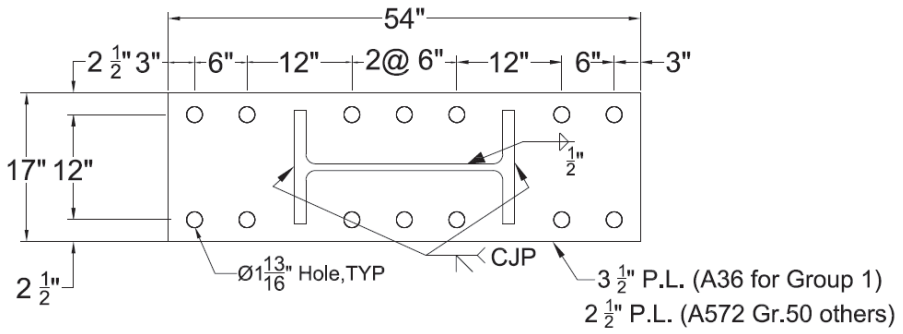

(b) Base Plate

Figure 2.2 Phase 1 Specimen Geometry and End Details (Strong-Axis)

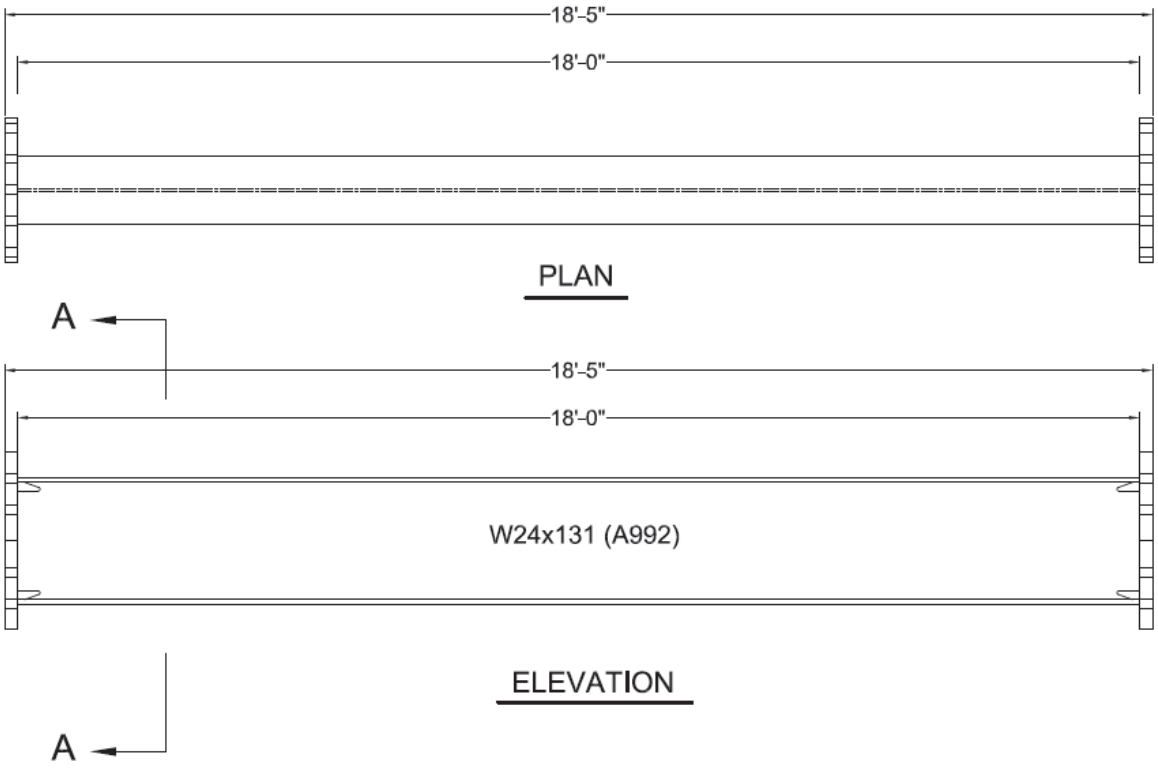

(a) Overall Dimentions

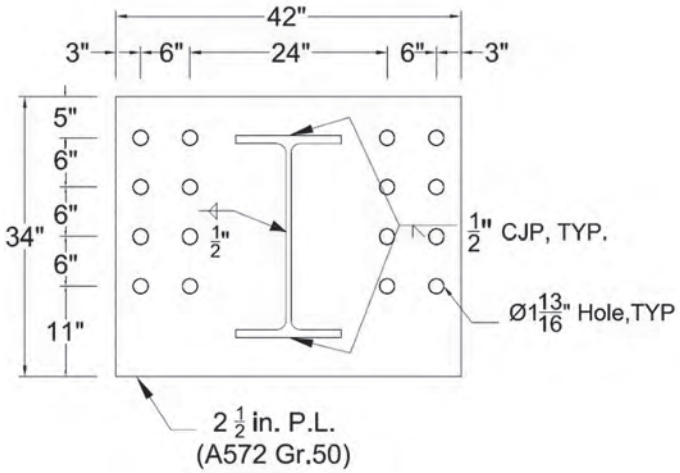

(b) Base Plate

Figure 2.3 Phase 1 Specimen Geometry and End Details (Weak-Axis)

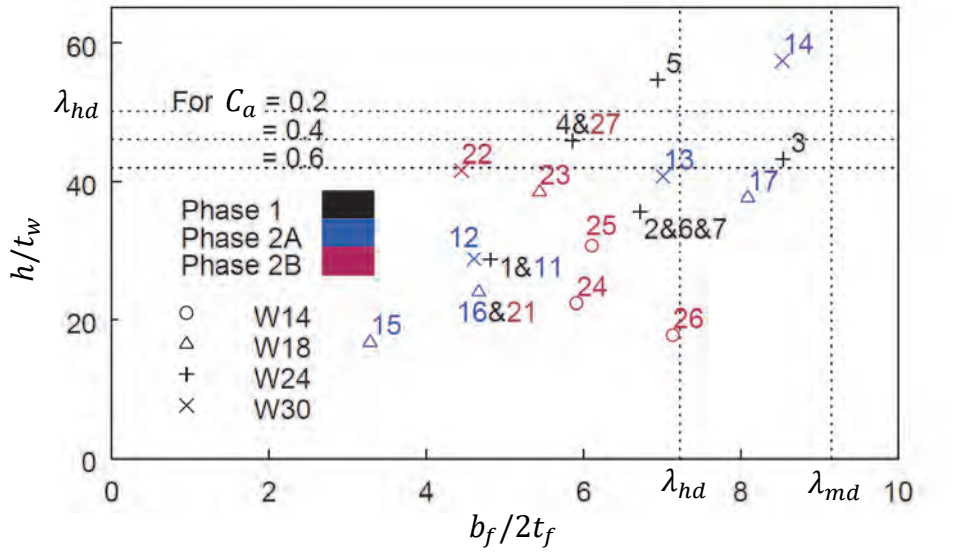

Figure 2.4 Distribution of Width-to-Thickness Ratios Annotated with Group Numbers

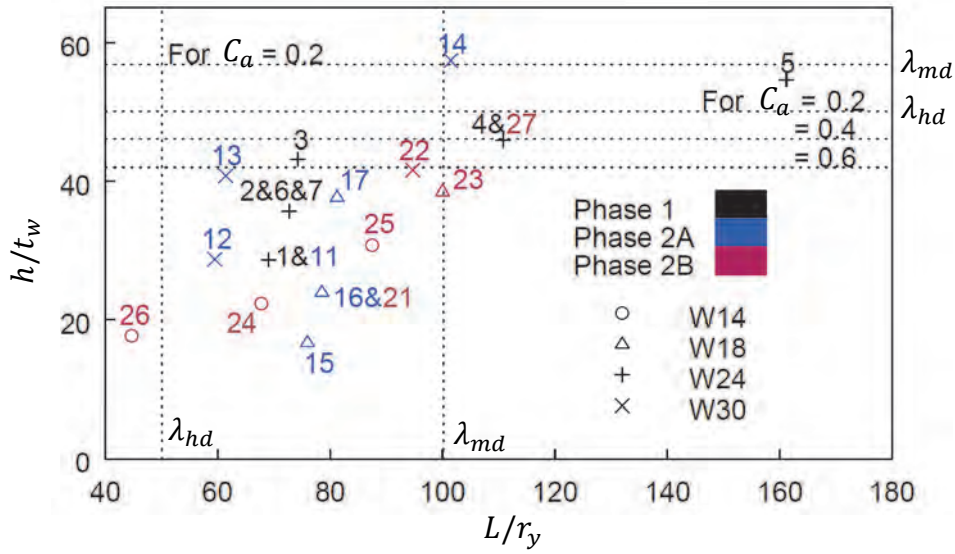

Figure 2.5 Distribution of L/r_y Ratios Annotated with Group Numbers

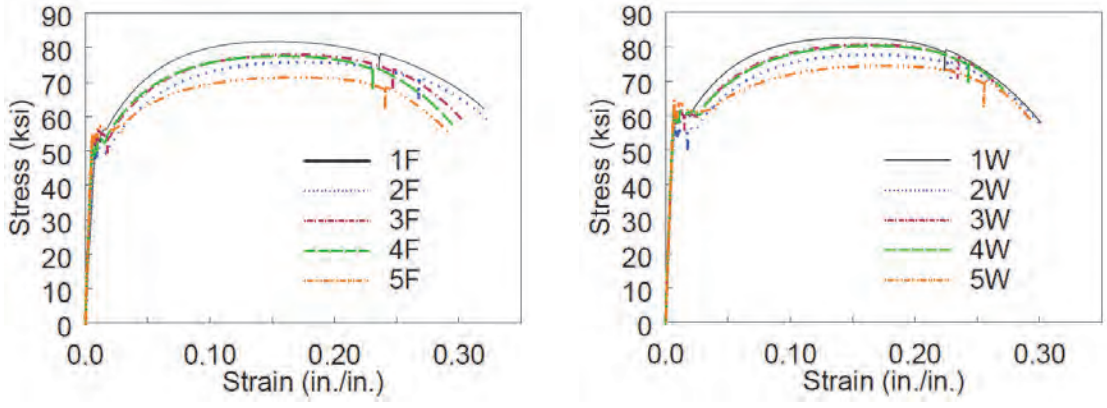

(a) Flange (b) Web

Figure 2.6 Phase 1 Engineering Strain versus Stress Curves

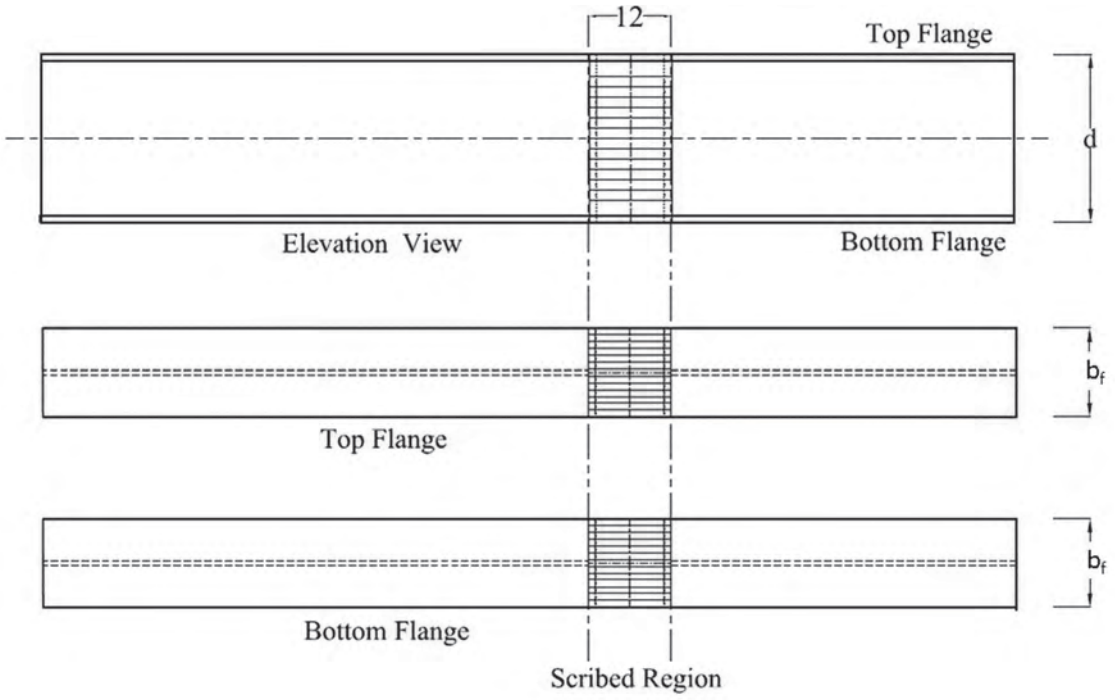

Figure 2.7 Residual Stress Measurements: Sectioning Locations

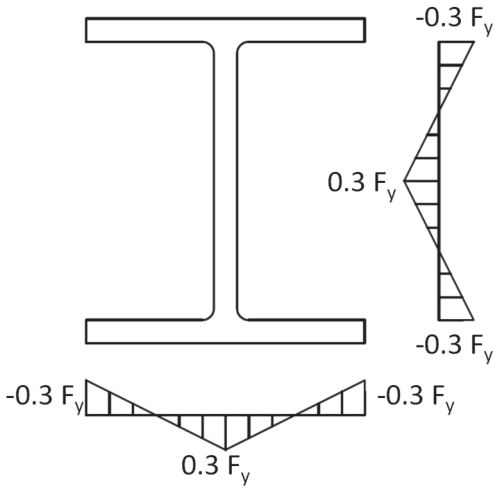

Figure 2.8 Idealized Residual Stress Distribution (Ziemian 2010)

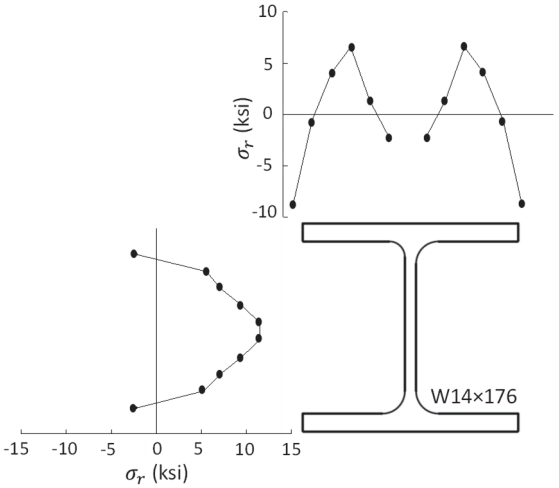

(a) W14×176

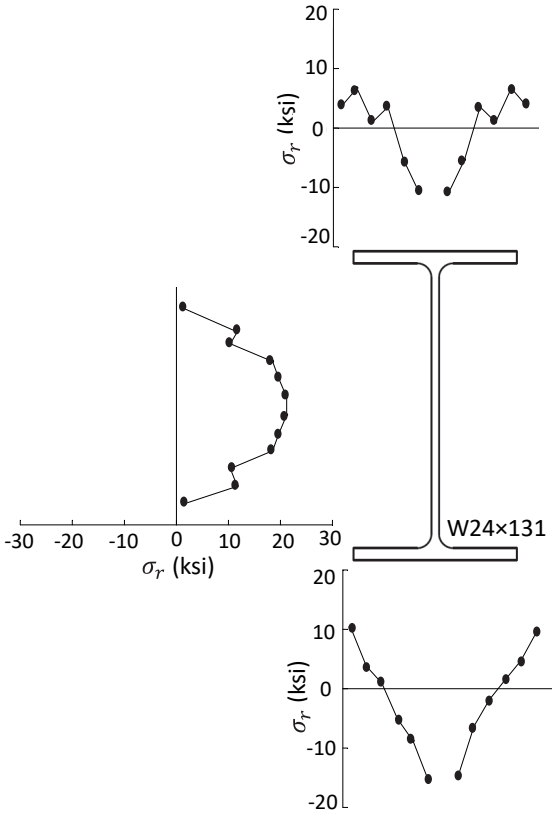

(b) W24×131

Figure 2.9 Measured Residual Stress Distributions

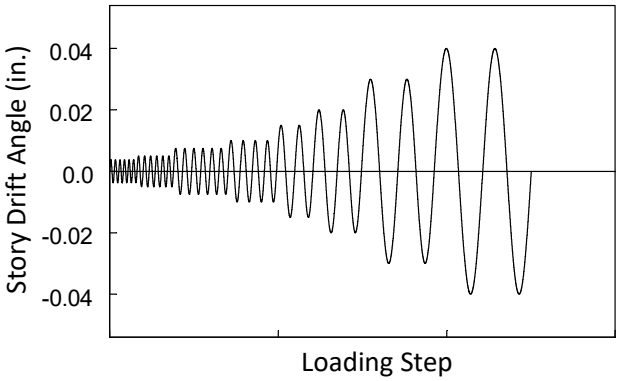

(a) AISC Loading Protocol

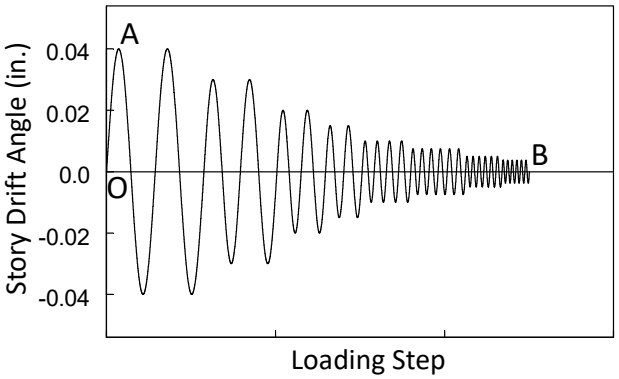

(b) Monotonic and Reversed AISC Loading Protocol

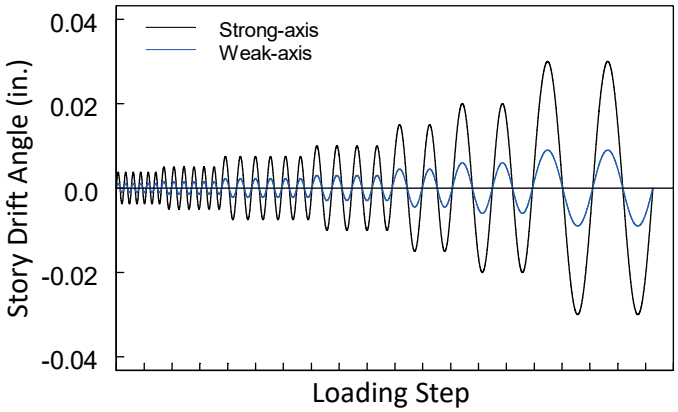

(c) Biaxial Loading Protocol

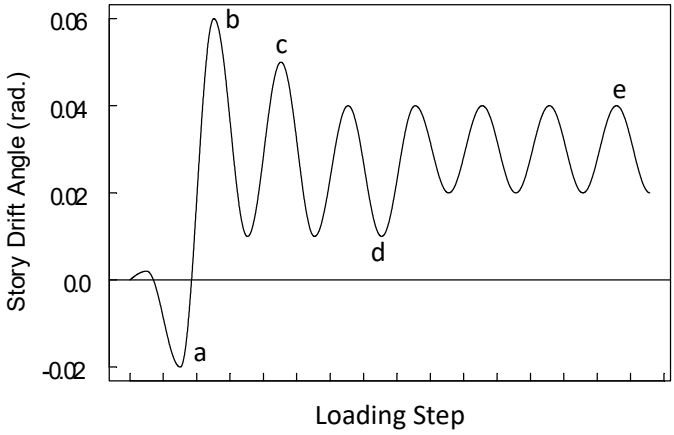

(d) Near-Fault Loading Protocol

Figure 2.10 Phase 1 Story Drift Angle Sequences

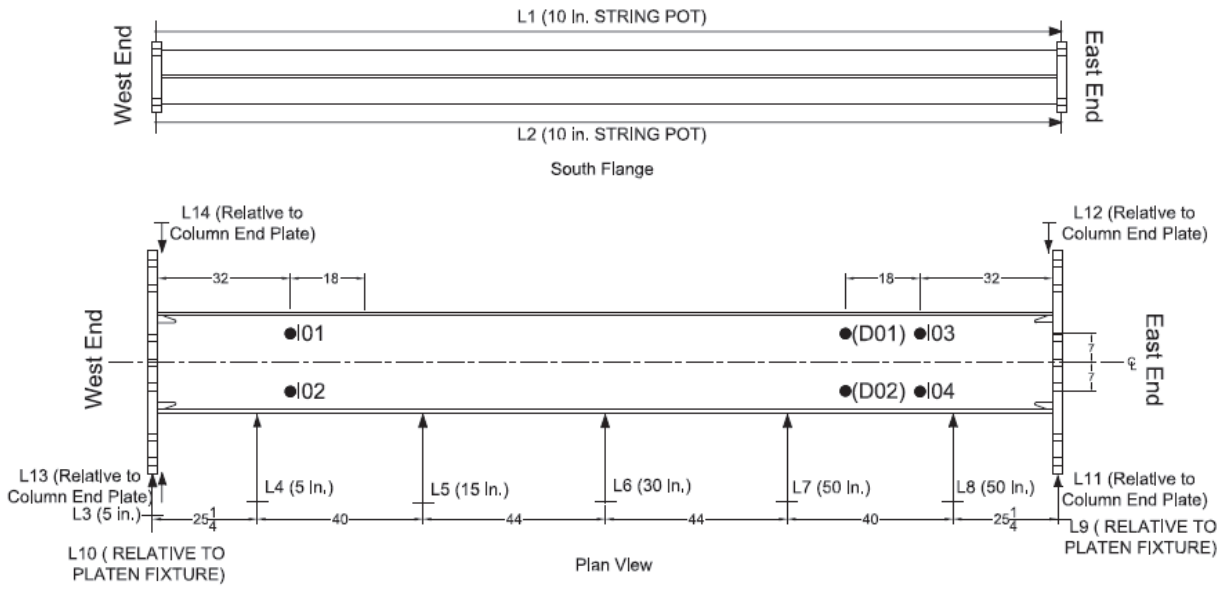

Figure 2.11 Phase 1 Displacement Transducer and Inclinometer Layout

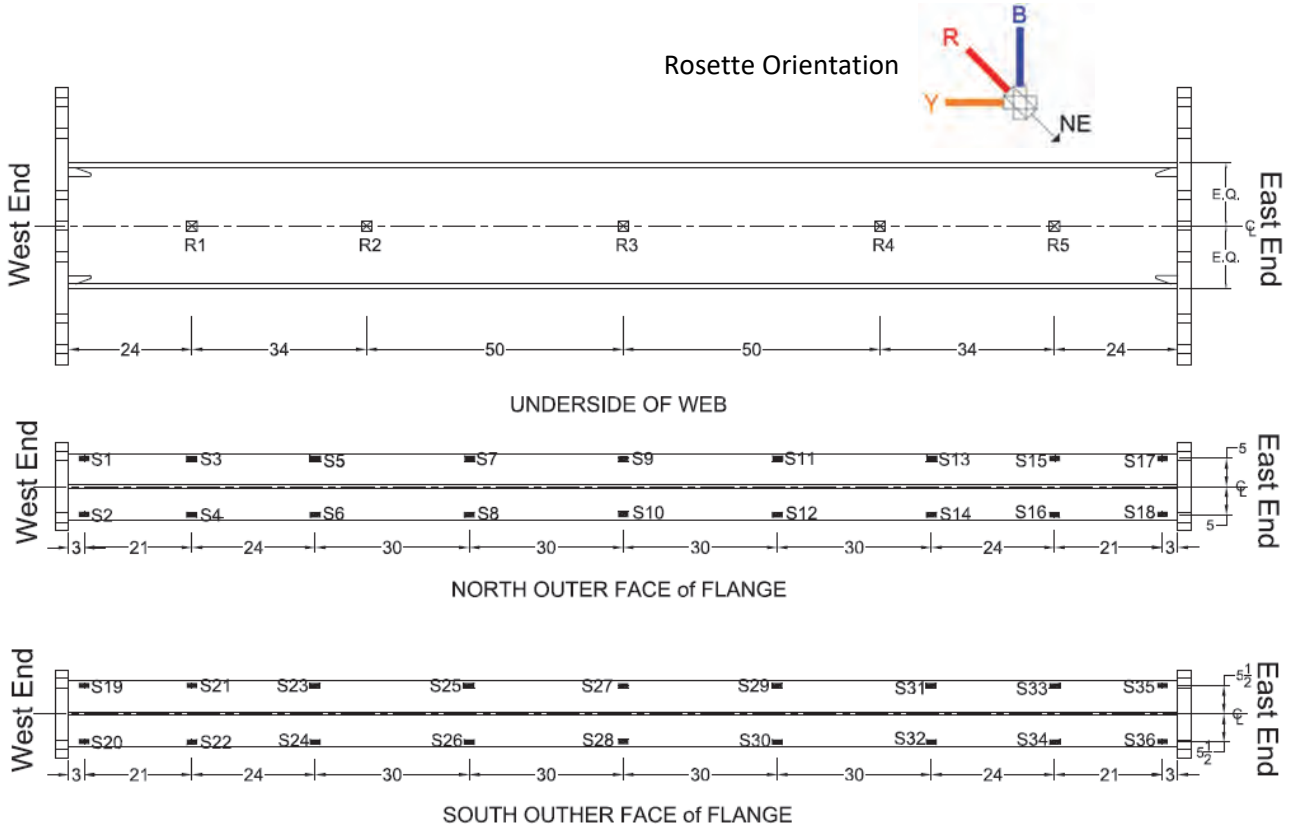

Figure 2.12 Phase 1 Rosette and Uniaxial Strain Gauge Layout

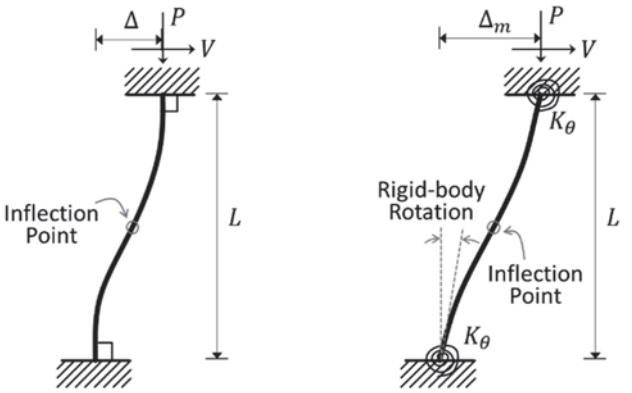

(a) (b)

Figure 2.13 Fixed-Fixed Beam-Column with Axial Load and Lateral Drift: (a) Ideal Boundary Conditions; (b) Actual Boundary Conditions

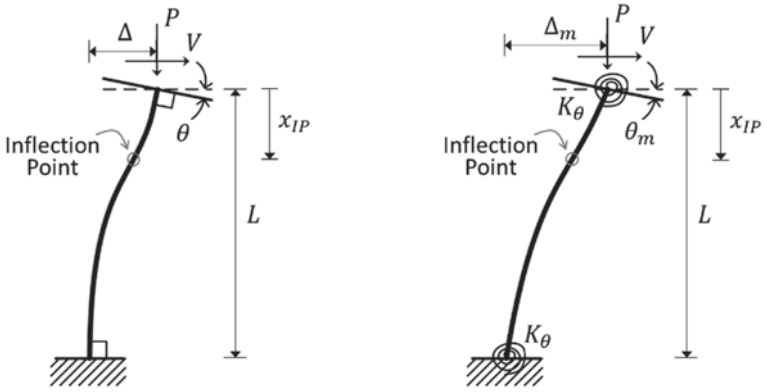

(a) (b)

Figure 2.14 Fixed-Rotating Beam-Column with Axial Load, Lateral Drift, and Top-End Rotation: (a) Ideal Boundary Conditions; (b) Actual Boundary Conditions

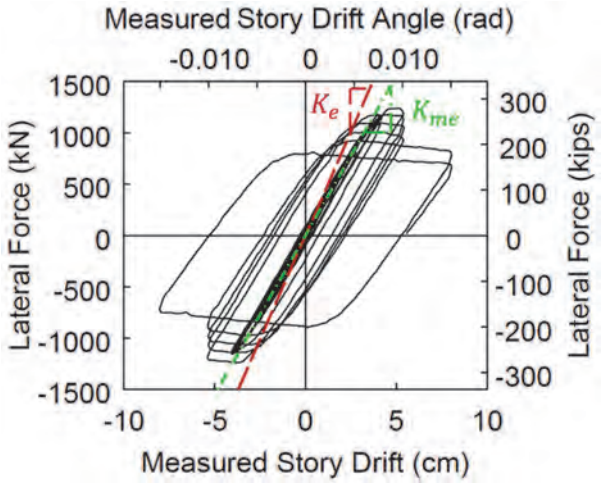

Figure 2.15 Global Response of Specimen 13M (W30×173) with Strong-Axis Bending

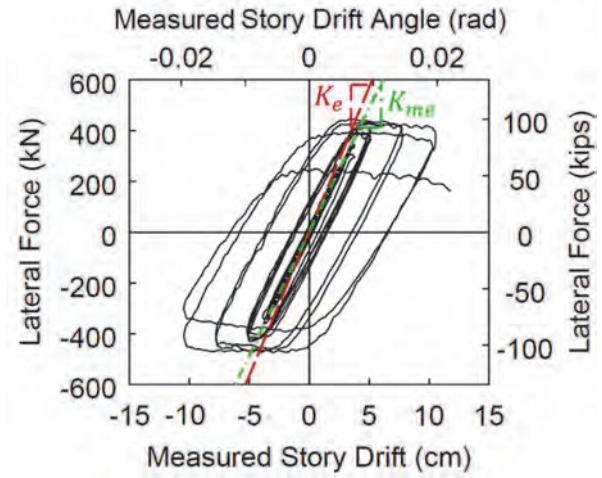

Figure 2.16 Global Response of Specimen 11H-BC (W24×176) with Strong-Axis Bending

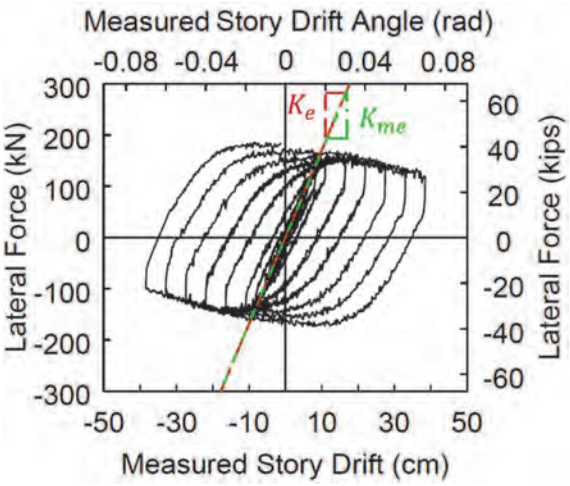

Figure 2.17 Global Response of Specimen 6L (W24×131) with Weak-Axis Bending

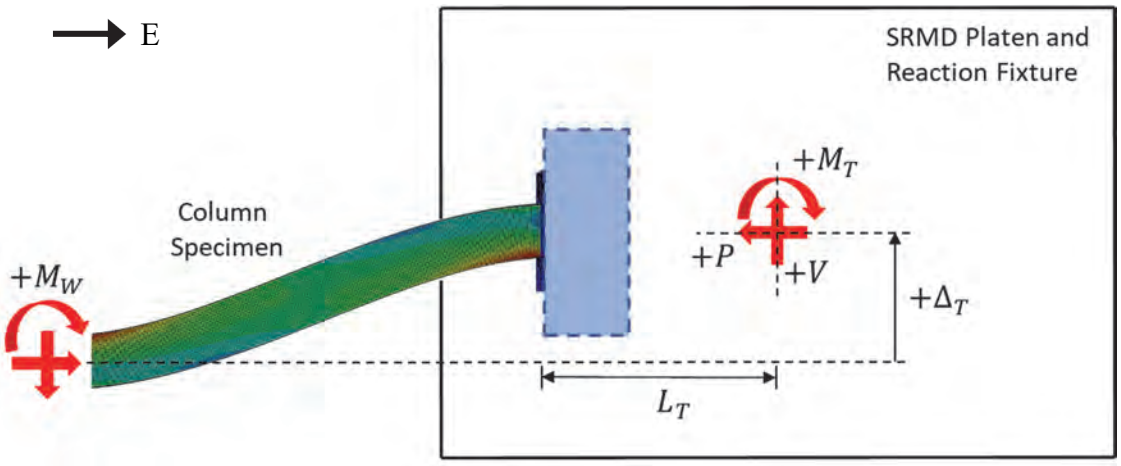

(a) Fixed-Fixed Boundary Condition

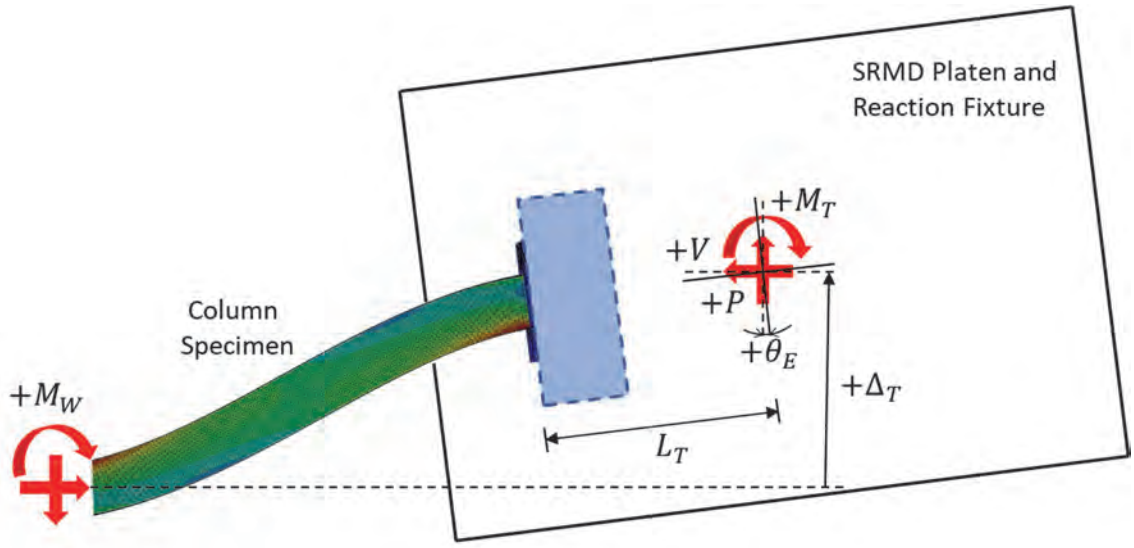

(b) Fixed-Rotating Boundary Condition

Figure 2.18 Platen Free Body Diagram

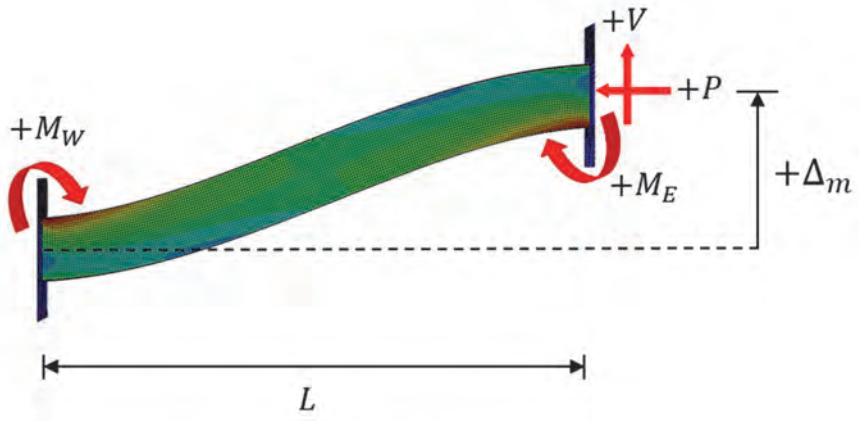

Figure 2.19 Sign Convention

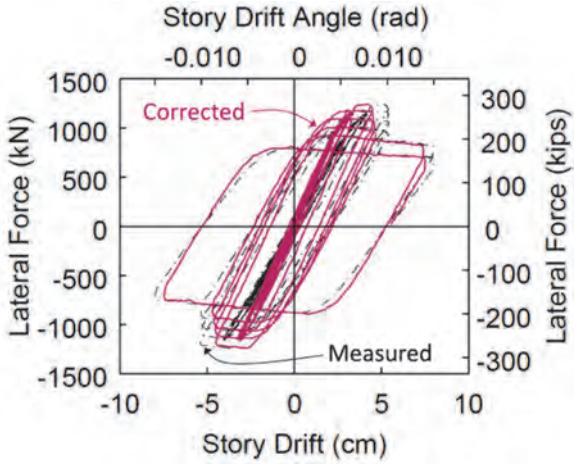

Figure 2.20 Corrected versus Uncorrected Hysteresis Response of Specimen 13M

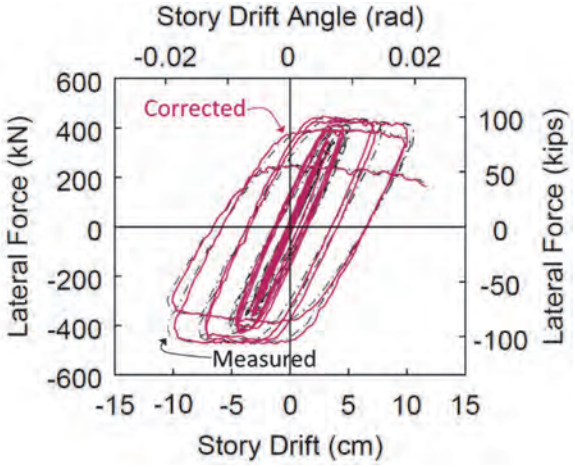

Figure 2.21 Corrected versus Uncorrected Hysteresis Response of Specimen 11H-BC

(a) East End (b) Web at West End (c) West End

Figure 2.22 Symmetric Flange Local Buckling (SFB) Mode of W14×176 Section with $C_a = 0.61$ (Newell and Uang 2008)

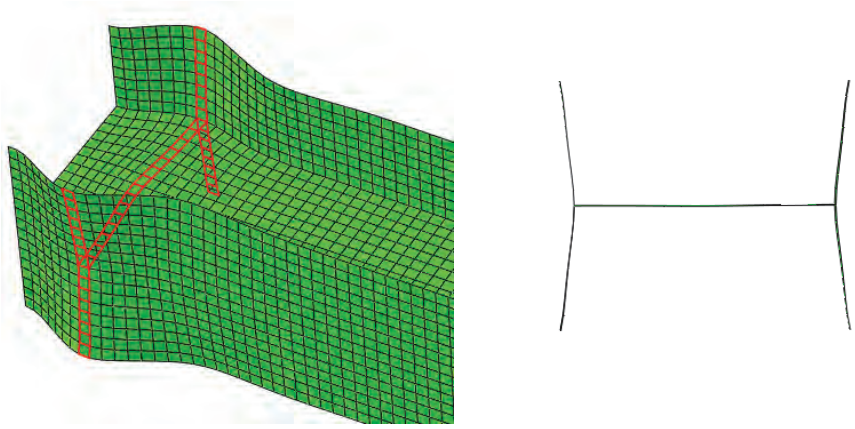

(a) Overall (b) Cross-sectional View

Figure 2.23 Flange Local Buckling Configuration in SFB

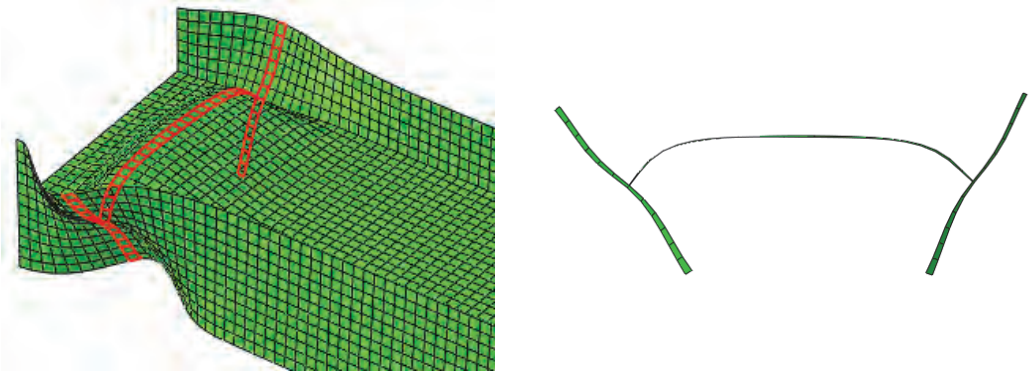

(a) Overall (b) Cross-sectional View

Figure 2.24 Flange and Web Local Buckling Configuration in ALB

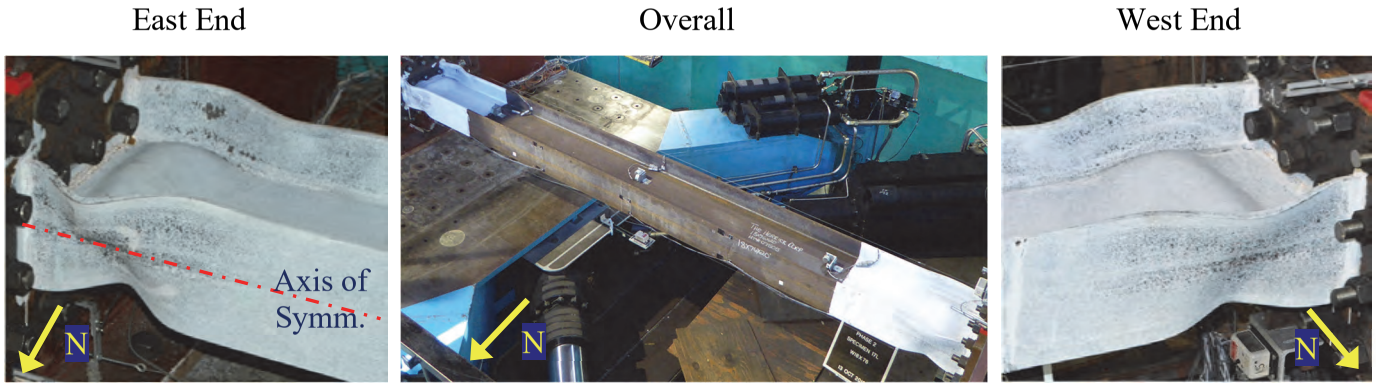

(a) *SDA* = 0.03 rad

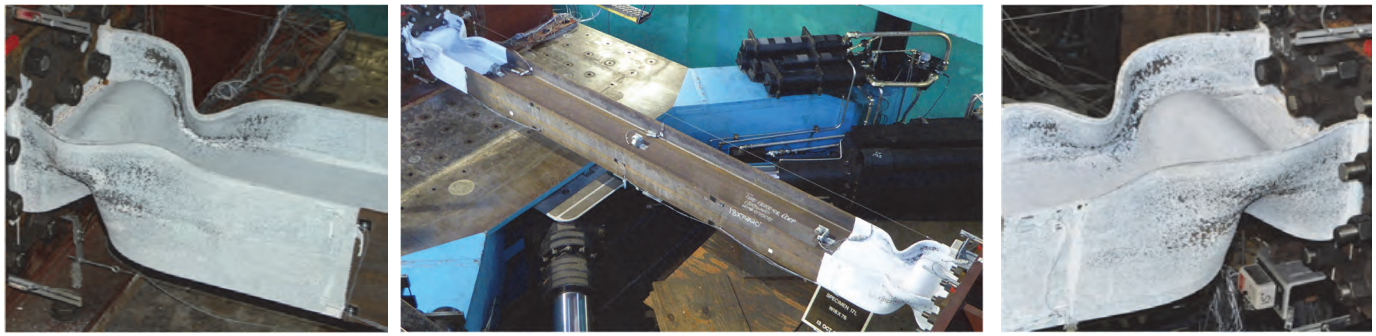

(b) *SDA* = 0.05 rad

Figure 2.25 Anti-Symmetric Local Buckling (ALB) Mode of W18×76 Column with C_a = 0.2 (Specimen 17L)

(a) Single-Curvature Coupled Buckling Mode of W24×84 Column with C_a = 0.2 (Specimen 27L)

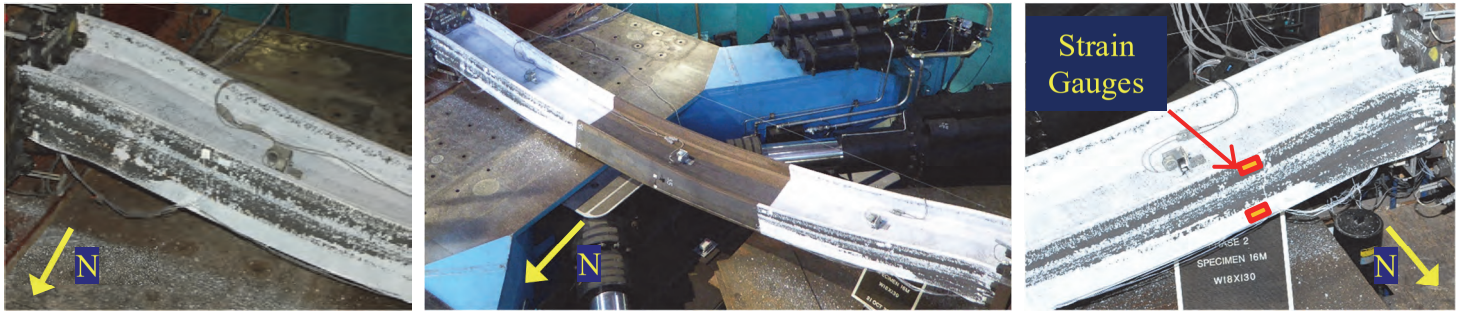

(b) Single-Curvature Coupled Buckling Mode of W18×130 Column with C_a = 0.4 (Specimen 16M)

(c) Reserve-Curvature Coupled Buckling Mode of W24×176 Column with C_a = 0.2 (Specimen 1L)

Figure 2.26 Coupled Buckling (CB) Mode

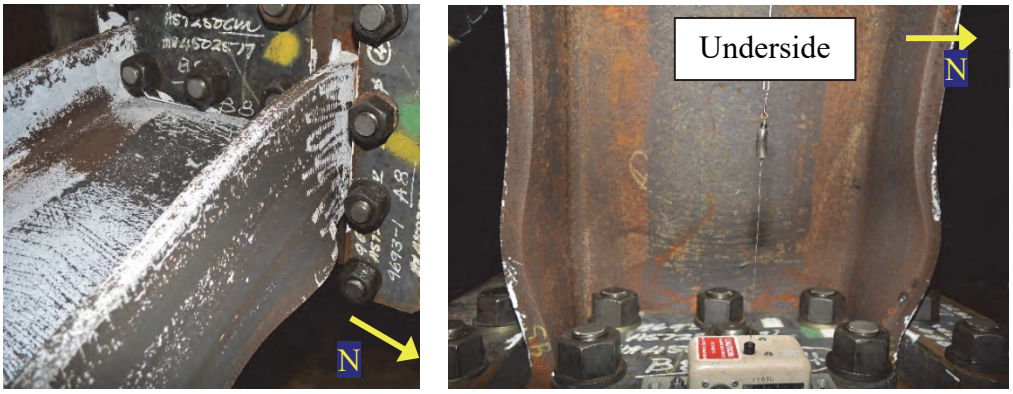

(a) Northwest Flange (b) West End

Figure 2.27 LTB-Induced Flange Local Buckling (Specimen 16M with W18×130 Section and C_a = 0.4)

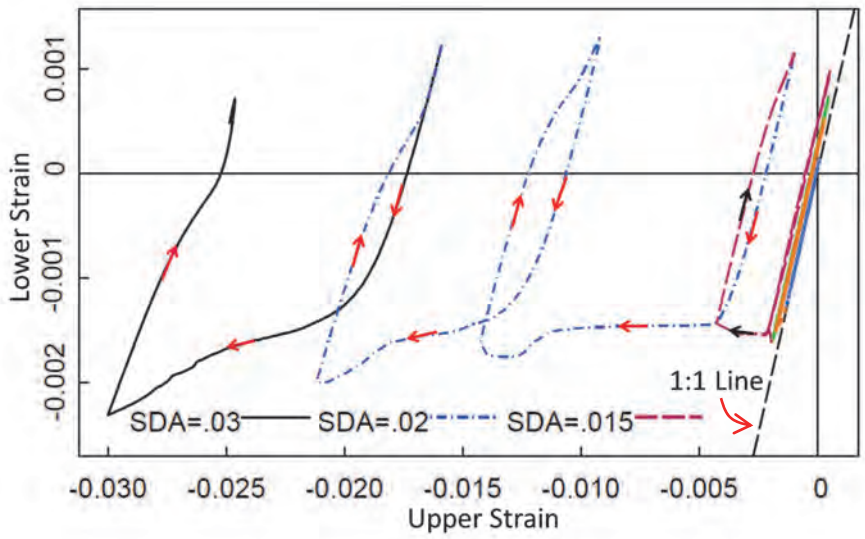

Figure 2.28 Nonuniform Strain Profile Across the Northwest Flange [see Figure 2.26(b)]

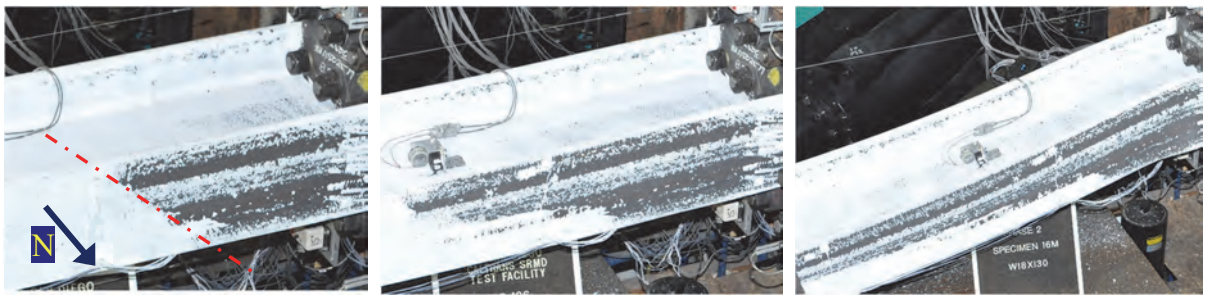

(a) *SDA* = 0.015 rad (b) *SDA* = 0.02 rad (c) *SDA* = 0.03 rad

Figure 2.29 Nonuniform (or Sloped) Flaking of Whitewash at West End (Specimen 16M with W18×130 Section, C_a = 0.4)

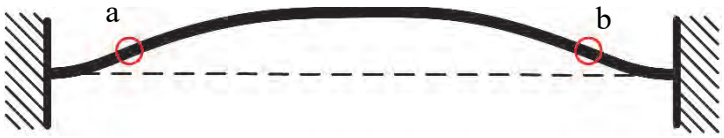

(a) Single Curvature

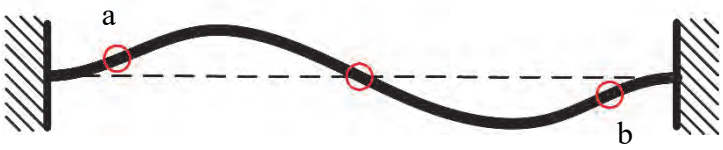

(b) Reserve or Double Curvature

Figure 2.30 Inflection Point Locations of Specimens with CB Failure Mode

3. TEST RESULTS: PHASE 1

3.1 Introduction

Measured responses and observed behavior of twenty-one specimens from Phase 1 testing are presented in this chapter. Figures are included to illustrate the progression of yielding, buckling, and the overall deformed configuration of each specimen as the magnitudes of the story drift angle (*SDA*) increased. Global responses of the specimens are presented in the form of lateral force (i.e., column shear), end moment, and axial shortening versus story drift plots. For simplicity, story drift angle in radian is also referred to as percent drift (e.g., *SDA* = 0.01 rad corresponds to 1 % drift). As discussed in Section 2.5, the AISC loading protocol applied 6, 6, 6, 4, and 2 cycles at 0.375 %, 0.5 %, 0.75 %, 1 %, and 1.5 % drift and greater, respectively, to the specimens.

Most Phase 1 specimens bended in reverse curvature in strong axis due to the applied lateral drift and boundary conditions; thus, the column flanges diagonal to each other at opposite ends experienced the same in-plane bending effect (either tension or compression). With respect to the test setup as shown in Figure 2.1(b), the northwest and southeast flanges were under flexural compression in the positive drift, and the same for the southwest and northeast flanges in negative drift. The terms “flange(s) under compression” or “compression flange(s)” and “flange(s) under tension” or “tension flange(s)” are used herein for briefness to describe this in-plane flexural effect in the specimens subjected to strong-axis cyclic drifts. To further facilitate column behavior explanation, positive and negative excursions referred to when a specimen was displaced in the positive and negative directions, respectively. In addition, failure mode classifications and certain phenomena defined in Section 2.8 are referenced here to help explain column behavior during testing.

3.2 Group 2 Specimens: Section W24×131

3.2.1 General

Test results of Group 2 specimens were presented first in this chapter to establish a referencing column behavior for comparison with that of the other specimen groups. Six specimens (Specimens 2Z, 2L, 2L-P, 2M, 2M-NF, and 2H) were tested in this group with

two repeated tests (Specimens 2M-R and 2H-R); test results of the latter were presented in Ozkula and Uang (2015). All were subjected to strong-axis bending. To investigate the effect of axial load on the column responses, four different levels of constant axial compression ($C_a = 0$, 0.2, 0.4, and 0.6) were used. To study the effect of lateral-drift loading sequences, Specimens 2L-P and 2M-NF were tested with the pushover and near-fault loading protocols (see Section 2.5), respectively, while the rest sustained the AISC loading protocol. As shown in Figure 2.4, AISC 341 classified the web and flanges of W24×131 section as highly ductile.

3.2.2 Specimen 2Z

Specimen 2Z was subjected to the AISC loading protocol without an axial load to examine the cyclic beam behavior. It was the only specimen tested without an axial load.

Initially, reusable haunches were installed at both column ends; they were intended to stiffen the end portions and thus prevent fractures at the column-to-end plate CJP welds (see Figure 3.1). This test setup resulted in a clear column length of 15 ft. The haunches were bolted to the end fixture but only bore against the column flanges. As a result, gaps between the haunches and the column flanges were observed as the specimen sustained cyclic lateral drifts, i.e., the haunches were ineffective. Thus, they were removed after the 4 % drift cycles; furthermore, they were not utilized in the remaining tests.

Specimen 2Z was cyclically tested up to 7 % drift; Figure 3.2 shows the overall deformed configuration at different drift levels. Figure 3.3 and Figure 3.4 show yielding and buckling progression at the member ends (whitewash paint was not applied at some portions of the column ends due to the initial installation of the haunches); web and flange local buckling in the plastic hinge regions was minimal even at 7 % drift. This was not the case for nominally identical specimens sustaining axial compression: their local buckles formed at lower drift levels with more significant amplitudes (see Section 3.2.3 to Section 3.2.7). During the positive excursion of the second 7 % drift cycle, a brittle flange fracture at the northeast weld access hole occurred as shown in Figure 3.5, prompting the termination of the test.

Figure 3.6 shows the global responses. Flexural strength degradation was not observed, and the column axial shortening was minimal.

Figure 3.1 Specimen 2Z: Reusable Haunches

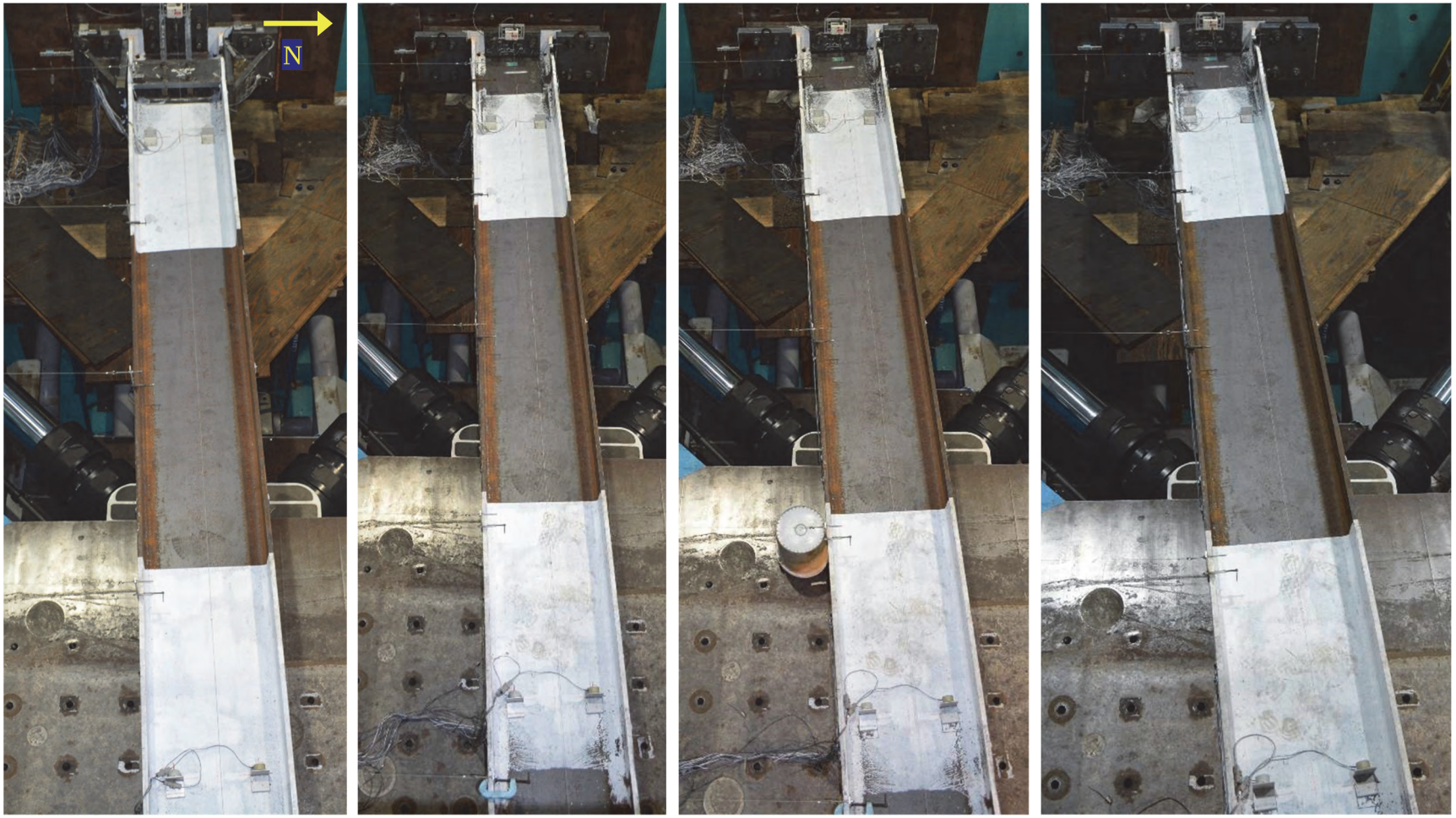

(a) *SDA* = 0.04 rad (b) *SDA* = 0.05 rad (c) *SDA* = 0.06 rad (d) *SDA* = 0.07 rad

Figure 3.2 Specimen 2Z: Overall Yielding and Buckling Progression

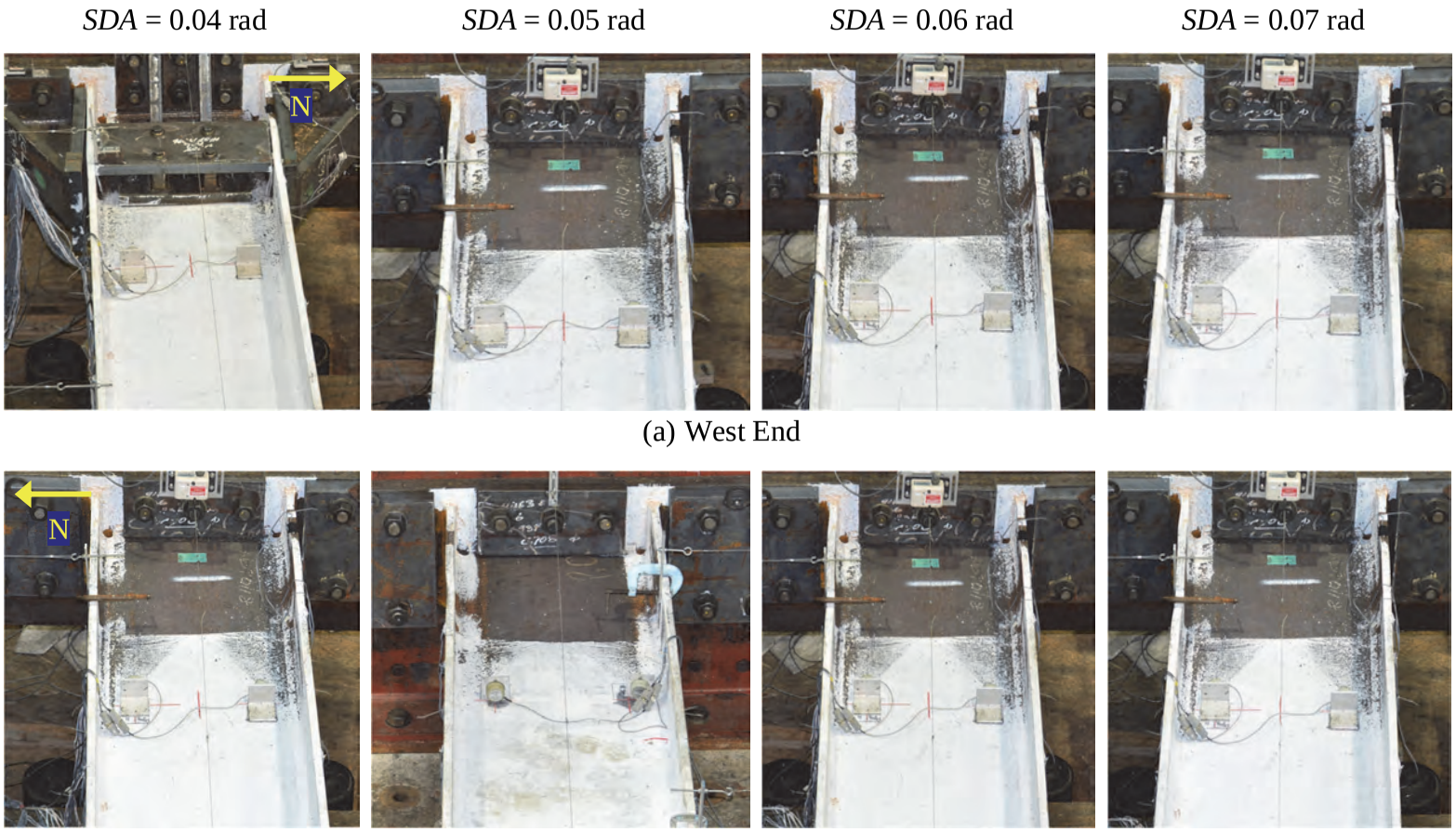

(a) West End

(b) East End

Figure 3.3 Specimen 2Z: Yielding and Buckling Progression at Member Ends (Top View)

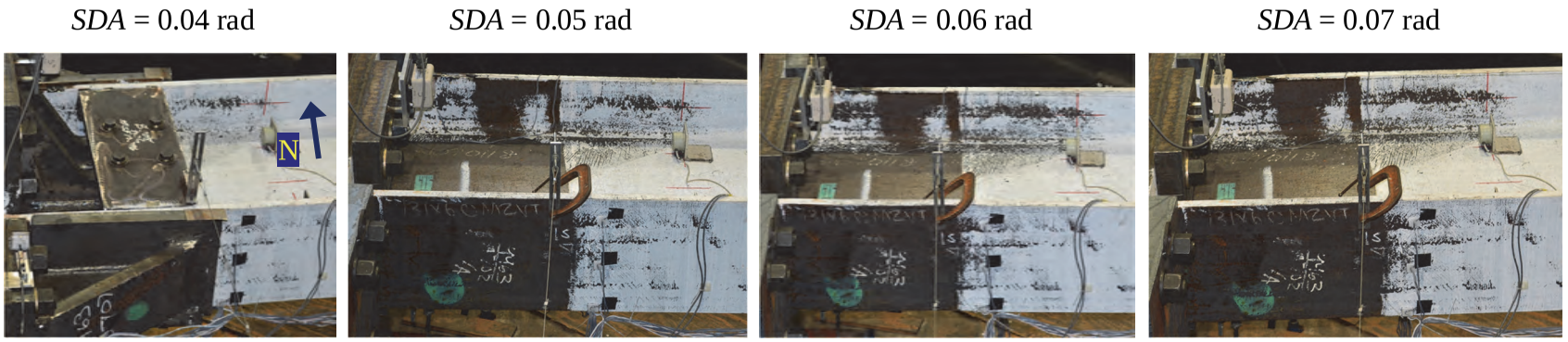

(a) West End

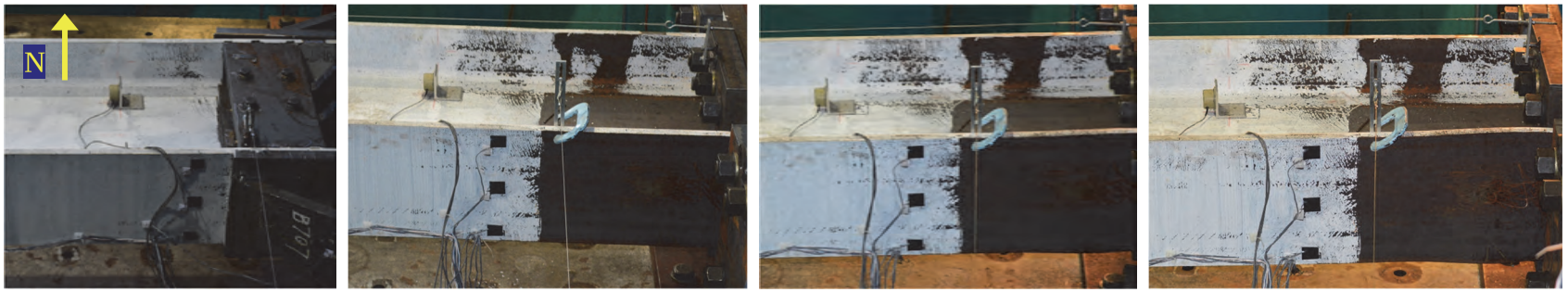

(b) East End

Figure 3.4 Specimen 2Z: Yielding and Buckling Progression at Member Ends

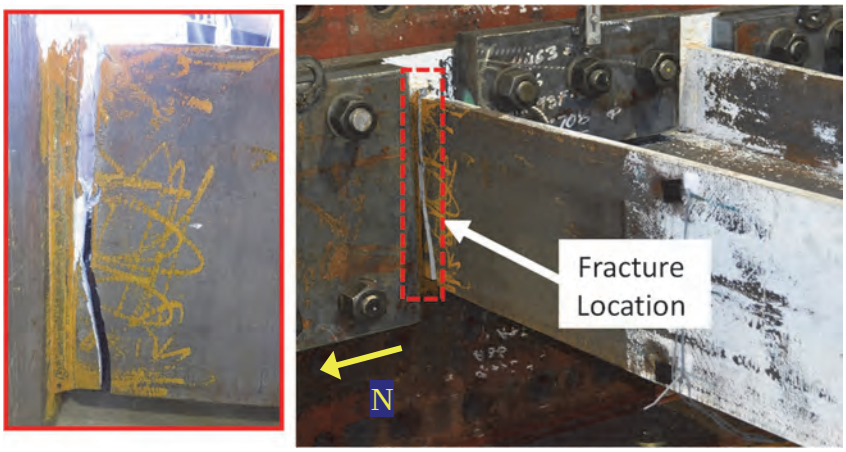

(a) Fracture at Northeast Flange

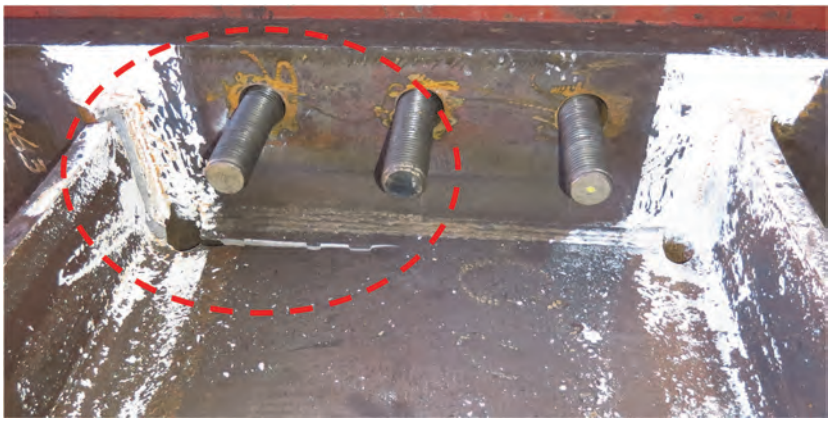

(b) Fracture at Weld Access Hole of the Northeast Flange

Figure 3.5 Specimen 2Z: Column Fracture at 7 % Drift

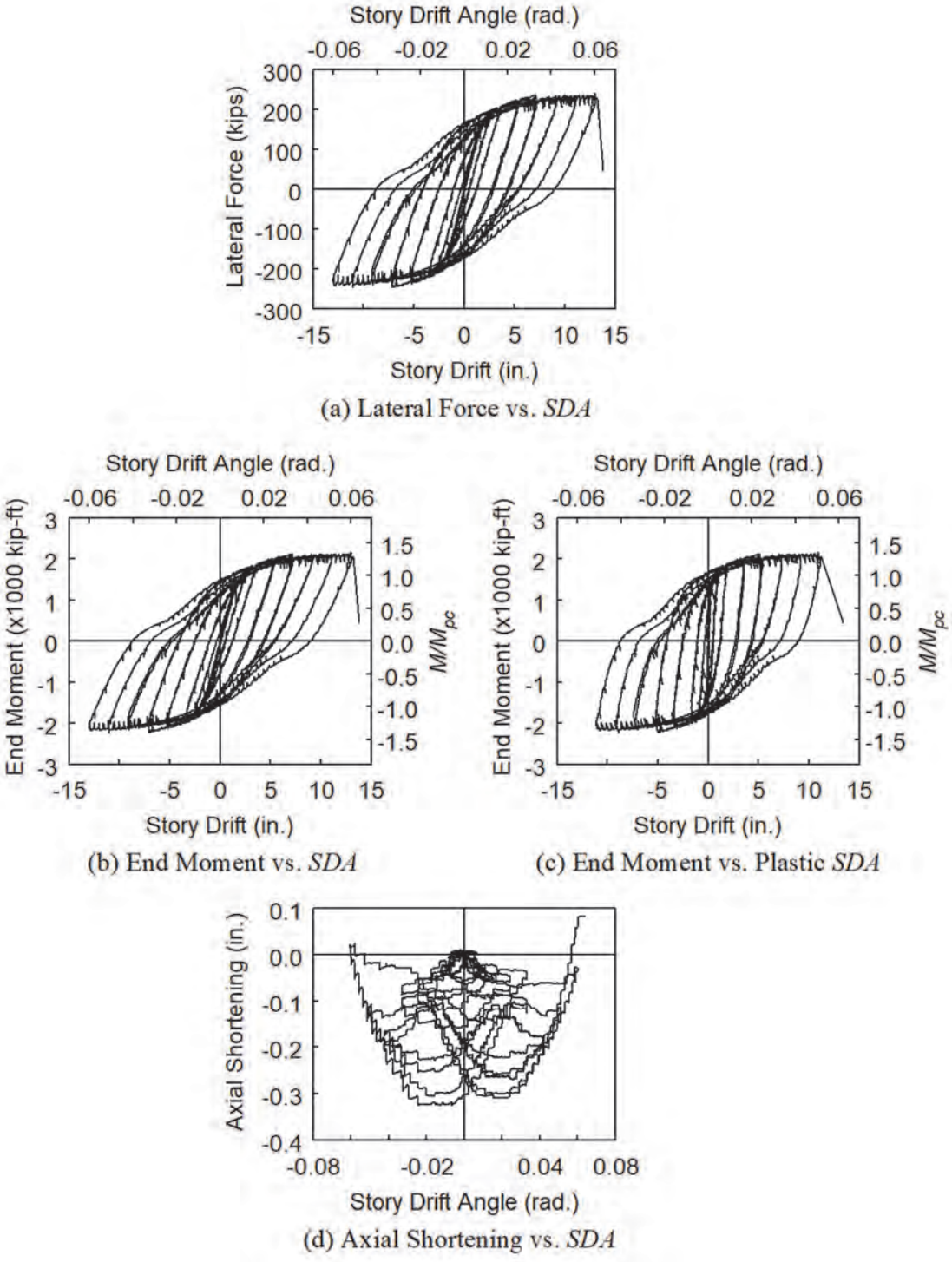

Figure 3.6 Specimen 2Z: Global Responses

3.2.3 Specimen 2L

Cyclic Test

Specimen 2L exhibited the ALB failure mode; yielding and buckling progression is depicted in Figure 3.7 to Figure 3.9. Web and flange local buckles initiated at 3 % drift; their amplitudes increased during the 4 % drift cycle, at which point the ALB configuration became obvious. Upward and downward web local buckling was observed at the west and east ends, respectively.

Figure 3.10 shows the global responses. A rapid growth in axial shortening triggered at 3 % drift corresponding to the onset of local buckling at both column ends; at this point, flexural strength also began to degrade. As the specimen underwent the first 4 % drift cycle, its flexural strength degraded to 81 % of the maximum moment capacity.

Compression Test

The AISC loading protocol was terminated after completing one cycle at 4 % drift in order to conduct a subsequent compression test to evaluate the gravity load-carrying capacity of the column in its deformed configuration. Unloaded in lateral force after the negative excursion of the 4 % drift cycle, the specimen exhibited approximately 6 in. residual lateral displacement [see Figure 3.10(a)]. With this deformed configuration, the applied axial compression was increased until a weak-axis flexural buckling was observed at the column midspan as shown in Figure 3.11(d) and Figure 3.12; the maximum recorded axial capacity was 1,465 kips [6517 kN], see Figure 3.14(a).

The plasticified and buckled column ends resulted from the AISC loading provided minimal weak-axis rotational stiffness. Thus, as shown in Figure 3.13, the deformed column could be idealized as a pinned-ended member with a clear span of 180 in. [4570 mm] (216 in. [5480 mm] minus the plastic hinge regions with approximately 36 in. [910 mm] total length per measurements). With this idealized configuration, the axial strength of the deformed column could be predicted as follows (AISC 2016b):

$$\frac{KL_h}{r_y} = \frac{1.0 \times 180}{2.97} = 60.6 \tag{3.1a}$$

$$F_{cr} = 38 \text{ ksi [264 MPa]} \tag{3.1b}$$

$$P_n = A_g F_{cr} = 1475 \text{ kips [6562 kN]} \tag{3.1c}$$

The predicted axial strength compared favorably with the test result.

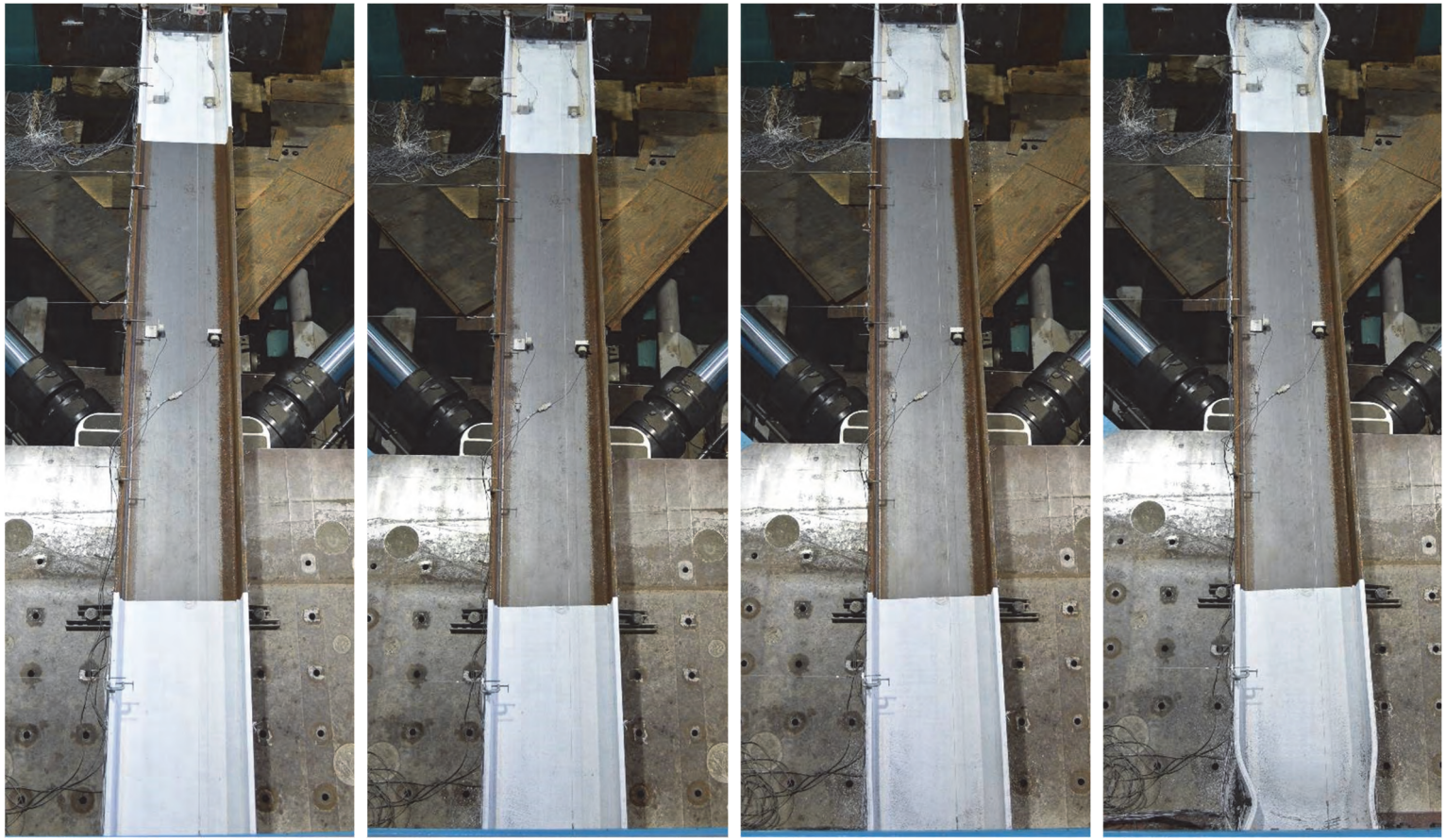

(a) *SDA* = 0.01 rad (b) *SDA* = 0.02 rad (c) *SDA* = 0.03 rad (d) *SDA* = 0.04 rad

Figure 3.7 Specimen 2L: Overall Yielding and Buckling Progression

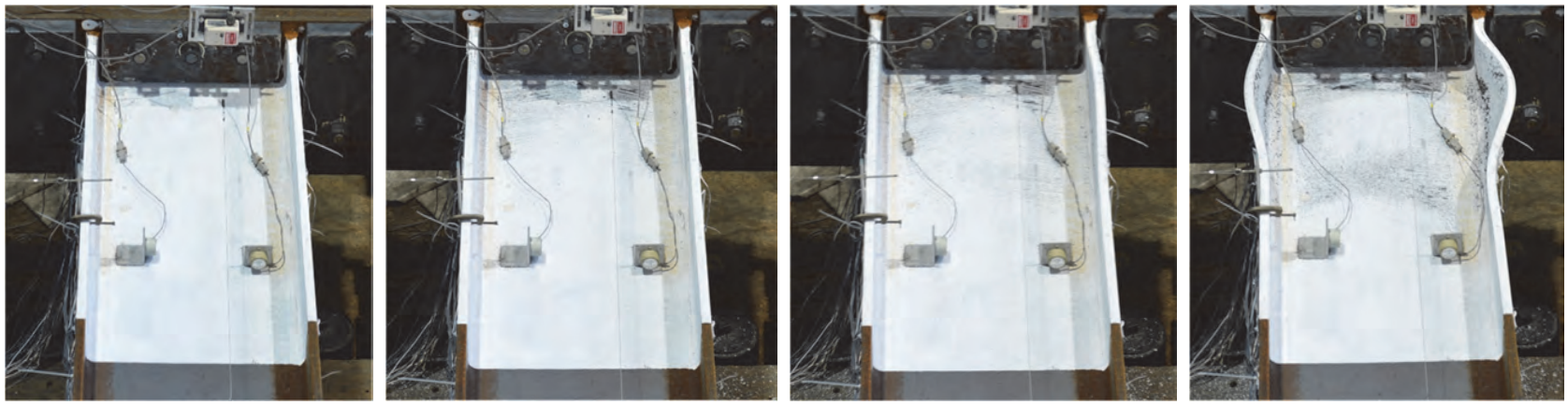

(a) West End

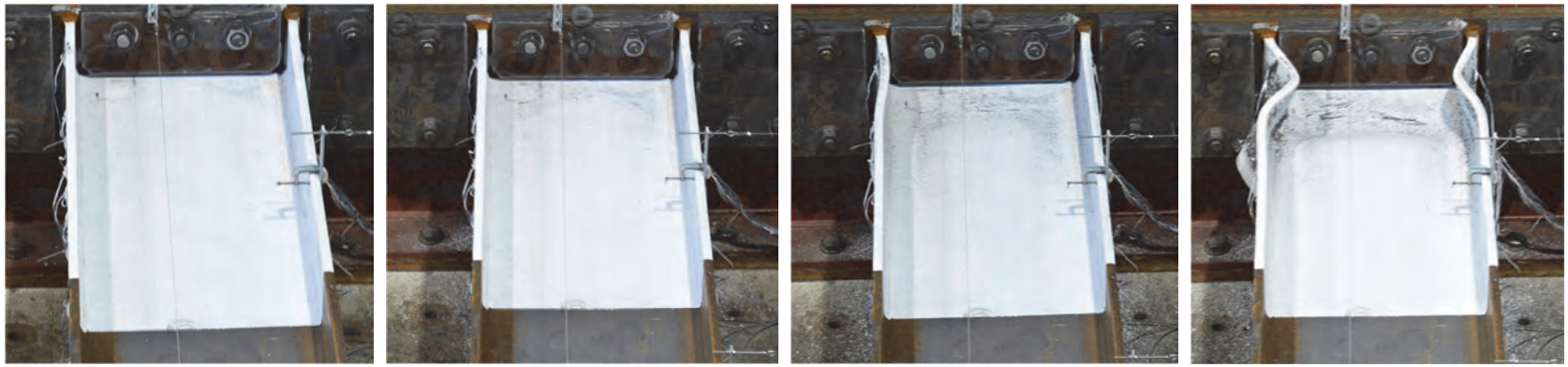

(b) East End

Figure 3.8 Specimen 2L: Yielding and Buckling Progression at Member Ends (Top View)

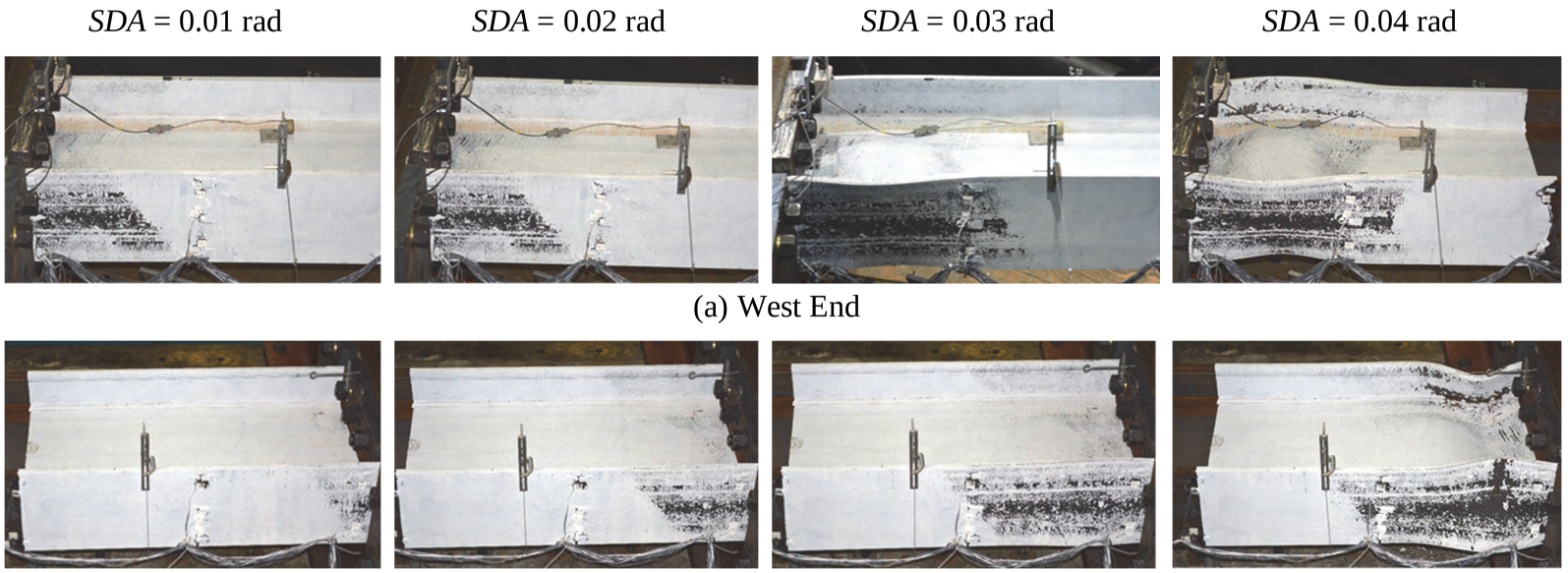

(a) West End

(b) East End

Figure 3.9 Specimen 2L: Yielding and Buckling Progression at Member Ends

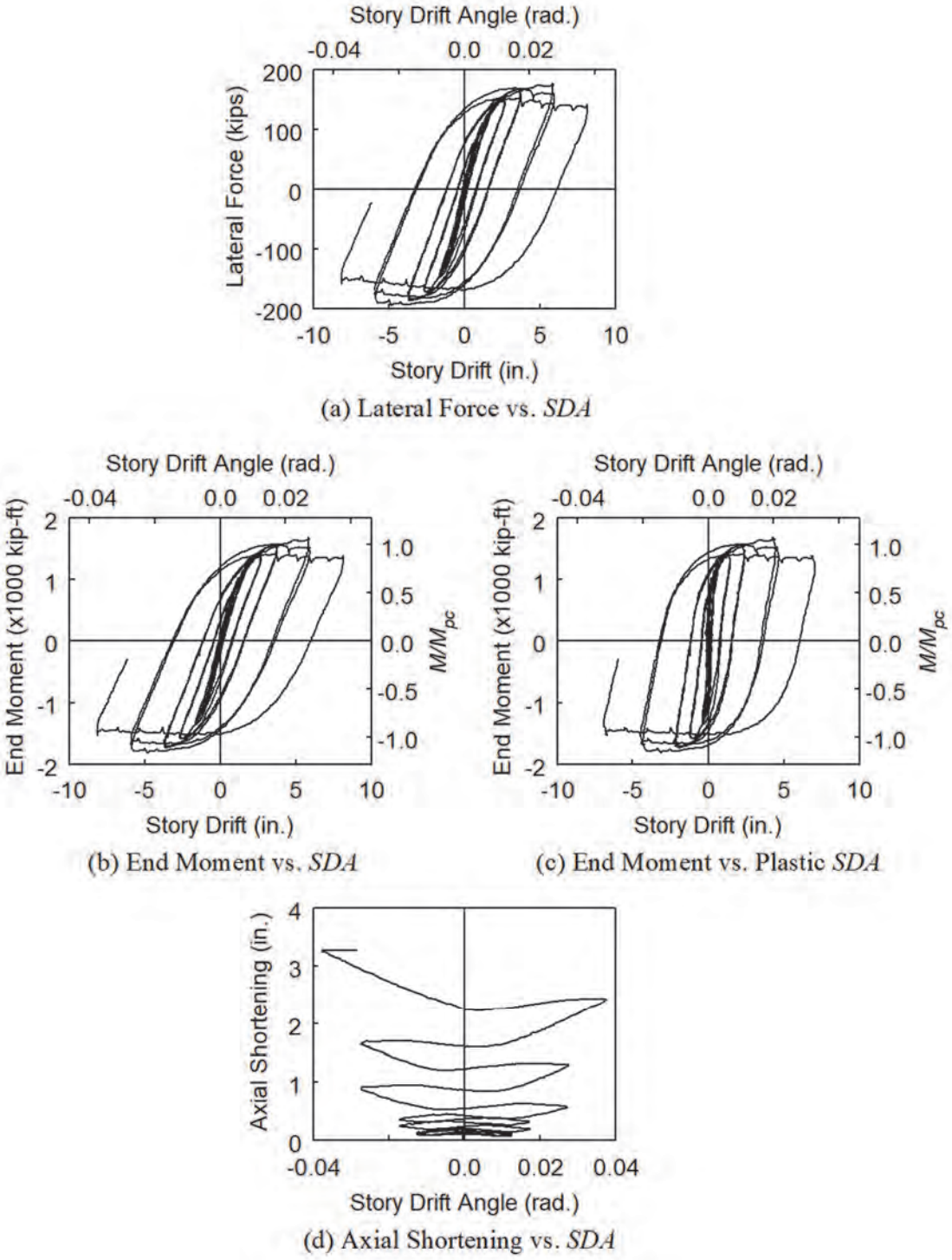

Figure 3.10 Specimen 2L: Global Responses

(a) P = 347 kips (Start of Pure Compression Test)

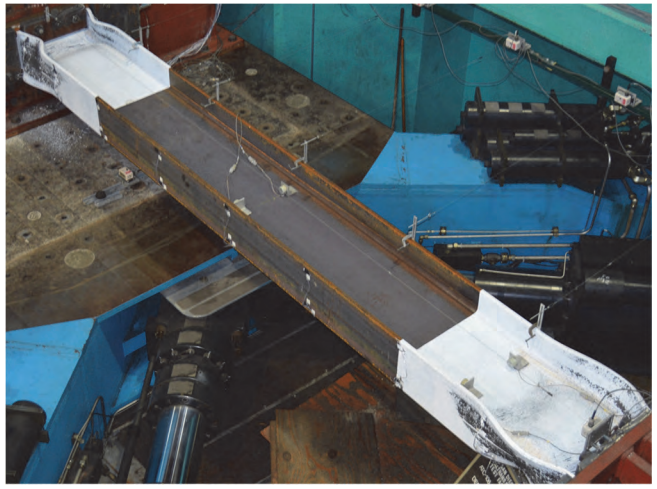

(b) P = 700 kips

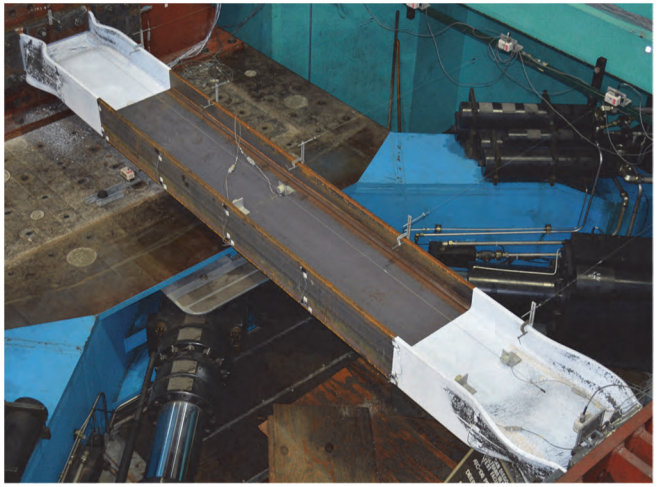

(c) P = 1400 kips

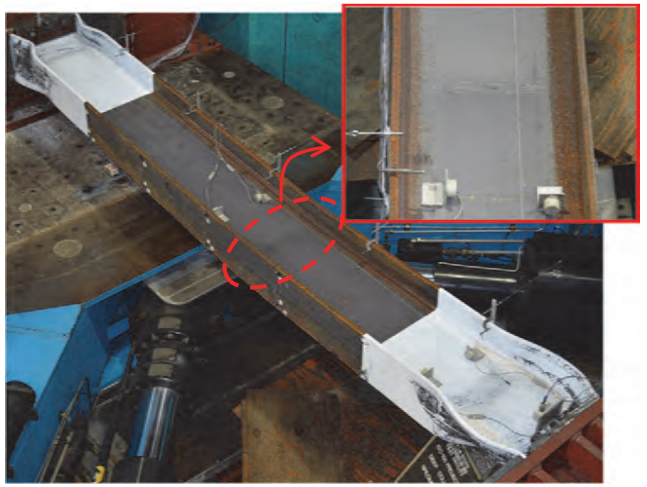

(d) P = 1500 kips

Figure 3.11 Specimen 2L: Pure Compression Test after Cyclic Loading Test

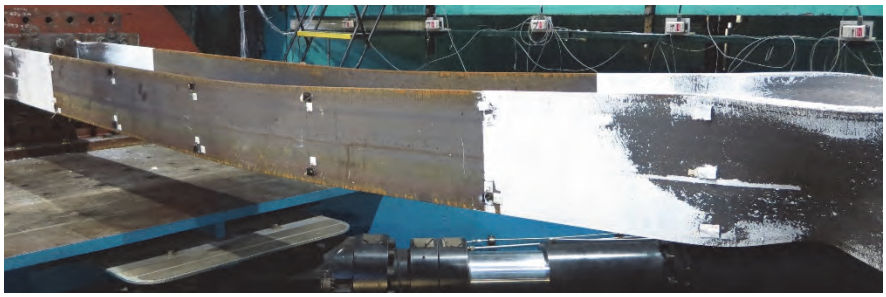

Figure 3.12 Specimen 2L: Weak-Axis Flexural Buckling at Midspan at End of Pure Compression Test

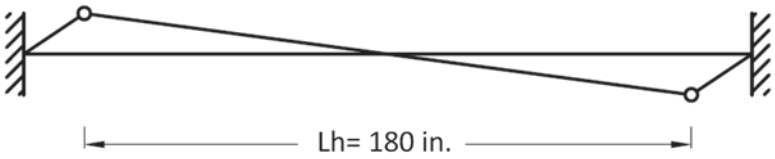

Figure 3.13 Specimen 2L: Pinned-Pinned Column Configuration after Cyclic Test

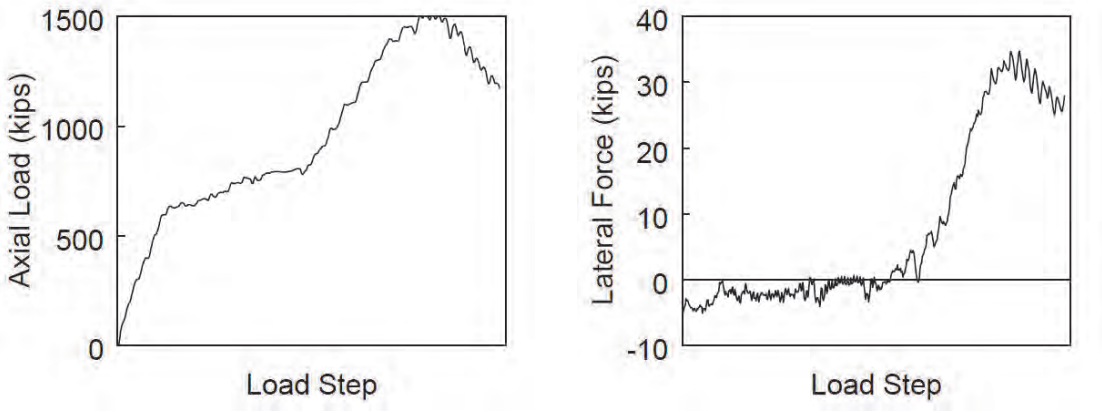

(a) Axial Load (b) Lateral Load

Figure 3.14 Specimen 2L: Axial and Lateral Load Histories (Compression Test)

3.2.4 Specimen 2L-P

Specimen 2L-P was monotonically pushed to 4 % drift in the positive direction, followed by the reversed AISC loading protocol (see Section 2.5). It exhibited the ALB failure mode; yielding and buckling progression is shown in Figure 3.15 to Figure 3.17. Minor amplitudes of flange local buckles at compression flanges were observed in the first positive excursion to 4 % drift. This was accompanied by minor web local buckling as well (more obvious at the east end). In the following negative excursion (beginning of the reversed AISC loading protocol), full-wave flange local buckles formed at the corresponding compression flanges. As the test continued with decreasing cyclic drift amplitudes, local buckling aggravated, and the full-wave ALB configuration became obvious at both column ends.

Figure 3.18 shows the global responses; the blue dashed line and the black solid line indicate the monotonic and cyclic responses, respectively. Flexural strength degradation was not observed in the monotonic response but shown in the cyclic response; for example, the end moment hysteresis of the second 3 % drift cycle showed lower peak values than those of the first cycle. This corresponded to the aggravating local buckles at member ends. About 80 % of the total axial shortening occurred during the 4 % and 3 % drift cycles. Specimen 2L-P, which exhibited the full-wave ALB configuration, shortened more than Specimen 2L with the half-wave ALB configuration [compare Figure 3.10(d) and Figure 3.18(d)]; this demonstrated the effect of lateral-drift loading sequences.

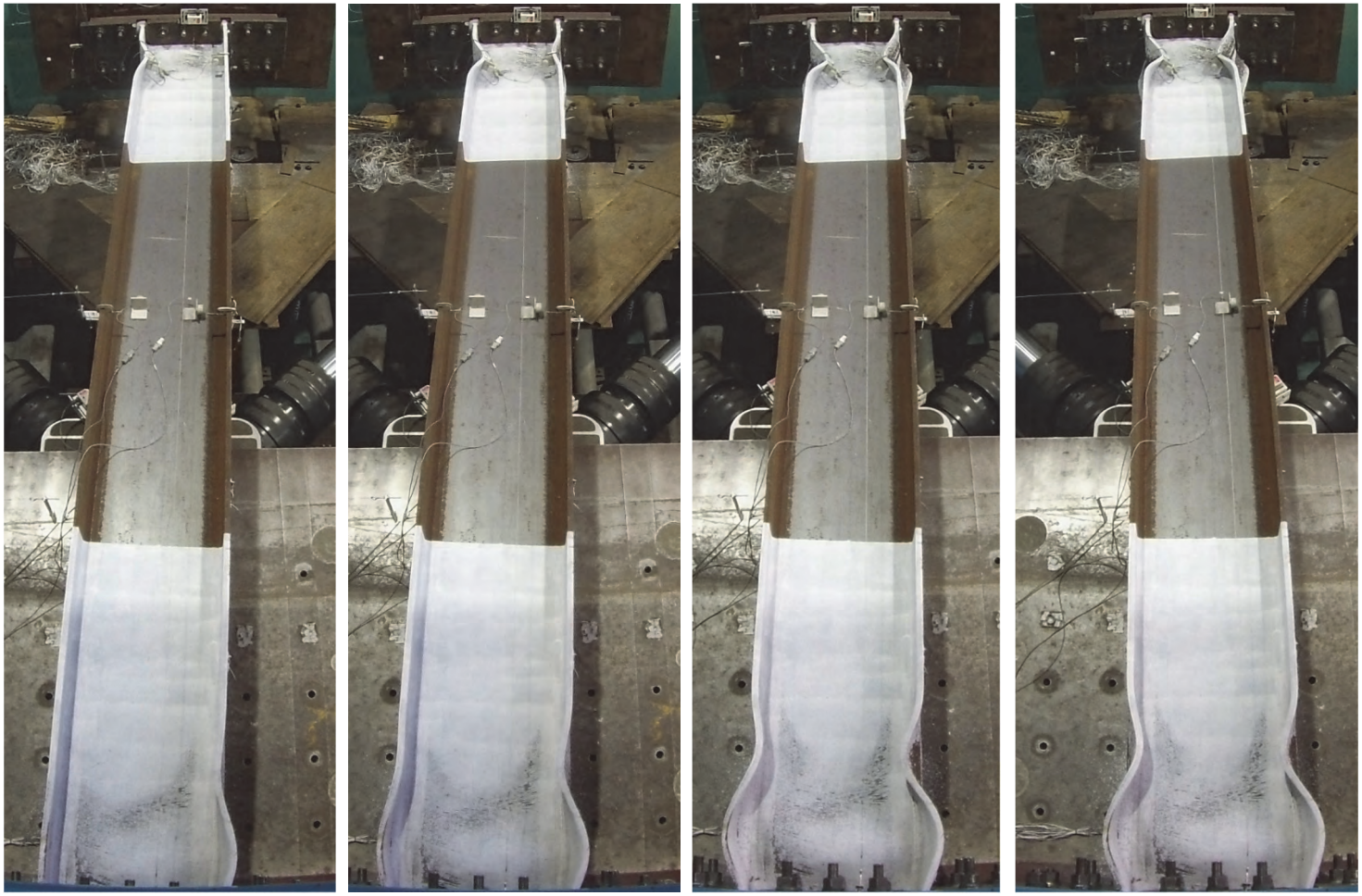

(a) *SDA* = 0.04 rad (b) *SDA* = 0.03 rad (c) *SDA* = 0.02 rad (d) *SDA* = 0.01 rad

Figure 3.15 Specimen 2L-P: Overall Yielding and Buckling Progression

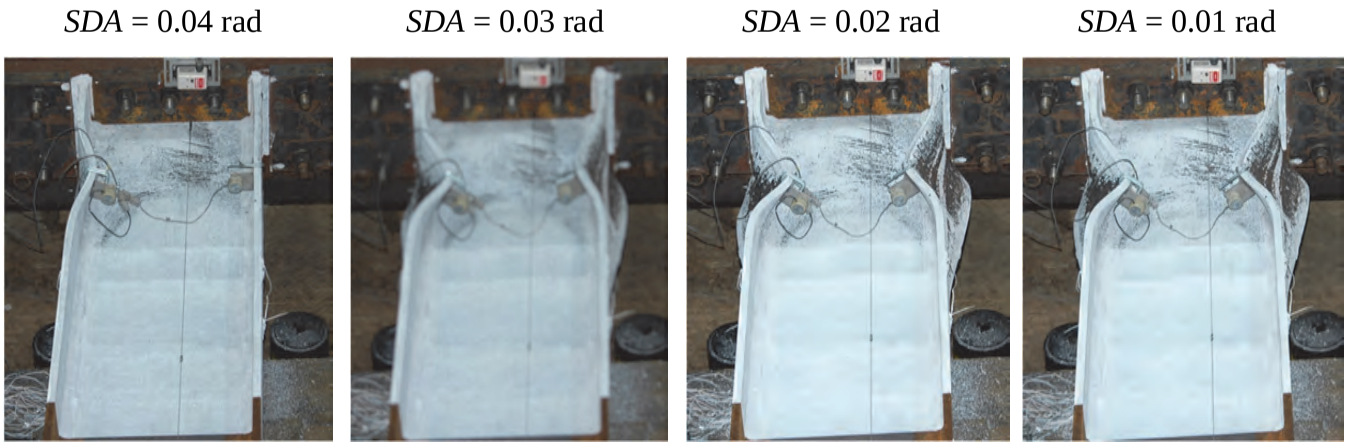

(a) West End

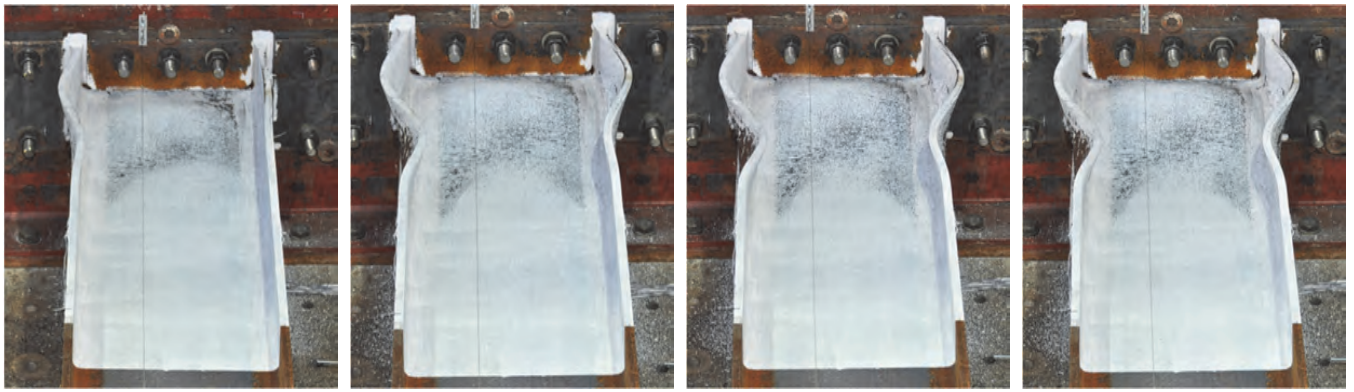

(b) East End

Figure 3.16 Specimen 2L-P: Yielding and Buckling Progression at Member Ends (Top View)

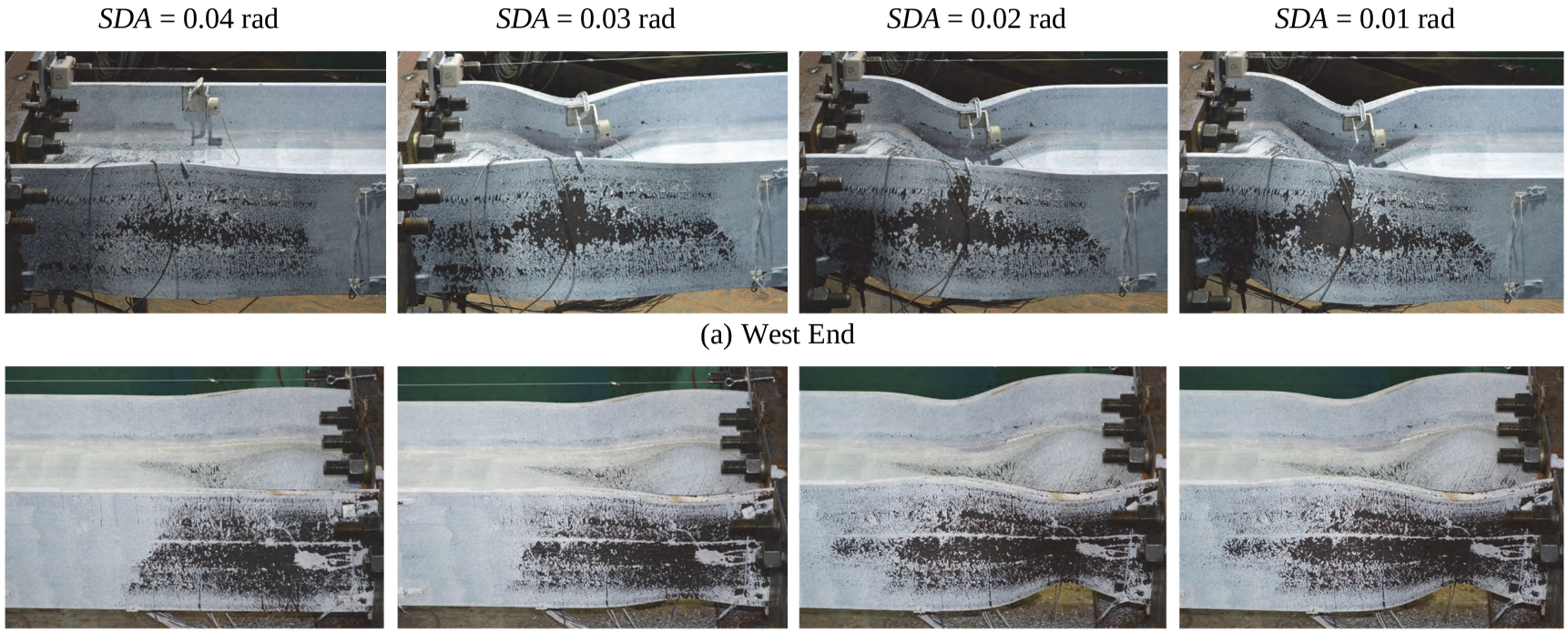

(a) West End

(b) East End

Figure 3.17 Specimen 2L-P: Yielding and Buckling Progression at Member Ends

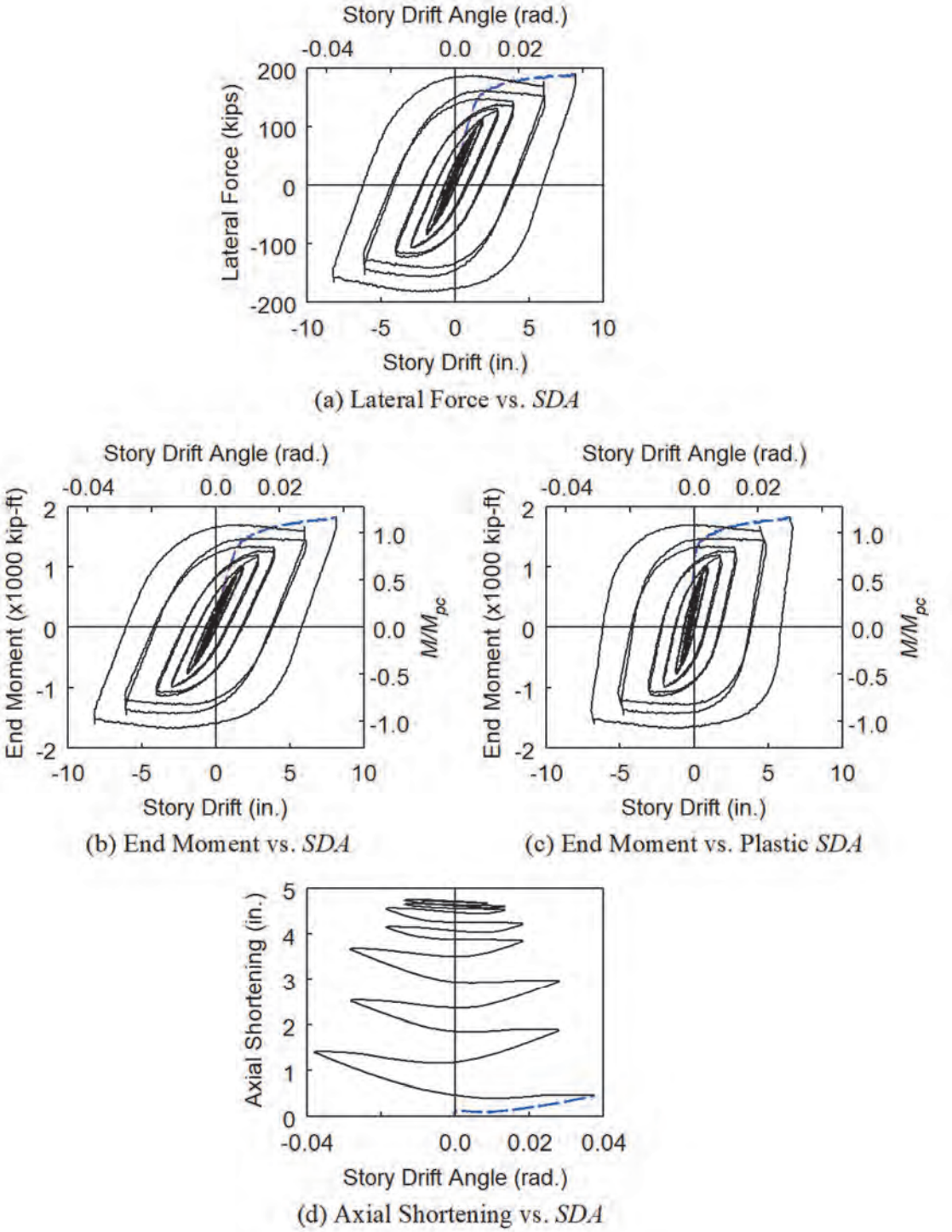

Figure 3.18 Specimen 2L-P: Global Responses

3.2.5 Specimen 2M

Specimen 2M exhibited the ALB failure mode; yielding and buckling progression is illustrated in Figure 3.19 to Figure 3.21. Web and flange local buckling initiated at 1.5 % drift. Their amplitudes grew during the 2 % and 3 % drift cycles, exhibiting the full-wave ALB configuration. The test was terminated after completing two cycles at 3 % drift due to excessive local buckling.

Global responses are shown in Figure 3.22. Flexural strength began to degrade during the 1.5 % drift cycles corresponding to the onset of local buckling at both ends; axial shortening also began to grow at an increasing rate beyond this point. At the end of the test, the column shortened by 9.1 in., i.e., 4.2 % of the undeformed column length.

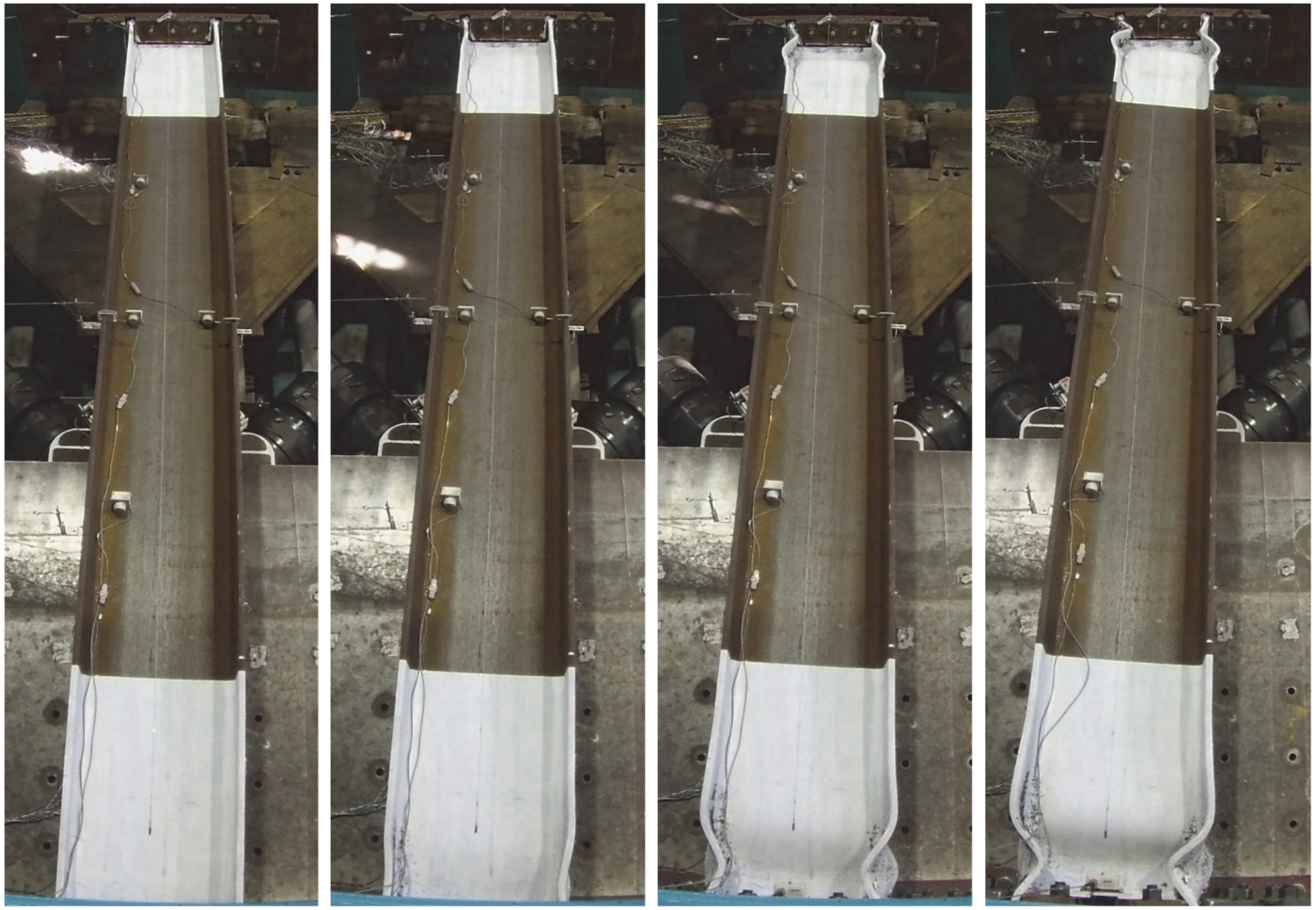

(a) *SDA* = 0.01 rad (b) *SDA* = 0.015 rad (c) *SDA* = 0.02 rad (d) *SDA* = 0.03 rad

Figure 3.19 Specimen 2M: Overall Yielding and Buckling Progression

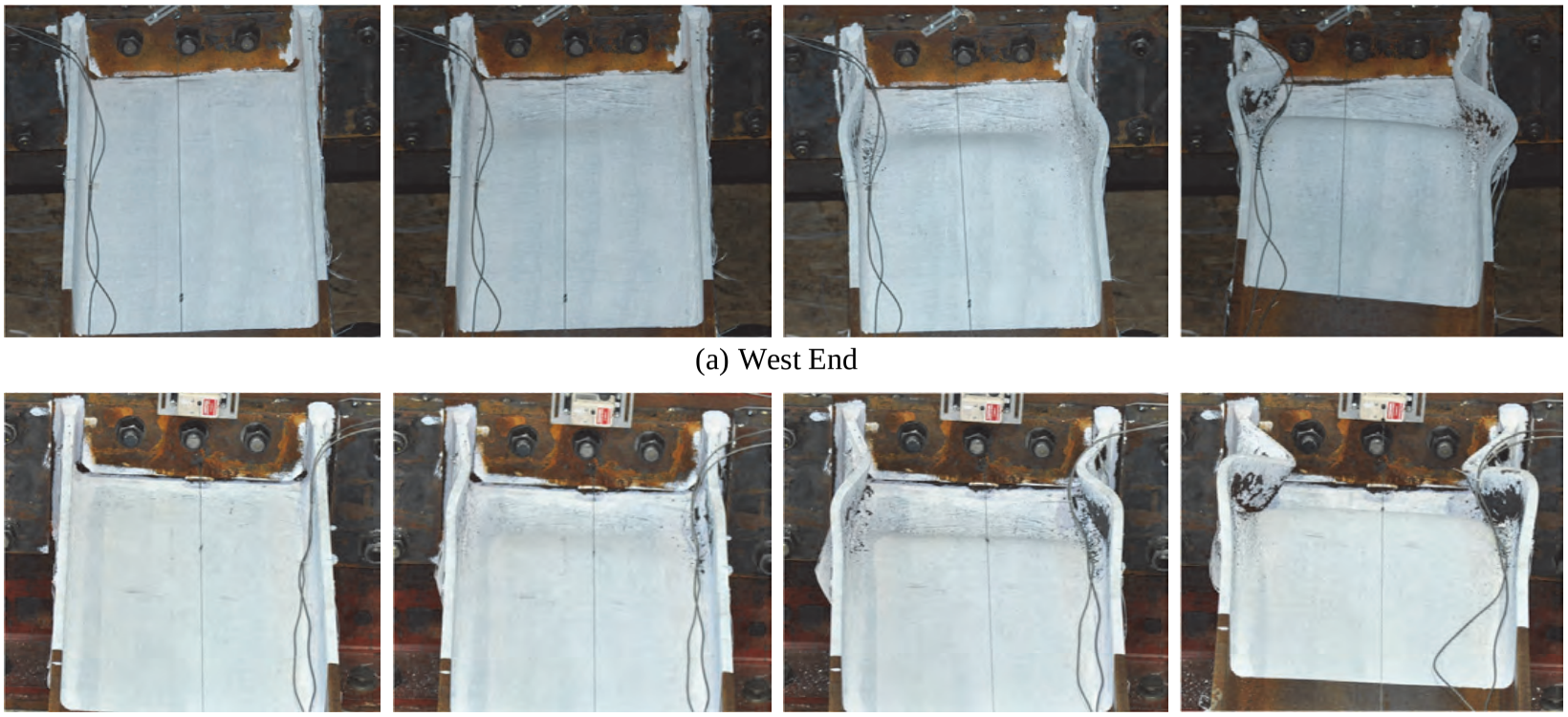

(a) West End

(b) East End

Figure 3.20 Specimen 2M: Yielding and Buckling Progression at Member Ends (Top View)

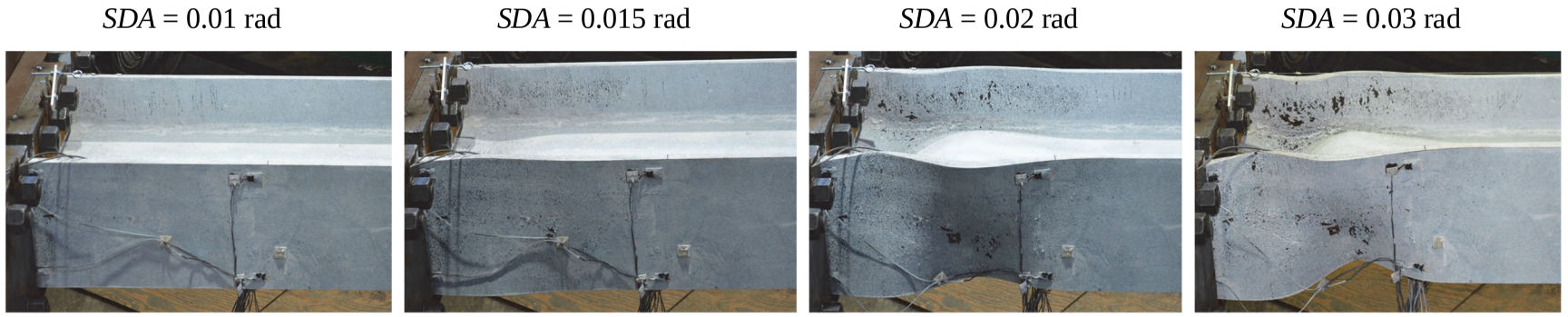

(a) West End

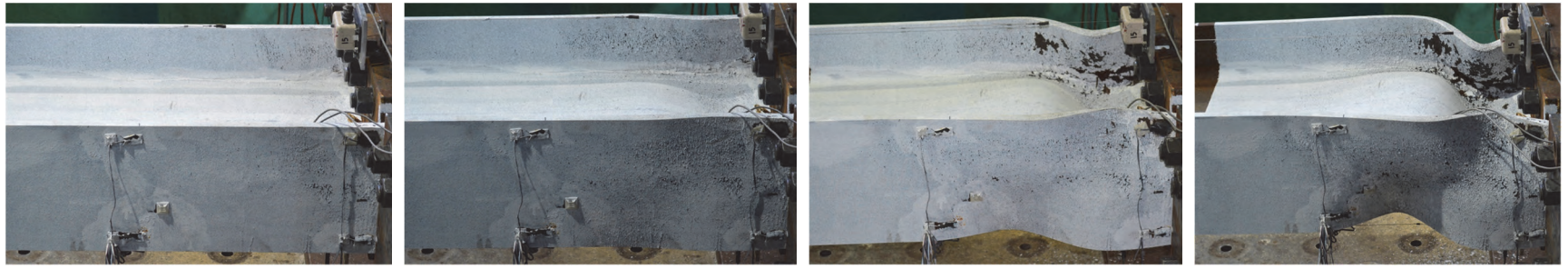

(b) East End

Figure 3.21 Specimen 2M: Yielding and Buckling Progression at Member Ends

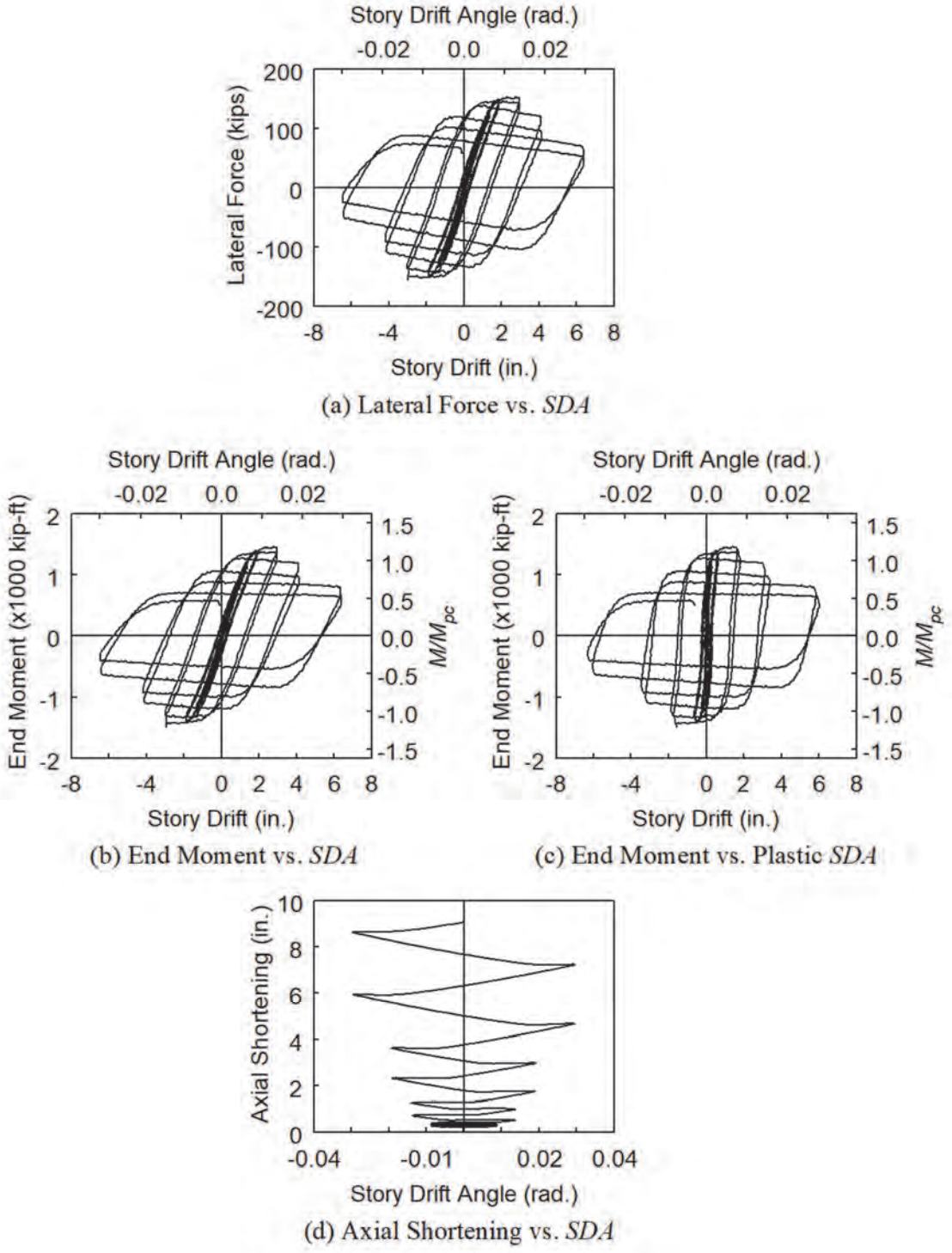

Figure 3.22 Specimen 2M: Global Responses

3.2.6 Specimen 2M-NF

Specimen 2M-NF sustained the near-fault loading protocol with the same level of axial compression applied to Specimen 2M. These tests were designed to examine the lateral-drift sequence effect. Specimen 2M-NF exhibited the ALB failure mode; yielding and buckling progression is illustrated in Figure 3.23 to Figure 3.25. Global responses are shown in Figure 3.26. The plastic moment capacity was reached during the first negative excursion to -2 % drift; local buckling was yet observed. In the following positive excursion to +6 % drift, web and flange local buckling with the ALB configuration was triggered, which concentrated at the corresponding compression flanges as shown in Figure 3.23(b).

Even though the successive drift cycles with lower amplitudes oscillated only in the positive-drift range, the southwest and northeast flanges still experienced in-plane flexural compression in the negative excursions because portions of the column ends had already established plastic deformation; otherwise, if they were still in elastic range, those flanges would only experience in-plane flexural compression when the specimen was displaced into the negative drift range. Accordingly, local buckles also began to form at those compressed flanges; note that, as shown in Figure 3.23(c), their amplitudes were initially smaller than those of the opposite flanges due to the unsymmetrical nature of the near-fault loading protocol. Later in the test, however, as shown in Figure 3.23(d) and (e), local buckling aggravated, and all flange local buckles exhibited relatively similar amplitudes.

Flexural strength degradation initiated as soon as local buckling was observed. That observed in the positive excursions was more severe than that observed in the negative excursions; again, the unsymmetrical loading protocol seemed to be the influencing factor. Column axial shortening grew proportionally to the severity of local buckling in the plastic hinge regions.

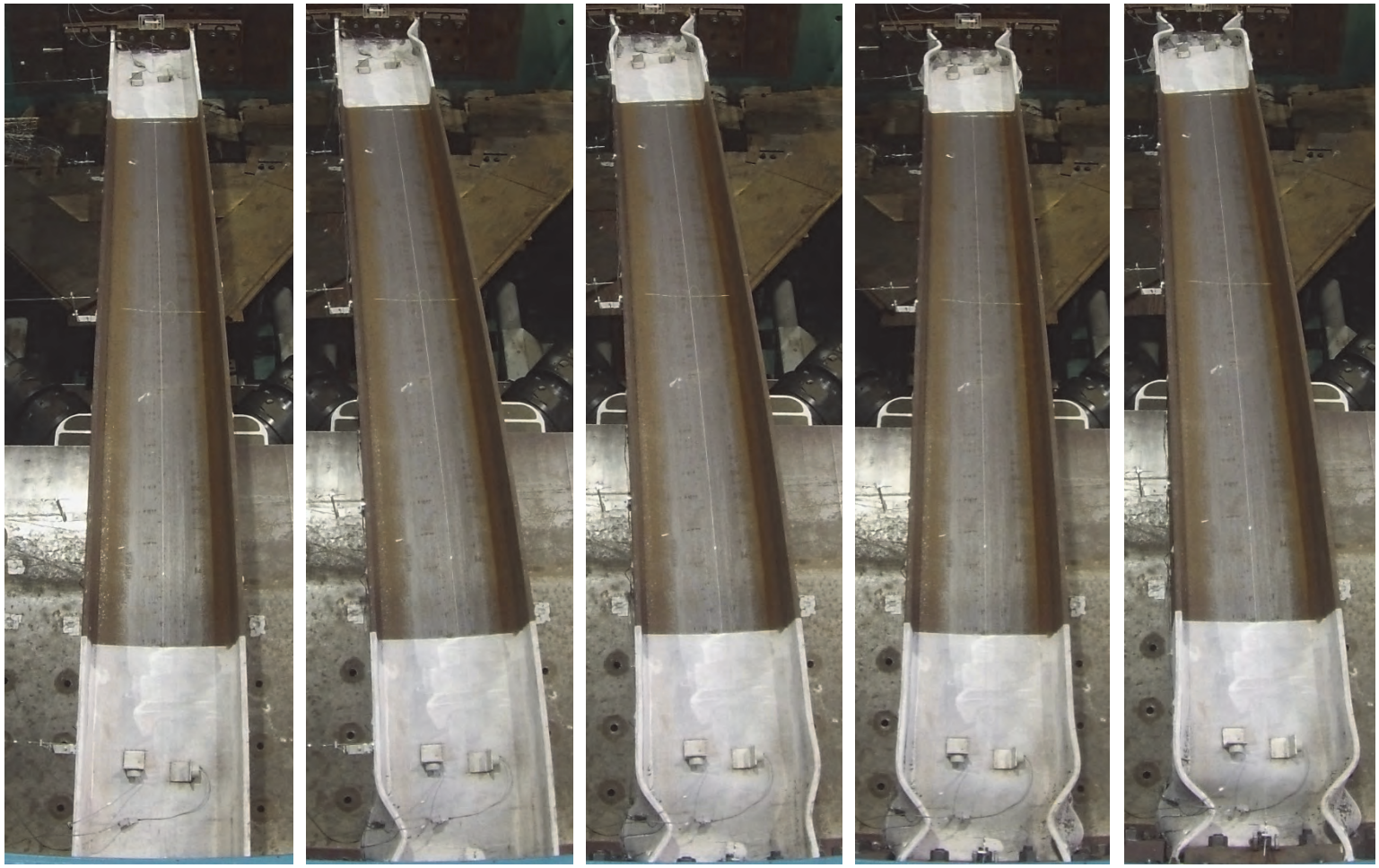

(a) *SDA* = -0.02 rad (b) *SDA* = +0.06 rad (c) *SDA* = +0.05 rad (d) *SDA* = +0.01 rad (e) *SDA* = +0.04 rad

Figure 3.23 Specimen 2M-NF: Overall Yielding and Buckling Progression

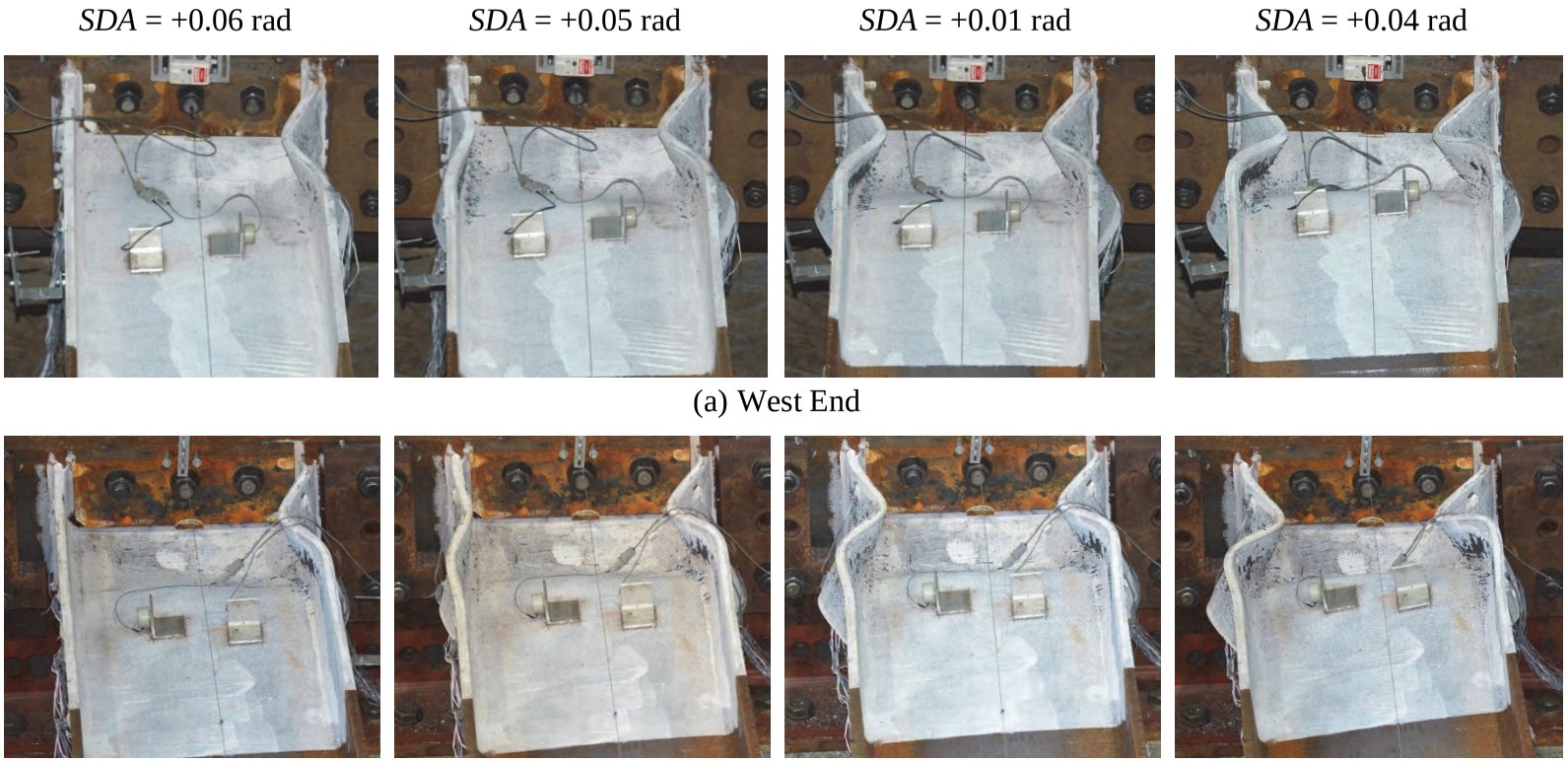

(a) West End

(b) East End

Figure 3.24 Specimen 2M-NF: Yielding and Buckling Progression at Member Ends (Top View)

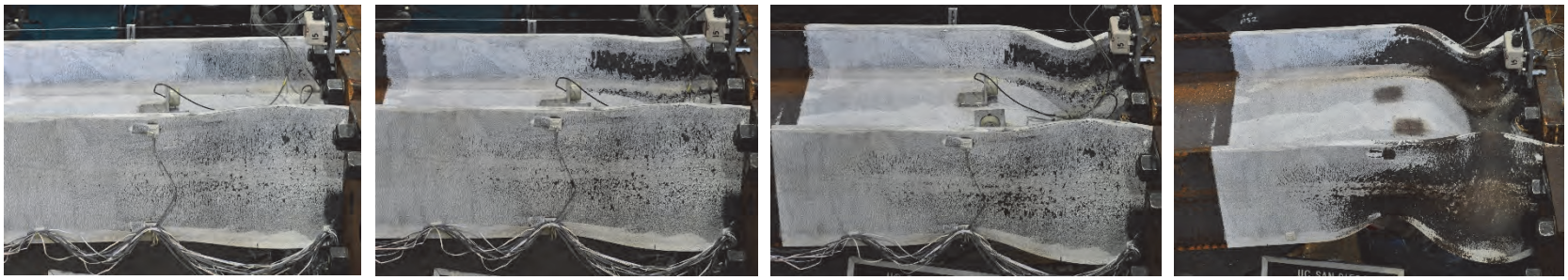

(a) West End

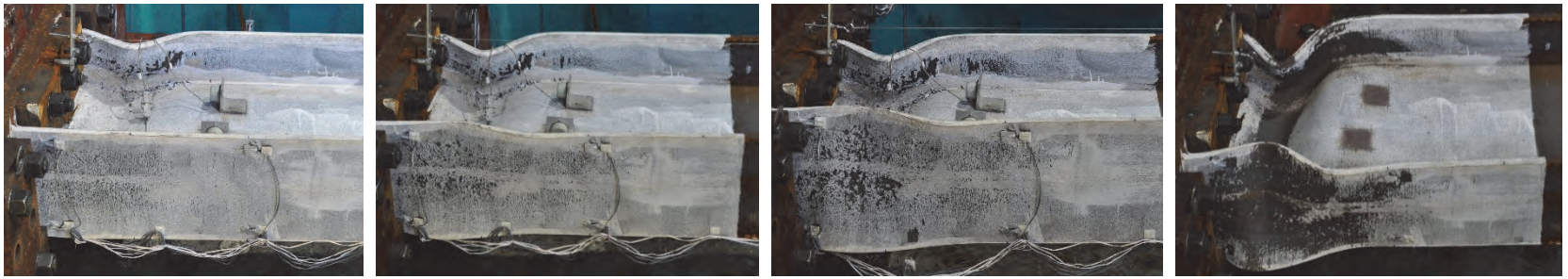

(b) East End

Figure 3.25 Specimen 2M-NF: Yielding and Buckling Progression at Member Ends

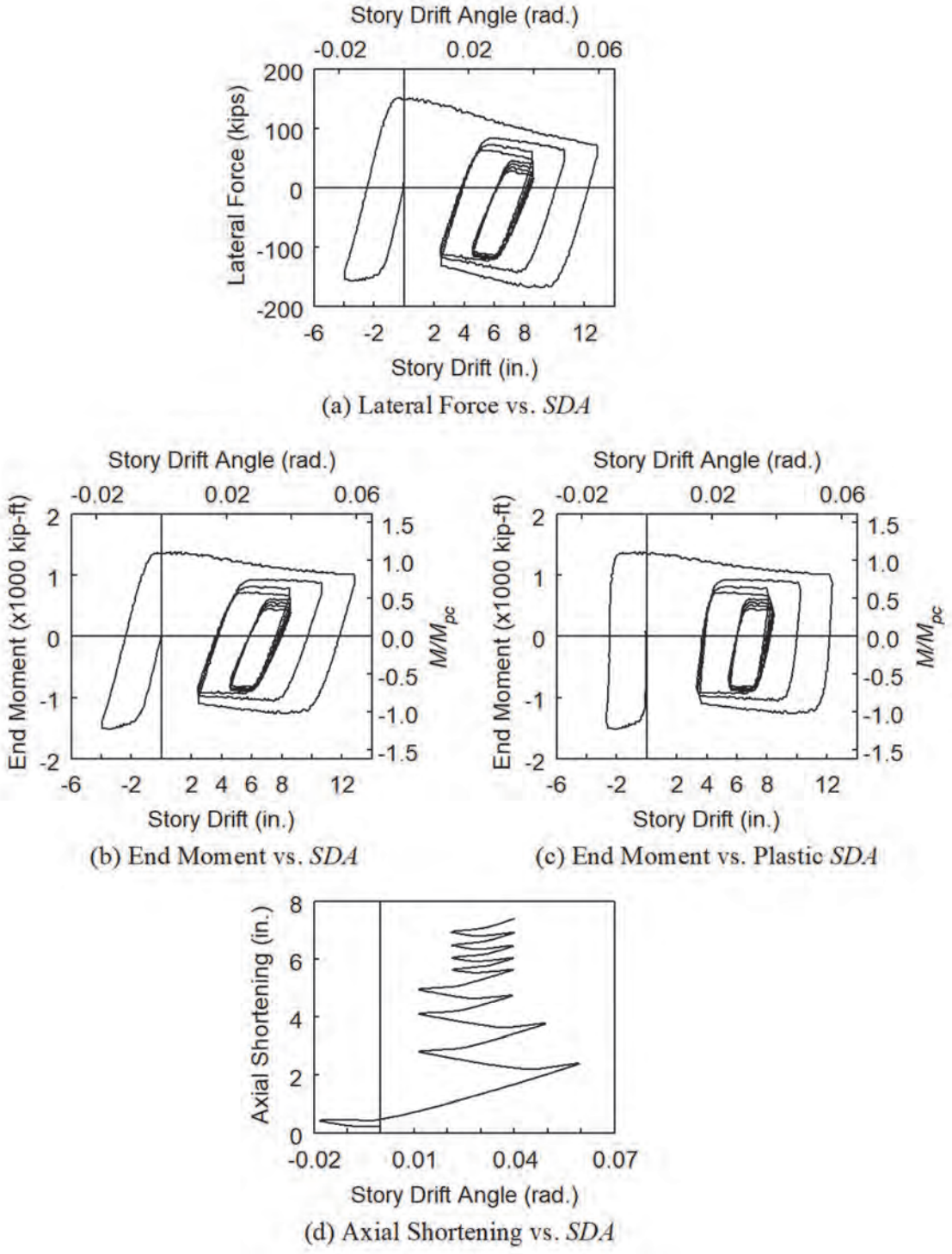

Figure 3.26 Specimen 2M-NF: Global Responses

3.2.7 Specimen 2H

Specimen 2H sustained the highest constant axial compression among all specimens in this group. It exhibited the ALB failure mode; yielding and buckling progression is depicted in Figure 3.27 to Figure 3.29. Due to the significant axial load, local buckling initiated as soon as the specimen reached 0.75 % drift; after completing six cycles at this drift level, the column flexural capacity degraded rapidly to 65 % of the maximum strength as shown in Figure 3.30(b). At 1 % and 1.5 % drifts, local buckling aggravated: the west and east ends exhibited the full- and half-wave ALB configurations, respectively. The test was terminated at 1.5 % drift after the first cycle due to excessive local buckling at both column ends.

3.2.8 Concluding Remarks

The effects of axial load levels and lateral-drift loading protocols on column behavior were investigated in Group 2 testing. In general, plastic rotation capacity and energy dissipation capacity of the columns decreased as their levels of axial load increased because the increase in axial demand expedited local buckling at the member ends, which triggered flexural strength degradation in the hysteresis. Since high-axial-load columns sustained fewer inelastic cycles before local buckles initiated, they also experienced less strain hardening. It is well established that axial compression reduced the plastic moment capacity of a cross-section. This in addition to the limited strain hardening contributed to lower flexural strengths in the high-axial-load columns.

Column axial shortening grew proportionally to the amplitudes of the local buckles; thus, it grew more rapidly at lower drift cycles for columns that sustained higher axial compression.

Both the axial-load and lateral-drift sequence parameters did not affect the governing failure mode of the specimens; all failed in the ALB mode. However, different loading sequences (i.e., AISC, monotonic, and near-fault) had influences on the hysteresis and its characteristics including strain hardening, maximum flexural strength, strength degradation, energy dissipation, and axial shortening.

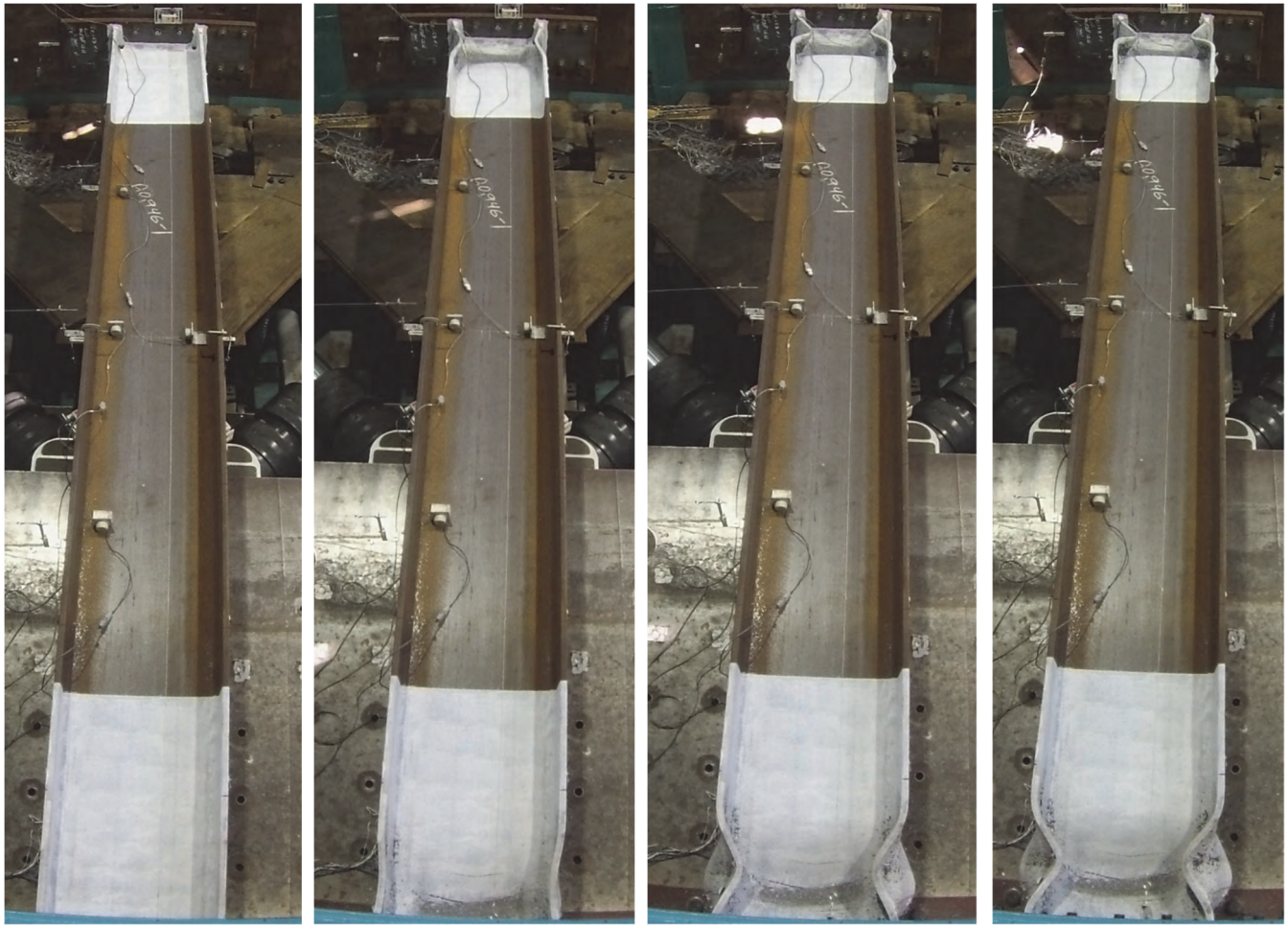

(a) *SDA* = 0.005 rad (b) *SDA* = 0.0075 rad (c) *SDA* = 0.01 rad (d) *SDA* = 0.015 rad

Figure 3.27 Specimen 2H: Overall Yielding and Buckling Progression

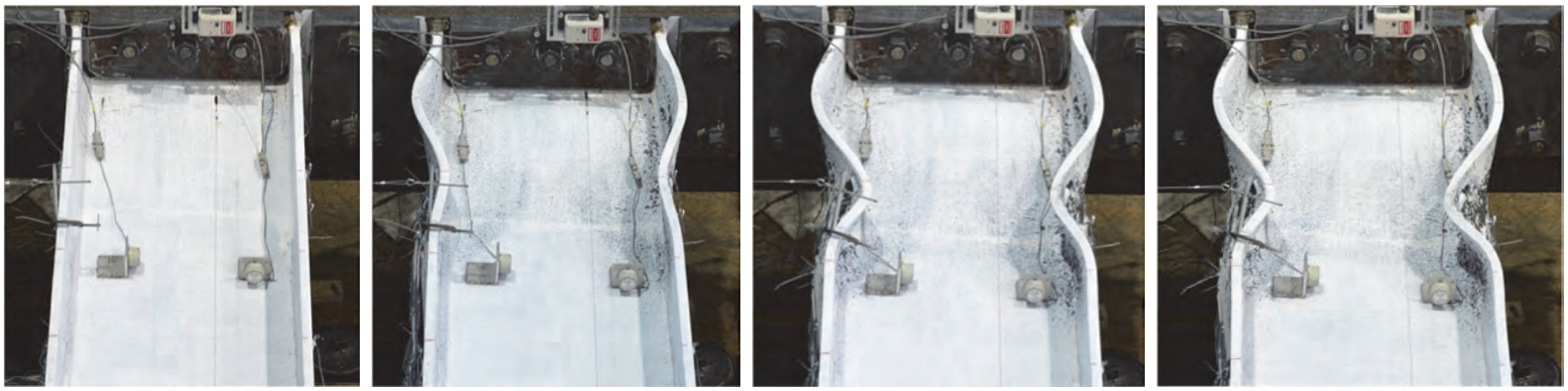

(a) West End

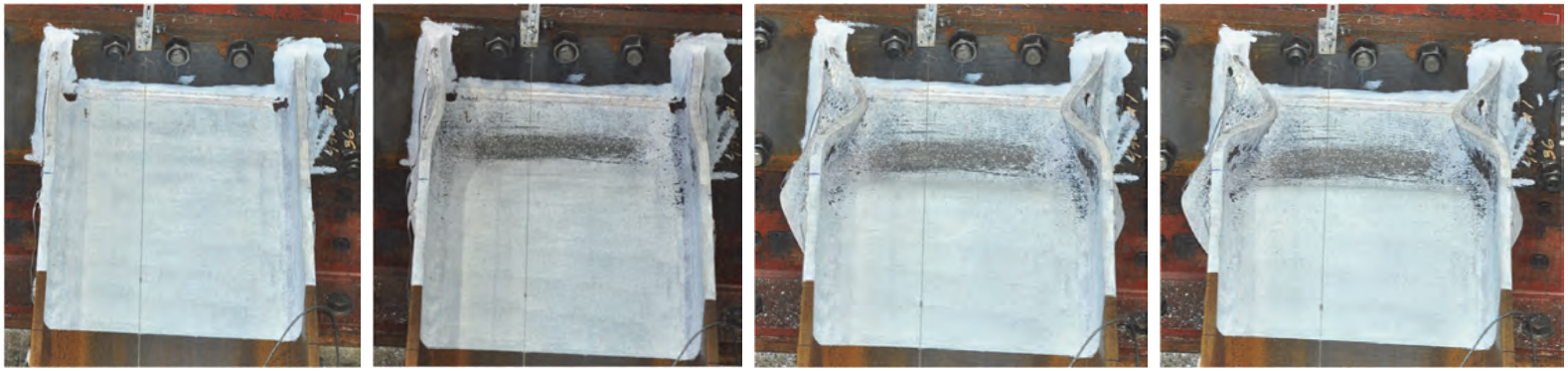

(b) East End

Figure 3.28 Specimen 2H: Yielding and Buckling Progression at Member Ends (Top View)

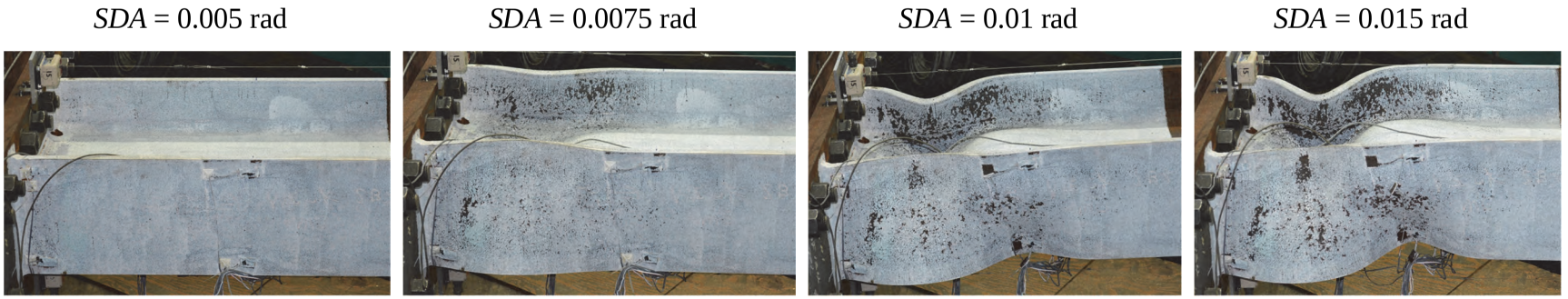

(a) West End

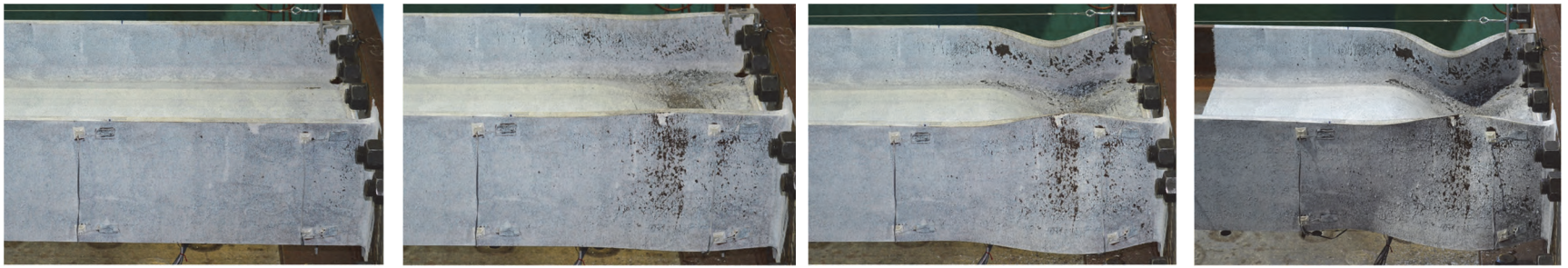

(b) East End

Figure 3.29 Specimen 2H: Yielding and Buckling Progression at Member Ends

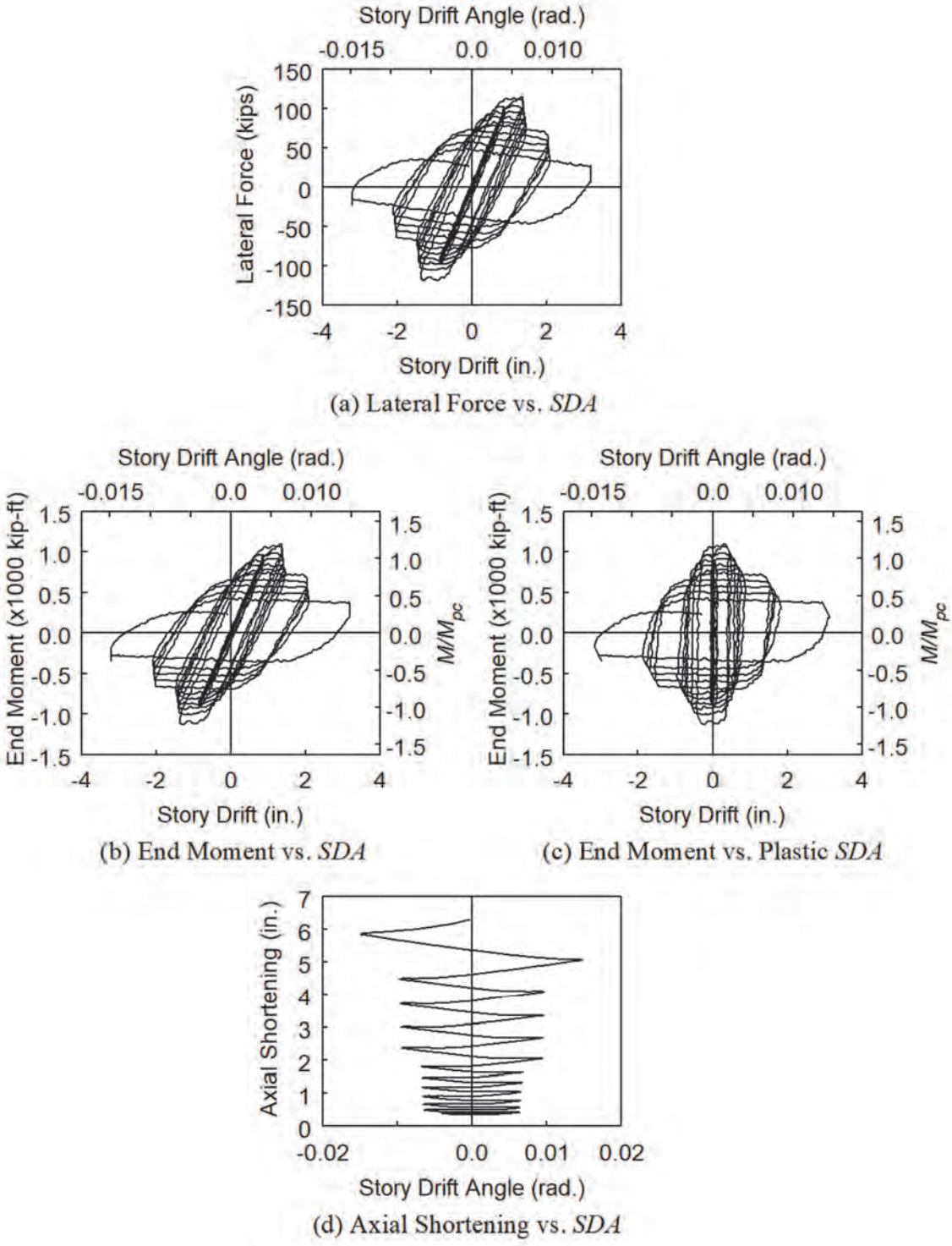

Figure 3.30 Specimen 2H: Global Responses

3.3 Group 1 Specimens: Section W24×176

3.3.1 General

To study the axial-load effect, three W24×176 columns were tested in this group with low, medium, and high levels of constant axial compression; all underwent the AISC loading protocol in the strong-axis bending direction. In comparison, section and member slenderness parameters of Group 1 specimens were more compact than those of Group 2 specimens (W24×131); thus, a more ductile cyclic behavior involving in-plane plastic hinging was expected. However, CB mode with out-of-plane, LTB-type global buckling was observed in testing.

3.3.2 Specimen 1L

The governing failure mode of Specimen 1L was CB with the double-curvature out-of-plane buckling configuration; yielding and buckling progression is illustrated in Figure 3.31 to Figure 3.33. At 3 % drift, the sloped flaking pattern was observed, indicating the tendency of out-of-plane buckling. At 4 % drift, LTB movements initiated at both ends, which aggravated at higher drifts (i.e., 5 % to 7 % drifts) as shown in Figure 3.31: during the positive excursion of each cycle, the positive-drift compression flanges (i.e., northwest and southeast flanges) buckled out of plane more, and the same happened for the negative-drift compression flanges during the negative excursion. These motions caused significant twisting in the specimen throughout the test. While the west end buckled downward generally, the east end buckled upward, forming the double-curvature configuration. The LTB-induced flange local buckles formed correspondingly to this out-of-plane curvatures, i.e., at the bottom and top half-width flanges of the west and east ends, respectively. The test was terminated after completing the positive excursion to 7 % drift due to excessive out-of-plane displacements.

Comparing Specimen 1L against Specimen 2L, the former had a stockier section, which allowed it to undergo the 3 % drift cycles without experiencing local buckling at both column ends; such occurred to the latter. Thus, the former sustained more inelastic drift cycles, experienced more strain hardening, and exhibited a flexural strength that was much higher than its reduced plastic moment capacity, M_{pc}, of the section [see Eq. (2.16)]; the hardening ratios, M_{max}/M_{pc}, were 1.40 and 1.17 for the former and latter, respectively.

With these hardening ratios, moment diagrams could be constructed for both specimens assuming the inflection points at midspan as shown in Figure 3.34. Consequently, the yielded length, i.e., the portion of the column end that became fully-plastic, could be estimated for each specimen; that of the former was twice as long as that of the latter. This yielded portion made the specimens more prone to global instability due to its reduced stiffness; indeed, LTB triggered in Specimen 1L with the longer yielded length.

Figure 3.35 shows the global responses. Flexural strength degradation and column axial shortening became apparent during the 5 % and higher drift cycles, corresponding to the significant LTB movements.

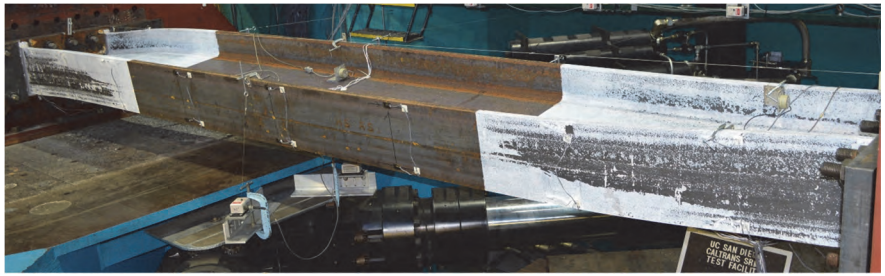

(a) *SDA* = +0.05 rad

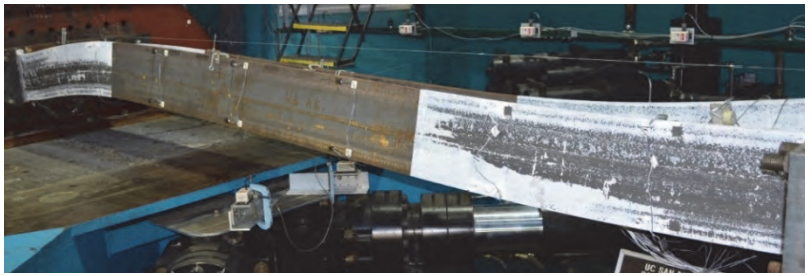

(b) *SDA* = -0.05 rad

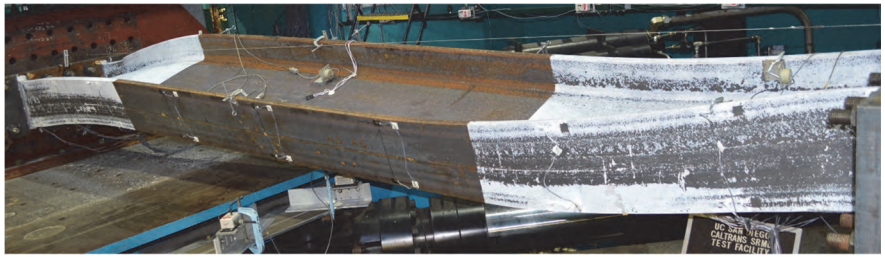

(c) *SDA* = +0.06 rad

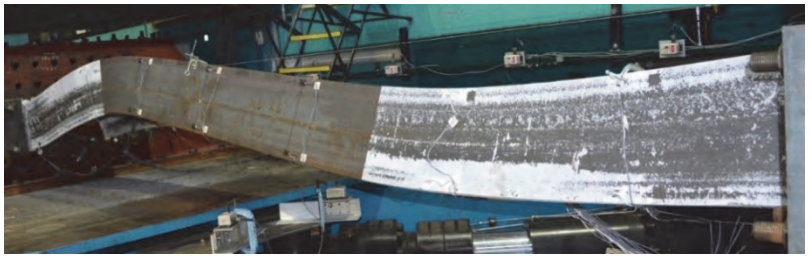

(d) *SDA* = -0.06 rad

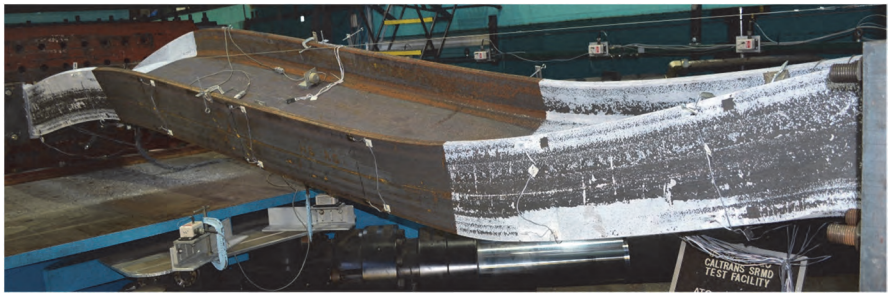

(e) *SDA* = +0.07 rad

Figure 3.31 Specimen 1L: Overall Yielding and Buckling Progression

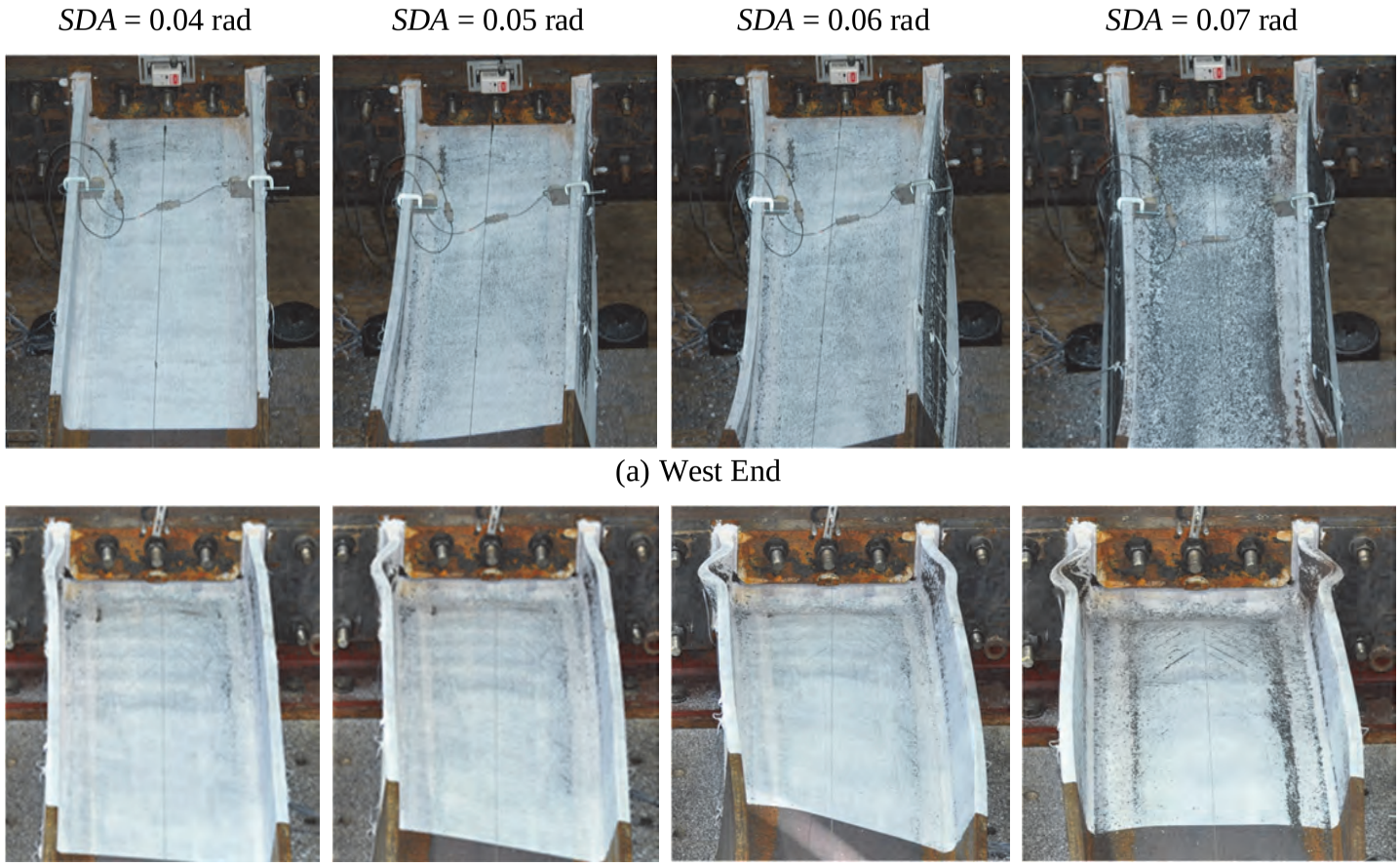

(a) West End

(b) East End

Figure 3.32 Specimen 1L: Yielding and Buckling Progression at Member Ends (Top View)

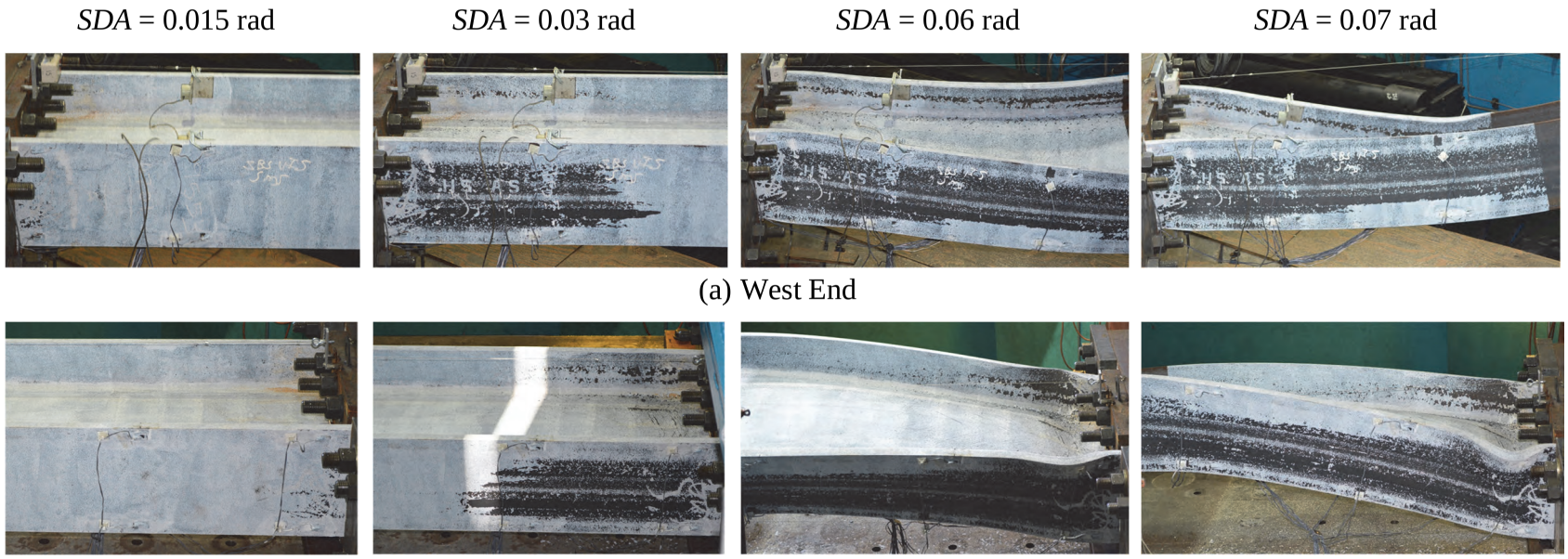

(a) West End

(b) East End

Figure 3.33 Specimen 1L: Yielding and Buckling Progression at Member Ends

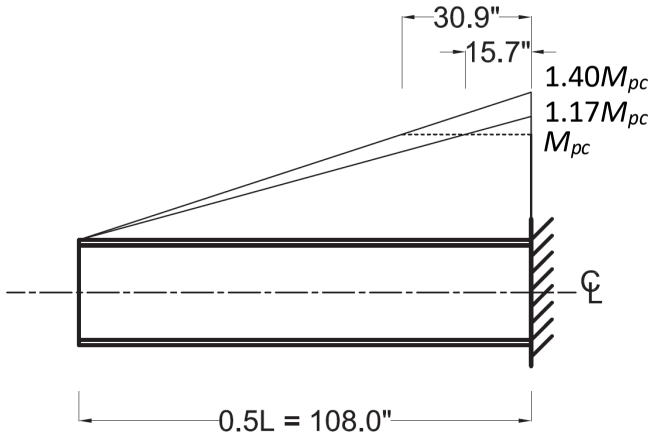

Figure 3.34 Specimen 1L: Comparison of Yielded Length

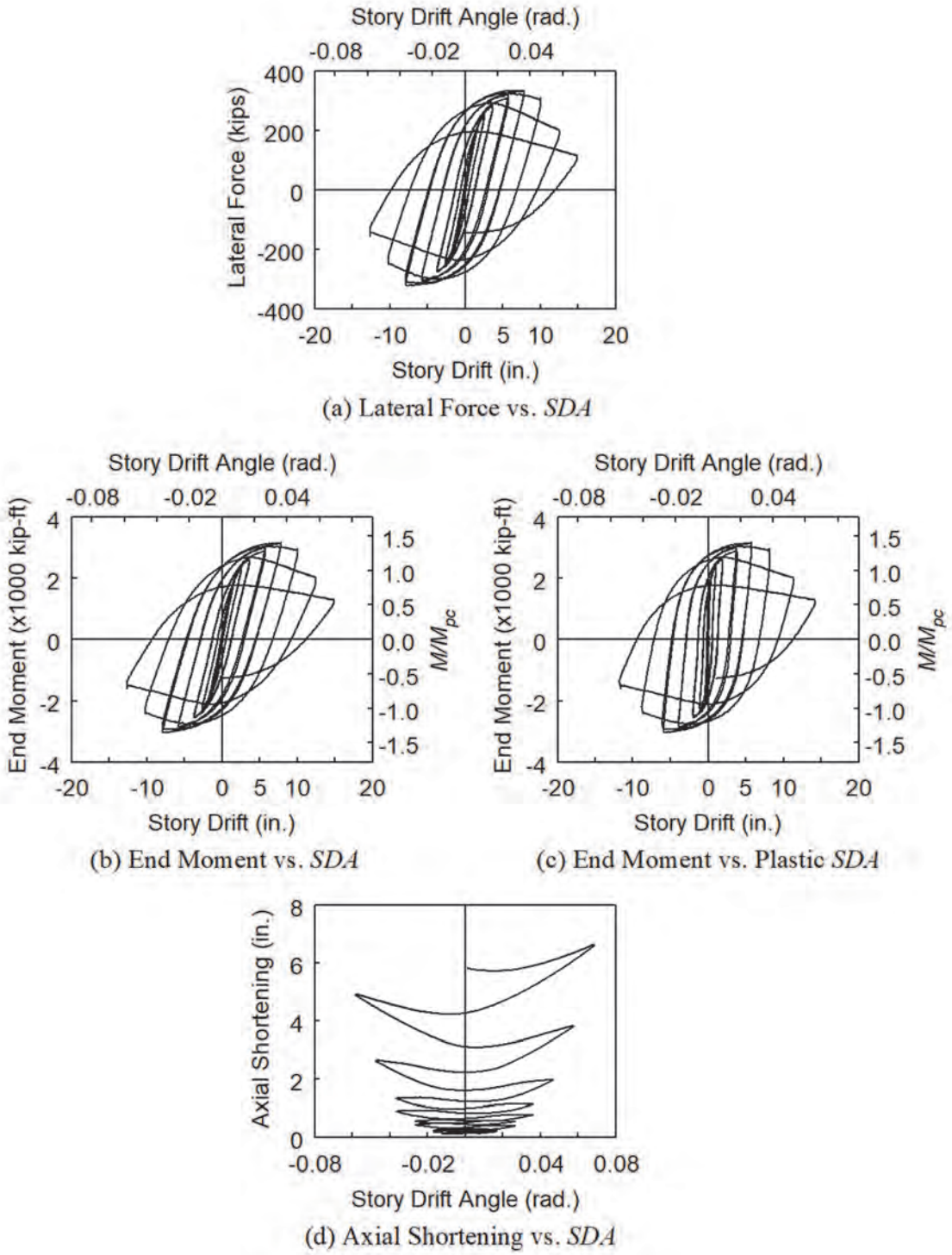

Figure 3.35 Specimen 1L: Global Responses

3.3.3 Specimen 1M

The governing failure mode of Specimen 1M was CB; yielding and buckling progression is illustrated in Figure 3.36 to Figure 3.38. At 1.5 % drift, the sloped flaking pattern in the flanges was observed. At 2 % drift, minor LTB movements initiated at both ends, which aggravated at higher drifts (i.e., 3 % to 4 % drifts) as shown in Figure 3.36: compression flanges buckled out of plane more during each cycle, causing significant twisting in the specimen. The out-of-plane curvatures induced flange local buckles at both column ends, which was also accompanied by web local buckling. Comparing Specimen 1M to Specimen 1L, web local buckles of the former exhibited higher amplitudes than those observed in the latter because of the increase in axial compression. The test was terminated after completing one cycle at 4 % drift due to significant loss in flexural strength.

Figure 3.39 shows the global responses. Flexural strength degradation and column axial shortening became apparent during the 3 % and 4 % drift cycles, corresponding to the significant LTB movements.

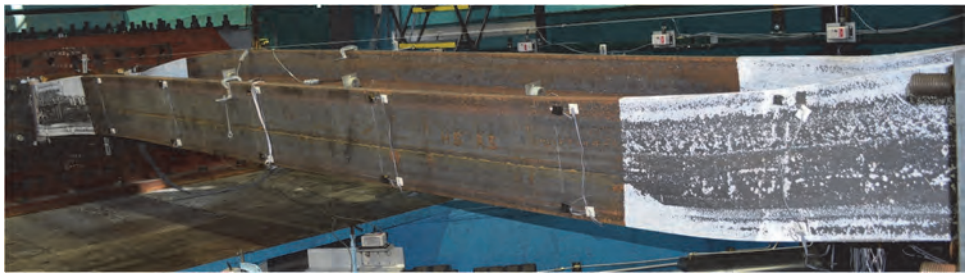

(a) *SDA* = +0.03 rad

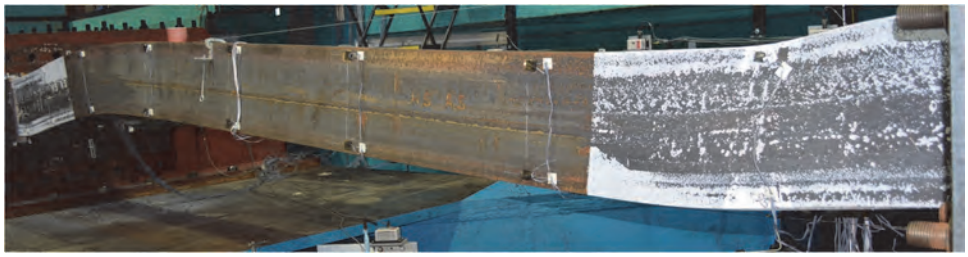

(b) *SDA* = -0.03 rad

(c) *SDA* = +0.04 rad

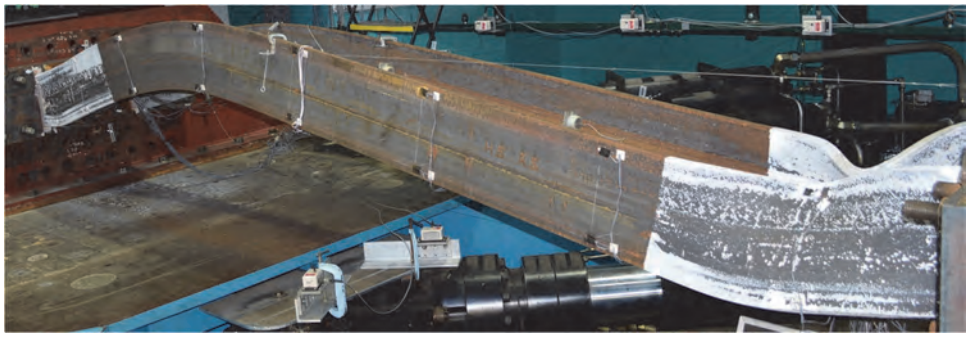

(d) *SDA* = -0.04 rad

Figure 3.36 Specimen 1M: Overall Yielding and Buckling Progression

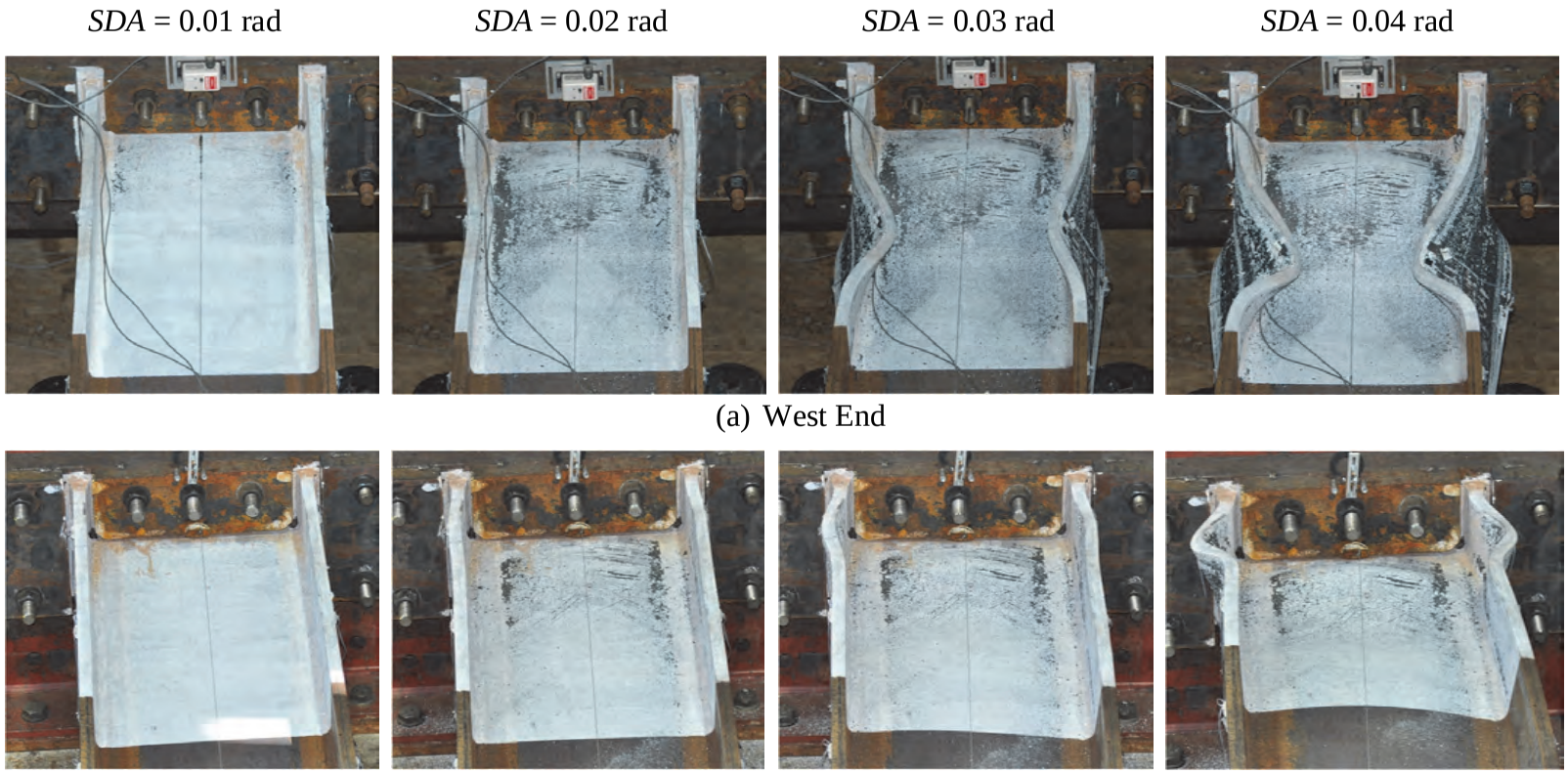

(a) West End

(b) East End

Figure 3.37 Specimen 1M: Yielding and Buckling Progression at Member Ends (Top View)

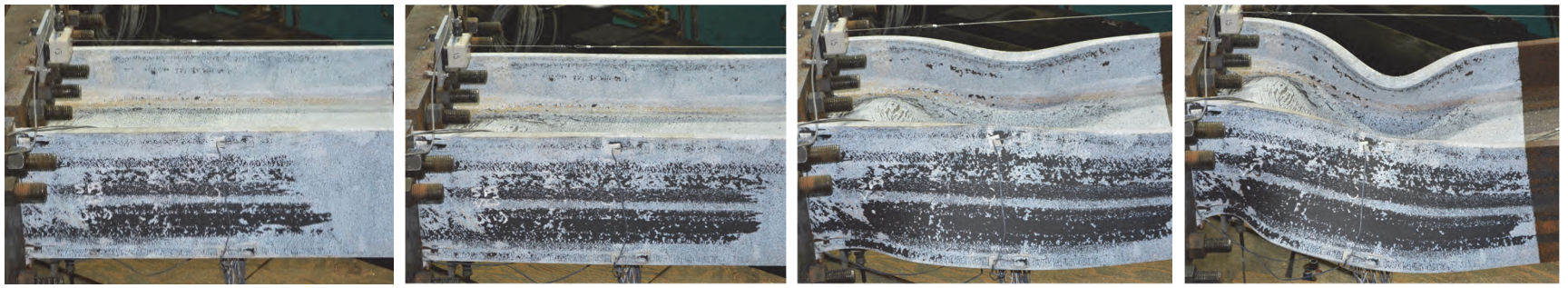

(a) West End

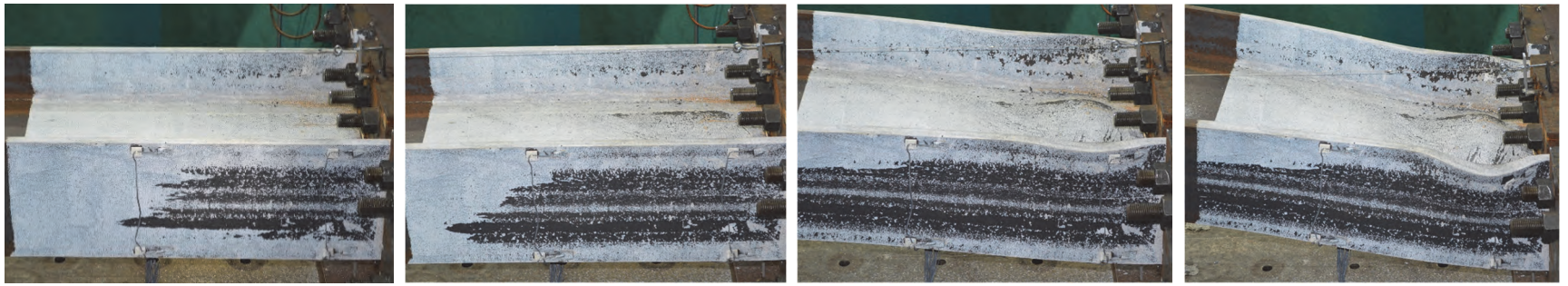

(b) East End

Figure 3.38 Specimen 1M: Yielding and Buckling Progression at Member Ends

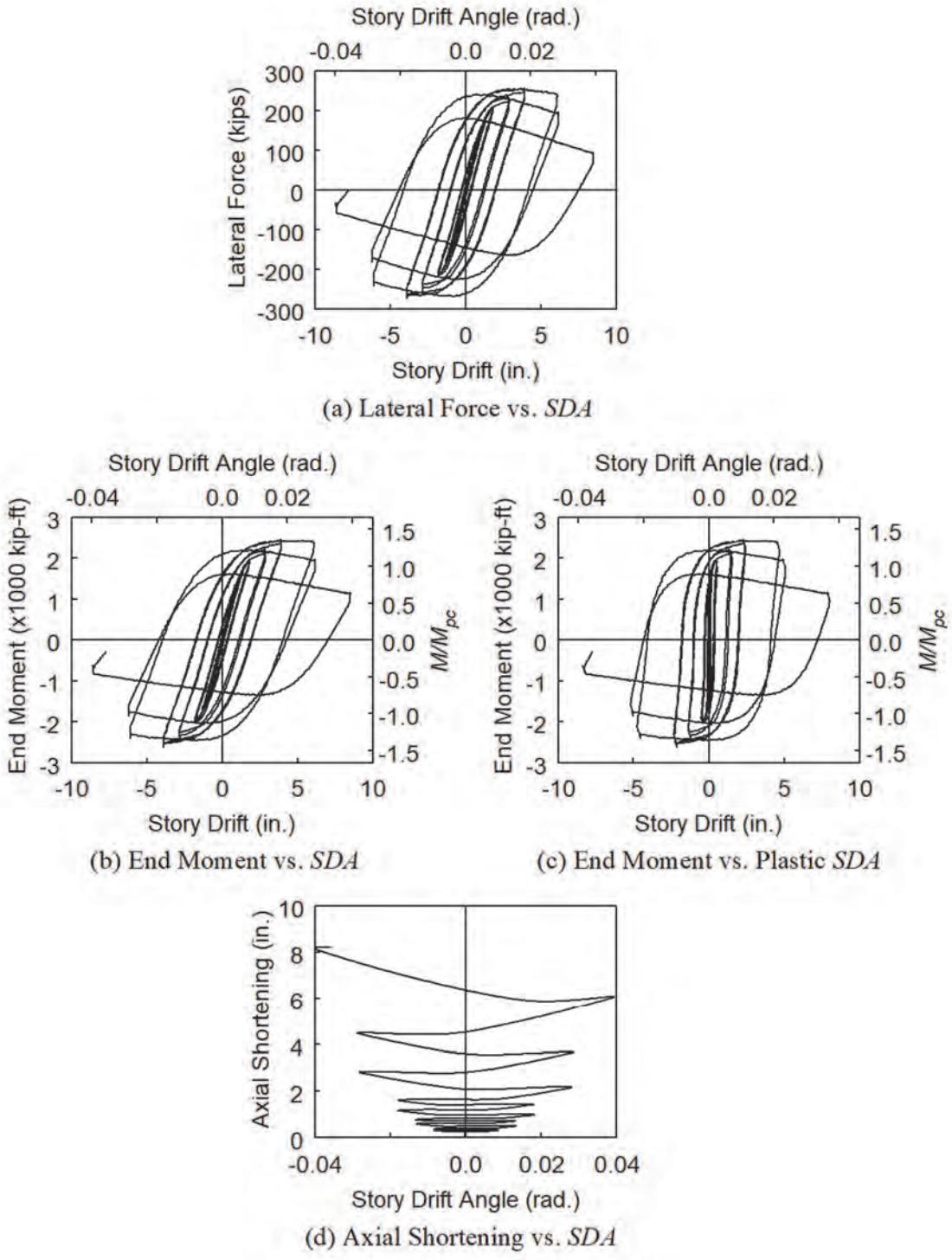

Figure 3.39 Specimen 1M: Global Responses

3.3.4 Specimen 1H

The governing failure mode of Specimen 1H was again CB; yielding and buckling progression is illustrated in Figure 3.40 to Figure 3.42. At 0.75 % drift, the sloped flaking pattern was observed (see Figure 3.42). At 1 % drift, slight LTB movements were observed; web and flange local buckling with minor amplitudes also initiated at both ends. At 1.5 % and 2 % drifts, LTB movements exacerbated; in the negative excursion of the first 2 % drift cycle, the midspan out-of-plane displacement grew rapidly as the specimen exhibited a flexural-type buckling configuration in single curvature (see Figure 3.43). At this point, the test was terminated due to significant flexural strength degradation as shown in Figure 3.44. The out-of-plane curvature also aggravated the flange local buckles on the upper half of the flanges at both column ends.

3.3.5 Concluding Remarks

Despite having a stockier section, Group 1 specimens did not fail by forming in-plane plastic hinges at column ends like that occurred among Group 2 specimens. On the contrary, they exhibited the CB failure mode involving out-of-plane LTB. Since the web and flanges were relatively stocky, they were less susceptible to local instability; as a result, Group 1 specimens underwent considerable strain hardening and developed longer yielded length than that observed in Group 2 specimens. This extensive yielded end portions of the columns deteriorated in stiffness, resulting in global instability in the form of LTB at the flanges under compression.

The effects of axial load levels on the CB columns (i.e., Group 1 specimens) were similar to those on the ALB columns (i.e., Group 2 specimens): plastic rotation capacity and energy dissipation capacity of the columns decreased as their levels of axial load increased. In addition, the beam-columns with the CB mode behaved more column-like when they sustained higher axial loads. For example, due to the higher uniform axial stress distribution in Specimen 1M, it exhibited more significant web local buckles than those observed in Specimen 1L. For Specimen 1H, the level of axial load was even more extreme, and as a result, its deformed configuration resembled flexural (or Euler) buckling about weak axis, which was a column-related global instability.

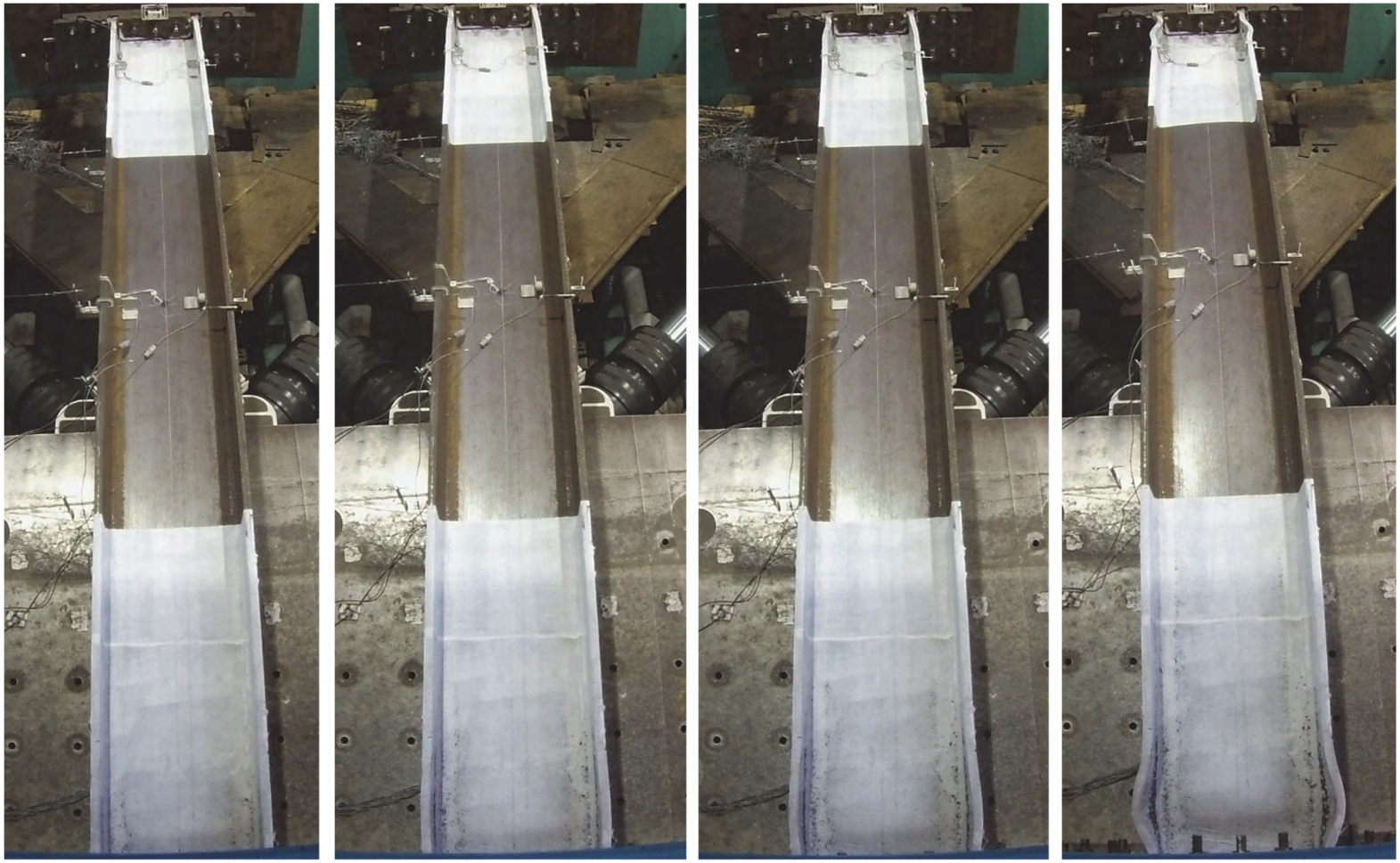

(a) *SDA* = 0.0075 rad (b) *SDA* = 0.01 rad (c) *SDA* = 0.015 rad (d) *SDA* = 0.02 rad

Figure 3.40 Specimen 1H: Overall Yielding and Buckling Progression

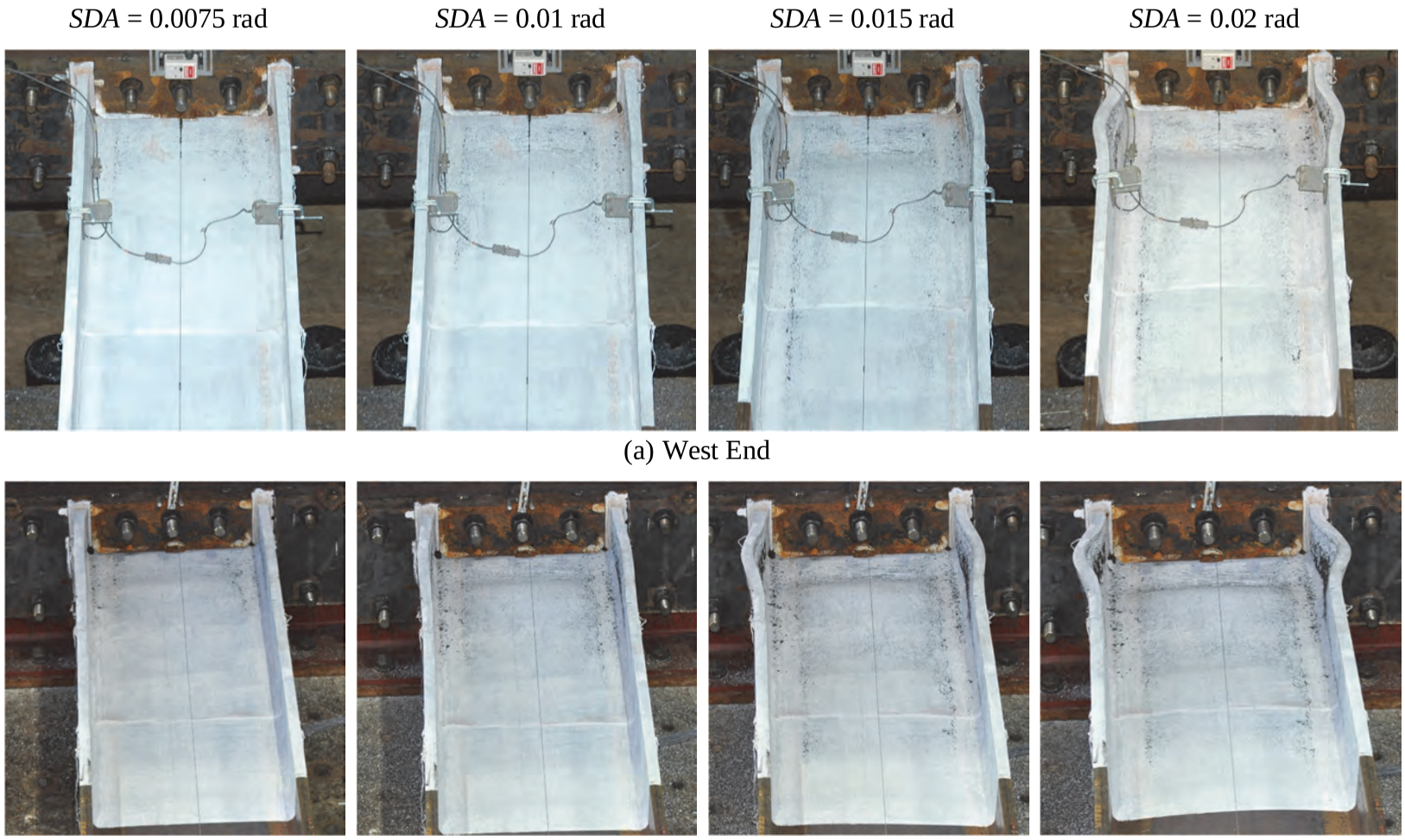

(a) West End

(b) East End

Figure 3.41 Specimen 1H: Yielding and Buckling Progression at Member Ends (Top View)

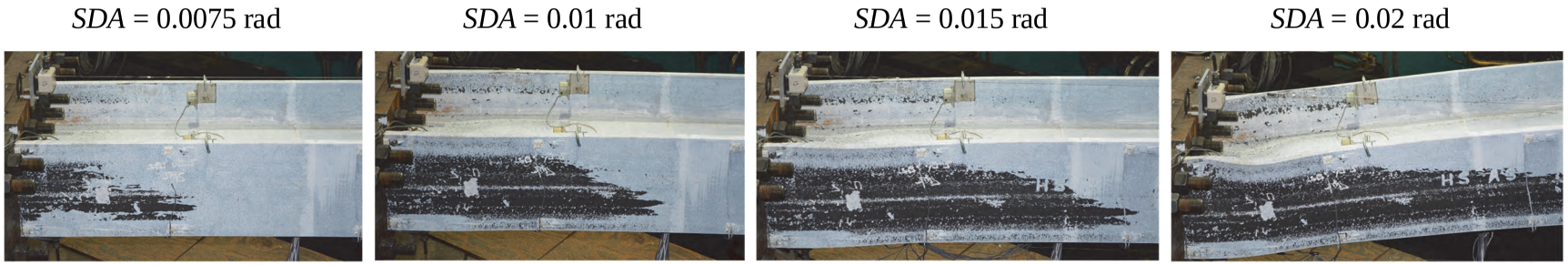

(a) West End

(b) East End

Figure 3.42 Specimen 1H: Yielding and Buckling Progression at Member Ends

Figure 3.43 Specimen 1H: Out-of-Plane Global Buckling at End of Test (Side View)

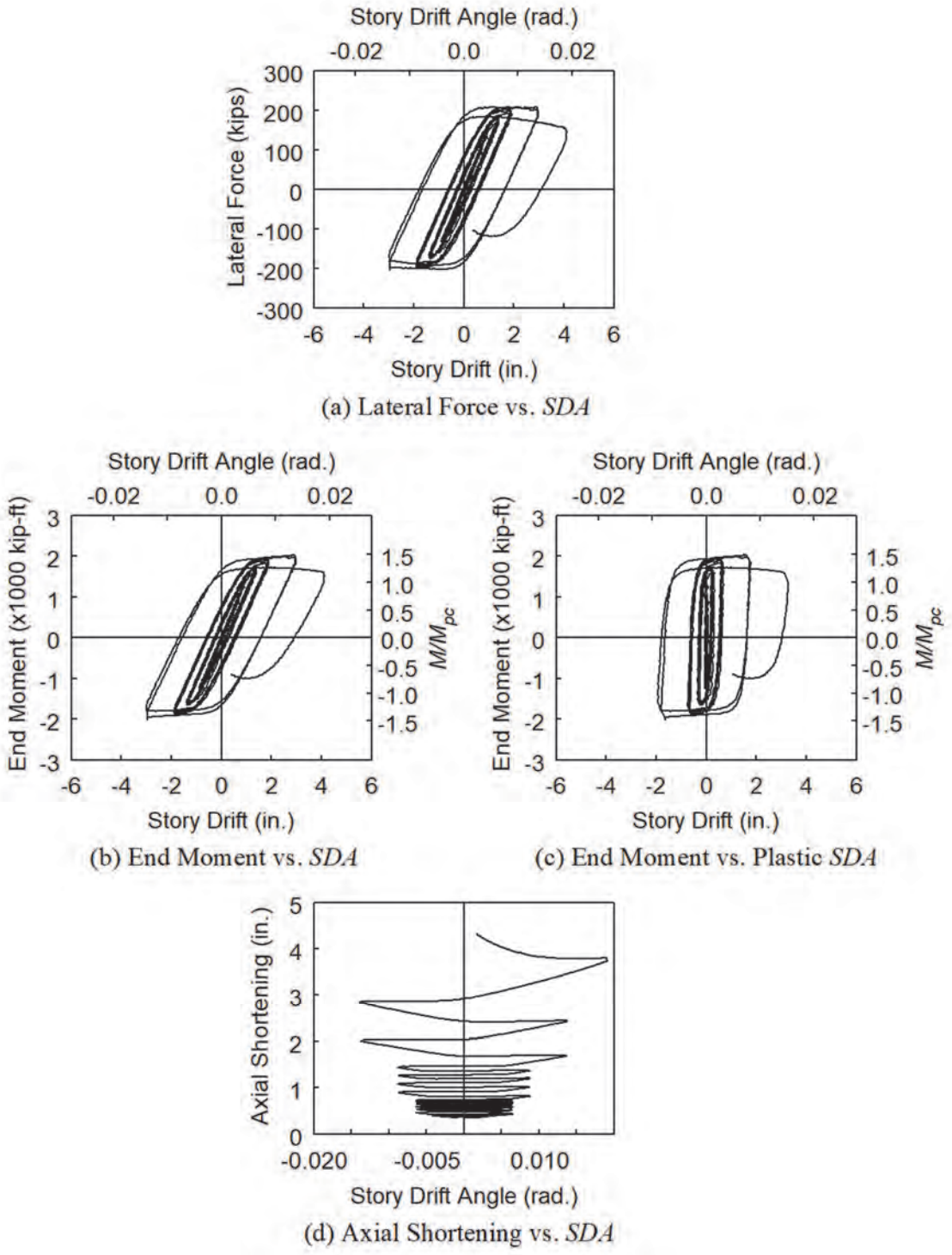

Figure 3.44 Specimen 1H: Global Responses

3.4 Group 3 Specimens: Section W24×104

3.4.1 General

Group 3 specimens had moderately ductile flanges and a highly ductile web for axial loads below the medium level (i.e., C_a = 0.4) per the AISC 341 classification. Comparing Group 3 to Group 2, section and member slenderness parameters of the former were slenderer than those of latter. Like the latter, the former exhibited ALB failure mode but with lower ductility capacities.

3.4.2 Specimen 3L

Yielding and buckling progression is illustrated in Figure 3.45 to Figure 3.47. Web and flange local buckling initiated at 2 % drift with the half-wave buckle set at each column end. Their amplitudes grew during the 3 % and 4 % drift cycles; additional web and flange local buckles also began to form. At this point, the deformed plastic hinges resembled the full-wave ALB configuration. At the west end, the sequence of web local buckling initiated with an upward apex followed by a downward apex; the order was opposite for the east end (see Figure 3.47). The flanges at each end buckled correspondingly to maintain perpendicular web-flange junctions. This series of buckle formation resulted in severely deformed column ends, which were accompanied by rigid-body twisting motions of the column portion between the buckled regions. These movements, however, should not be confused with those related with LTB observed in Group 1 testing. The test was terminated after completing two cycles at 4 % drift due to excessive local buckling and significant loss in flexural strength.

Global responses are shown in Figure 3.48. Flexural strength began to degrade during the 2 % drift cycles corresponding to the onset of local buckling at both ends; axial shortening also began to grow at an increasing rate at this point.

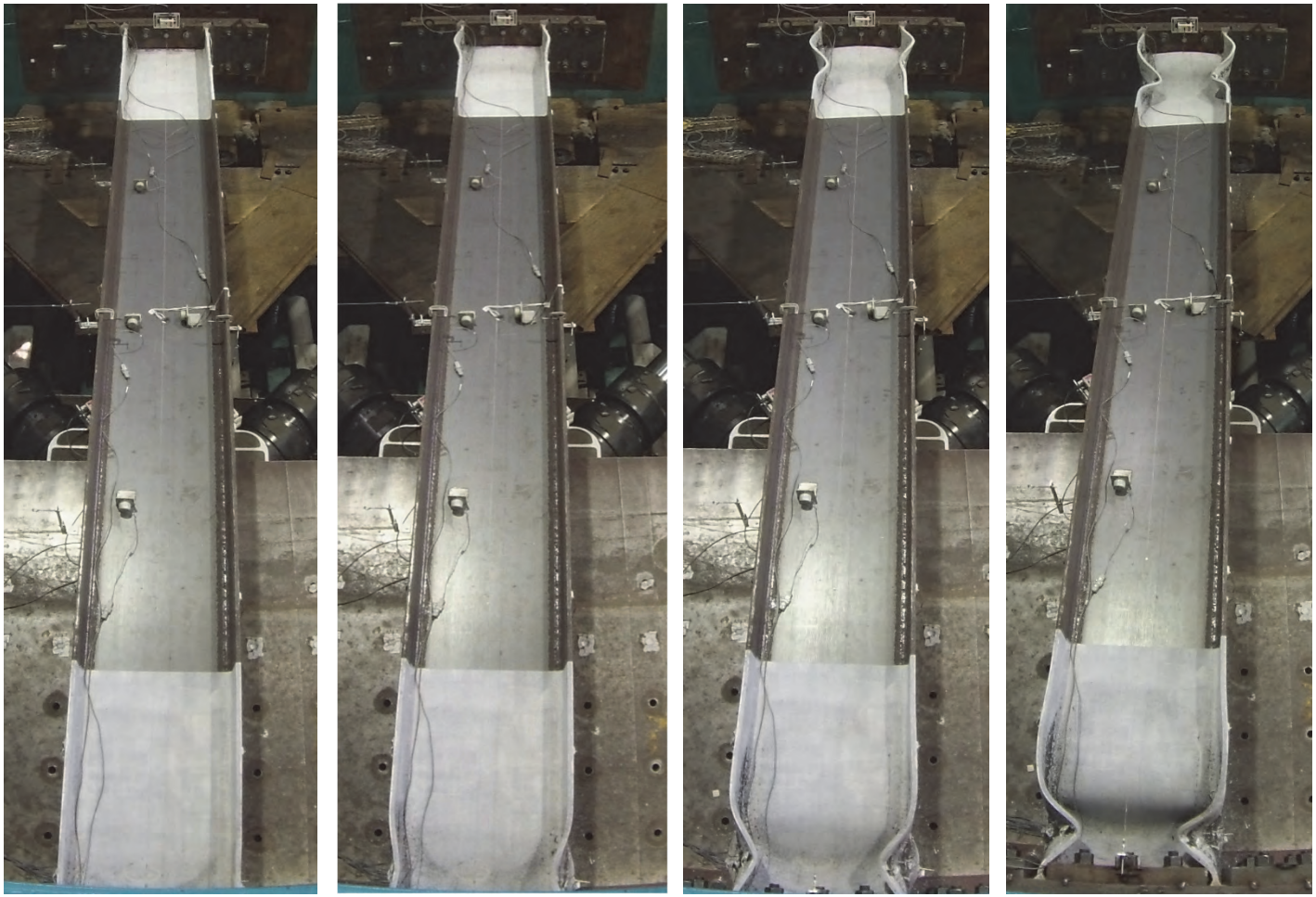

(a) *SDA* = 0.015 rad (b) *SDA* = 0.02 rad (c) *SDA* = 0.03 rad (d) *SDA* = 0.04 rad

Figure 3.45 Specimen 3L: Overall Yielding and Buckling Progression

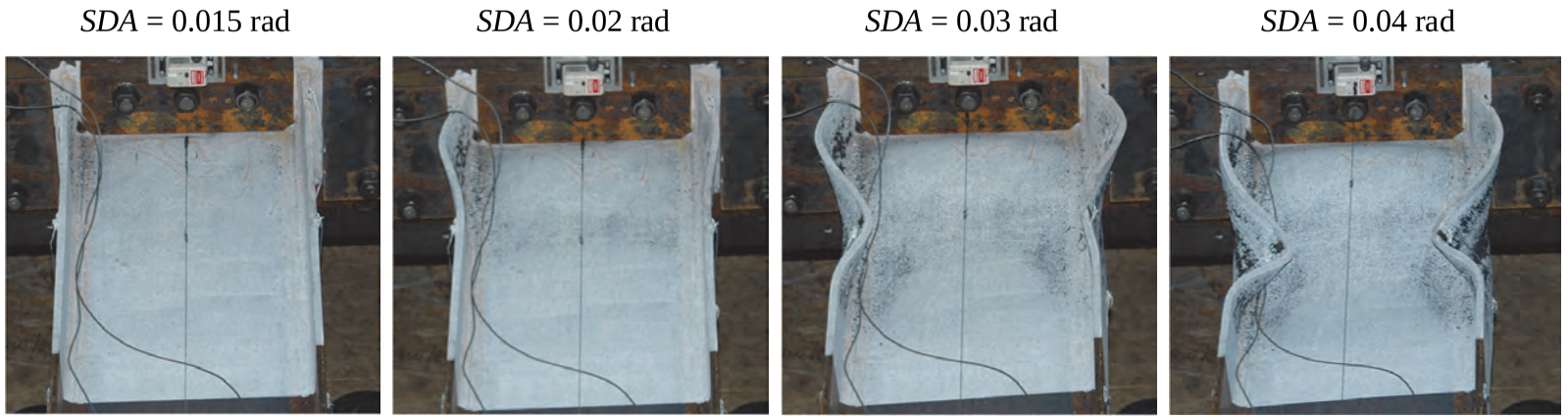

(a) West End

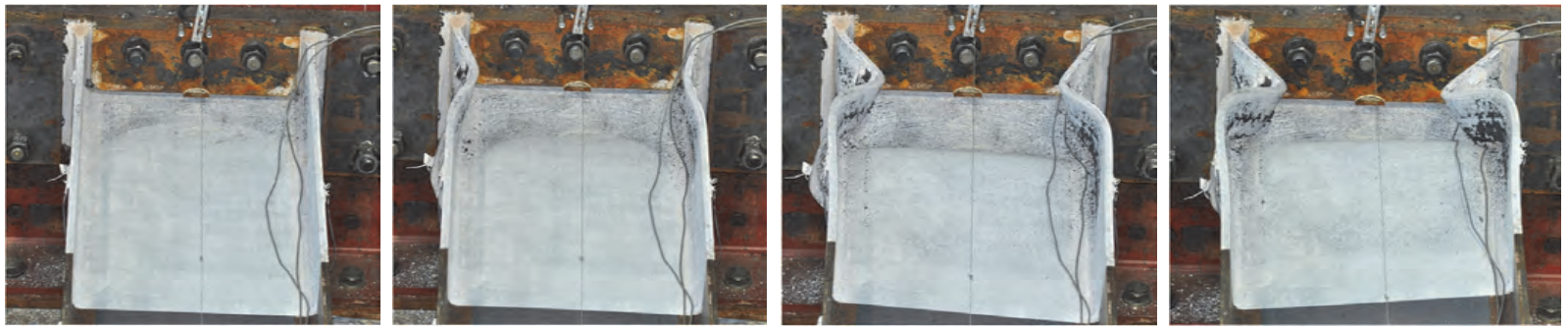

(b) East End

Figure 3.46 Specimen 3L: Yielding and Buckling Progression at Member Ends (Top View)

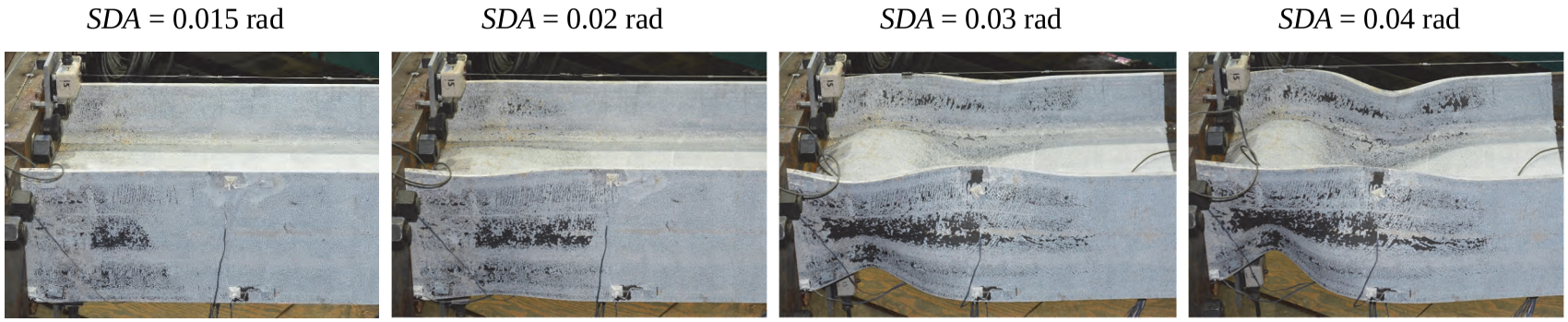

(a) West End

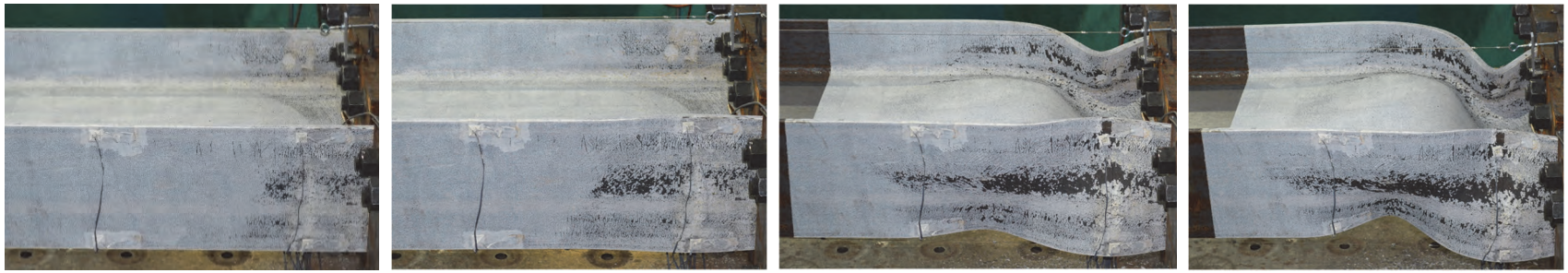

(b) East End

Figure 3.47 Specimen 3L: Yielding and Buckling Progression at Member Ends

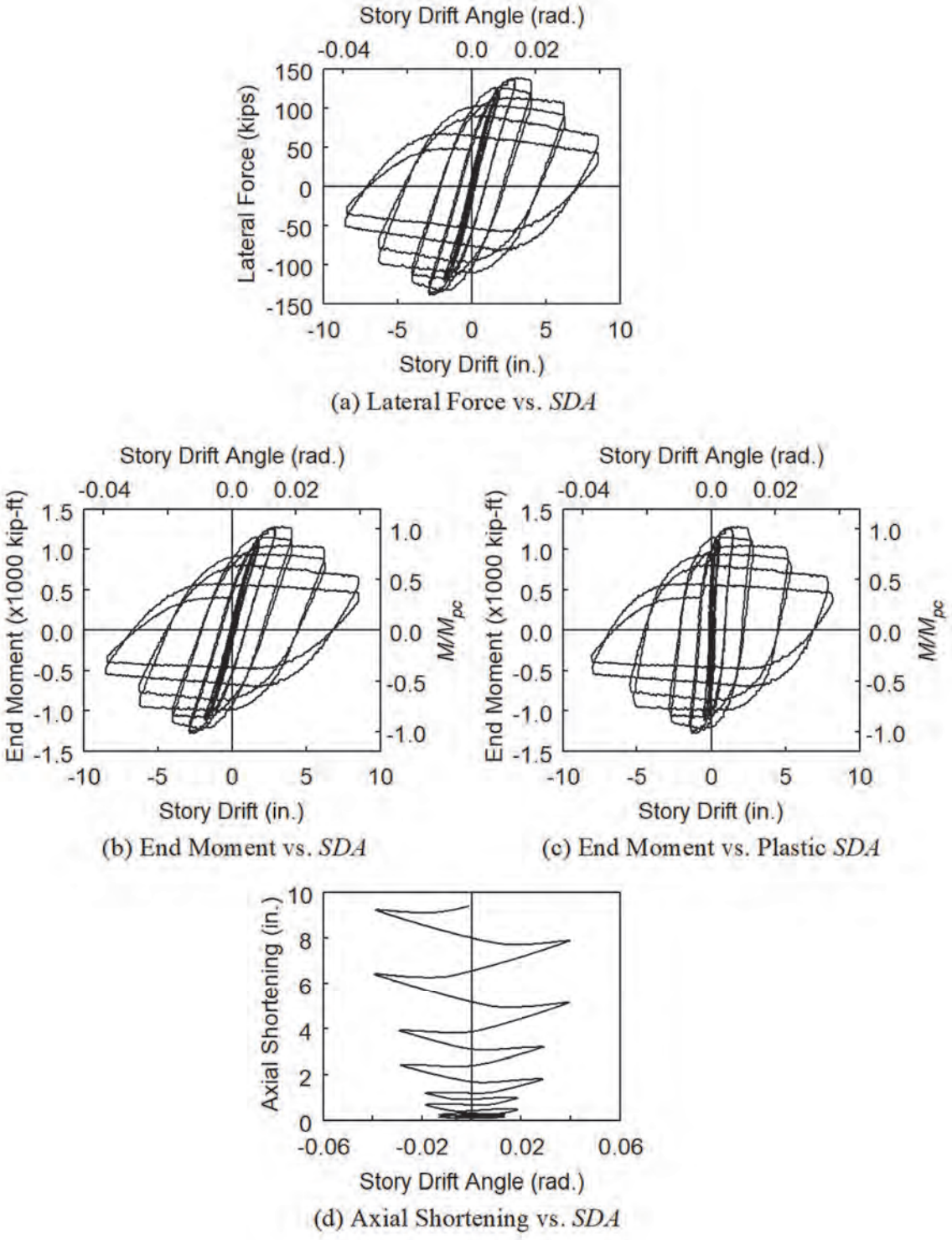

Figure 3.48 Specimen 3L: Global Responses

3.4.3 Specimen 3M

Specimen 3M exhibited the ALB failure mode; yielding and buckling progression is illustrated in Figure 3.49 to Figure 3.51. Web and flange local buckling initiated at 0.75 % drift. Their amplitudes grew during the 1 % and 1.5 % drift cycles: the half- and full-wave ALB configurations were observed at the west and east ends, respectively. The test was terminated after completing two cycles at 1.5 % drift due to significant flexural strength degradation.

Global responses are shown in Figure 3.52. Flexural strength began to degrade during the 0.75 % drift cycles corresponding to the onset of local buckling at both ends. Axial shortening aggravated drastically during the 1 % and 1.5 % drift cycles as local buckles became more apparent.

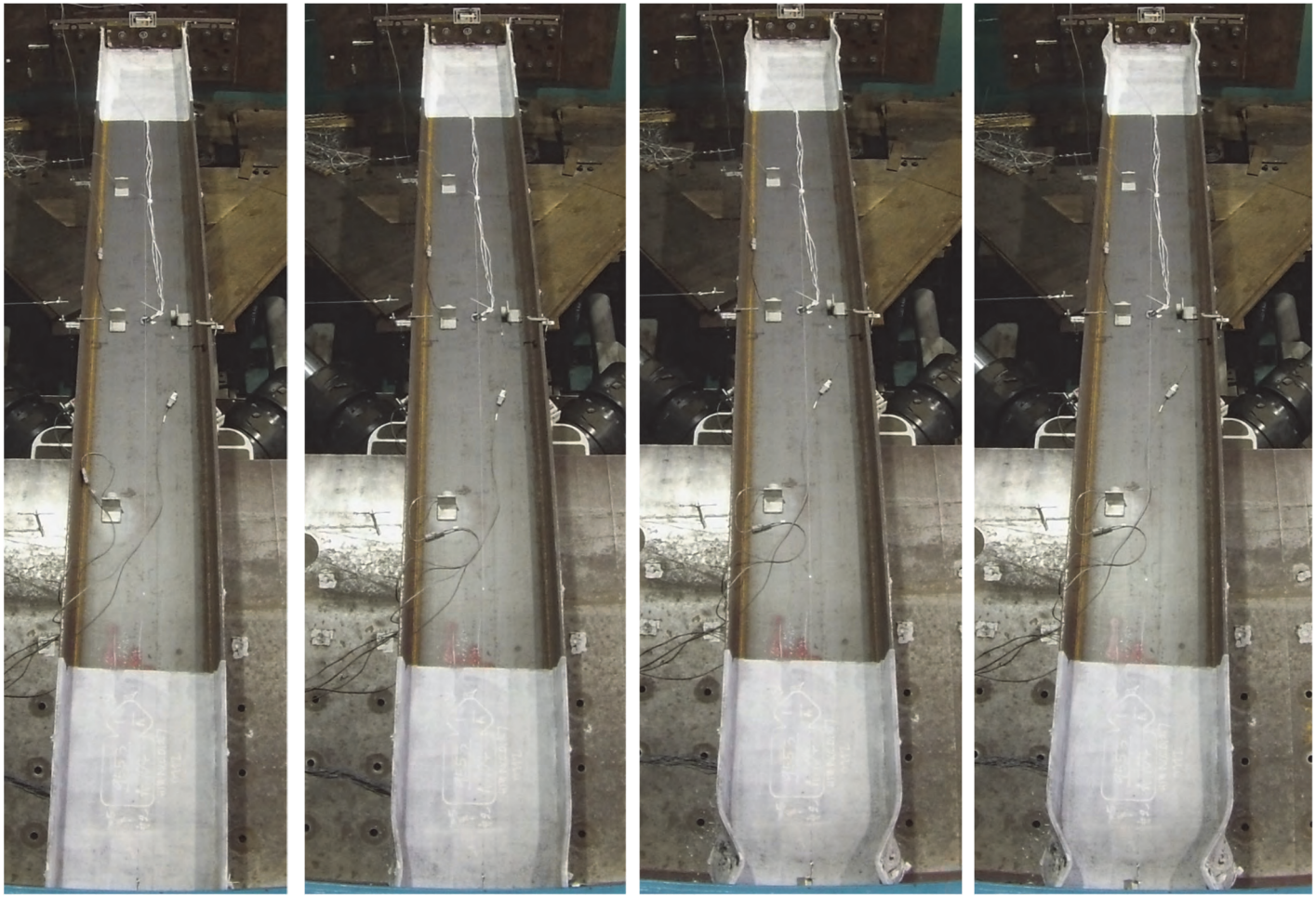

(a) *SDA* = 0.005 rad (b) *SDA* = 0.0075 rad (c) *SDA* = 0.01 rad (d) *SDA* = 0.015 rad

Figure 3.49 Specimen 3M: Overall Yielding and Buckling Progression

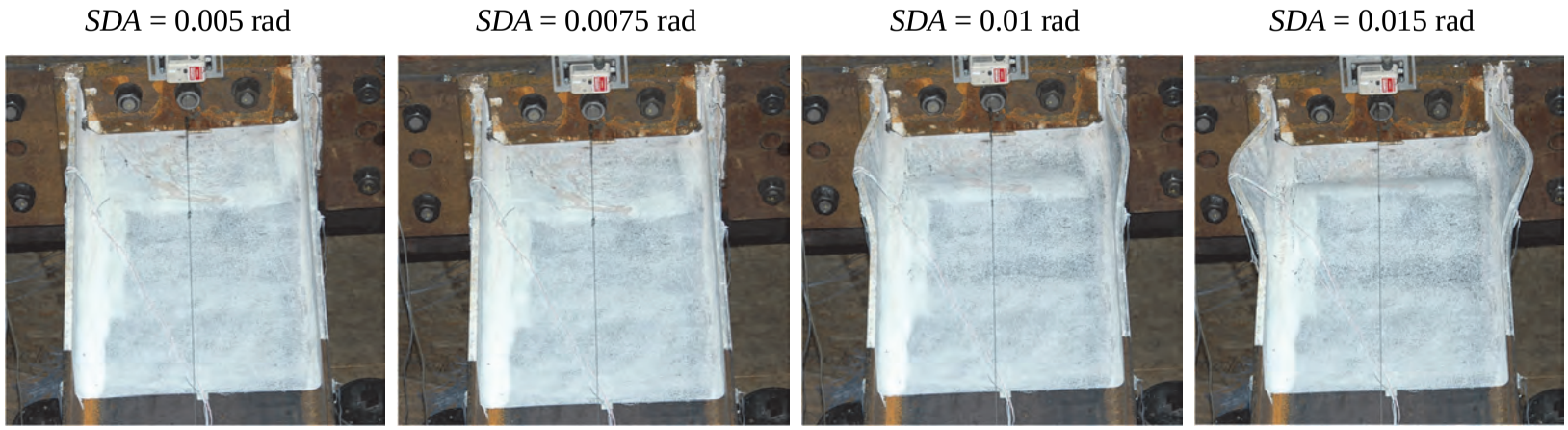

(a) West End

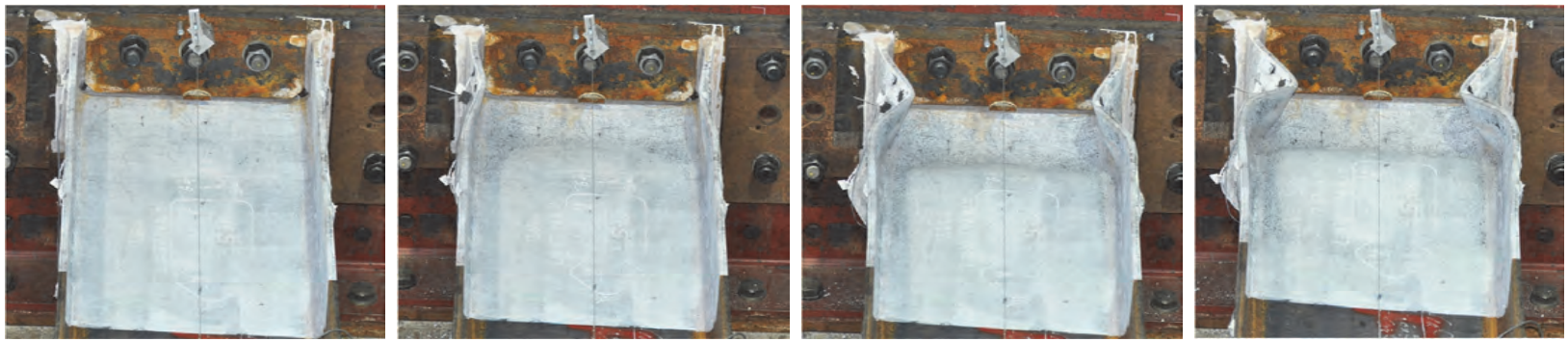

(b) East End

Figure 3.50 Specimen 3M: Yielding and Buckling Progression at Member Ends (Top View)

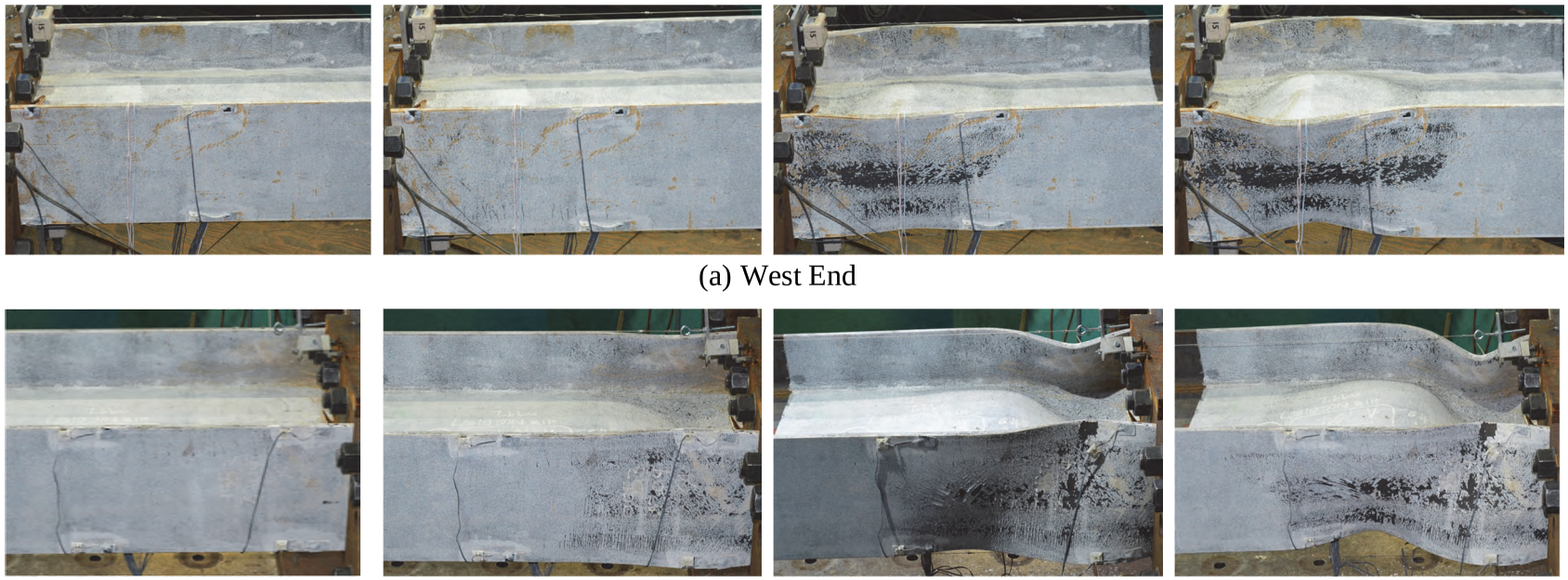

(a) West End

(b) East End

Figure 3.51 Specimen 3M: Yielding and Buckling Progression at Member Ends

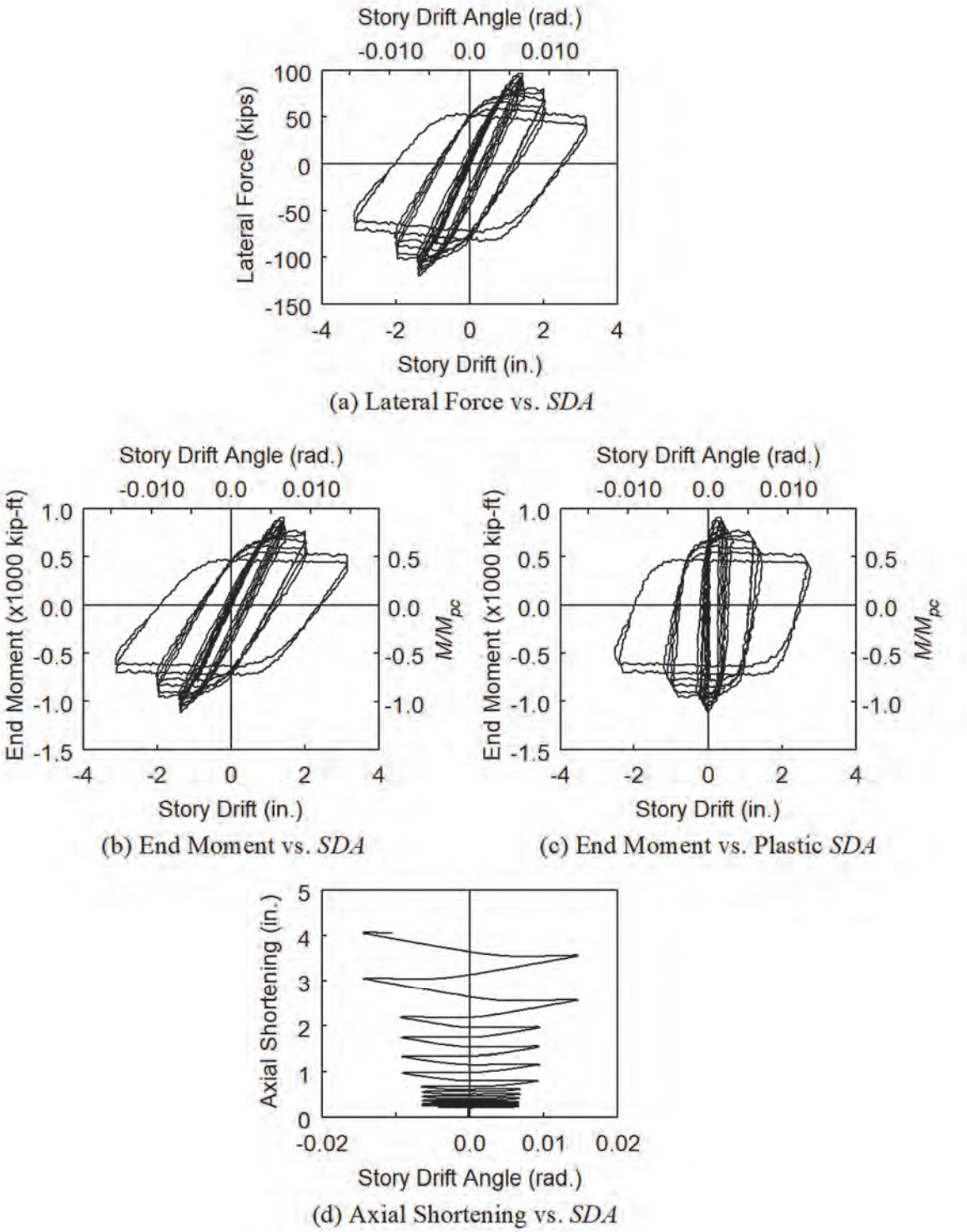

Figure 3.52 Specimen 3M: Global Responses

3.4.4 Specimen 3H

Specimen 3H sustained the highest constant axial compression among all specimens in this group. It exhibited the ALB failure mode; yielding and buckling progression is depicted in Figure 3.53 to Figure 3.55. Due to the significant axial load, local buckling initiated as soon as the specimen reached 0.75 % drift; after completing six cycles at this drift level, the column flexural capacity degraded rapidly to 34 % of the maximum strength as shown in Figure 3.56(b). At this point, the deformed plastic hinges resembled the full-wave ALB configuration, which became more apparent at 1 % drift. The test was terminated after completing two cycles at 1 % drift due to significant flexural strength degradation. As shown in Figure 3.56(d), column axial shortening grew rapidly during the 0.75 % and 1 % drift cycles corresponding to the formation of local buckles.

3.4.5 Concluding Remarks

The effects of axial load levels on Group 3 specimens were similar to those observed with Group 2 specimens: plastic rotation capacity and energy dissipation capacity of the columns decreased as their levels of axial load increased. In addition, with slenderer web and flanges, Group 3 specimens exhibited less ductile hysteresis compared to those of Group 2 specimens: local buckling initiated at 2 %, 0.75 %, and 0.75 % drifts for Specimens 3L, 3M, and 3H, respectively, while that initiated at 3 %, 1.5 %, and 0.75 % drifts for Specimens 2L, 2M, and 2H, respectively. The latter was also able to sustain more inelastic drift cycles than the former before experiencing significant loss in flexural strength. This illustrated the effect of section slenderness parameters.

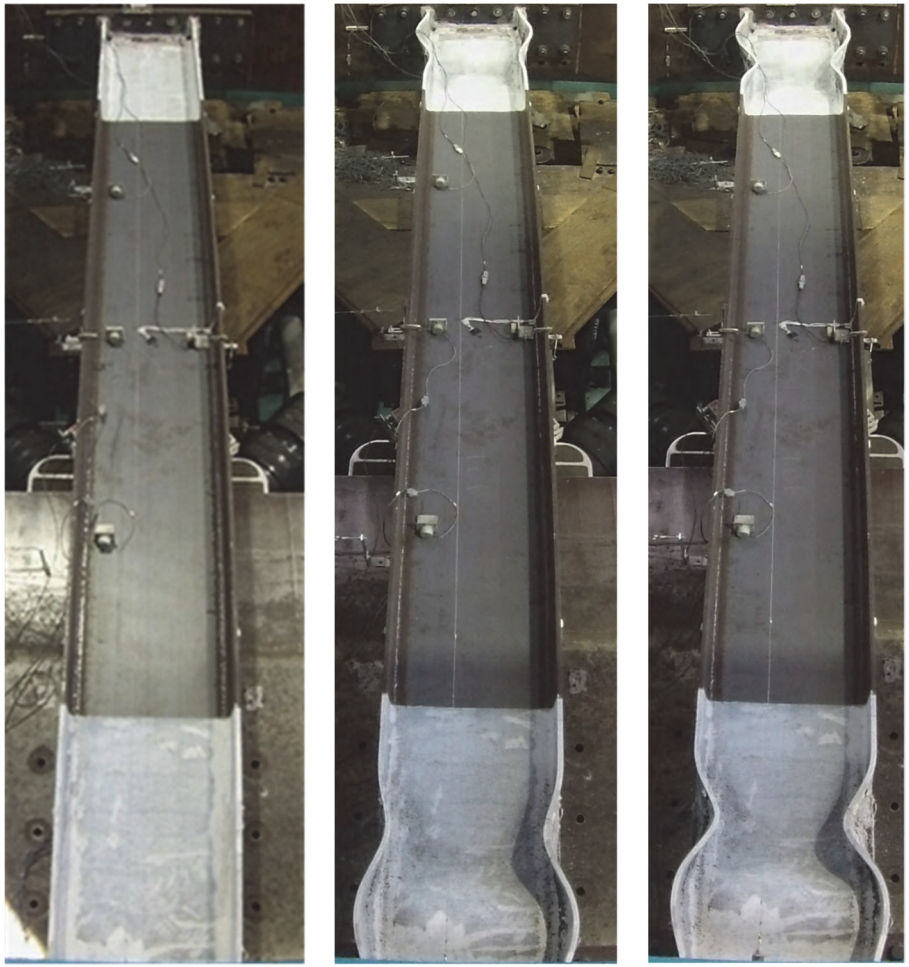

(a) *SDA* = 0.005 rad (b) *SDA* = 0.0075 rad (c) *SDA* = 0.01 rad

Figure 3.53 Specimen 3H: Overall Yielding and Buckling Progression

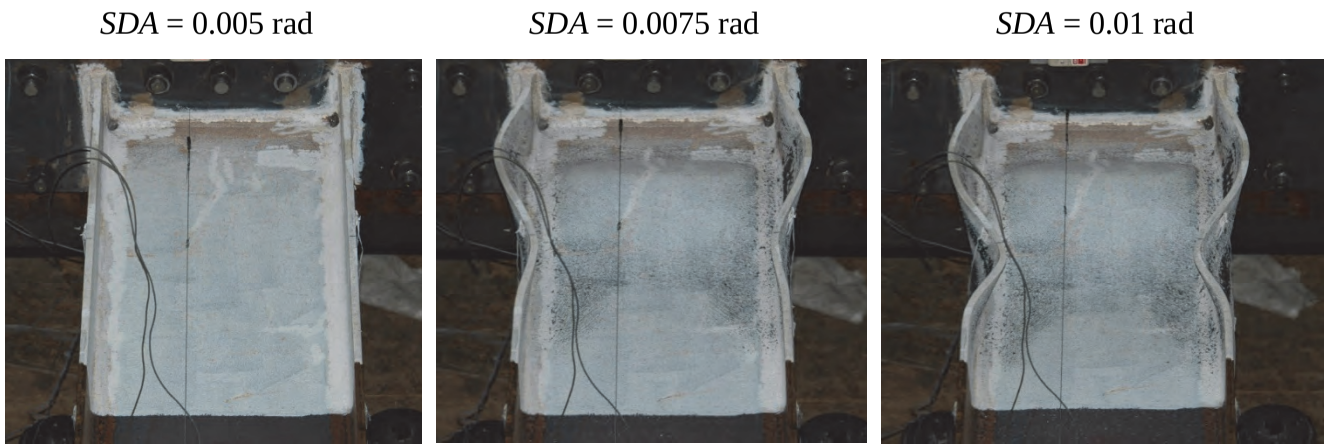

(a) West End

(b) East End

Figure 3.54 Specimen 3H: Yielding and Buckling Progression at Member Ends (Top View)

SDA = 0.005 rad | *SDA* = 0.0075 rad | *SDA* = 0.01 rad

(a) West End

(b) East End

Figure 3.55 Specimen 3H: Yielding and Buckling Progression at Member Ends

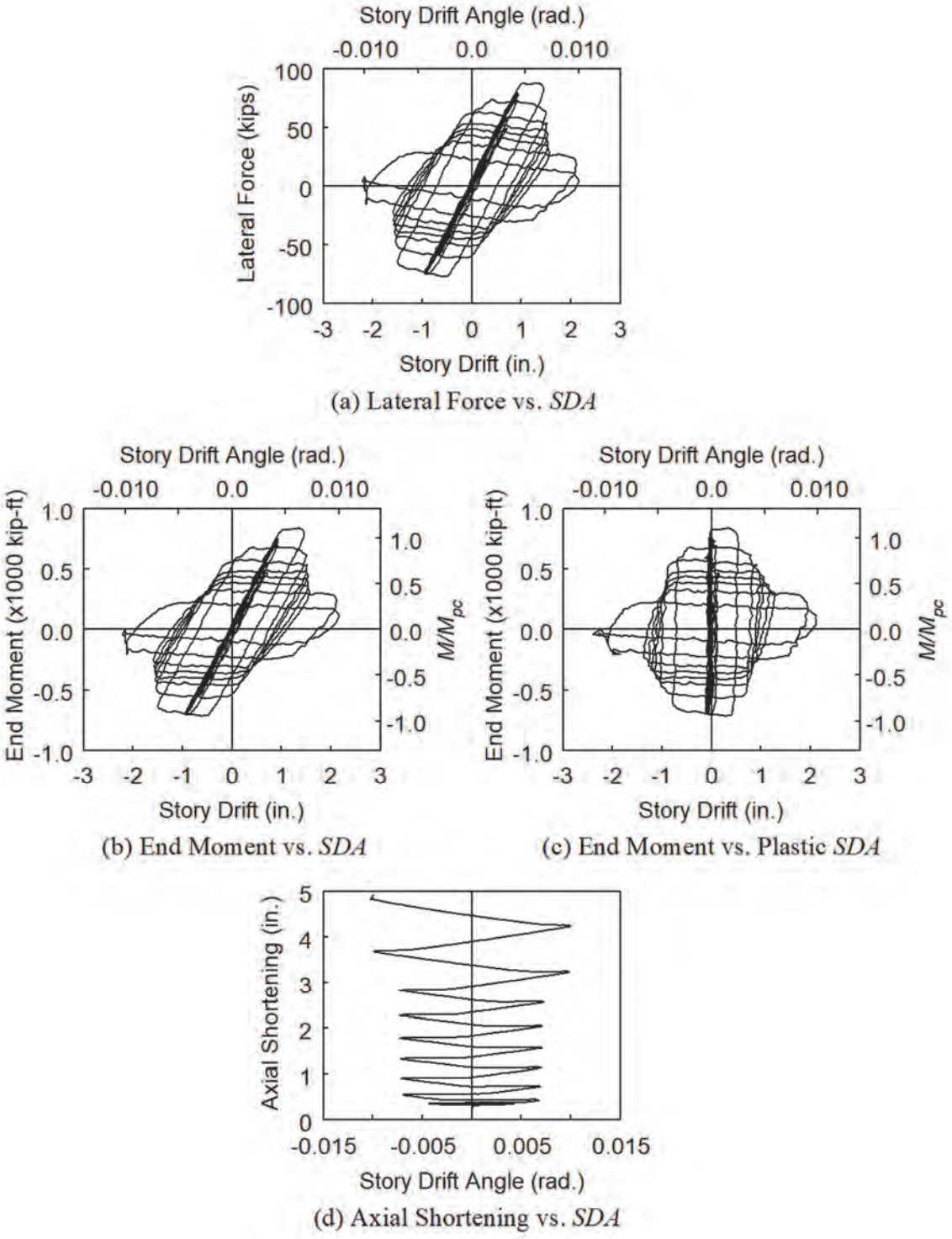

Figure 3.56 Specimen 3H: Global Responses

3.5 Group 4 Specimens: Section W24×84

3.5.1 General

Group 4 specimens had highly ductile flanges and a moderately ductile web for axial loads above the low level (i.e., C_a = 0.2) according to AISC 341. In comparison, the web was slenderer than those of Groups 1, 2, and 3, and the flange slenderness fell between that of Groups 1 and 2. In addition, the member slenderness parameter, L/r_y, of Group 4 specimens was about 50 % greater than those of the first three groups.

3.5.2 Specimen 4L

The governing failure mode of Specimen 4L was CB; yielding and buckling progression is illustrated in Figure 3.57 to Figure 3.59. At 1.5 % drift, minor web and flange local buckling was observed at both ends. It aggravated at 2 % drift and was accompanied by minor LTB movements. At 3 % drift, the LTB movements became apparent, exhibiting the double-curvature configuration [see Figure 3.60(a)].

Global responses are shown in Figure 3.61. Flexural strength began to degrade during the 2 % drift cycles when local buckling exacerbated; this combined with the aggravating out-of-plane buckling during the 3 % drift cycles caused the strength degradation to become more drastic. After completing two cycles at 3 % drift, flexural strength reduced to 46 % of the maximum moment capacity; the AISC cyclic loading was stopped at this point. Development of axial shortening followed the same trend as that of the flexural strength deterioration.

After the AISC loading, the specimen was subjected to a dynamic test with the near-fault lateral-displacement history as shown in Figure 3.62. The deformed configuration at the end of the dynamic test is shown in Figure 3.60(b): the global buckling amplitudes were amplified. Global responses are shown in Figure 3.63.

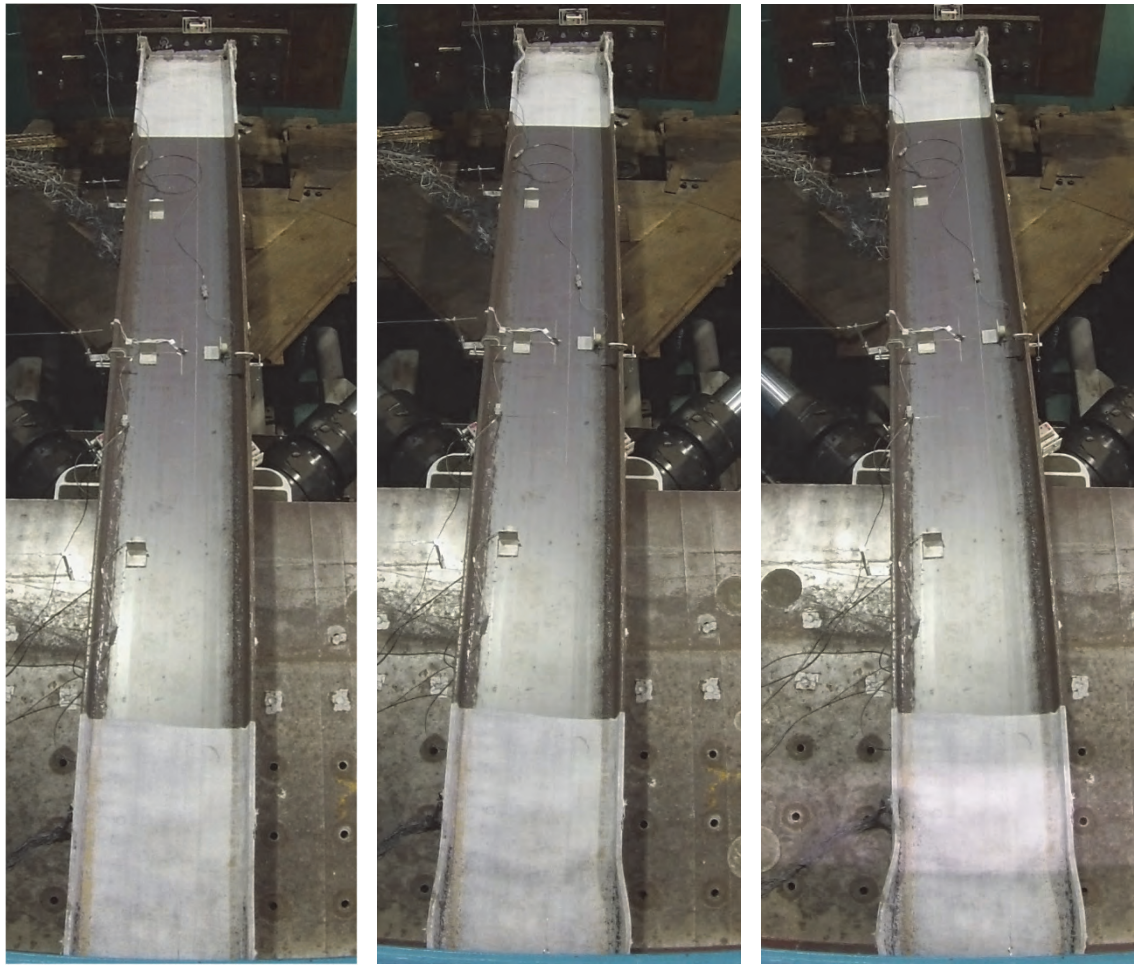

(a) *SDA* = 0.015 rad (b) *SDA* = 0.02 rad (c) *SDA* = 0.03 rad

Figure 3.57 Specimen 4L: Overall Yielding and Buckling Progression

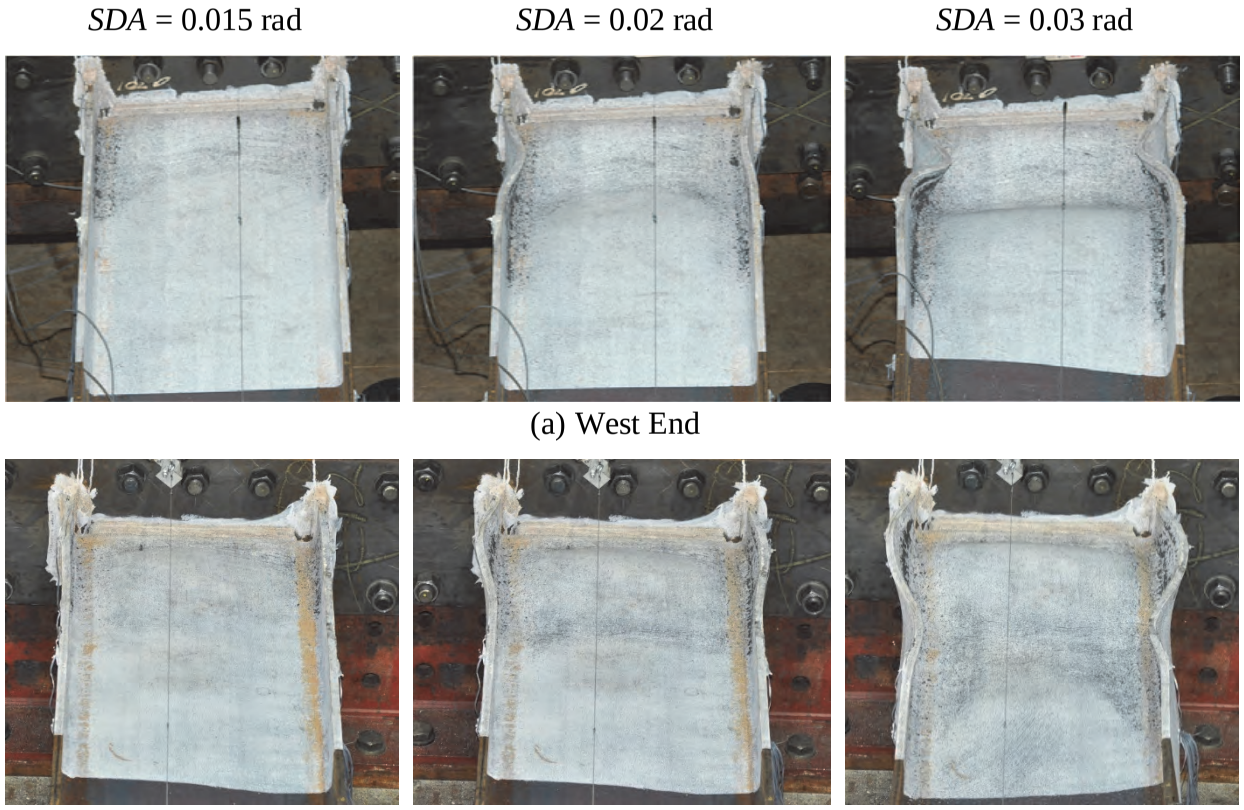

(a) West End

(b) East End

Figure 3.58 Specimen 4L: Yielding and Buckling Progression at Member Ends (Top View)

SDA = 0.015 rad | *SDA* = 0.02 rad | *SDA* = 0.03 rad

(a) West End

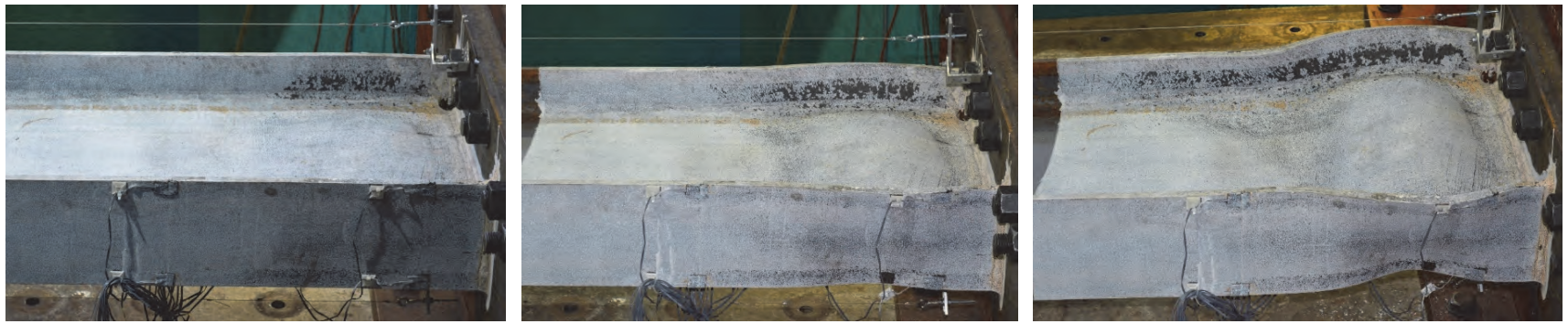

(b) East End

Figure 3.59 Specimen 4L: Yielding and Buckling Progression at Member Ends

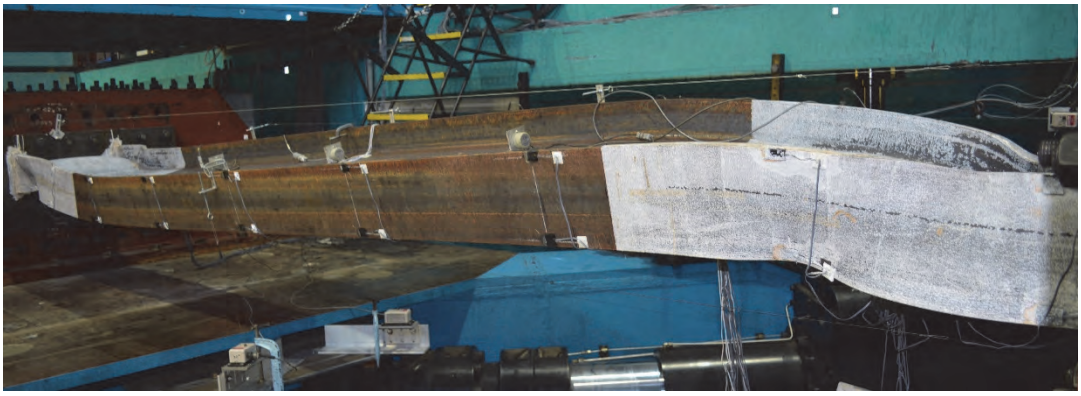

(a) *SDA* = 0.03 rad

(b) End of the Subsequent Near-fault Loading

Figure 3.60 Specimen 4L: Out-of-Plane Global Buckling at End of Tests (Side View)

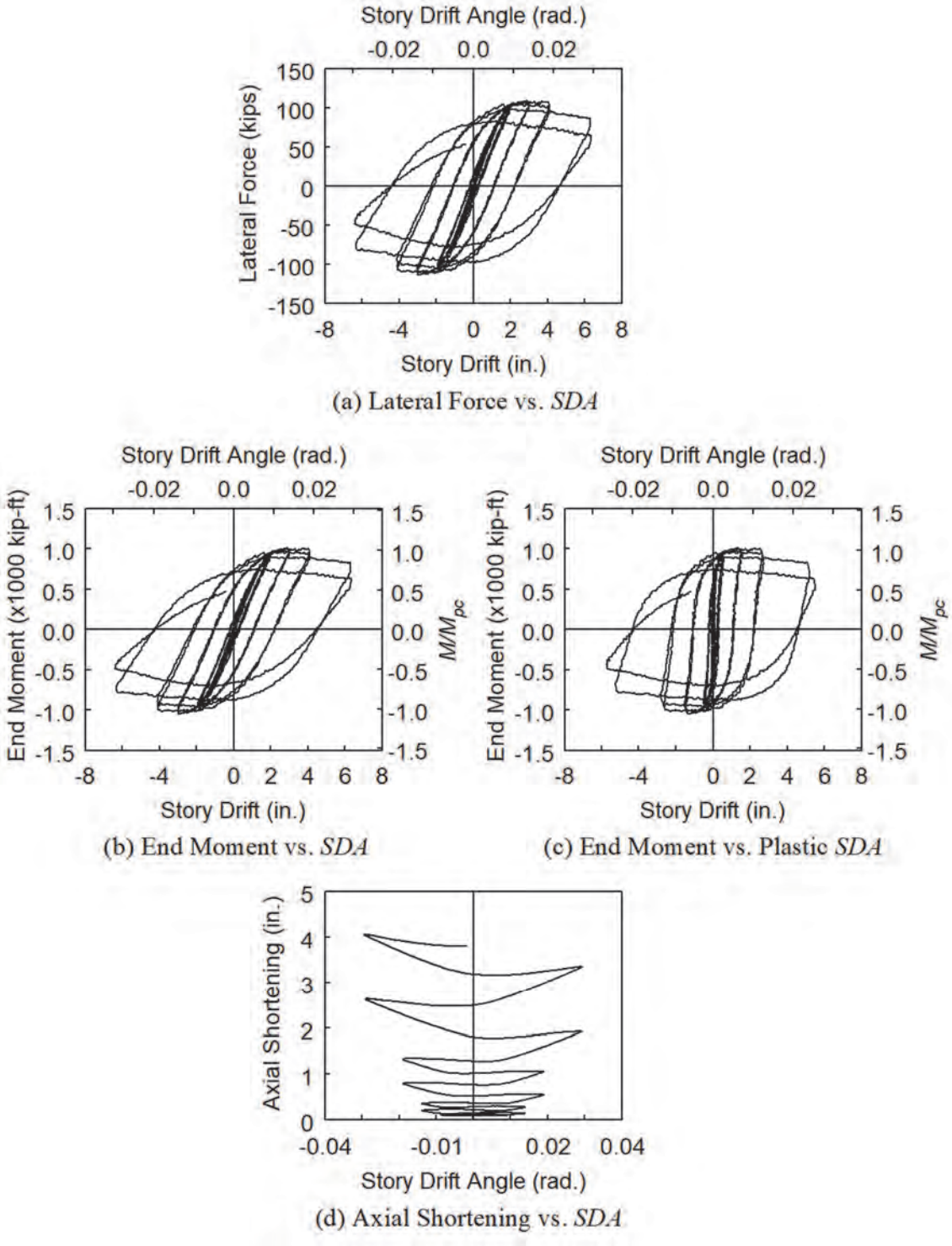

Figure 3.61 Specimen 4L: Global Responses

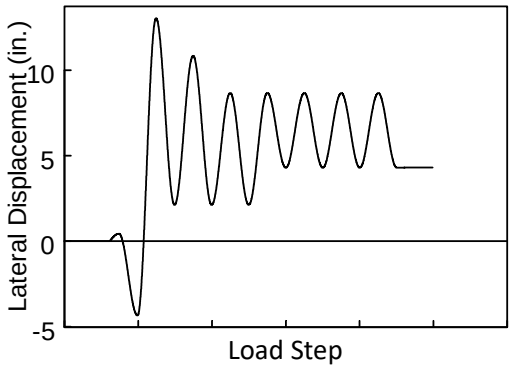

Figure 3.62 Specimen 4L: Dynamic, Near-Fault Lateral-Displacement History

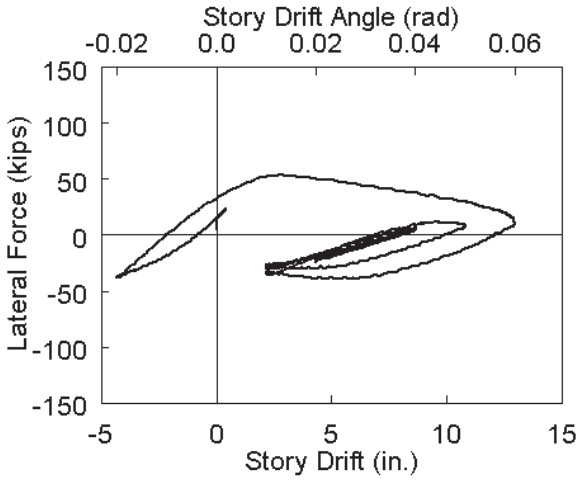

Figure 3.63 Specimen 4L: Dynamic Test Global Responses

3.5.3 Specimen 4M

The governing failure mode of Specimen 4M was CB; yielding and buckling progression is illustrated in Figure 3.64 to Figure 3.67. At 1 % drift, web and flange local buckles formed at both ends. Noticeable out-of-plane movements initiated at 1.5 % drift. As the specimen sustained the 2 % drift cycles, both local and global amplitudes increased; the double-curvature configuration was observed as shown in Figure 3.65(a). During the negative excursion of the second 2 % drift cycle, out-of-plane displacement grew drastically as shown in Figure 3.65(b); flexural strength also degraded drastically and almost vanished [see Figure 3.68(a)]. This prompted the termination of the test. Resulting from formation of local buckles at both column ends, flexural strength degradation and axial shortening were moderate during the 1 % drift cycles. They became more drastic during the 1.5 % and 2 % drift cycles due to the additional contribution from the out-of-plane buckling and displacements.

3.5.4 Concluding Remarks

Like Group 1 specimens, Group 4 specimens exhibited the CB failure mode. However, the instability sequence of the latter started with local buckling at the member ends and then followed by global out-of-plane buckling; the order was reversed for the former, i.e., LTB movements initiated first then induced flange local buckling at the member ends. The former, indeed, had a much more compact web, which could stabilize the flanges better and delay local buckling during the cyclic tests.

With similar web slenderness to that of Group 3 specimens, Group 4 specimens appeared to form local buckles at the same drift levels as those observed in Group 3 testing: at 2 % and 1 % drifts for Specimens 4L and 4M, respectively, and at 2 % and 0.75 % drifts for Specimens 3L and 3M, respectively. This signified that web slenderness seemed to be an important parameter influencing the column behavior.

The axial-load effect was the same as that observed in the prior groups, plastic rotation capacity of the columns decreased as the levels of axial load increased. Furthermore, like Group 1 specimens with the CB failure mode, Group 4 beam-columns tended to behave more column-like when they sustained higher axial loads. For instance, the final deformed configuration of Specimen 4M seemed to resemble the single-curvature configuration, which signified flexural buckling of a column.

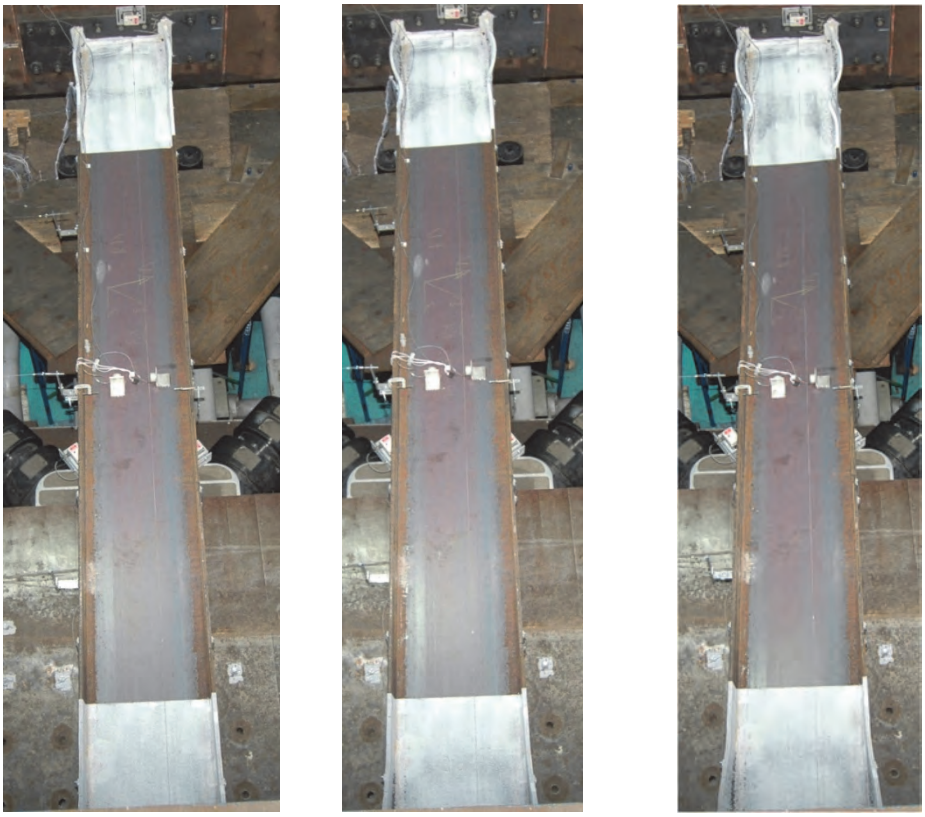

(a) *SDA* = 0.01 rad (b) *SDA* = 0.015 rad (c) *SDA* = 0.02 rad

Figure 3.64 Specimen 4M: Overall Yielding and Buckling Progression

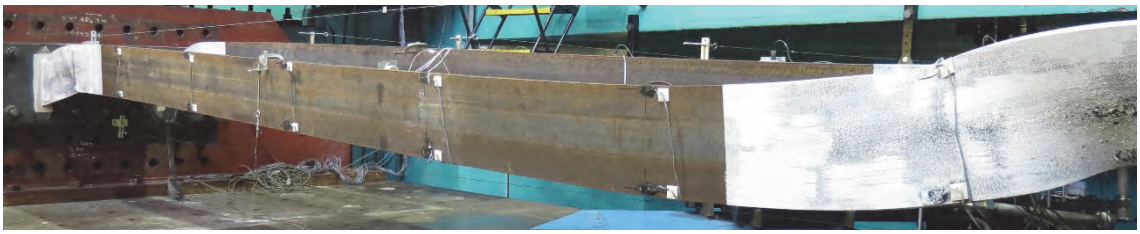

(a) SDA = +0.02 rad (2nd Cycle)

(b) SDA = -0.02 rad (2nd Cycle)

Figure 3.65 Specimen 4M: Overall Yielding and Buckling Progression (Side View)

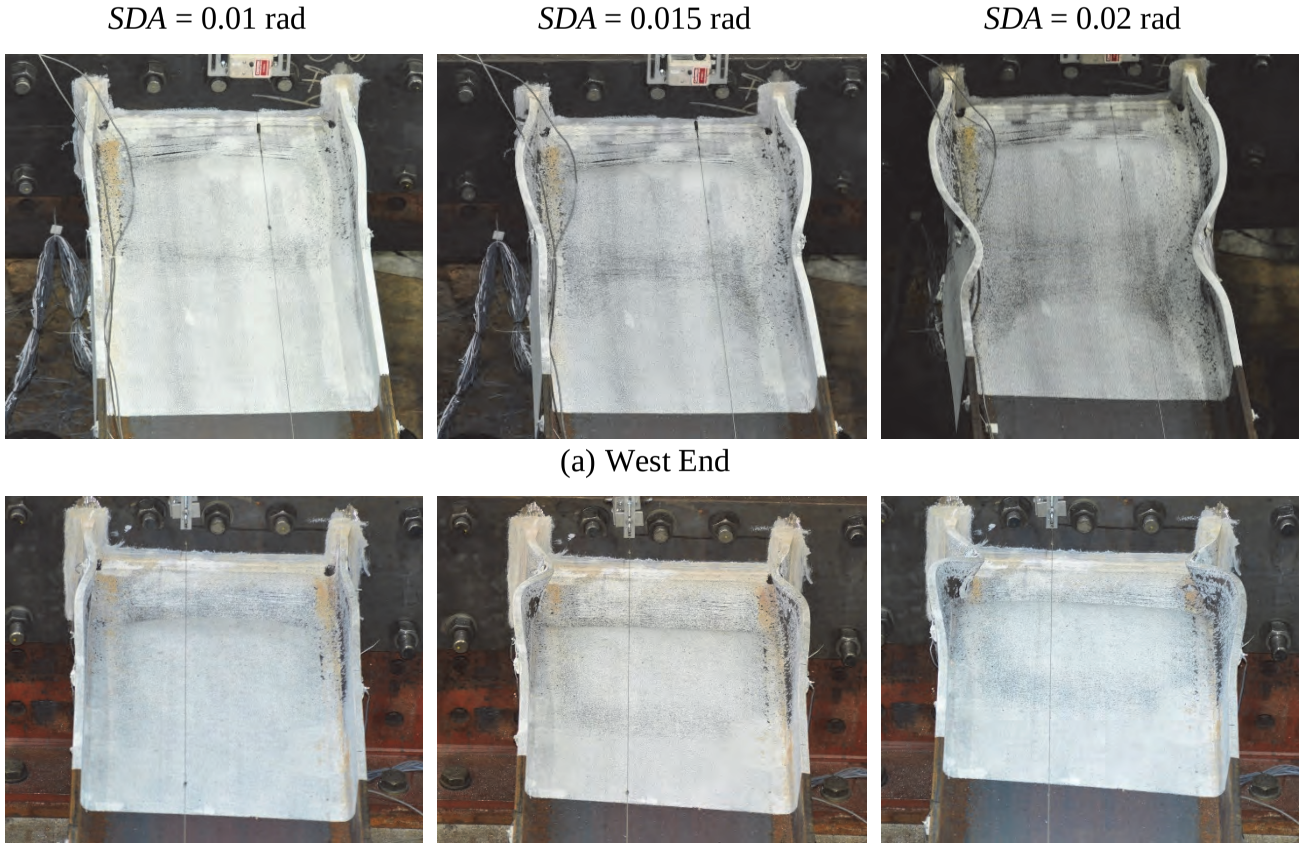

(a) West End

(b) East End

Figure 3.66 Specimen 4M: Yielding and Buckling Progression at Member Ends (Top View)

SDA = 0.01 rad | *SDA* = 0.015 rad | *SDA* = 0.02 rad

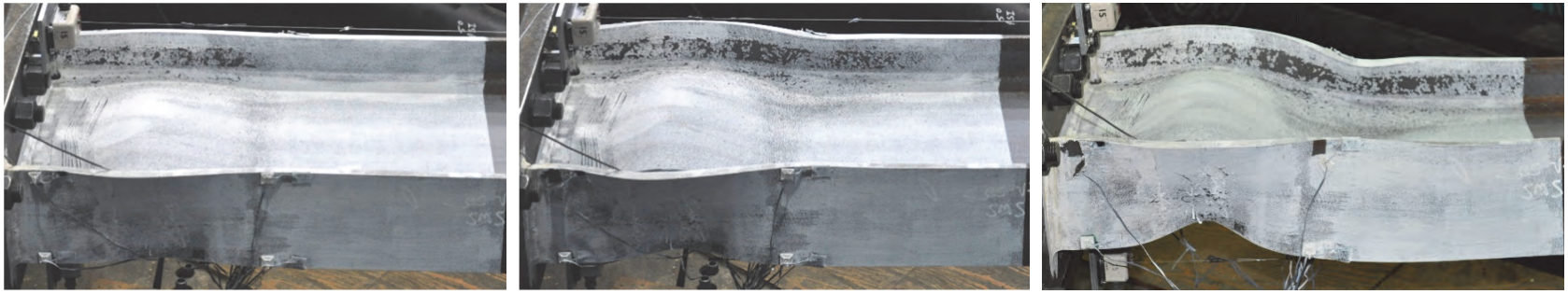

(a) West End

(b) East End

Figure 3.67 Specimen 4M: Yielding and Buckling Progression at Member Ends

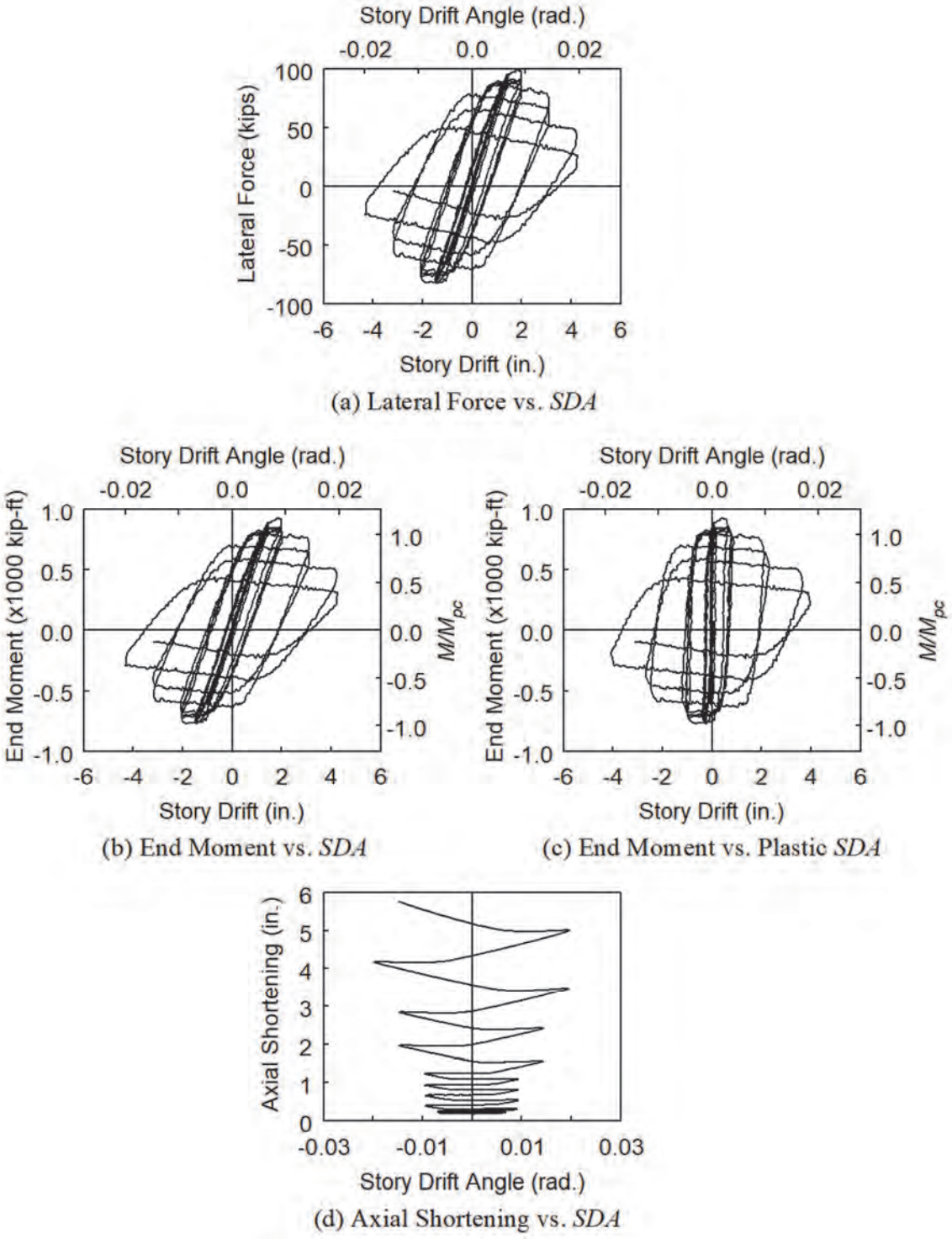

Figure 3.68 Specimen 4M: Global Responses

3.6 Group 5 Specimens: Section W24×55

3.6.1 General

Per AISC 341, Group 5 specimens had highly ductile flanges and a moderately ductile web when the axial load level was low (i.e., C_a = 0.2); the web would fail to meet the seismic compactness requirement for medium and high axial load levels. The specimens were also prone to out-of-plane global instability due to their high L/r_y ratio (=161.2). Indeed, they experienced LTB early on during the AISC loading before they could undergo significant plastic deformation: strain gauge data confirmed that limited portions at the column ends yielded before the LTB events. Originally, the low, medium, and high levels of axial load, i.e., C_a = 0.2, 0.4, and 0.6, were planned for testing each specimen in this group, respectively. However, test results of Specimen 5M had shown a premature elastic global buckling; consequently, an inelastic cyclic response was not obtained to fulfill the research objectives. Therefore, the last specimen was not subjected to the high axial load level as originally planned; instead, it was subjected to an average low-medium level of axial compression, i.e., C_a = 0.3, and was named Specimen 5LM.

3.6.2 Specimen 5L

Figure 3.69 to Figure 3.71 show the yielding and buckling progression. At 0.75 % drift, limited yielding was observed at both column ends. LTB global instability was triggered at 1 % drift; it exacerbated at 1.5 % and 2 % drifts during which significant twisting was observed in the entire column. The resulting out-of-plane curvatures induced flange local buckles at both column ends. As shown in Figure 3.72, flexural strength began to degrade drastically at 1.5 % drift when LTB movements became significant; it almost vanished after the 2 % drift cycles were completed. At this point, the test was terminated; the column shortened by 2.7 in. mainly due to the out-of-plane amplitudes.

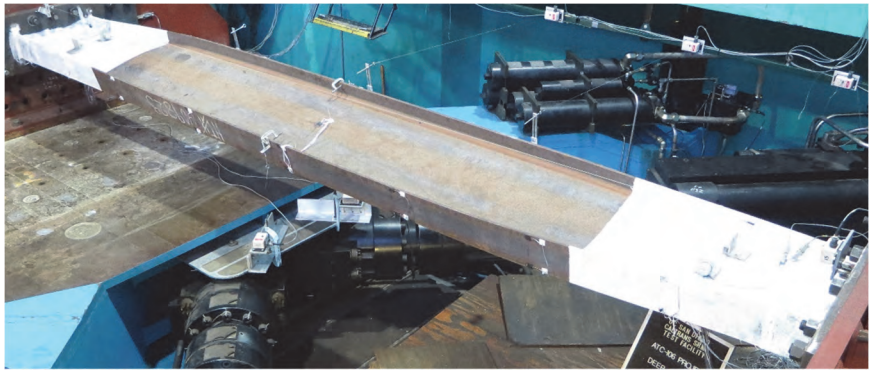

(a) *SDA* = +0.015 rad

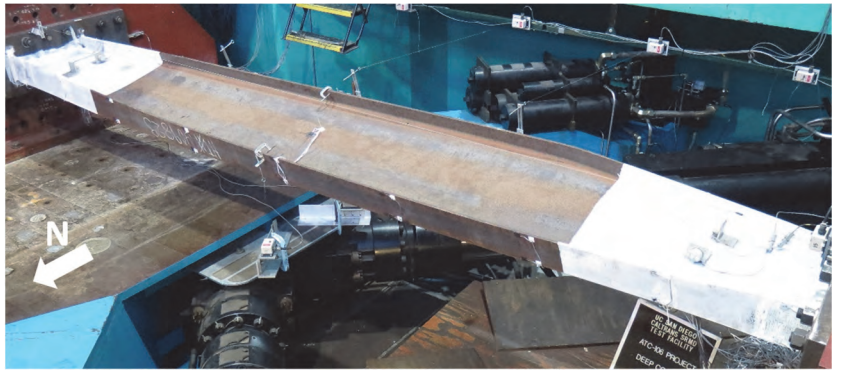

(b) *SDA* = -0.015 rad

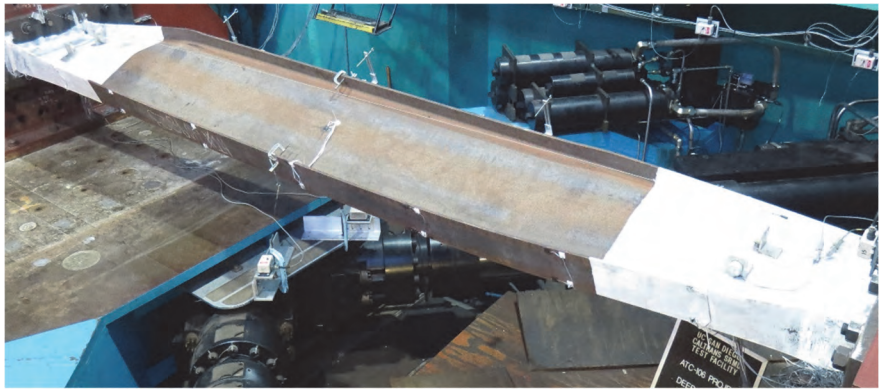

(c) *SDA* = +0.02 rad

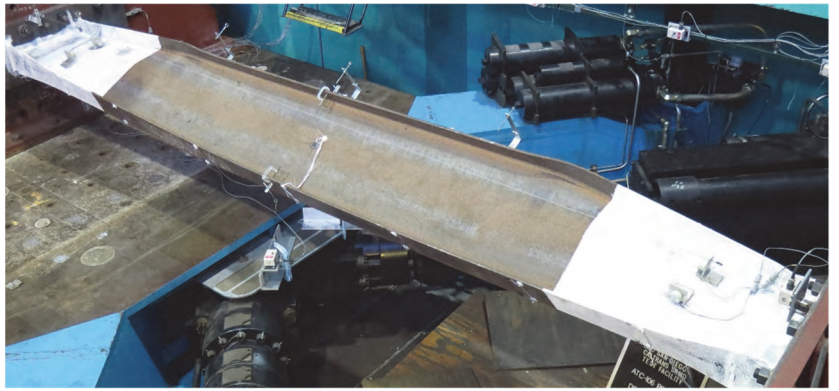

(d) *SDA* = -0.02 rad

Figure 3.69 Specimen 5L: Overall Yielding and Buckling Progression

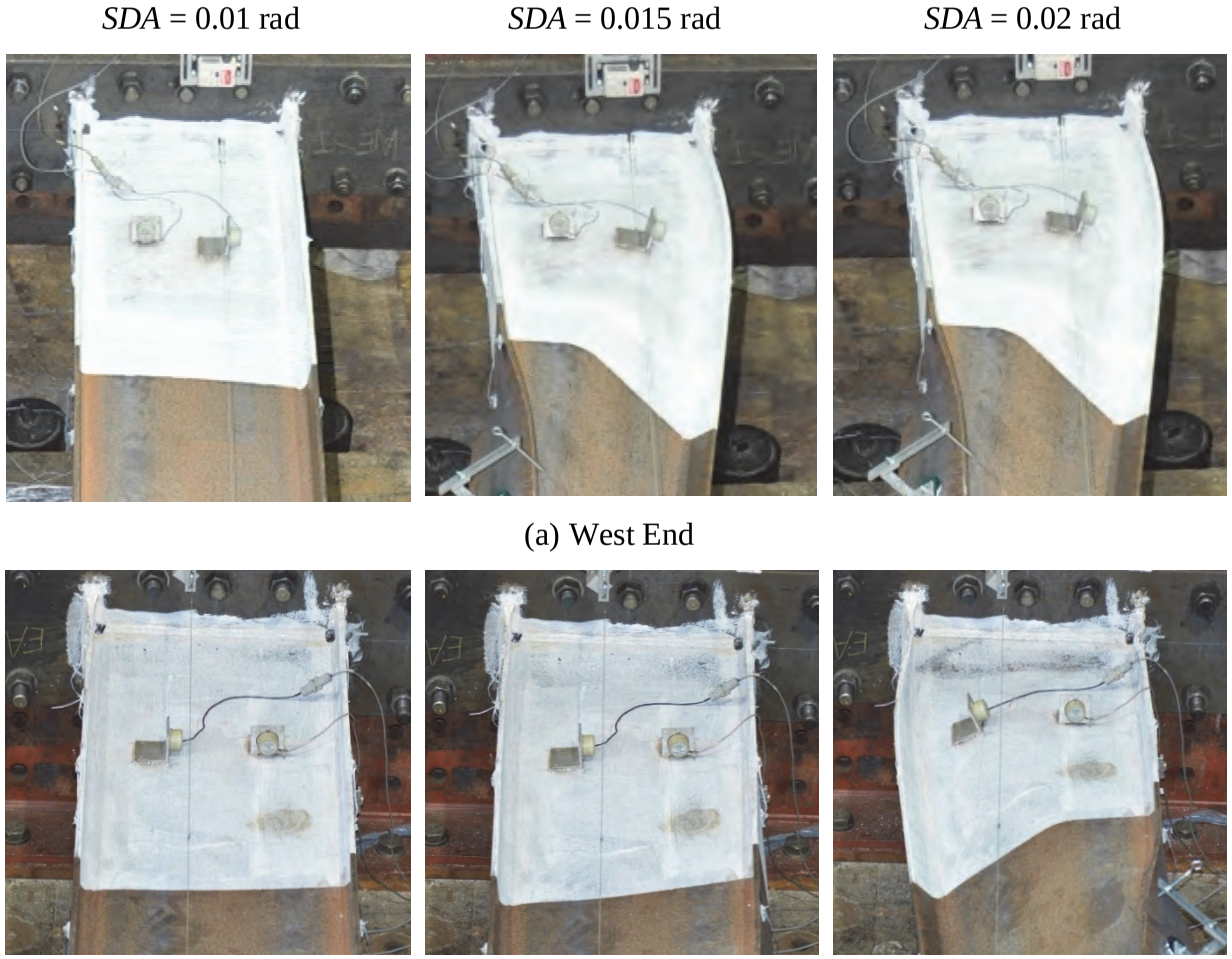

(a) West End

(b) East End

Figure 3.70 Specimen 5L: Yielding and Buckling Progression at Member Ends (Top View)

SDA = 0.01 rad | *SDA* = 0.015 rad | *SDA* = 0.02 rad

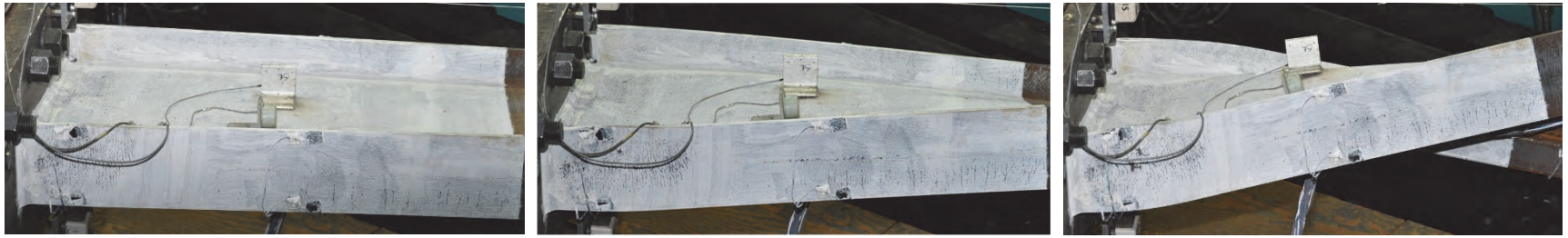

(a) West End

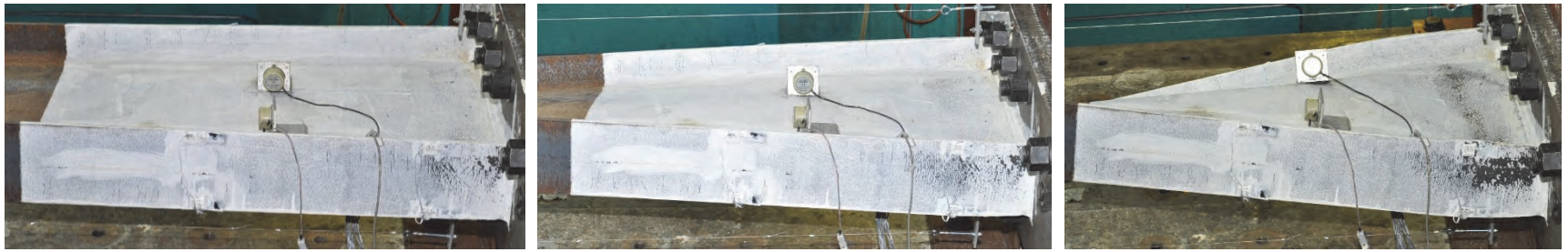

(b) East End

Figure 3.71 Specimen 5L: Yielding and Buckling Progression at Member Ends

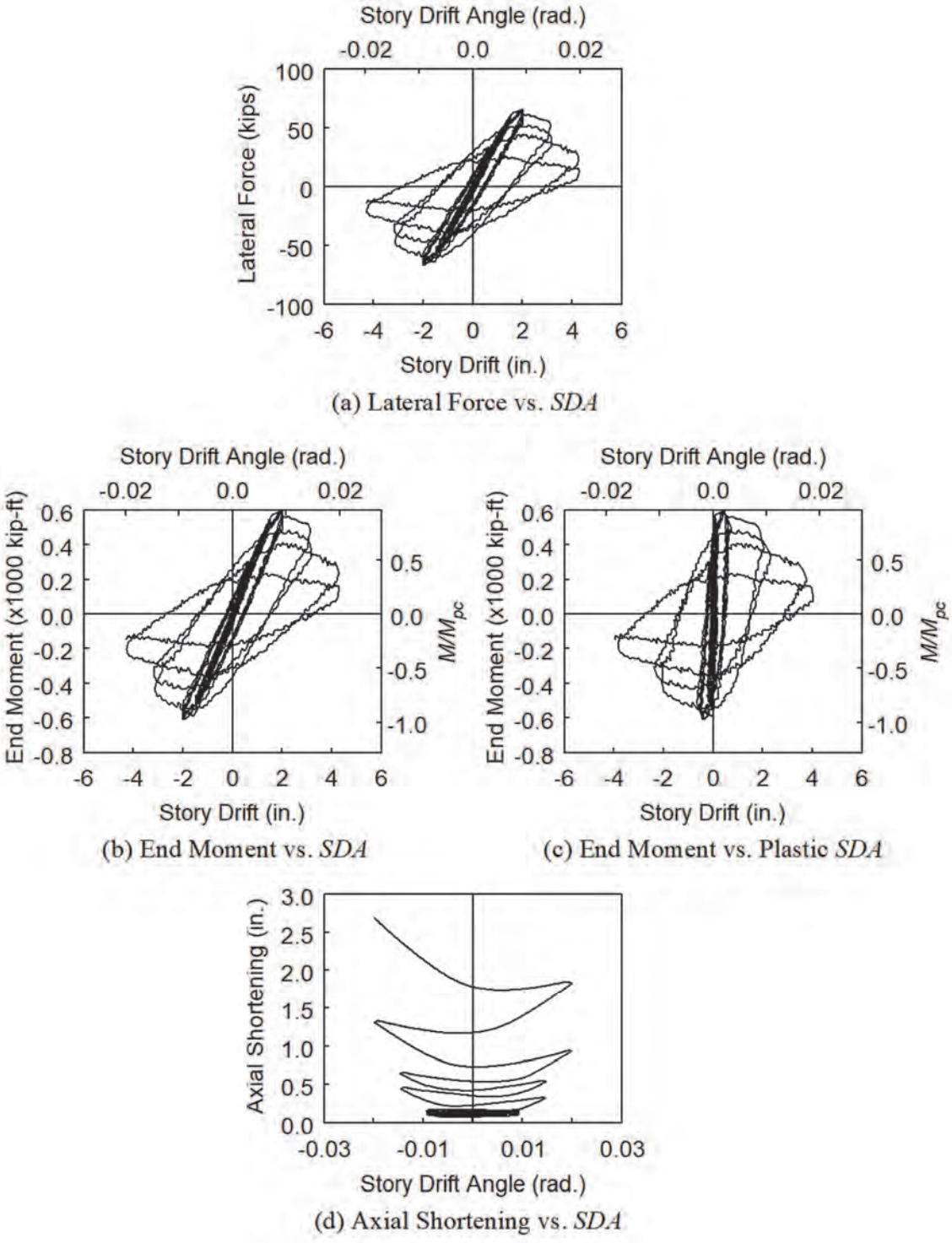

Figure 3.72 Specimen 5L: Global Responses

3.6.3 Specimen 5LM

With C_a = 0.3, the web slenderness (=54.6) just exceeded the limiting value (=53.9) for a moderately ductile section. Yielding and buckling progression is illustrated in Figure 3.73 to Figure 3.75. At 0.75 % drift, the specimen experienced minor elastic LTB. The LTB movements became more apparent at 1 % drift, resulting in significant flexural strength degradation as shown in Figure 3.76. The test was terminated during the negative excursion of the third 1 % drift cycle as the specimen exhibited weak-axis flexural buckling behavior; its moment capacity almost vanished at this point. Minor web and flange local buckles were observed at the east end.

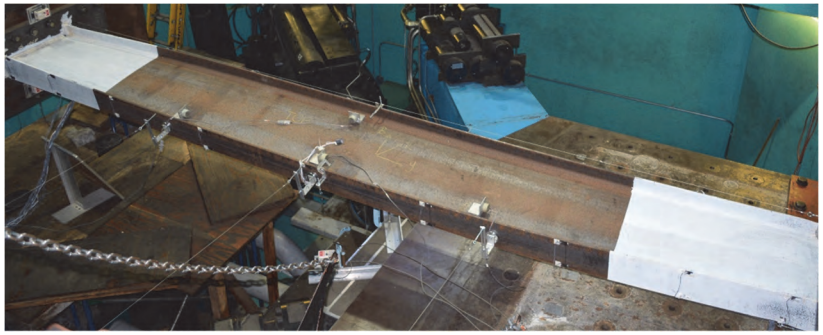

(a) *SDA* = +0.01 rad (2nd Cycle)

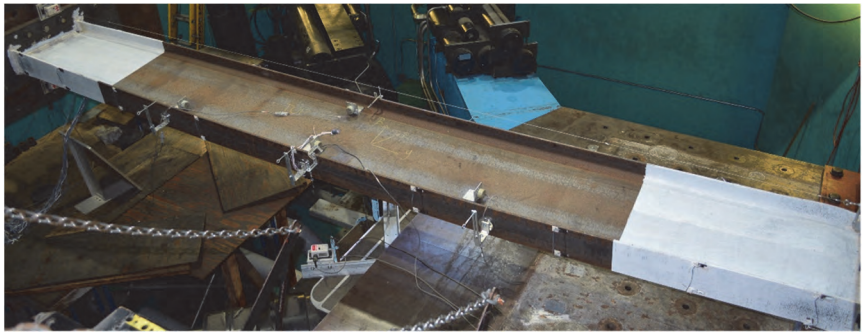

(b) *SDA* = -0.01 rad (2nd Cycle)

(c) *SDA* = +0.01 rad (3rd Cycle)

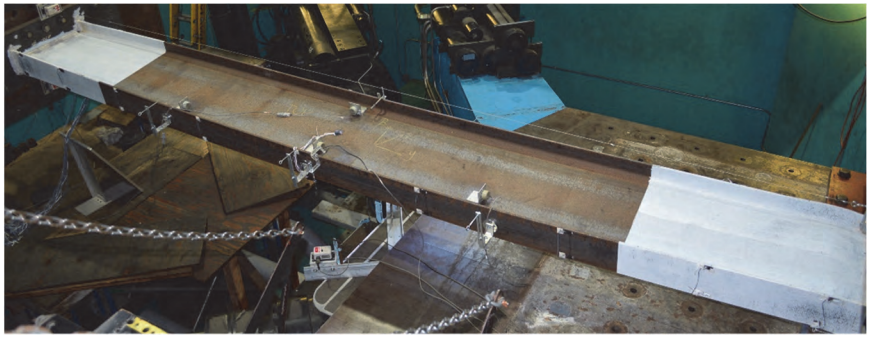

(d) *SDA* = -0.01 rad (3rd Cycle)

Figure 3.73 Specimen 5LM: Overall Yielding and Buckling Progression

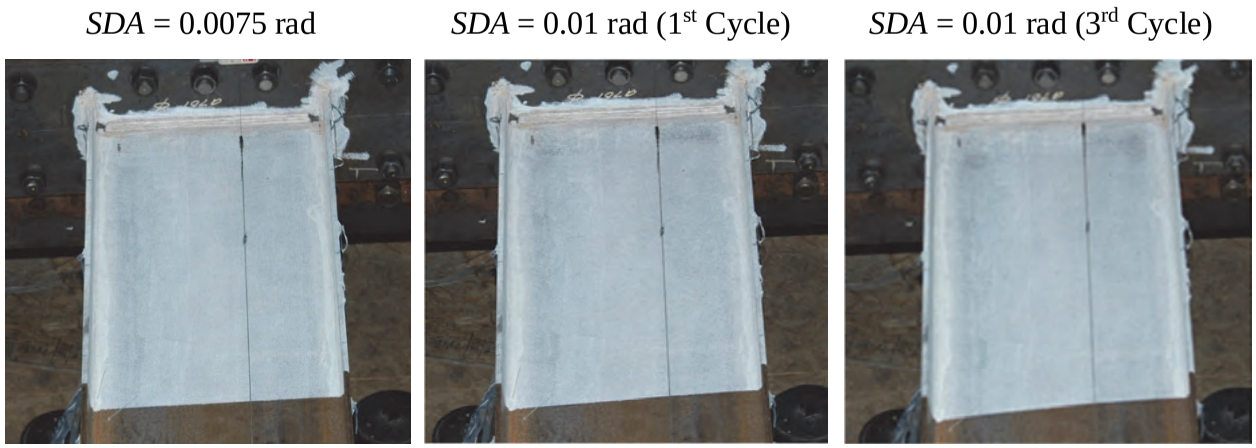

(a) West End

(b) East End

Figure 3.74 Specimen 5LM: Yielding and Buckling Progression at Member Ends (Top View)

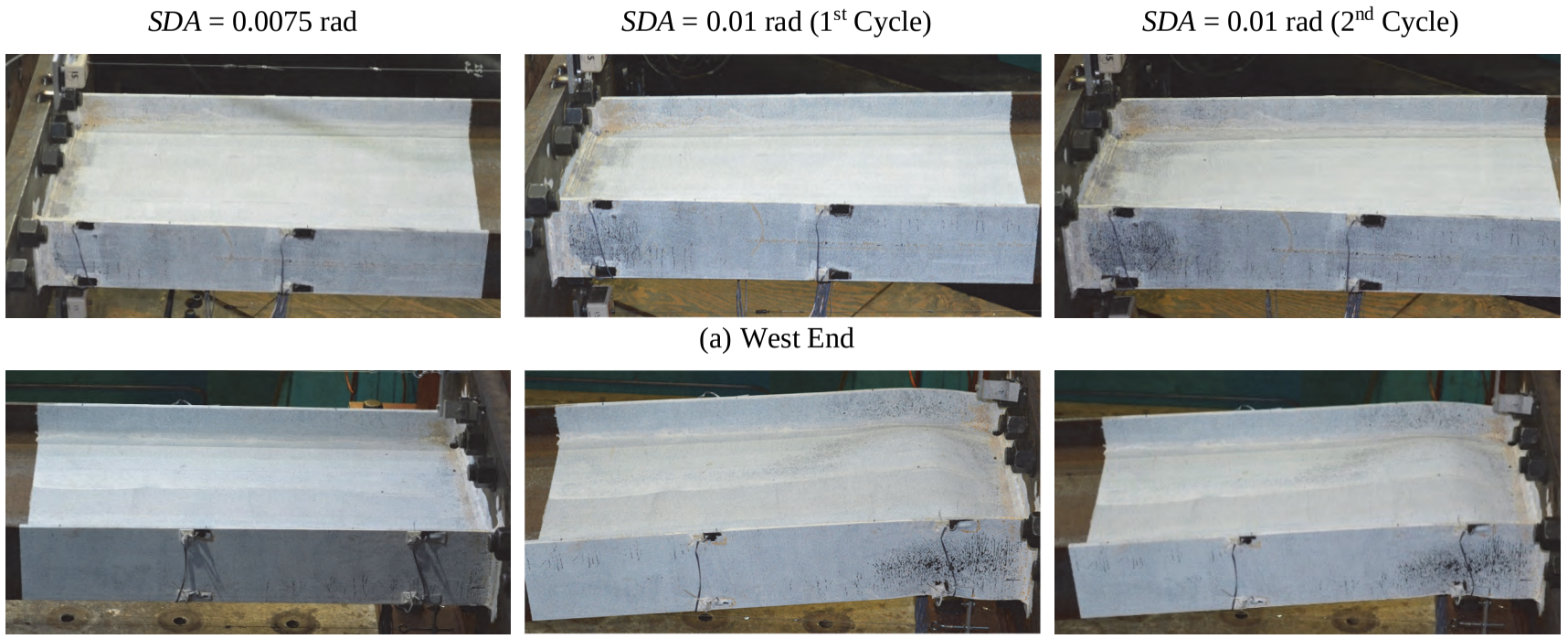

(a) West End

(b) East End

Figure 3.75 Specimen 5LM: Yielding and Buckling Progression at Member Ends

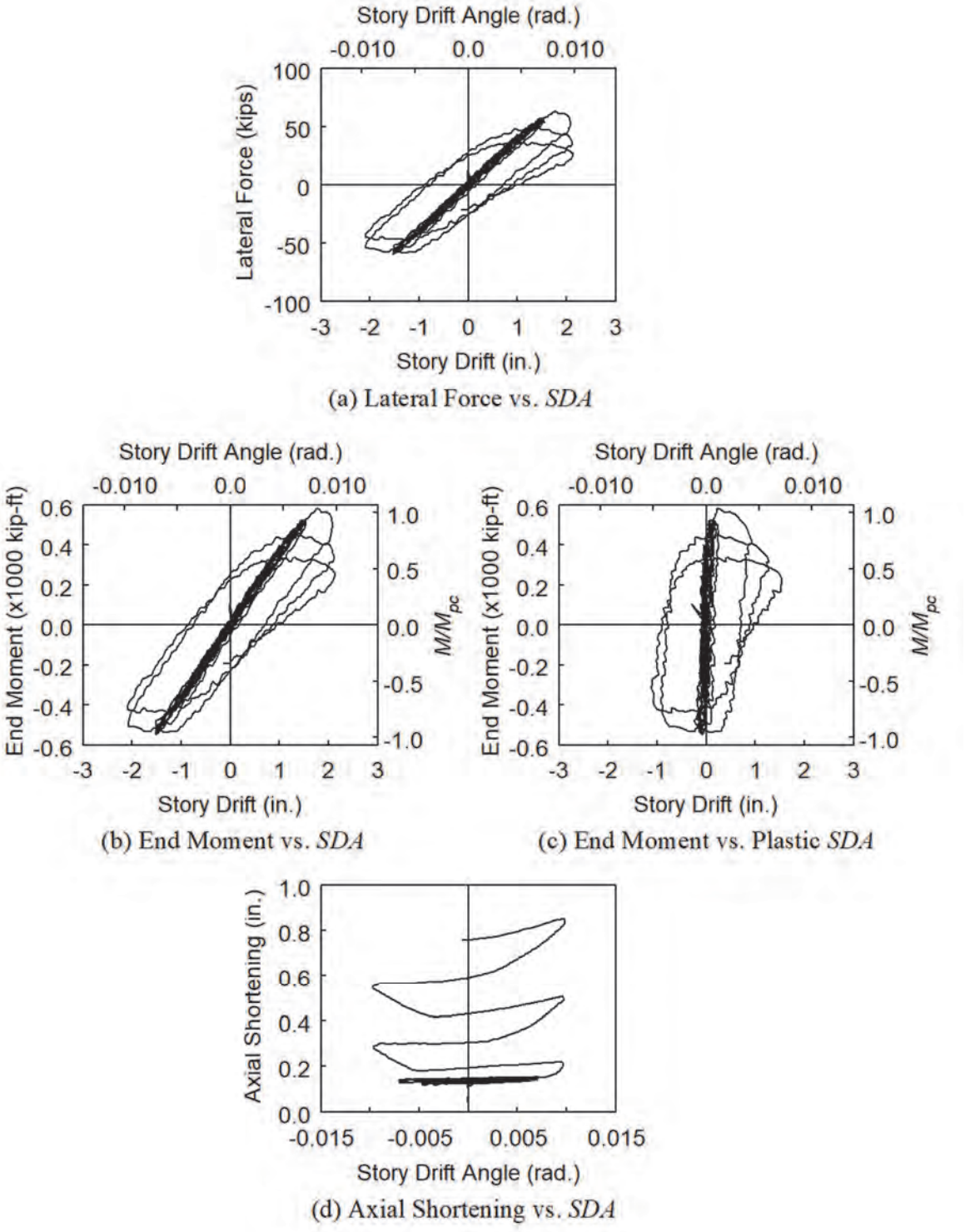

Figure 3.76 Specimen 5LM: Global Responses

3.6.4 Specimen 5M

The web slenderness (= 54.6) exceeded the limiting value (= 50.9) for a moderately ductile section. Since this specimen would be subjected to the highest axial compression among all Group 5 specimens, it was expected to experience global instability at an even lower drift level than that observed previously (i.e., at 1 % and 0.75 % drifts for Specimens 5L and 5LM, respectively). Since applying small-amplitude drift cycles would fail the specimen prematurely and produce a hysteresis unusable in this study, the AISC loading protocol was modified for this specimen: the 0.325 % and 0.5 % drift cycles were skipped, and the loading would begin with the 0.75 % drift cycles.

Yielding and buckling progression is illustrated in Figure 3.77 and Figure 3.78. During the first and second cycles at 0.75 % drift, minor LTB movements were observed. They exacerbated during the following cycles, resulting in significant flexural strength degradation as shown in Figure 3.79. During the negative excursion of the fourth 0.75 % drift cycle, the specimen exhibited weak-axis flexural buckling; this behavior was also observed in Specimen 5LM. At this instant, the member moment capacity almost vanished, prompting the end of the test. The significant out-of-plane amplitude also aggravated web and flange local buckles at the east end.

3.6.5 Concluding Remarks

Group 5 specimens experienced LTB early on during the AISC loading before they could undergo significant plastic deformation (e.g., in-plane plastic hinging at column ends). As a result, they exhibited very nonductile behavior. Out-of-plane global buckling was observed in Group 1 and Group 4 testing as well; however, significant plastic deformation had already developed in those specimens prior to the initiation of the out-of-plane movements. Thus, their hystereses were more ductile. Specimens 5LM and 5M sustained considerable axial loads. As a result, the column-type (as opposed to the beam-type) behavior dominated their failure configurations, i.e., weak-axis flexural buckling was their final deformed configurations, which was accompanied by a rapid loss in their flexural strengths.

(a) *SDA* = -0.0075 rad (3rd Cycle)

(b) *SDA* = +0.0075 rad (4th Cycle)

(c) *SDA* = -0.0075 rad (4th Cycle)

Figure 3.77 Specimen 5M: Overall Yielding and Buckling Progression

SDA = +0.0075 rad (3rd Cycle)

SDA = -0.0075 rad (4th Cycle)

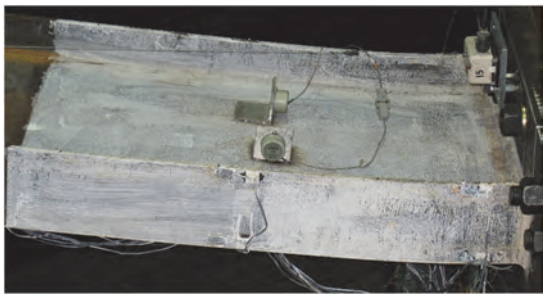

(a) West End

(b) East End

Figure 3.78 Specimen 5M: Yielding and Buckling Progression at Member Ends

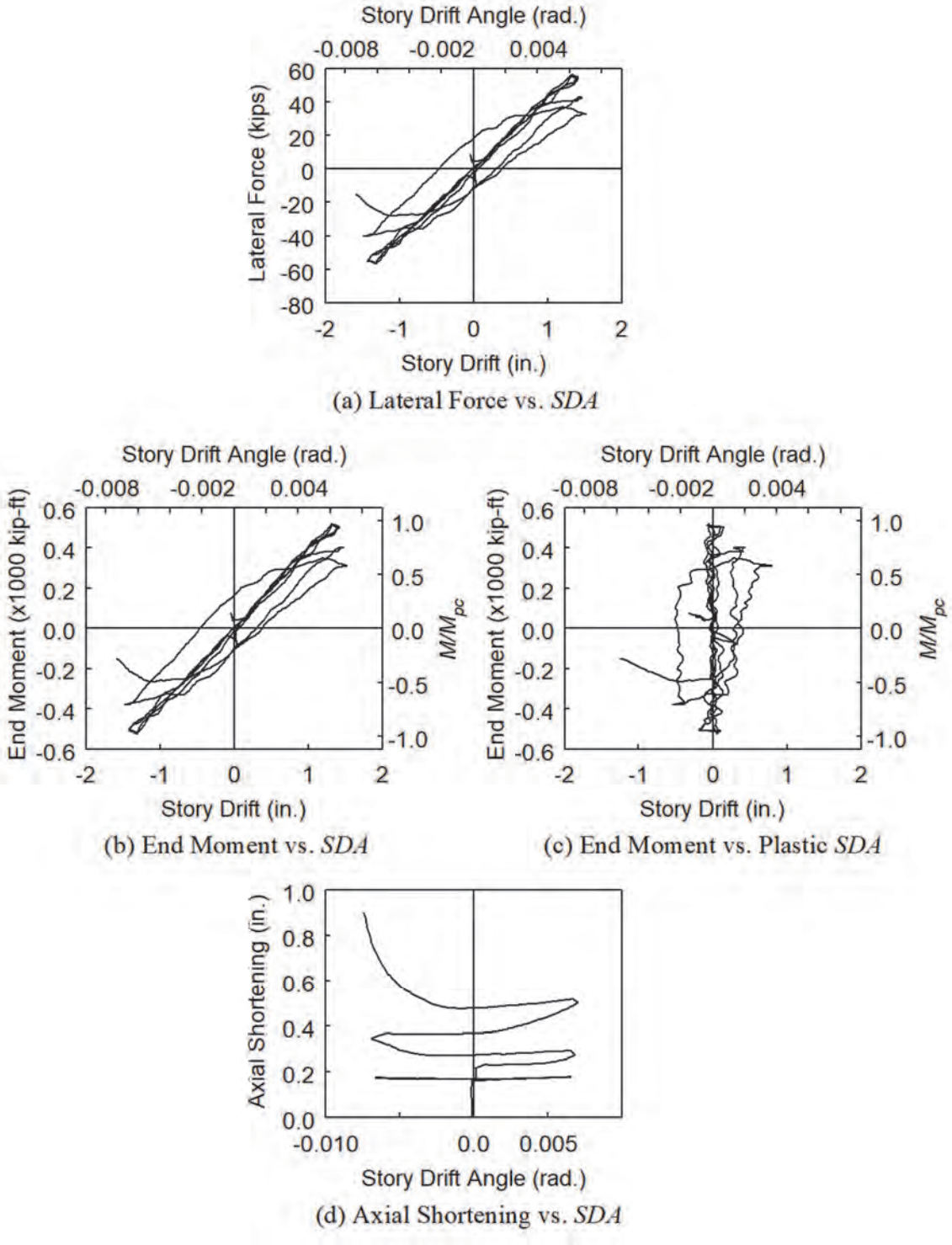

Figure 3.79 Specimen 5M: Global Responses

3.7 Group 6 Specimens: Section W24×131 with Weak-Axis Bending

3.7.1 General

Groups 2 and 6 had the same W24×131 section; they were subjected to strong- and weak-axis bending, respectively, to investigate the effect of bending directions on column behavior. Originally, the low, medium, and high levels of axial load, i.e., C_a = 0.2, 0.4, and 0.6, were proposed for testing each specimen in this group, respectively. Testing of Specimen 6L had demonstrated a very ductile response, showing no sign of local buckling even at 7 % drift. Specimen 6H was tested next, and it showed the similar behavior: limited local buckling relative to that observed in its counterpart specimen bended in the strong-axis direction (i.e., Specimen 2H). Accordingly, it was determined that testing the last specimen with the medium axial load level would add no significance to the finding already discovered from the previous two tests. It was of interest to investigate the lateral-drift loading sequence effect associated with the weak-axis bending. Therefore, the last specimen, Specimen 6L-P, was tested with the pushover loading protocol (discussed in Section 2.5).

3.7.2 Specimen 6L

Yielding progression is illustrated in Figure 3.80 and Figure 3.81; no local buckling developed even at 7 % drift. Consequently, flexural strength degradation and significant axial shortening were not observed in the global responses as shown in Figure 3.82. Note that the axial shortening response shows the initial shortening part due to the applied constant axial compression; this initial portion stayed constant as the baseline. Corresponding to the AISC loading, the remaining history oscillated about this baseline with a minor growth mainly due to curvature shortening as opposed to local buckling; the latter would produce more significant axial shortening. This oscillating axial shortening was the result of the reduction in longitudinal distance between the two column ends, which resulted from the bended specimen maintaining its arclength as it underwent the AISC lateral-drift cycles; therefore, the oscillating magnitudes grew proportionally to the applied drift levels.

The AISC loading was ended after one cycle at 7 % drift was completed. Then, a pure compression test was conducted to evaluate the gravity load-carrying capacity of the

yielded specimen. The pure compression test was ended when the specimen exhibited weak-axis flexural buckling, which was also accompanied by web and flange local buckles at the bent, as shown in Figure 3.83; the maximum compressive strength was 1,627 kips.

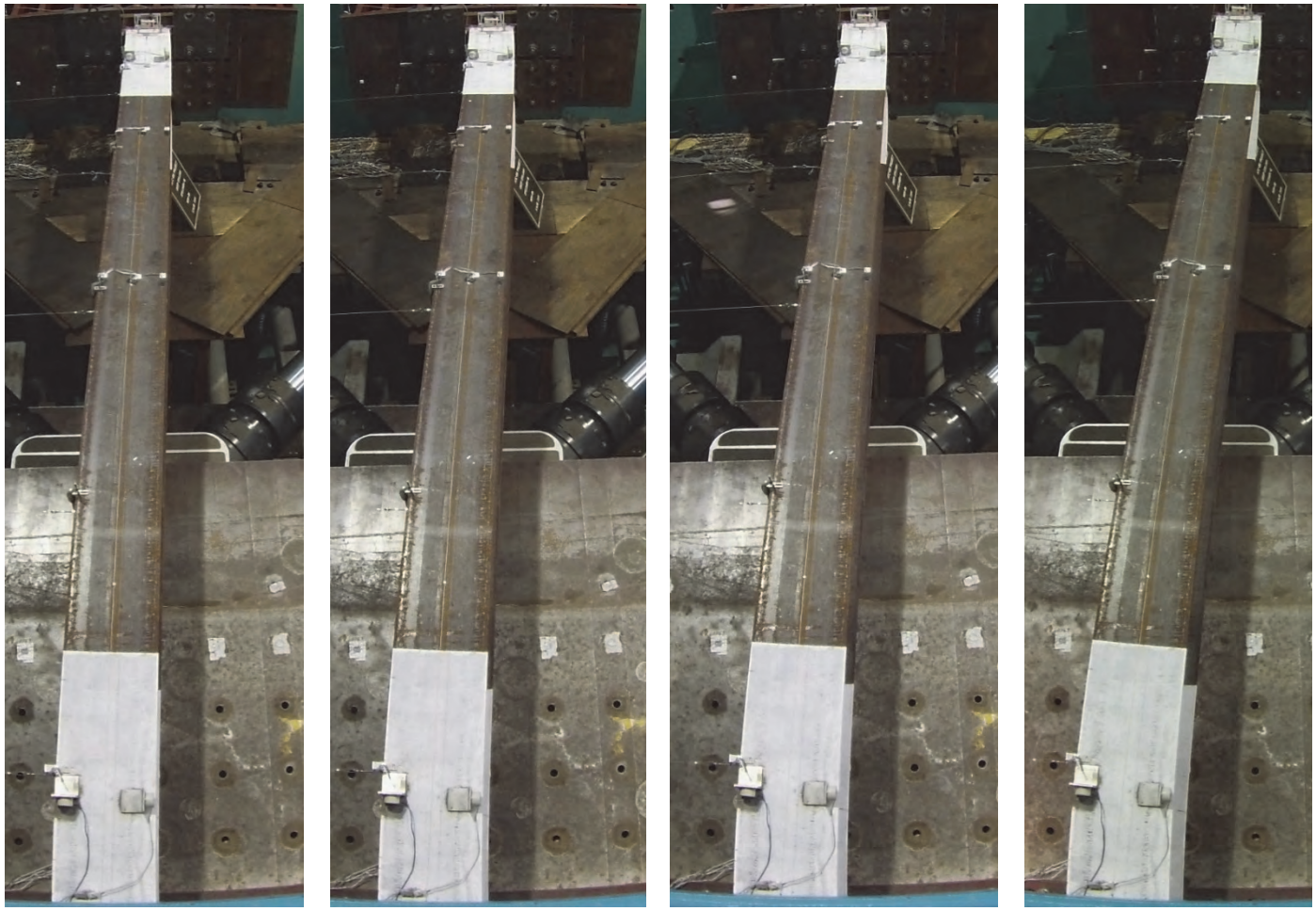

(a) *SDA* = 0.04 rad (b) *SDA* = 0.05 rad (c) *SDA* = 0.06 rad (d) *SDA* = 0.07 rad

Figure 3.80 Specimen 6L: Overall Yielding and Buckling Progression

SDA = 0.04 rad | *SDA* = 0.05 rad | *SDA* = 0.06 rad | *SDA* = 0.07 rad

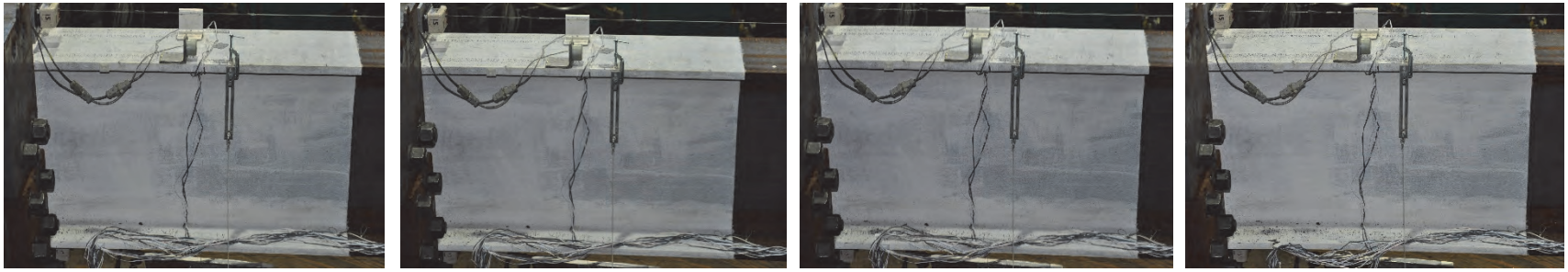

(a) West End

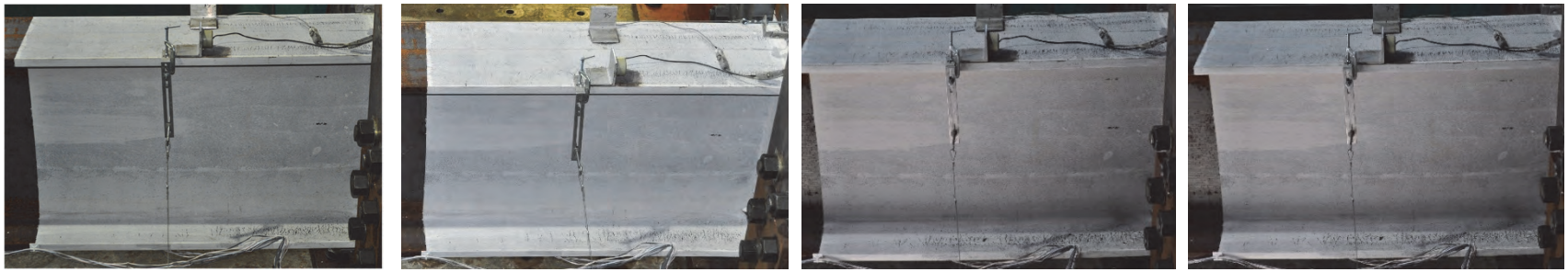

(b) East End

Figure 3.81 Specimen 6L: Yielding Progression at Member Ends

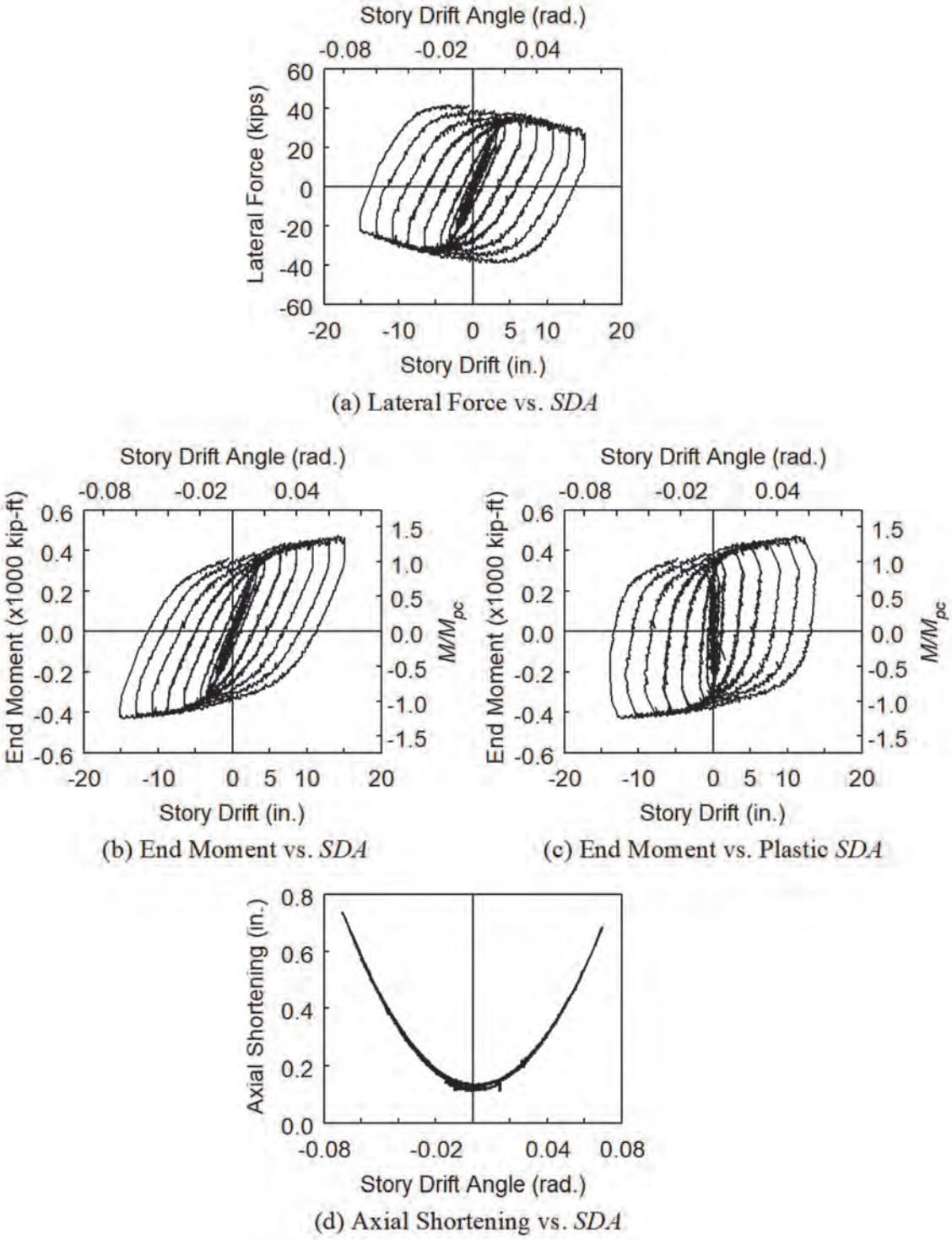

Figure 3.82 Specimen 6L: Global Responses

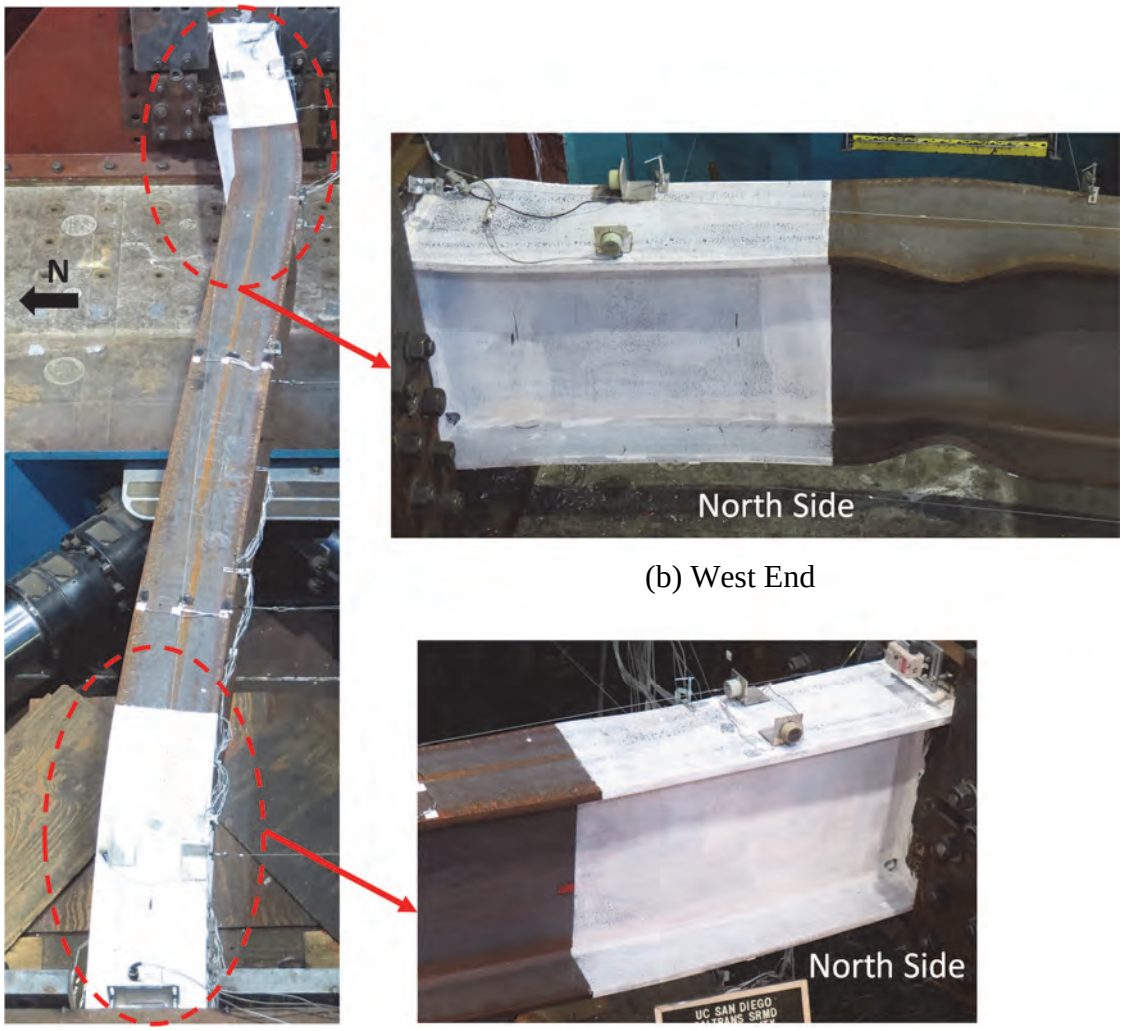

(b) West End

(a) Top View

(c) East End

Figure 3.83 Specimen 6L: Deformed Configuration after Pure Compression Test

3.7.3 Specimen 6L-P

Specimen 6L-P was monotonically pushed to 7 % drift in the positive direction followed by the reversed AISC loading protocol (see Section 2.5). Like Specimen 6L, it exhibited very ductile behavior; local buckling did not occur, and only yielding was observed at the member ends as shown in Figure 3.84 to Figure 3.85. Since it showed insignificant damage and no strength degradation after the reversed AISC drift cycles were completed, the test was continued with an additional drift cycle at 0.10 rad *SDA* to evaluate the ductility limit of the specimen. Still, even at this extreme lateral-drift level, the specimen remained very ductile and did not develop local buckling as shown in Figure 3.86.

Figure 3.87 shows the global responses; the blue, black, and red colors indicate the monotonic, reversed AISC cyclic, and 10 % drift responses, respectively. Flexural strength degradation was not observed [see Figure 3.87(b)]. Negative stiffness in the global response plot of Figure 3.87(a) reflects the significant P-Δ effect because the specimen was subjected to weak-axis bending. In addition, the axial shortening response shows the same oscillating behavior as that observed in Specimen 6L; permanent axial shortening was not significant.

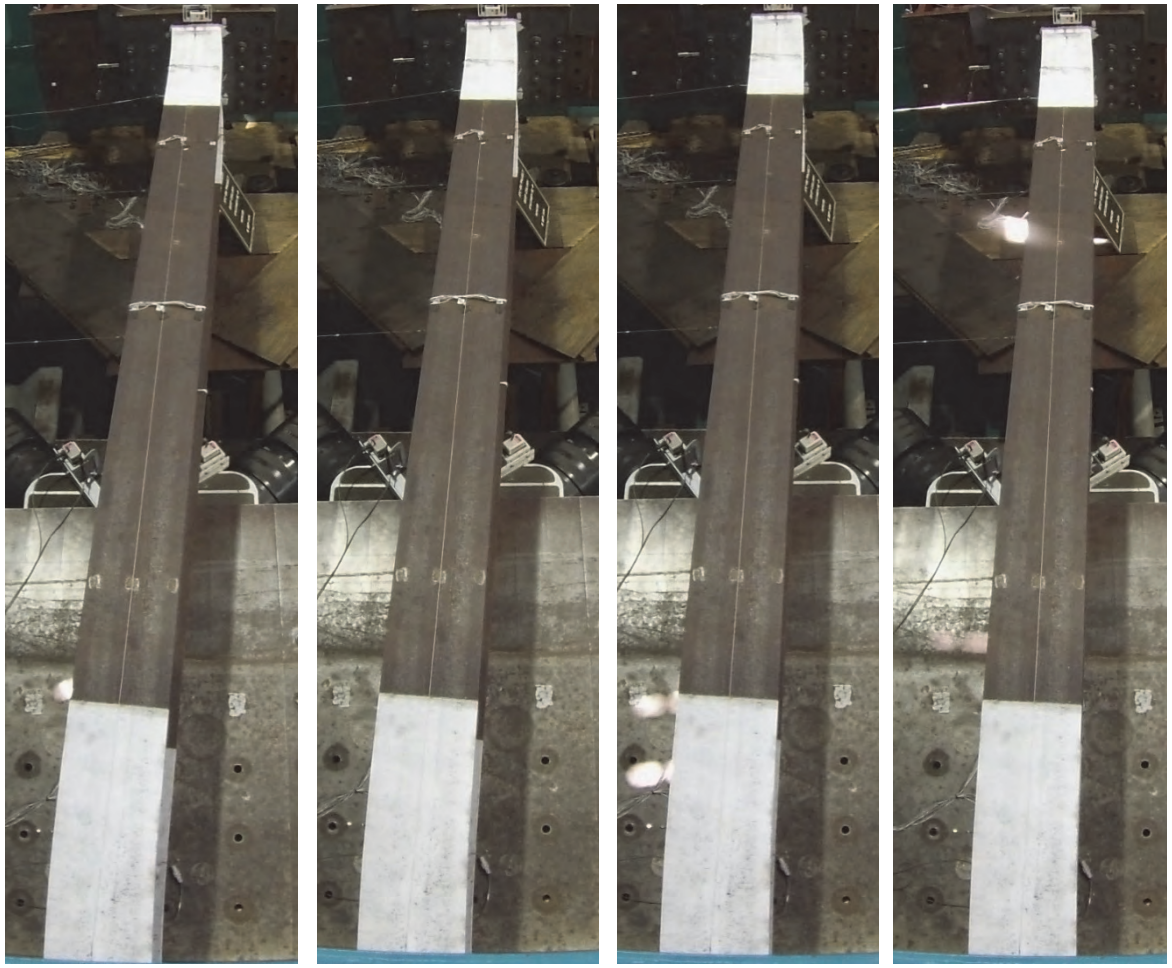

(a) *SDA* = 0.07 rad (b) *SDA* = 0.06 rad (c) *SDA* = 0.05 rad (d) *SDA* = 0.04 rad

Figure 3.84 Specimen 6L-P: Overall Yielding and Buckling Progression

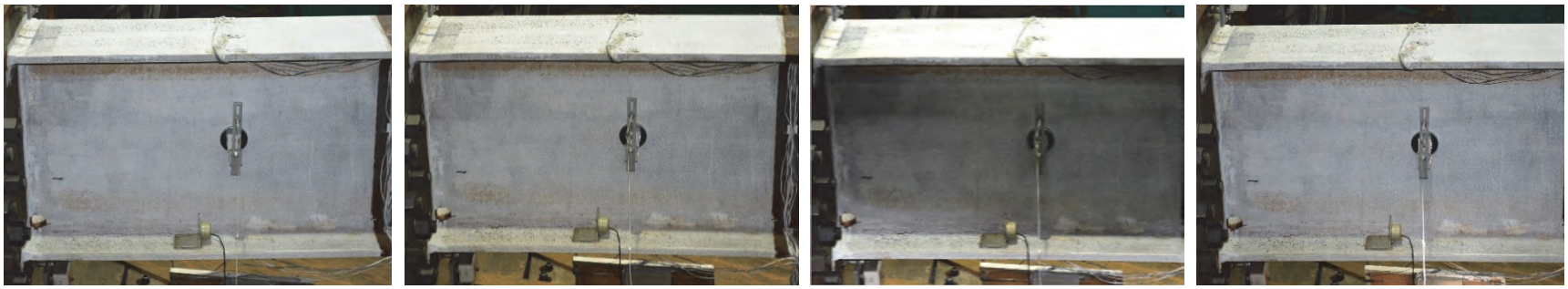

(a) West End

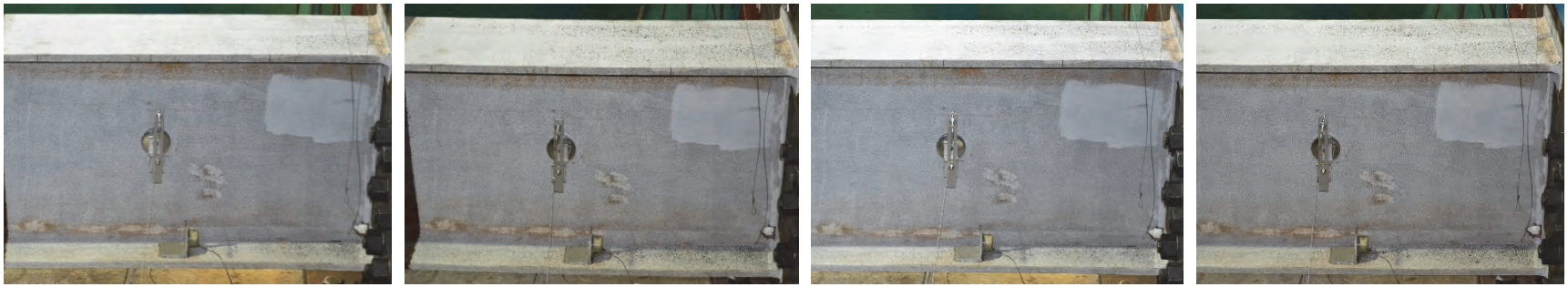

(b) East End

Figure 3.85 Specimen 6L-P: Yielding and Buckling Progression at Member Ends

(a) Top View

(b) West End

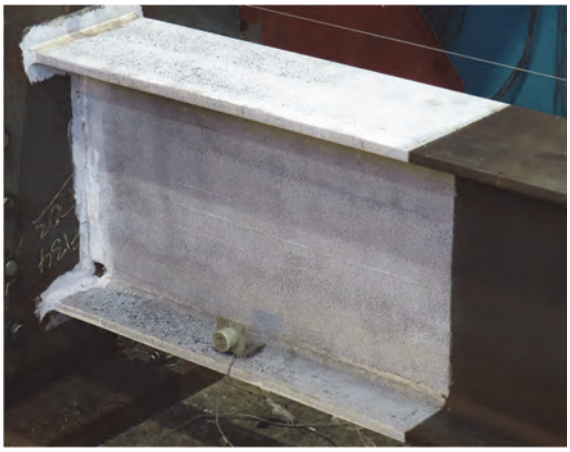

(c) East End

Figure 3.86 Specimen 6L-P: Deformed Configuration at 10 % drift

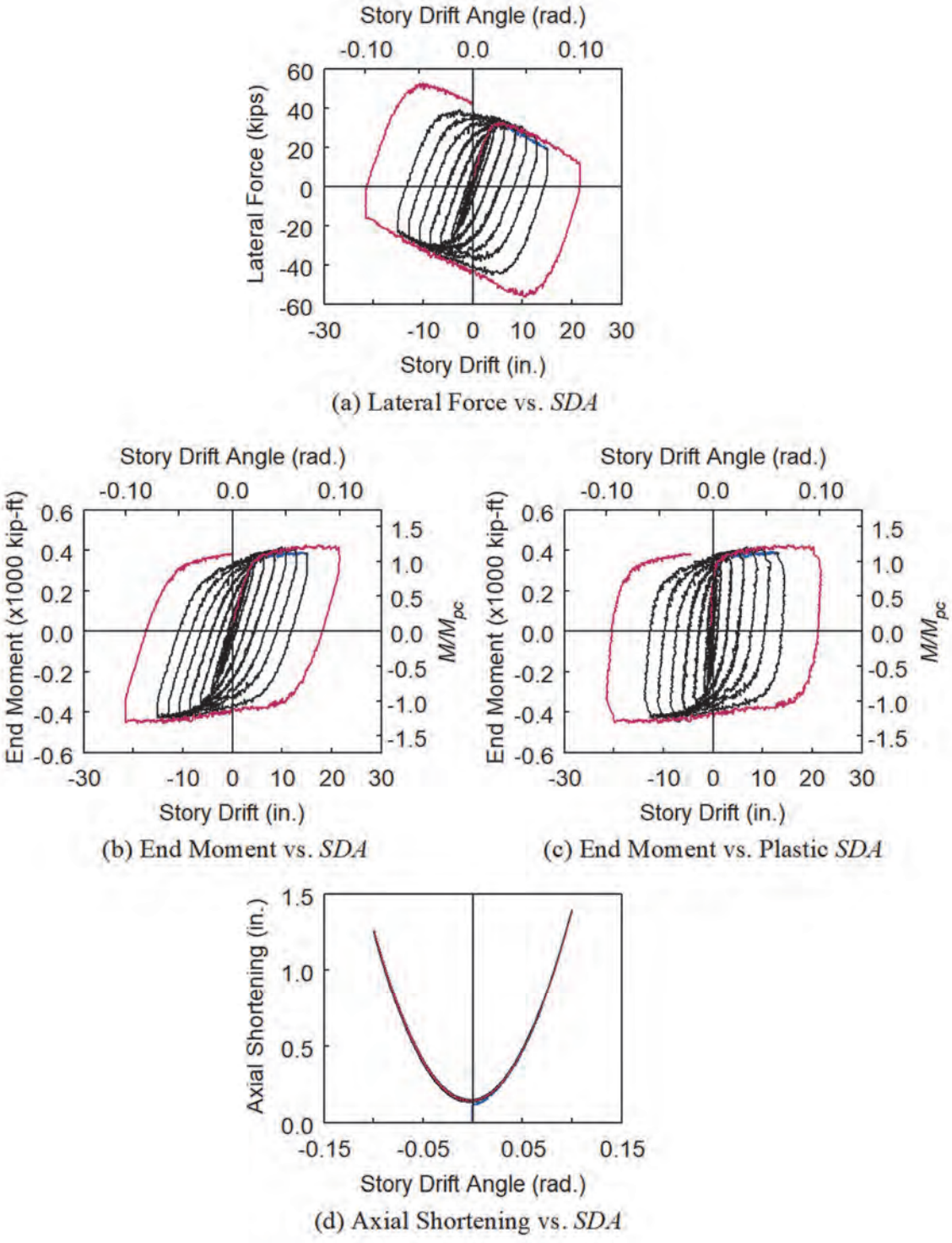

Figure 3.87 Specimen 6L-P: Global Responses

3.7.4 Specimen 6H

Yielding and buckling progression is illustrated in Figure 3.88 and Figure 3.89. Since this specimen sustained the highest axial load among all Group 6 specimens, it experienced web and flange local buckling to some degree. Such buckling initiated at 3 % drift and became more apparent at 4 % drift.

Global responses are shown in Figure 3.90. The global response plot in Figure 3.90(a) shows a very significant degrading trend as a result of the P-Δ effect. Axial shortening began to grow more rapidly at 3 % drift corresponding to the onset of local buckling. Note that this axial shortening as the result of the local buckles was permanent and exhibited significant magnitudes; this was not observed in Specimens 6L and 6L-P.

3.7.5 Concluding Remarks

Subjected to weak-axis bending, Group 6 specimens showed excellent ductility higher than that of Group 2 specimens with the same section, which underwent strong-axis bending. Even for Specimen 6H with the high level of axial compression, only limited local buckling was developed. AISC 341 mandates the same seismic compactness requirements for column under either strong- or weak-axis bending. Test results has shown that this practice is too conservative since ductility observed in weak-axis bending tests is much higher than that observed in strong-axis bending tests of nominally identical specimens under the same axial load levels.

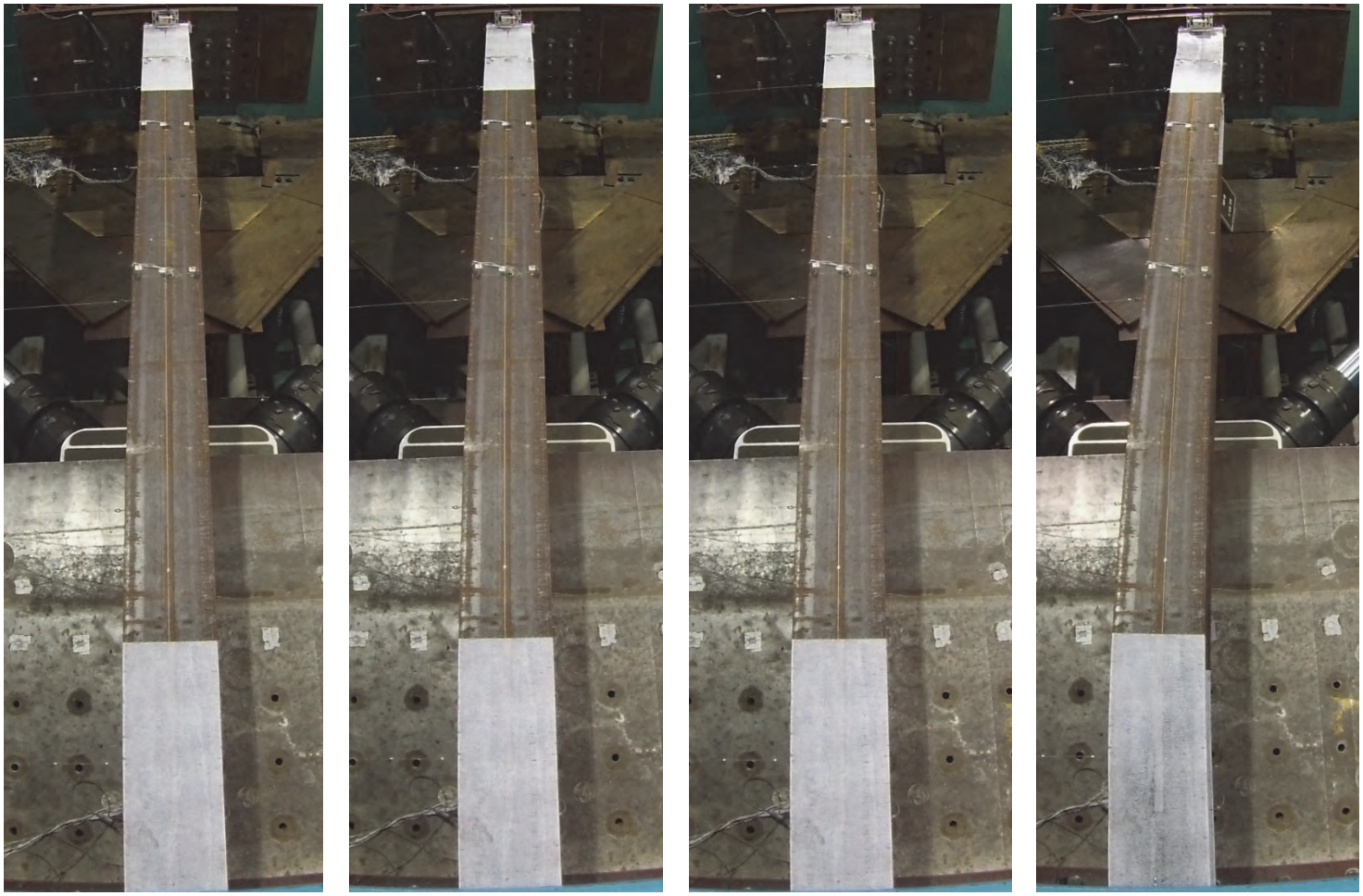

(a) *SDA* = 0.015 rad (b) *SDA* = 0.02 rad (c) *SDA* = 0.03 rad (d) *SDA* = 0.04 rad

Figure 3.88 Specimen 6H: Overall Yielding and Buckling Progression

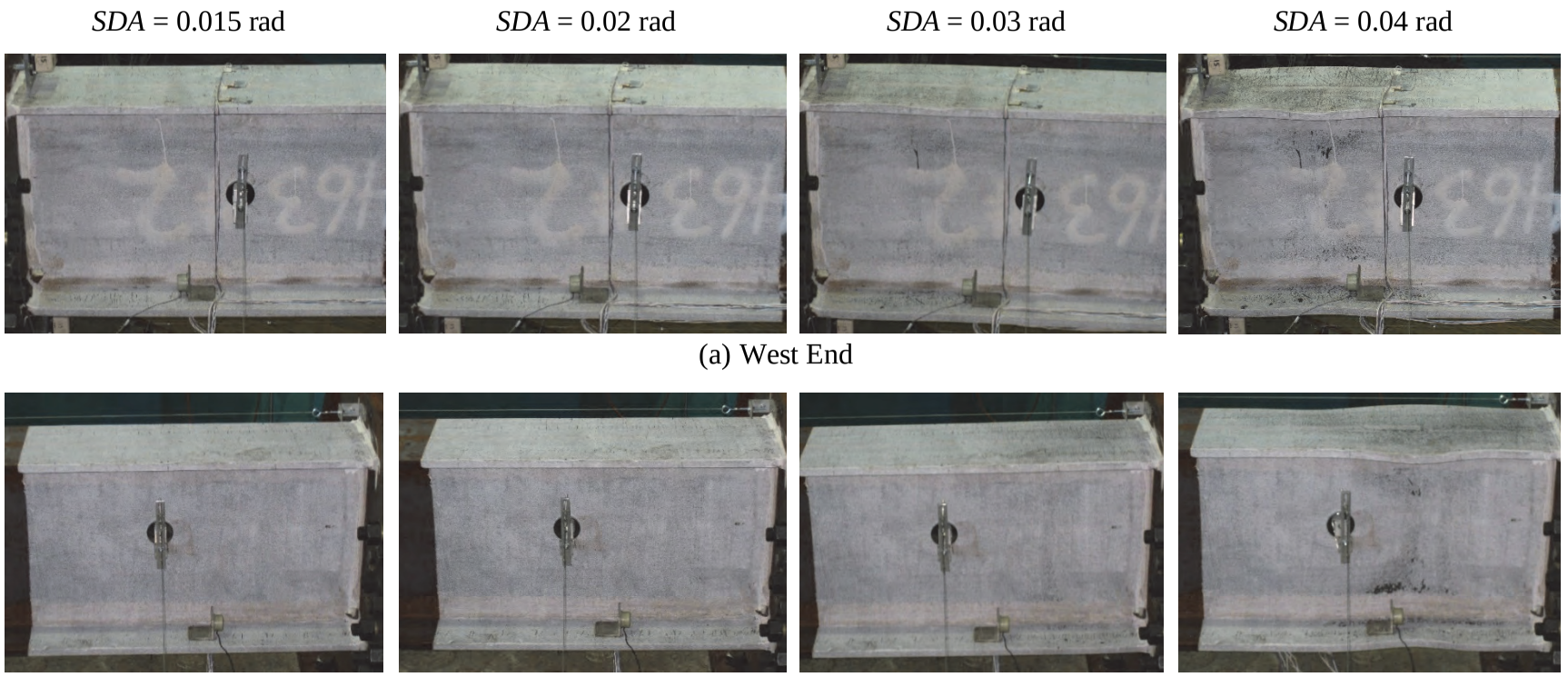

(a) West End

(b) East End

Figure 3.89 Specimen 6H: Yielding and Buckling Progression at Member Ends

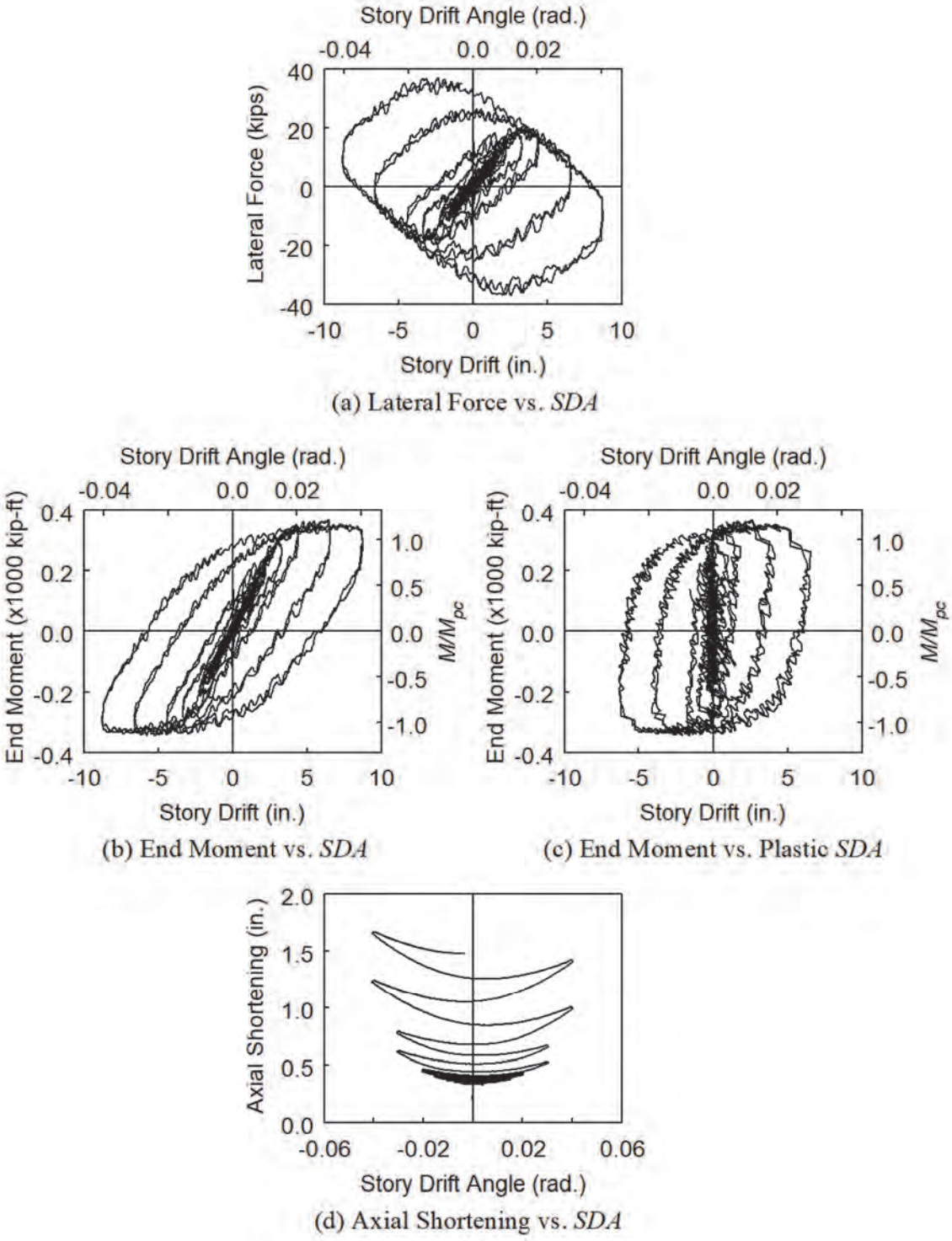

Figure 3.90 Specimen 6H: Global Responses

3.8 Group 7 Specimen: Section W24×131 with Biaxial Bending

3.8.1 General

Only Specimen 7M was tested in this group to evaluate the effect of biaxial bending. The corresponding test results were compared with those of nominally identical Specimen 2M, which only sustained bending in the strong-axis direction.

3.8.2 Test Results

Specimen 7M exhibited the ALB failure mode; yielding and buckling progression is illustrated in Figure 3.91 to Figure 3.93. Web and flange local buckling initiated at 1.5 % drift. Their amplitudes grew during the 2 % and 3 % drift cycles, exhibiting the full-wave ALB configuration. The test was terminated after completing two cycles at 3 % drift due to excessive local buckling and significant loss in flexural strength.

Global responses are shown in Figure 3.94. Strong-axis flexural strength began to degrade during the 1.5 % drift cycles corresponding to the onset of local buckling at both ends; axial shortening also began to grow at an increasing rate at this point. At the end of the test, the column shortened by 9.2 in., i.e., 4.3 % of the undeformed column length.

3.8.3 Concluding Remarks

Specimen 7M behave very similarly to Specimen 2M, signifying that the effect of biaxial loading is not significant. To some degree, the strong-axis flexural strength of the former appeared to deteriorate at a slightly faster rate than that of the latter during the last few cycles of testing.

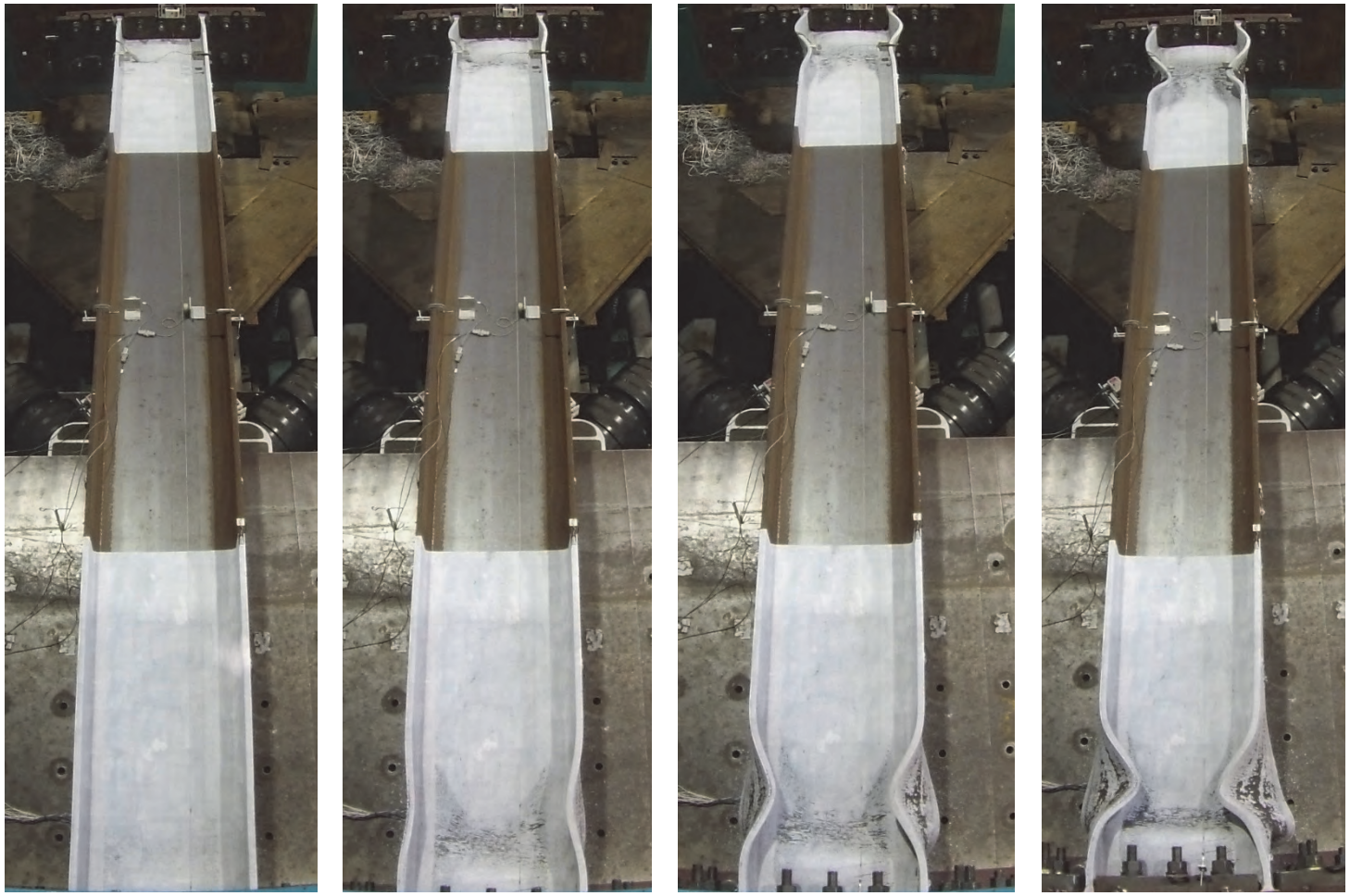

(a) *SDA* = 0.01 rad (b) *SDA* = 0.015 rad (c) *SDA* = 0.02 rad (d) *SDA* = 0.03 rad

Figure 3.91 Specimen 7M: Overall Yielding and Buckling Progression

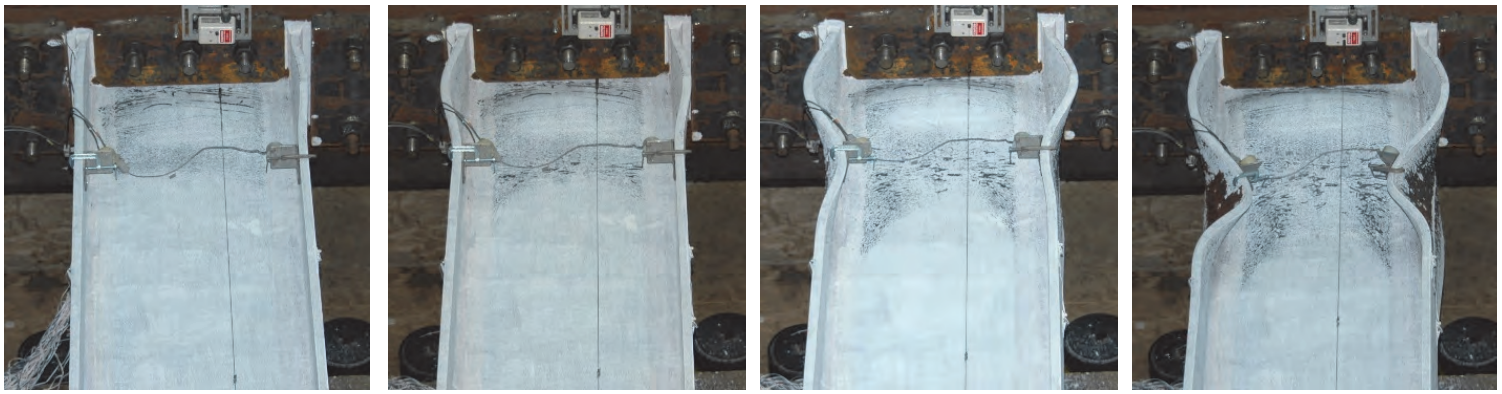

(a) West End

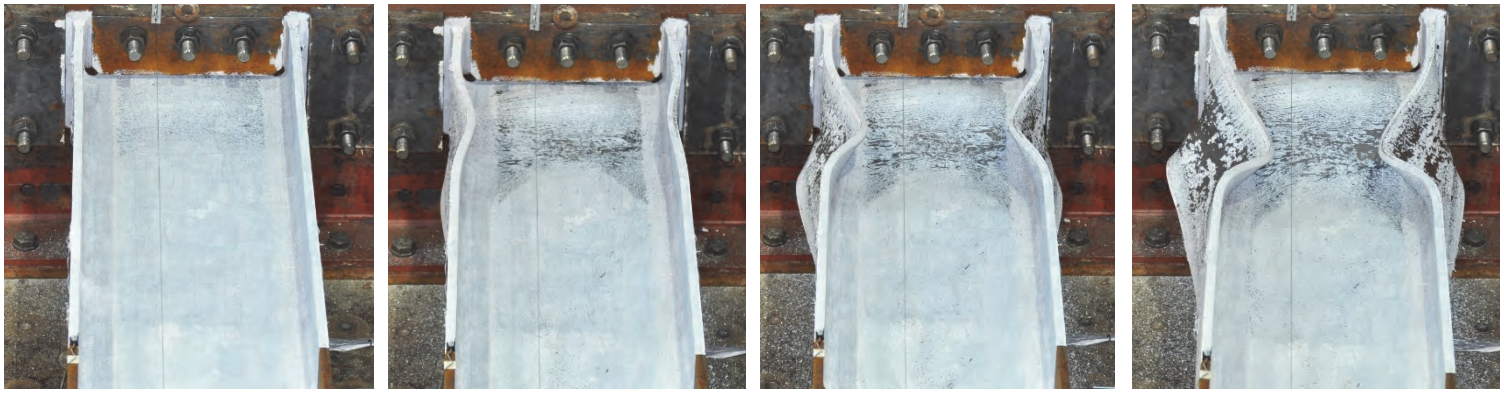

(b) East End

Figure 3.92 Specimen 7M: Yielding and Buckling Progression at Member Ends (Top View)

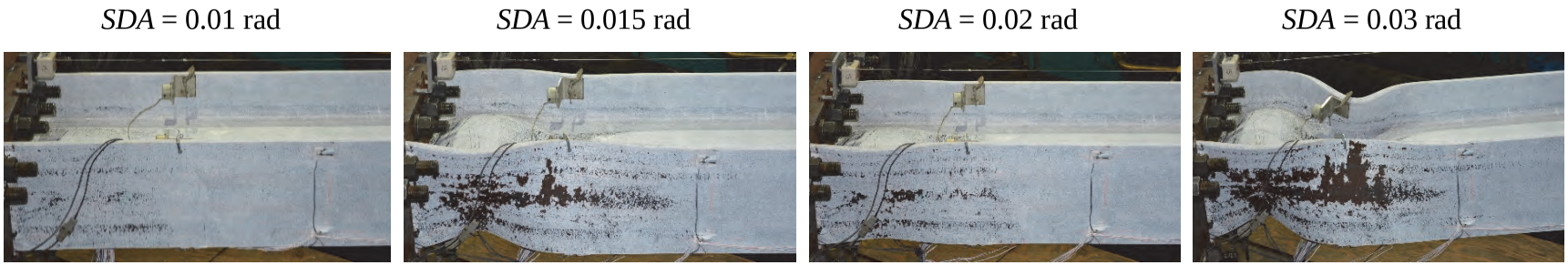

(a) West End

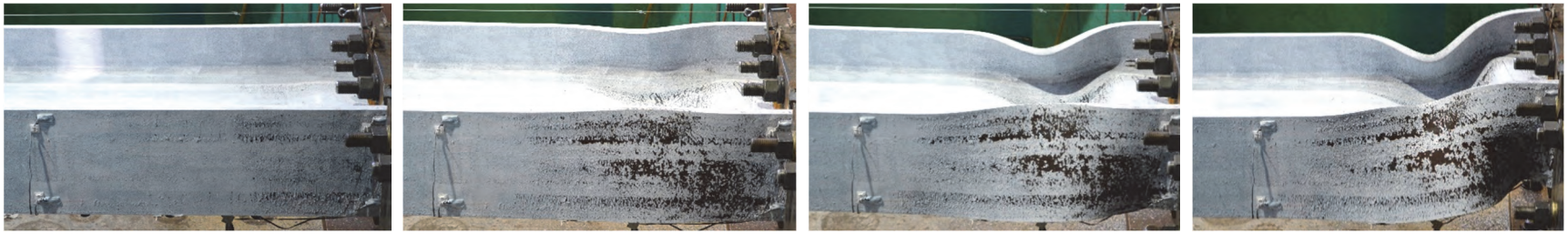

(b) East End

Figure 3.93 Specimen 7M: Yielding and Buckling Progression at Member Ends

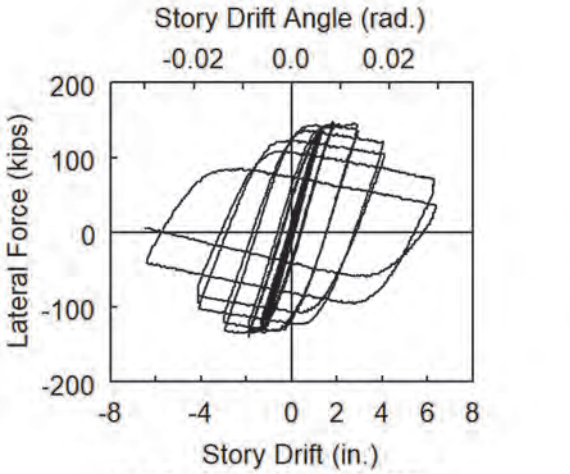

(a) Lateral Force vs. *SDA*

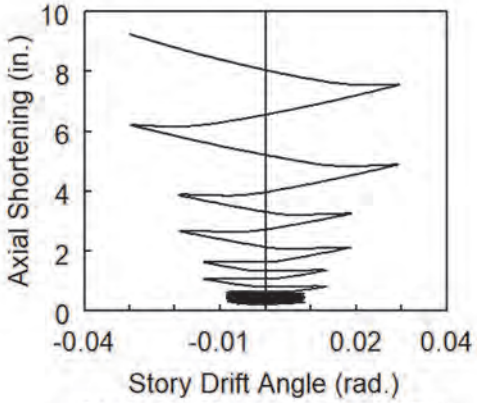

(b) Axial Shortening vs. *SDA*

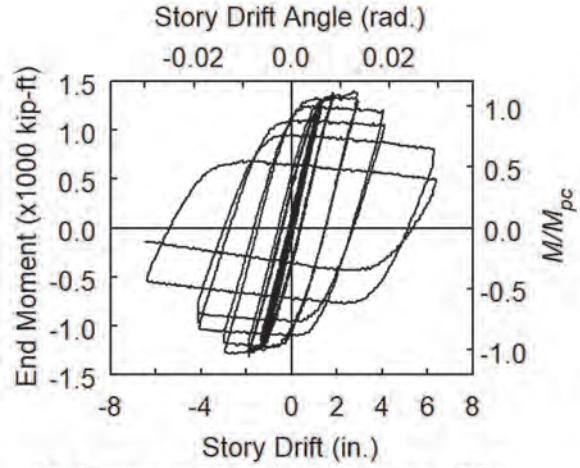

(c) Strong-axis End Moment vs. *SDA*

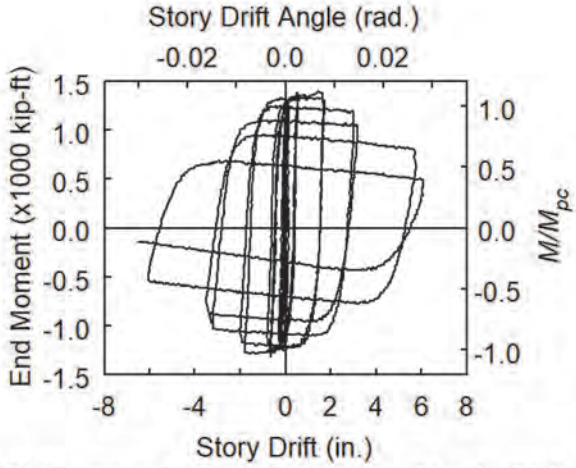

(d) Strong-axis End Moment vs. Plastic *SDA*

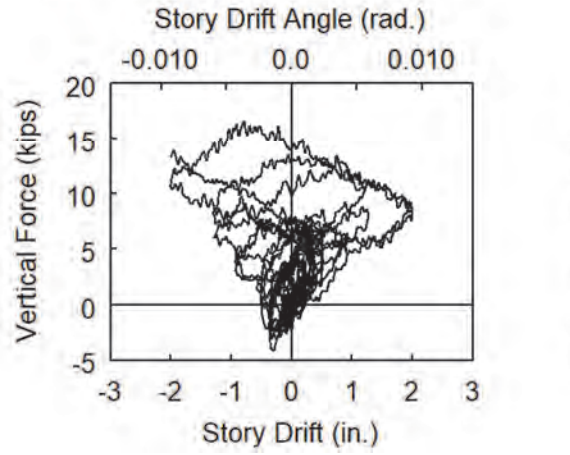

(e) Vertical Force vs. *SDA*

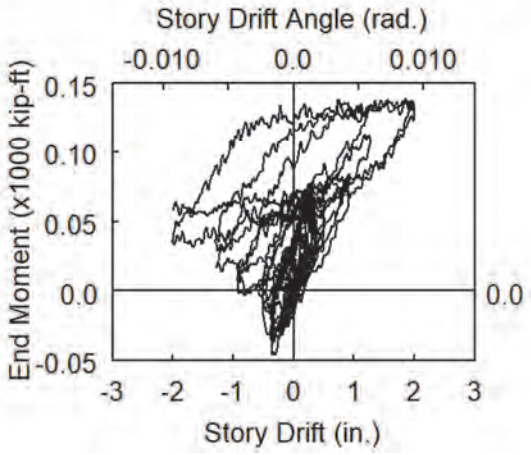

(f) Weak-axis End Moment vs. *SDA*

Figure 3.94 Specimen 7M: Global Responses

4. TEST PROGRAM: PHASE 2A

4.1 Introduction

Five different W24 sections were tested in Phase 1. Phase 2A encompassed testing of twelve deep wide-flange (i.e., W18, W24, and W30) columns with similar test setup and loading protocols used in Phases 1. See Table 4.1 for the test matrix.

In Phase 1 testing, fixed-fixed boundary conditions were used. Therefore, fixed-fixed boundary conditions were mainly used in this phase to allow a direct comparison between Phase 1 and Phase 2A results. Except for Specimen 11H-VA, which was tested with a varying axial load to investigate the response of an exterior column during a seismic event, all specimens were tested with constant axial loads. To evaluate the boundary condition effect, three specimens were tested with fixed-rotating boundary conditions (see Section 4.5). All specimens in this phase were tested in strong-axis bending

4.2 Test Setup

Phase 2A testing was conducted in the Seismic Response Modification Device (SRMD) Test Facility at the University of California, San Diego. The setup of Phase 2A testing remained essentially the same as that used in Phase 1 (see Section 2.2). Figure 4.1 and Figure 4.2 show the typical specimen geometries and details of the bolted end connection. The outer member length including end plate thicknesses of all specimens was 18 ft. [5480 mm]. End plates of 3-in. [75 mm] thick were welded to Groups 11, 12, and 13 specimens, and those of 2-in. [50 mm] thick were used for the remaining.

4.3 Design of Test Specimens

Seven “deep” wide-flange sections for a total of twelve specimens were included in Phase 2A testing (see Table 4.1). Figure 2.4 illustrates distribution of the section slenderness parameters of test specimens with respect to the seismic compactness limits specified in AISC 341 (AISC 2016a). Figure 2.5 shows distribution of the L/r_y ratios. In Phase 1, an “unexpected” coupled buckling involving out-of-plane, global-type buckling was observed during testing of Group 1 specimens (W24×176) and Group 4 specimens (W24×84). In Phase 2A, Group 11 specimens were assigned the same section as Group 1 specimens, and one (Specimen 11M) was tested to confirm if the same failure mode could

be reproduced. In addition, three W30 and three W18 sections were included in Phase 2A testing to achieve two goals: (1) to investigate whether findings from Phase 1 (testing of W24 sections) can be applied to deeper (e.g., W30) and shallower (e.g., W18) columns with similar slenderness parameters, and (2) to expand the section slenderness database. Regarding the first objective, Group 12, 13, 16, and 17 specimens were assigned with W30 and W18 sections that had similar section slenderness parameters compared to some W24 sections (Groups 1, 2, and 3) from Phase 1 testing. Regarding the second objective, Groups 14 and 15 were assigned with W30×90 and W18×192 sections, respectively, to extend the range of the web and flange slenderness database. Group 1 section (W24×176) was the stockiest section tested in Phase 1. Group 15 section (W18×192) was even stockier.

In Phase 1, Group 5 specimens failed due to elastic lateral-torsional buckling without plastic hinging at member ends because their L/r_y (= 161.2) was much larger than other specimens. Consequently, inelastic cyclic response associated with the section slenderness characteristics of Group 5 specimens was not obtained. Group 14 specimen had a similar h/t_w, a larger $b_f/2t_f$, but a much lower L/r_y (= 101.4) compared to those of the Group 5 specimens, making it less prone to elastic LTB. Testing of Group 14 member was designed to fill this data gap.

The same specimen-labeling approach used in Phase 1 study (see Section 2.3) was implemented in Phase 2 study with some additions. Designation "LM" indicated that the applied axial load magnitude was the average of the low and medium levels, i.e., $C_a = 0.3$. All Phase 2A specimens were subjected to inelastic cyclic drift except for Specimen 12LM-P, which was tested monotonically to obtain a monotonic backbone curve for comparison with the cyclic backbone curve of its counterpart, Specimen 12LM. Three specimens with "BC" designation were tested with fixed-rotating boundary conditions to examine the effect of rotation at the top end of first-story columns resulting from beam flexibility. Specimen 11H-VA ("VA" for "Varying Axial Load") was subjected to varying axial load to simulate the response of a first-story exterior column in an SMF. All other specimens were subjected to constant axial loads for interior column scenarios.

4.4 Steel Material Properties

ASTM A992 was specified for all beam-column specimens, and A572 Gr. 50 steel was specified for the end plates. Table 4.2 summarizes mechanical properties of the specimens; coupons were taken from both webs and flanges for material testing. The engineering stress versus engineering strain relationships are shown in Figure 4.3.

4.5 Testing Procedure and Loading Protocols

The same testing procedure and AISC loading protocol used in Phase 1 testing were used for constant axial load tests of Phase 2 study. To investigate the behavior of a first-story exterior column in an SMF, Specimen 11H-VA was tested with the AISC loading protocol in conjunction with the varying axial load sequence illustrated in Figure 4.4(b). The compressive axial load applied to this specimen fluctuated about a gravity load of $C_a = 0.45$. In addition, the cyclic axial load variation grew proportionally to the levels of lateral drift; this simulated the overturning-moment effect that amplified as the multistory moment frame displaced at higher amplitudes. At a certain drift level, plastification was expected at beam ends and the overturning moment would stabilize. Accordingly, the axial load range was capped to $C_a = 0.3$ to $C_a = 0.6$ at 1.0 % drift and beyond.

In Phase 1, all specimens were tested with fixed-fixed boundary conditions. Since in real application the top end of first-story columns in an SMF experiences rotation due to the flexibility of the connected beams, fixed-rotating boundary conditions were implemented in testing of three specimens (Specimens 11H-BC, 13M-BC, and 16M-BC) in Phase 2A. For this test program, cyclic end rotations [Figure 4.4(c)] were applied to the moving end of these specimens in-phase with and proportional to the AISC lateral drift sequence [Figure 4.4(a)]. The applied end rotations were expressed as follow:

$$\theta_m = \xi_m \left(\frac{\Delta_m}{L}\right) \tag{4.1}$$

A three-bay, four-story SMF designed by Harris and Speicher (2015) was analyzed to determine an approximate ξ_m value for this test program. Based on a nonlinear, time-history analysis of this structure with 14 ground motions, scaled to match the Design Earthquake per ASCE 7, the top end rotation and the first-story drift angle were similar in

magnitude. Values of ξ_m used in this test program are summarized in Table 2.4. ξ_m was initially set to 1 for all fixed-rotating specimens; but due to human error, Specimen 11H-BC with W24×176 shape was tested with a slightly larger ξ_m value of 1.12.

4.6 Instrumentation

Displacement transducers, inclinometers, strain gauge rosettes, and uniaxial strain gauges were used to measure global and local responses. Figure 4.5 shows displacement transducer and inclinometer layout. Figure 4.6 shows rosette and uniaxial strain gauge locations. Movements of the platen and their associated forces in six degrees of freedom were also recorded.

4.7 Data Reduction

See Section 2.7.

Table 4.1 Test Matrix for Phase 2A Testing

Group No.	Section	Specimen Designation	L (ft)	Slenderness			Column Axial Load		Parameter of Interest	Predicted Buckling Mode[a]
				$\frac{b_f}{2t_f}$	$\frac{h}{t_w}$	$\frac{L}{r_y}$	C_a	P_u (kips)		
11	W24×176	11M	17½	4.81	28.7	69.1	0.4	931	1M Repeat	Coupled Buckling
		11H-VA					0.3 to 0.6	698 to 1396	Varying Axial Load Effect	
		11H-BC					0.6	1396	Boundary Condition Effect	
12	W30×261	12LM	17½	4.59	28.7	59.5	0.3	1040	Section Depth Effect (Similar to Group 1)	Coupled Buckling
		12LM-P							Loading Sequence Effect	
13	W30×173	13M	17½	7.04	40.8	61.4	0.4	916	Section Depth Effect (Similar to Group 2)	In-plane Plastic Hinging
		13M-BC							Boundary Condition Effect	
14	W30×90	14L	17⅔	8.52	57.5	101.4	0.2	237	More Slender than Group 5	In-plane Plastic Hinging
15	W18×192	15L	17⅔	3.27	16.7	76.0	0.2	506	More Compact than Group 1	Coupled Buckling
16	W18×130	16M	17⅔	4.65	23.9	78.5	0.4	689	Section Depth Effect (Similar to Group 1)	
		16M-BC							Boundary Condition Effect	
17	W18×76	17L	17⅔	8.11	37.8	81.2	0.2	201	Section Depth Effect (Similar to Group 3)	In-plane Plastic Hinging

[a] Per the prediction of Ozkula et al. (2017).

Table 4.2 Steel Mechanical Properties for Phase 2A Testing

Group No.	Section	Comp.	Yield Stress (ksi)	Tensile Strength (ksi)	Elong.[c] (%)	Heat No.
11	W24×176	Flange	52.1	83.5	33.2	27469
		Web	51.4	82.7	36.1	
12	W30×261	Flange	54.6	75.6	38.3	451709
		Web	59.6	74.4	41.0	
13	W30×173	Flange	57.3	73.6	41.7	450564
		Web	67.2	79.7	37.0	
14	W30×90	Flange	58.3	73.7	37.1	417509
		Web	62.7	75.9	38.1	
15	W18×192	Flange	55.3	77.4	36.3	432017
		Web	60.8	77.1	39.6	
16[a]	W18×130	Flange	49.9	79.0	34.5	12986
		Web	53.3	78.8	34.8	
16[b]		Flange	52.1	71.2	40.9	354162
		Web	56.6	71.9	40.1	
17	W18×76	Flange	57.3	75.3	38.5	7505
		Web	54.8	66.1	32.3	

[a] Specimen 16M.

[b] Specimen 16M-BC.

[c] Elongations are based on a 2-in. gauge length.

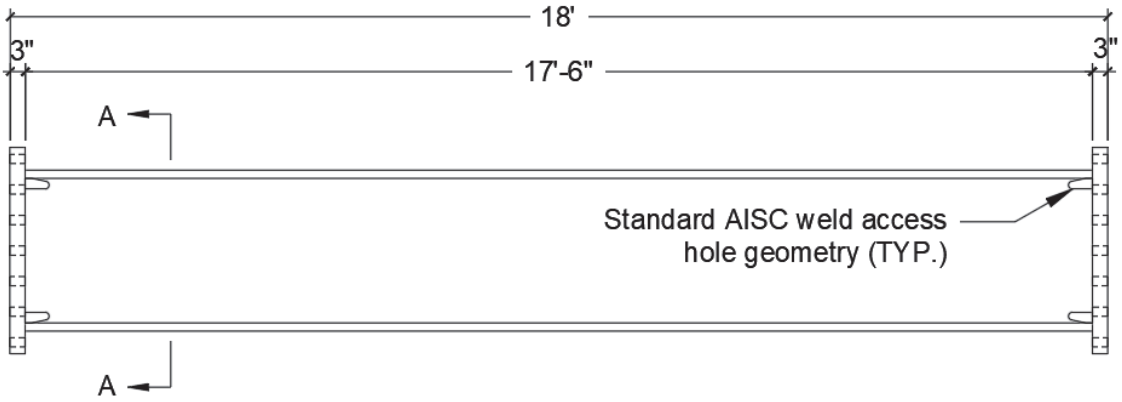

PLAN

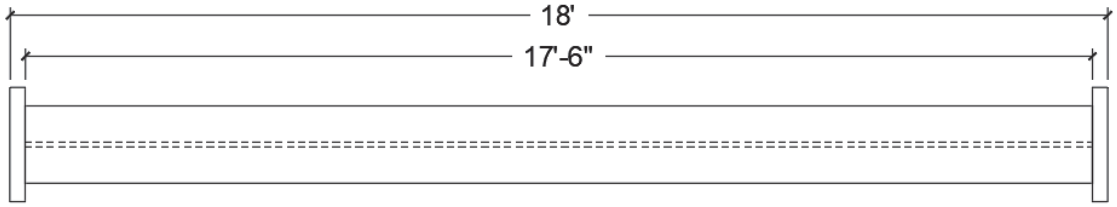

ELEVATION

(a) Overall Dimensions

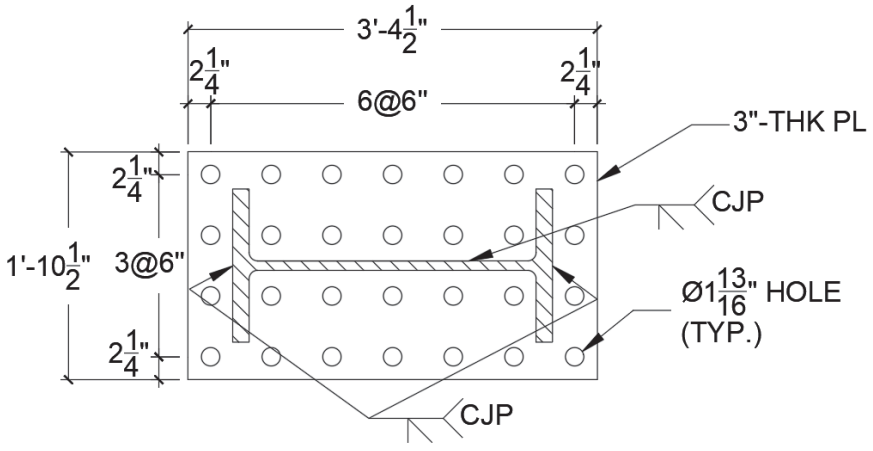

(b) Section A-A

Figure 4.1 Phase 2A Specimen Geometries and End Details (Groups 11 to 13)

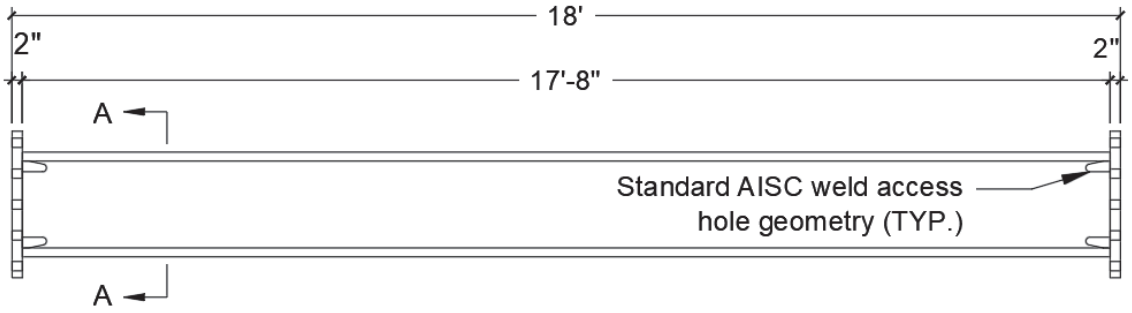

PLAN

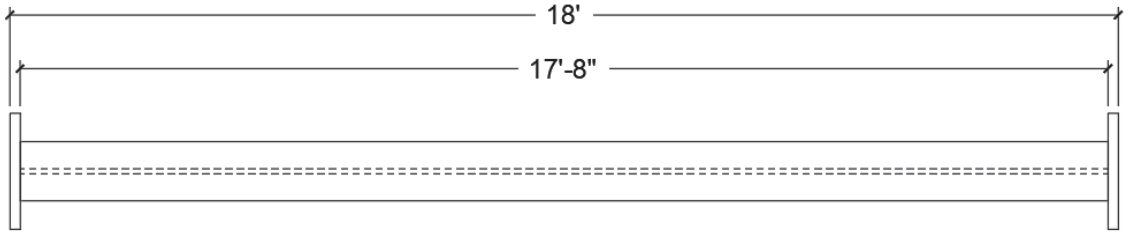

ELEVATION

(a) Overall Dimensions

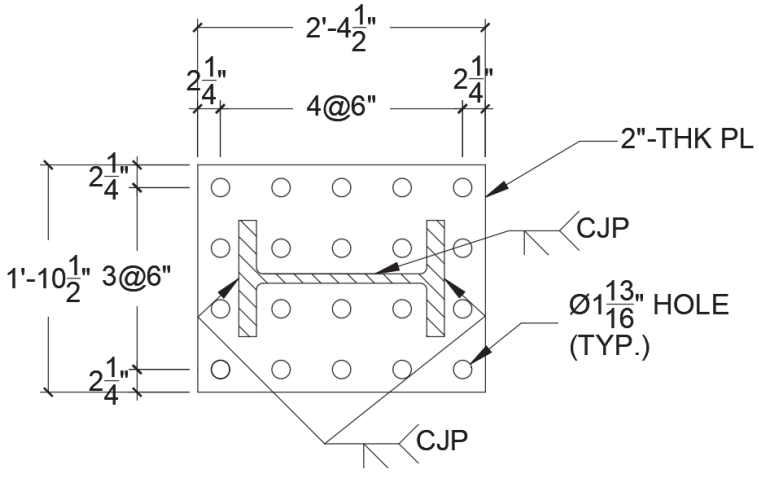

(b) Section A-A

Figure 4.2 Phase 2A Specimen Geometries and End Details (Groups 14 to 17)

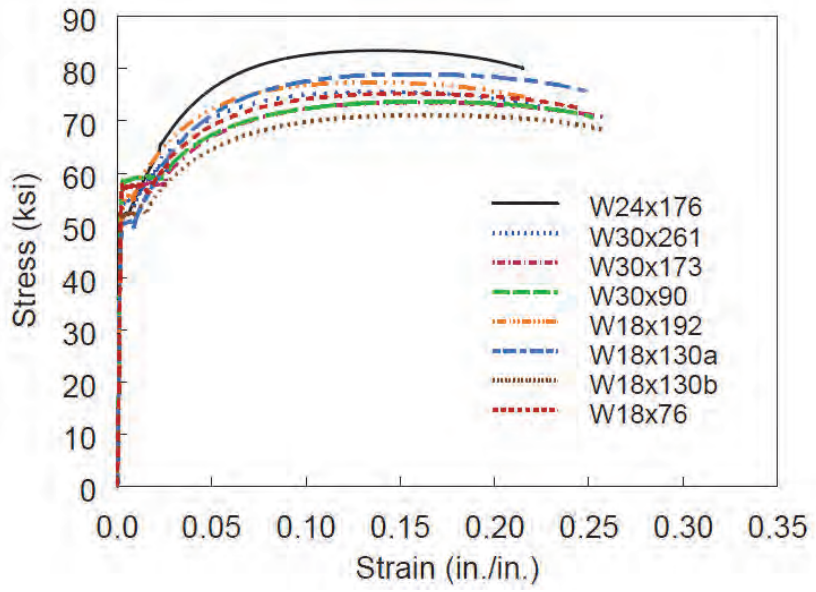

(a) Flange

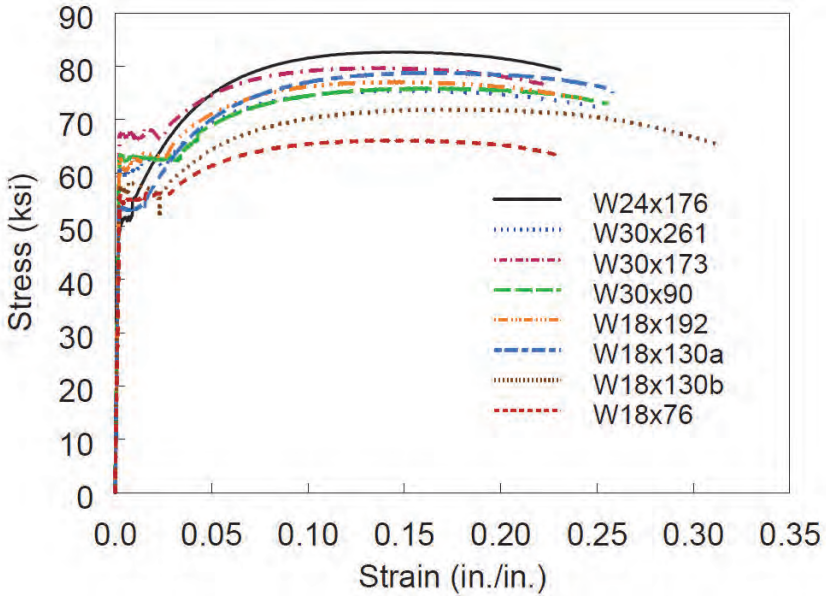

(b) Web

Figure 4.3 Phase 2A Engineering Strain versus Stress Curves

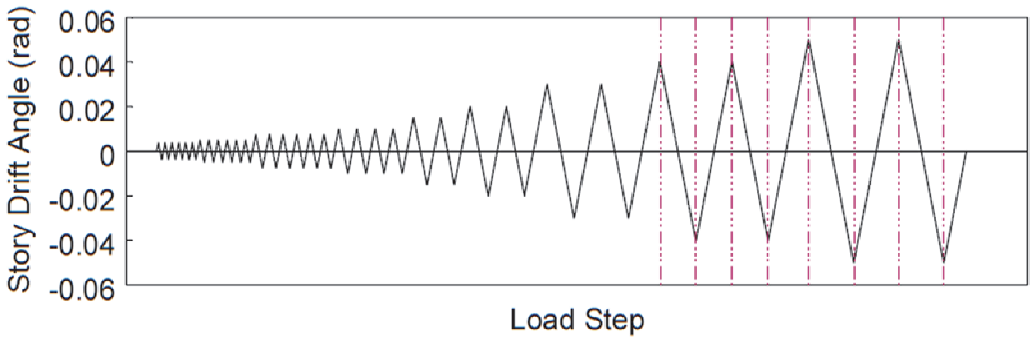

(a) AISC Story Drift Angle Loading Protocol

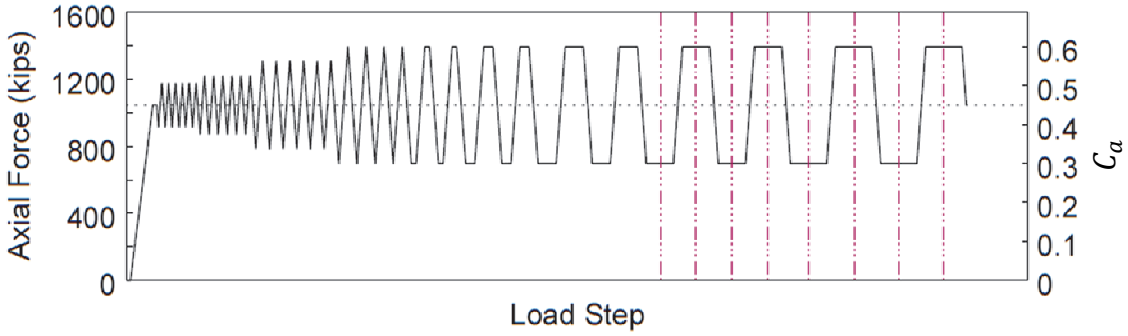

(b) Varying Axial Load Sequence for Specimen 11H-VA

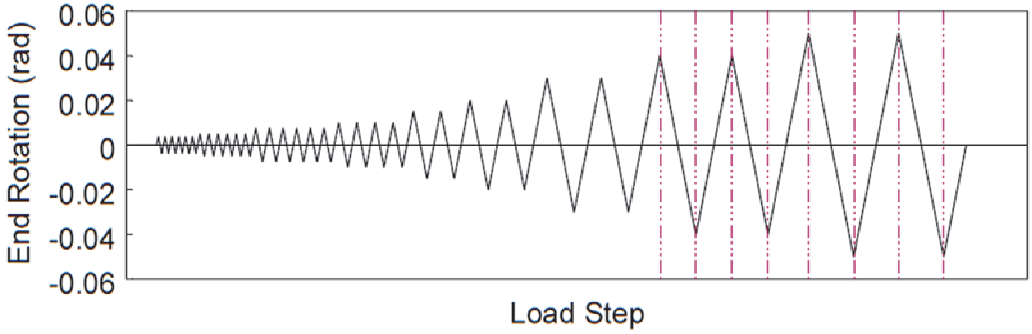

(c) Moving End Rotation Sequence

Figure 4.4 Phase 2A Cyclic Loading Schemes

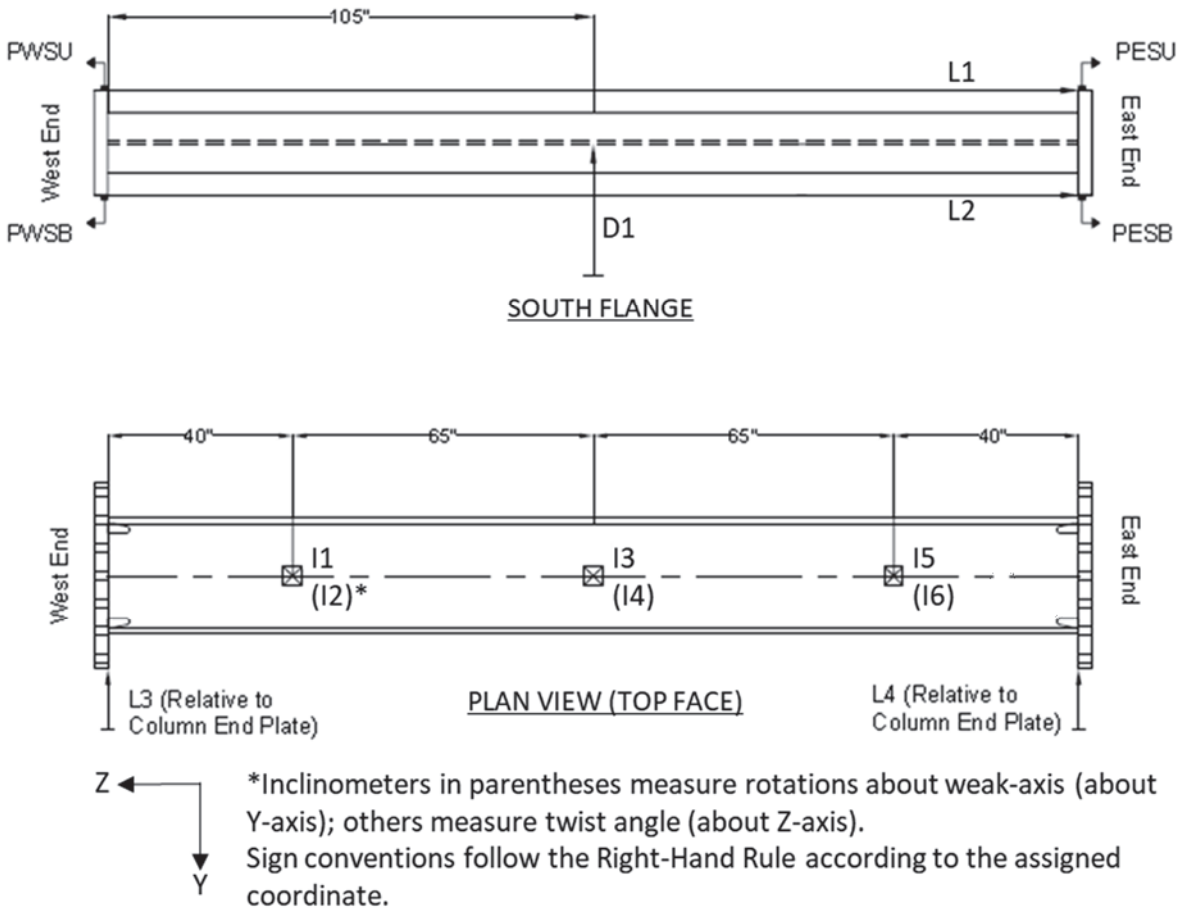

Figure 4.5 Displacement Transducer and Inclinometer Layout

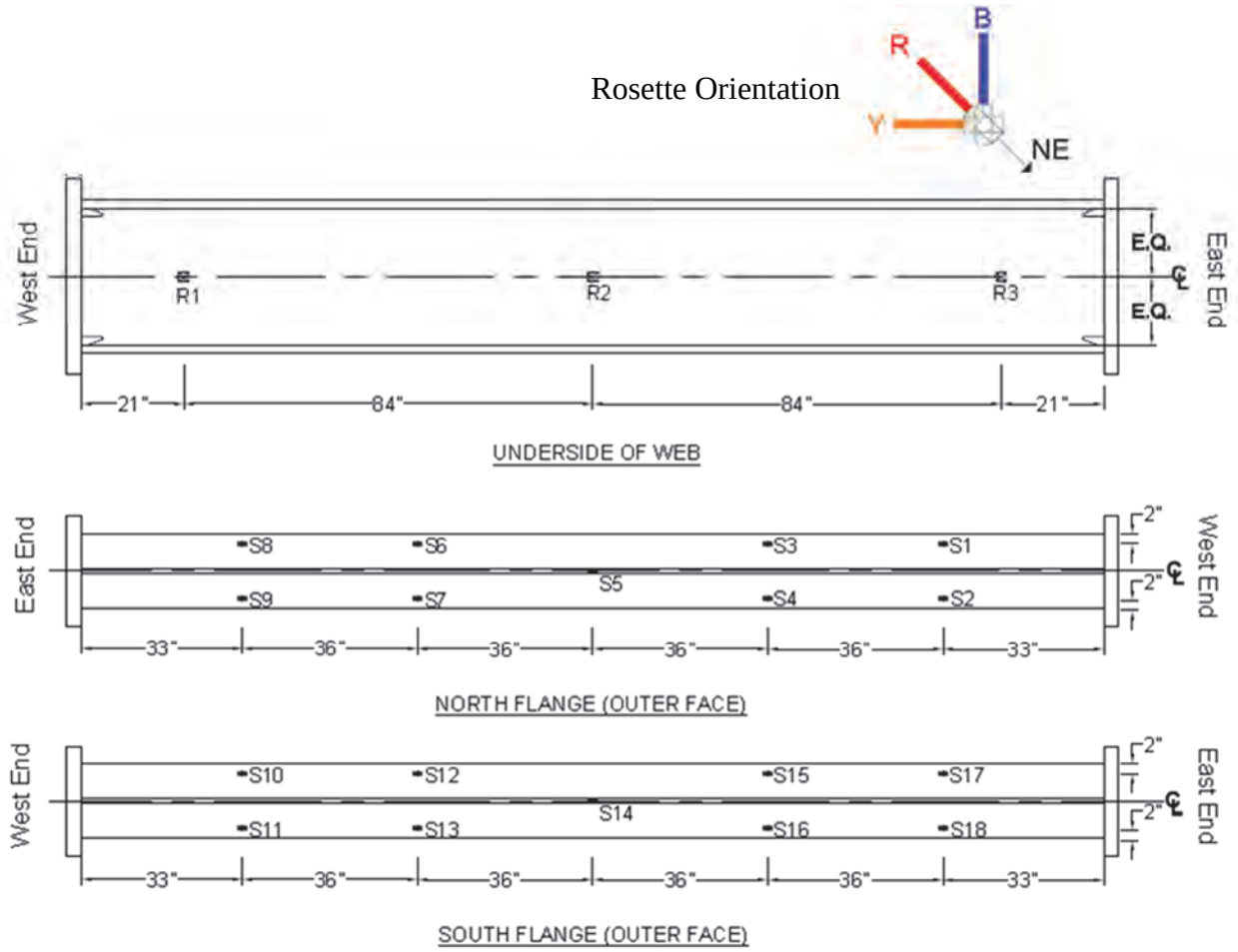

Figure 4.6 Rosette and Uniaxial Strain Gauge Layout

5. TEST RESULTS: PHASE 2A

5.1 Introduction

Measured responses and observed behavior of twelve specimens from Phase 2A testing are presented in this chapter. Except for Specimen 12LM-P, which was loaded monotonically, all specimens were subjected to the AISC cyclic loading protocol. Figures and global response plots are presented in the same manner as those presented in Chapter 3. An out-of-plane (OOP) displacement at the column midspan is also reported for some specimens. For consistency, terminologies used in Chapter 3 to describe the test results of Phase 1 testing are also utilized in this chapter. In addition, failure mode classifications and certain phenomena defined in Section 2.8 are referenced here to help explain observed column behavior.

5.2 Group 11 Specimens: Section W24×176

5.2.1 General

Group 11 comprised three W24×176 columns labeled as Specimens 11M, 11H-VA, and 11H-BC. The shape was identical to that of Group 1 specimens in Phase 1 testing, which experienced the CB failure mode. Specimen 11M was subjected to constant axial compression with $C_a = 0.4$ and served as a re-test of Specimen 1M in Phase 1 testing to confirm that the same failure mode could be reproduced. Specimen 11H-VA underwent varying axial compression ($C_a = 0.3$ to 0.6) to simulate an exterior column response. Both Specimens 11M and 11H-VA were tested with fixed-fixed boundary conditions. Specimen 11H-BC was subjected to constant axial compression with $C_a = 0.6$ and the end rotation sequence (see Section 2.5) to simulate rotation at the top end of first-story columns in real application.

5.2.2 Specimen 11M

The governing failure mode of Specimen 11M is CB with the single-curvature out-of-plane buckling configuration. Yielding as well as local and global buckling progression is illustrated in Figure 5.1 and Figure 5.2. At 1 % drift, the sloped flaking pattern initiated. At 1.5 % drift, minor LTB movements initiated at the west end. In addition, web and flange local buckles with minor amplitudes were observed at both ends. Thus, the sequence of

local and global instabilities was not obvious for this specimen; both appeared to initiate at 1.5 % drift. LTB of the specimen aggravated at 2 % and 3 % drifts: during the positive excursion of each drift cycle, the positive-drift compression flanges buckled out of plane more, and the same happened for the negative-drift compression flanges during the negative excursion. As a result, the specimen experienced significant twisting and downward movement with higher out-of-plane amplitude observed toward the west end. LTB-type movement was limited at the east end; instead, it appeared to exhibit the ALB configuration. Indeed, yielding seemed more uniform and localized at the east end during 2 % and 3 % drifts compared to that at the west end. Note that both this specimen and the nominally identical Specimen 1M experienced the same CB mode, except that the latter had a double-curvature, out-of-plane movement (see Figure 3.36).

LTB-induced flange local buckling at the bottom half-width flanges at both ends as shown with arrows in Figure 5.2 for SDA = 0.03 rad exacerbated corresponding to the drastic downward movement of the column. The excessive out-of-plane displacement prompted the termination of testing. During the attempt to unload the specimen after the test was terminated, the northeast flange ruptured across the entire flange width near the end plate (see Figure 5.3). The rupture appeared to initiate from the column web weld access hole. Figure 5.4 shows local buckling configurations at both column ends at the end of test.

Figure 5.5 shows the global responses. Flexural strength degradation was obvious during the 3 % drift cycles when LTB aggravated. Axial shortening was moderate during the 1.5 % and 2 % drift cycles due to the observed local buckling and moderate out-of-plane movements. As their amplitudes increased during the 3 % drift cycles, axial shortening grew rapidly. As shown in Figure 5.5(d) and Figure 5.5(e) respectively, the column axial shortening history and the out-of-plane displacement history were similar in shape, indicating that the two quantities had a direct correlation due to geometry of the deformed specimen.

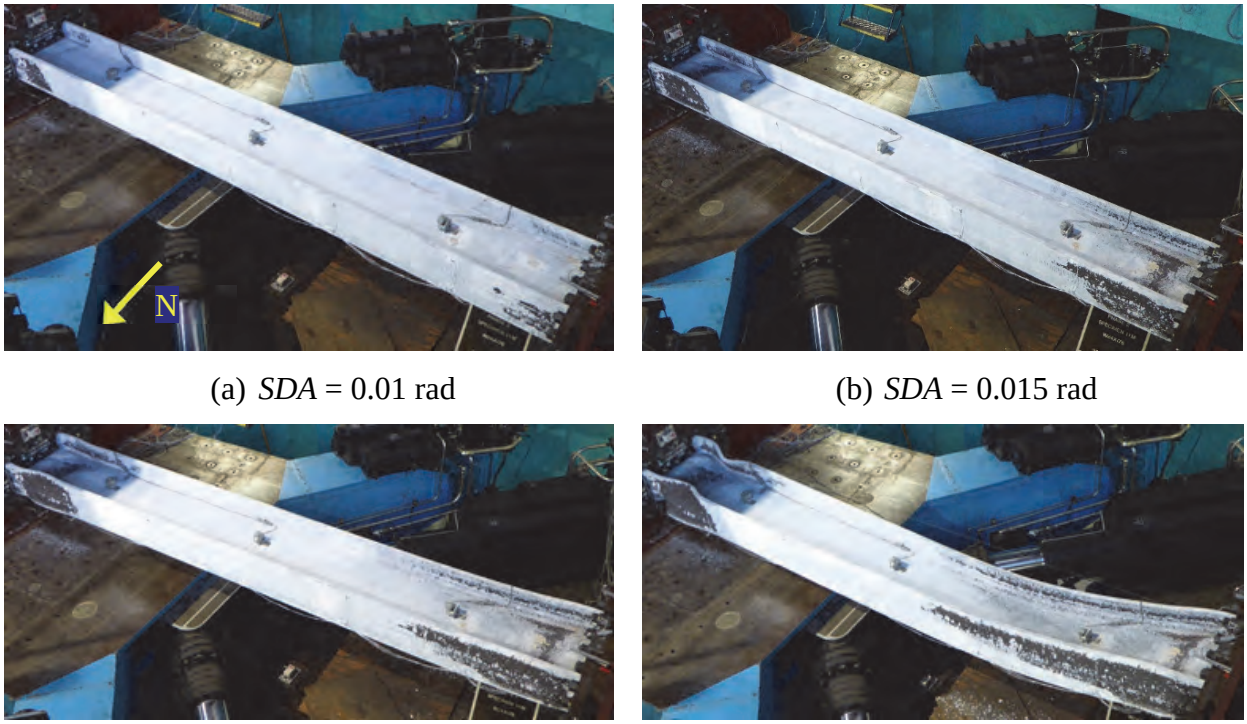

(a) *SDA* = 0.01 rad (b) *SDA* = 0.015 rad

(c) *SDA* = 0.02 rad (d) *SDA* = 0.03 rad

Figure 5.1 Specimen 11M: Overall Yielding and Buckling Progression

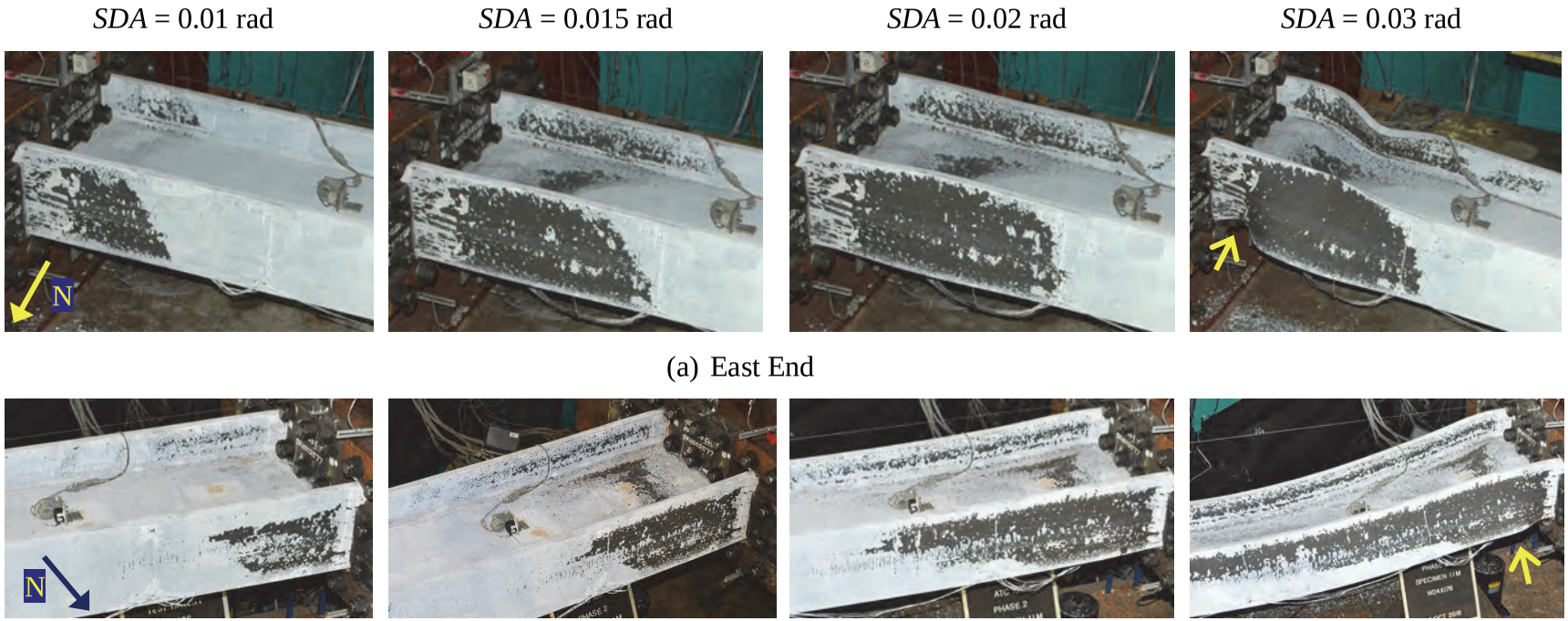

(a) East End

(b) West End

Figure 5.2 Specimen 11M: Yielding and Buckling Progression at Member Ends

Figure 5.3 Specimen 11M: Column Fracture at End of Test (Northeast Flange)

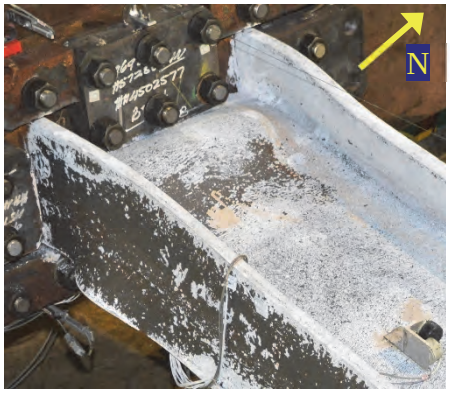

(a) Southwest Flange

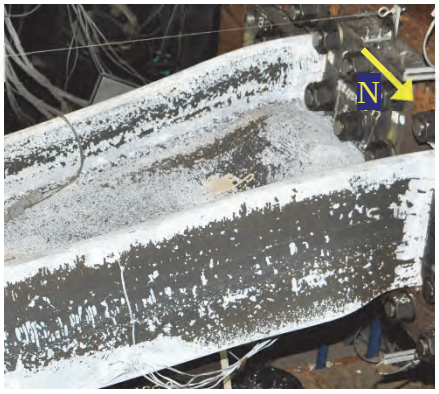

(b) Northwest Flange

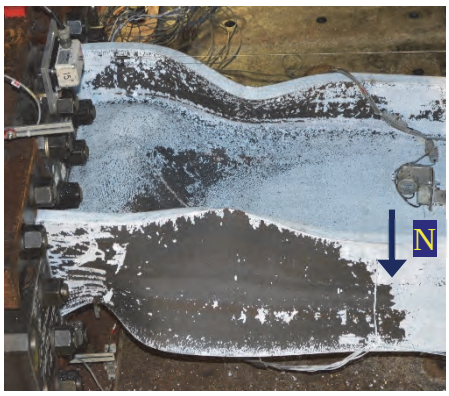

(c) Northeast Flange

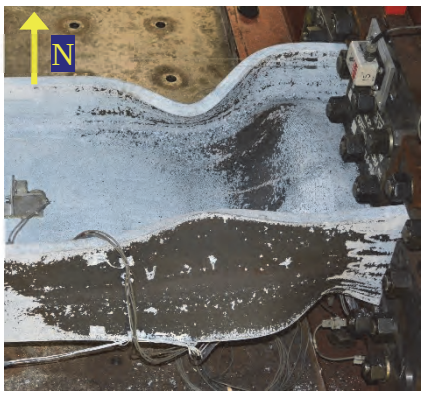

(d) Southeast flange

Figure 5.4 Specimen 11M: Local Buckling at End of Test

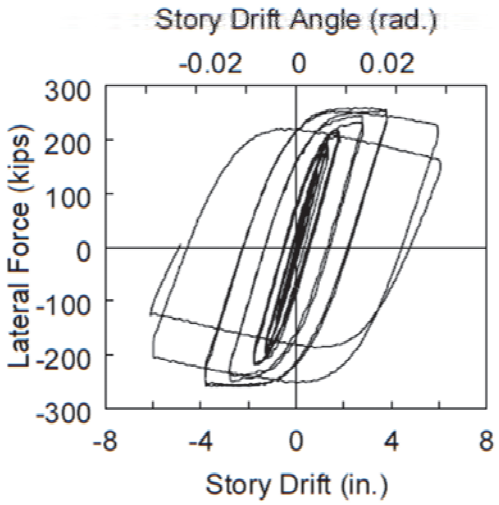

(a) Lateral Force vs. *SDA*

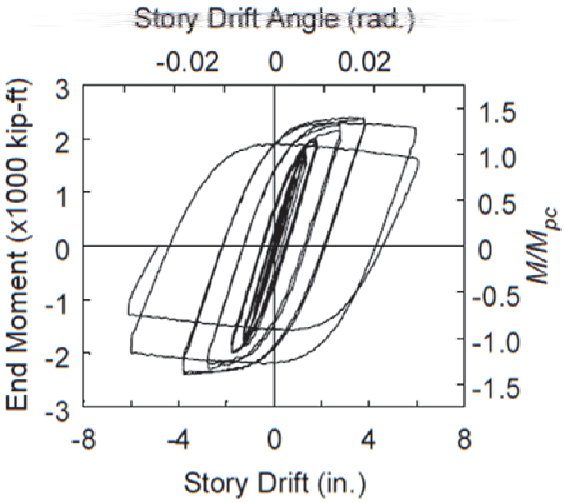

(b) End Moment vs. *SDA*

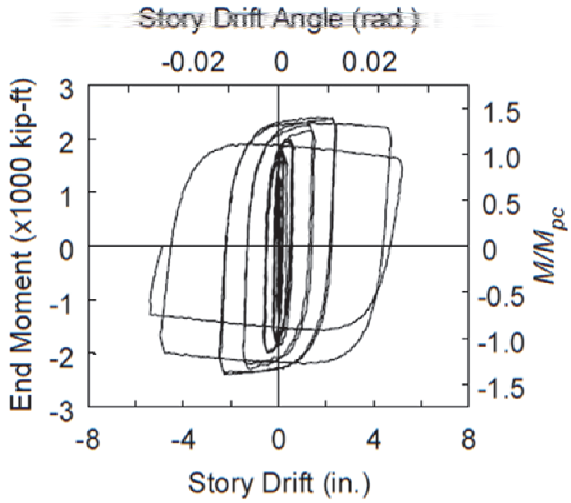

(c) End Moment vs. Plastic *SDA*

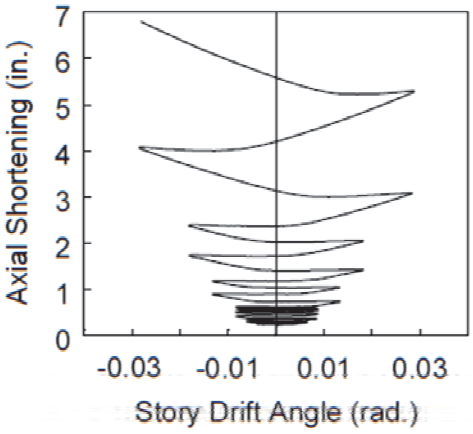

(d) Axial Shortening vs. *SDA*

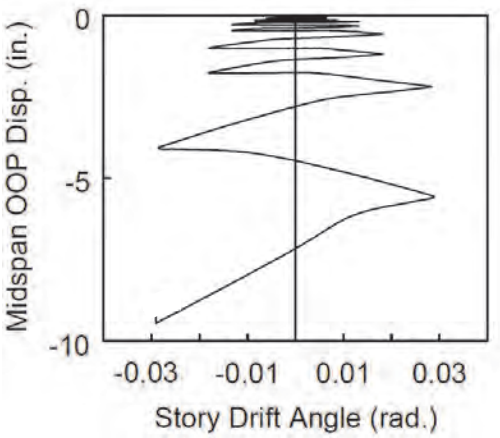

(e) Midspan OOP Disp. vs. *SDA*

Figure 5.5 Specimen 11M: Global Responses

5.2.3 Specimen 11H-VA

The governing failure mode of Specimen 11H-VA is CB with the single-curvature out-of-plane buckling configuration. This specimen was subjected to the varying axial load sequence in conjunction with the AISC loading protocol (see Figure 4.4). The lowest and highest axial compression ($C_a = 0.3$ to 0.6) was reached in the positive and negative drift, respectively. Yielding and buckling progression is illustrated in Figure 5.6 to Figure 5.8.

The sloped flaking pattern initiated at 1 % drift. At 1.5 % drift, minor LTB movements initiated at both ends. At 2 % and 3 % drifts, LTB of the specimen aggravated; during each cycle, compression flanges in the negative drift buckled out of plane in the downward direction more than those in positive drift since the former experienced a higher axial compression than the latter. Expansion of the sloped flaking pattern of the former demonstrated the immensity of their out-of-plane movements; in contrast, whitewash flaking of the latter was relatively limited corresponding to their less aggressive out-of-plane movements. The test was terminated after completing the first cycle at 3 % drift due to excessive out-of-plane buckling. Figure 5.9 shows the ALB configuration (with minor amplitudes) at both column ends at the end of test.

Figure 5.10 shows the global responses. The end moment response indicated maximum flexural strengths of 1,980 kip-ft and 2,580 kip-ft [2685 kN-m and 1155 kN-m] for the negative and positive excursions, respectively; the latter was 30 % greater than the former because it sustained only half of the axial load applied to the former. Flexural strength degradation was apparent in the negative excursion of the 3 % drift cycle corresponding to the severe LTB observed during testing. Axial shortening grew rapidly, starting at 2 % drift corresponding to the aggravated out-of-plane, LTB-type movements.

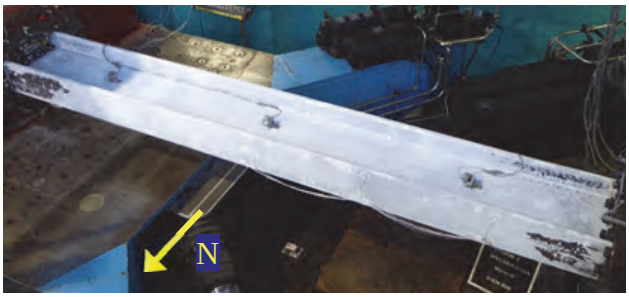

(a) *SDA* = 0.01 rad

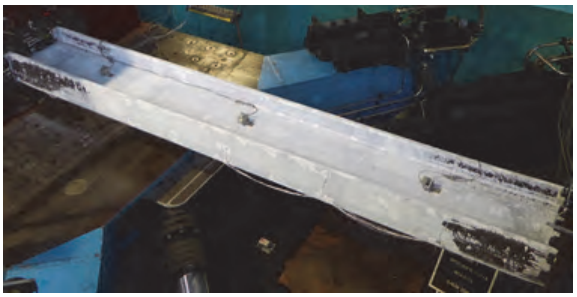

(b) *SDA* = 0.015 rad

(c) *SDA* = 0.02 rad

(d) *SDA* = 0.03 rad

Figure 5.6 Specimen 11H-VA: Overall Yielding and Buckling Progression

(a) *SDA* = 0.02 rad

(b) *SDA* = 0.03 rad

Figure 5.7 Specimen 11H-VA: Overall Yielding and Buckling Progression (Sideview)

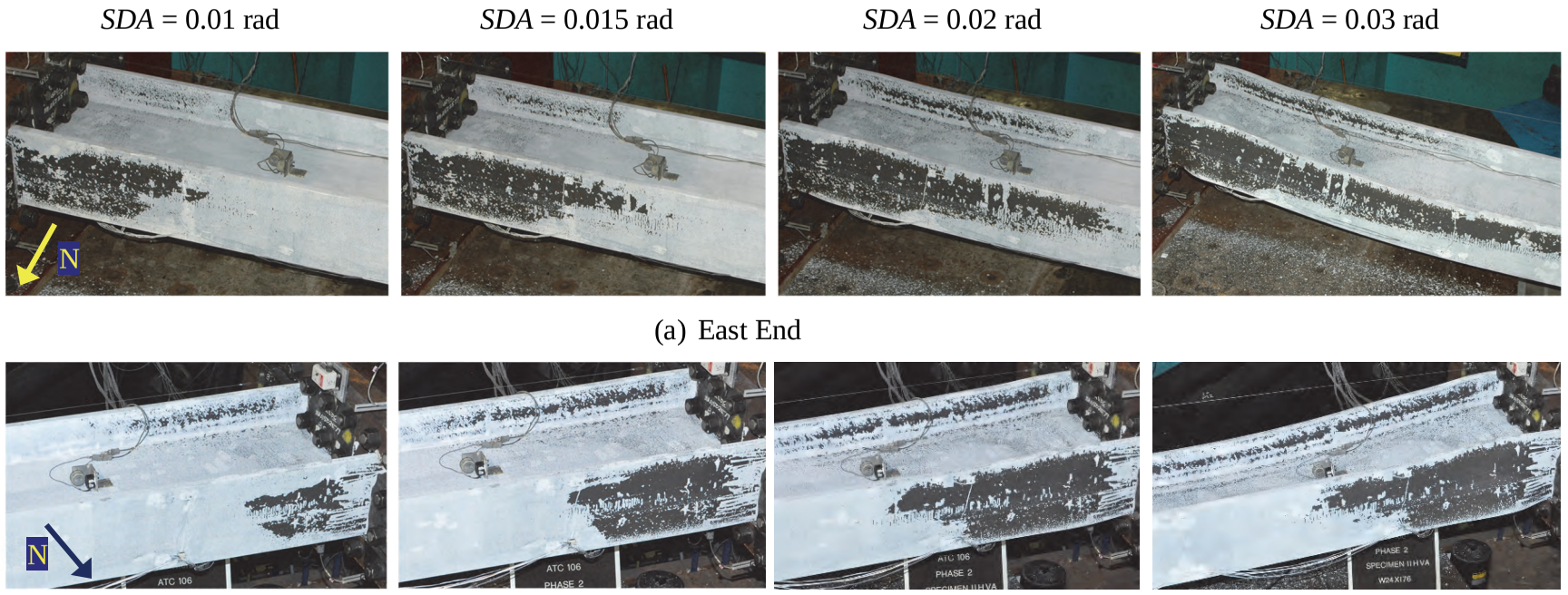

Figure 5.8 Specimen 11H-VA: Yielding and Buckling Progression at Member Ends

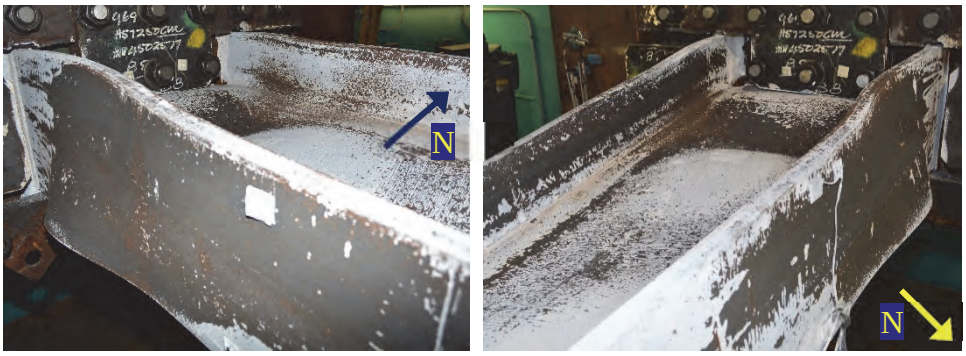

(a) Southwest Flange (b) Northwest Flange

(c) Northeast Flange (d) Southeast Flange

(e) West End (Top View) (f) East End (Top View)

Figure 5.9 Specimen 11H-VA: Local Buckling at End of Test

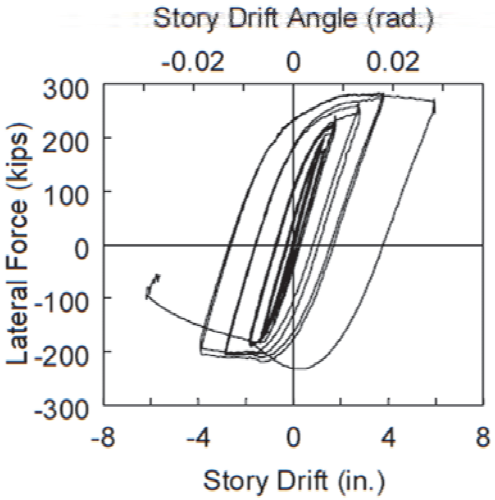

(a) Lateral Force vs. *SDA*

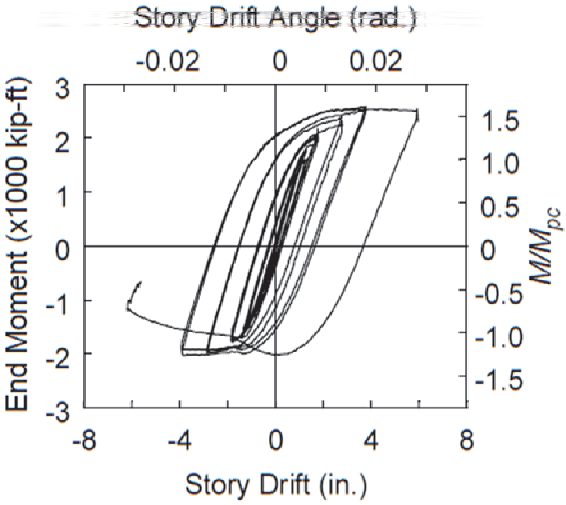

(b) End Moment vs. *SDA*

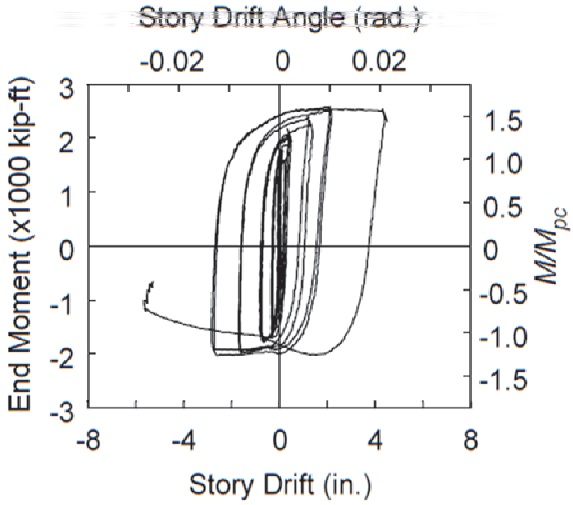

(c) End Moment vs. Plastic *SDA*

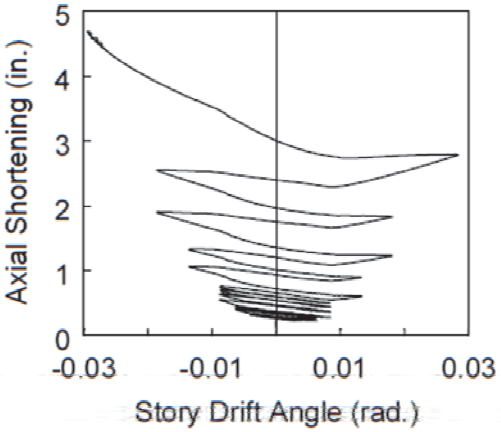

(d) Axial Shortening vs. *SDA*

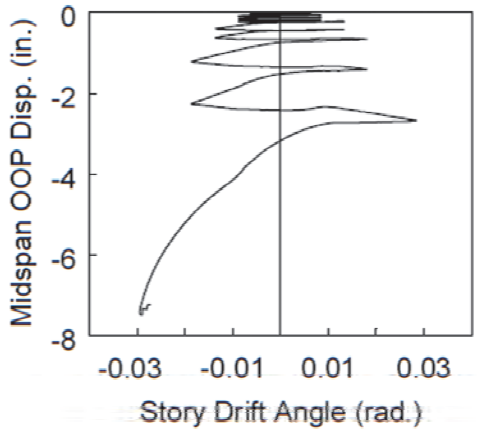

(e) Midspan OOP Disp. vs. *SDA*

Figure 5.10 Specimen 11H-VA: Global Responses

5.2.4 Specimen 11H-BC

The governing failure mode of Specimen 11H-BC is CB with the single-curvature out-of-plane buckling configuration. Yielding and buckling progression is illustrated in Figure 5.11 and Figure 5.13. No significant deformation was observed at the east (or rotating) end until 2 % drift was reached. In contrast, the sloped flaking pattern initiated at 1 % drift at the west (or fixed) end. At 1.5 % drift, downward LTB movements initiated at the west end; a web local buckle with a minor amplitude was also observed. LTB of the specimen exacerbated at 2 % drift: the west flange under compression in positive drift and that in negative drift buckled out of plane more during the positive and negative excursions of each cycle, respectively. This induced flange local buckling at the bottom half-width flanges at the west end as shown with arrows in Figure 5.13 (for SDA = 0.02 and 0.0225 rad) and Figure 5.12. The test was terminated after reaching 2.25 % drift due to the excessive out-of-plane buckling. Note the contrast between the extents of yielding at the west (i.e., fixed) and east (i.e., rotating) ends by the end of the test. Flaking pattern at the east end [see Figure 5.13(a)], which did not spread across the flange width, at 2 % drift and beyond was mainly caused by LTB, not in-plane bending.

Figure 5.14 shows the global responses. Flexural strength at the west end degraded significantly during the 2 % drift cycles when LTB at the west end became more severe. In addition, the axial shortening rate was boosted at 1.5 % drift due to the onset of LTB.

A comparison of the responses of this specimen and a nominally identical Specimen 1H with fixed-fixed boundary conditions shows the following effects of end rotation: (1) the lateral strength was reduced from 206 kips to 104 kips [916 kN to 463 kN] (a 50 % reduction), (2) the lateral stiffness was reduced from 154.3 kips/in to 64.9 kips/in [26,970 kN/mm to 11,365 kN/m] (a 58 % reduction), (3) the strength degradation was delayed leading to a higher ductility capacity, and (4) the axial shortening upon completing the first positive excursion at 2 % drift was reduced from 3.75 in. to 1.36 in. [95 mm to 35 mm].

5.2.5 Concluding Remarks

Group 11 testing demonstrated that the same CB failure mode observed in Phase 1 testing could be reproduced. Furthermore, the effects of varying axial load and fixed-rotating boundary conditions did not alter the governing failure mode associated with this section.

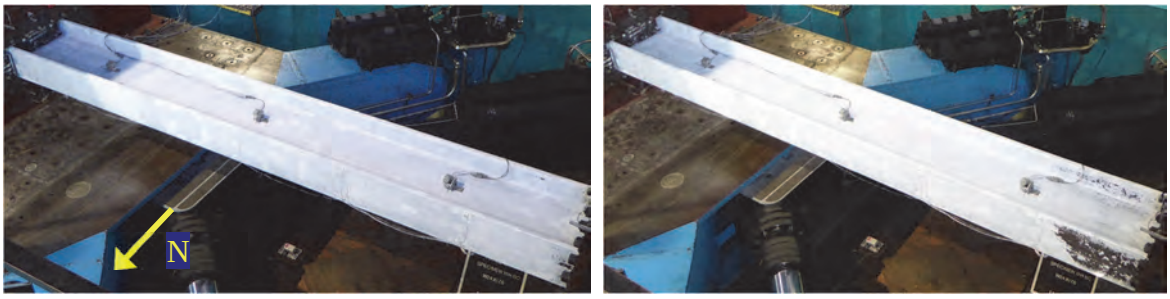

(a) *SDA* = 0.0075 rad (b) *SDA* = 0.01 rad

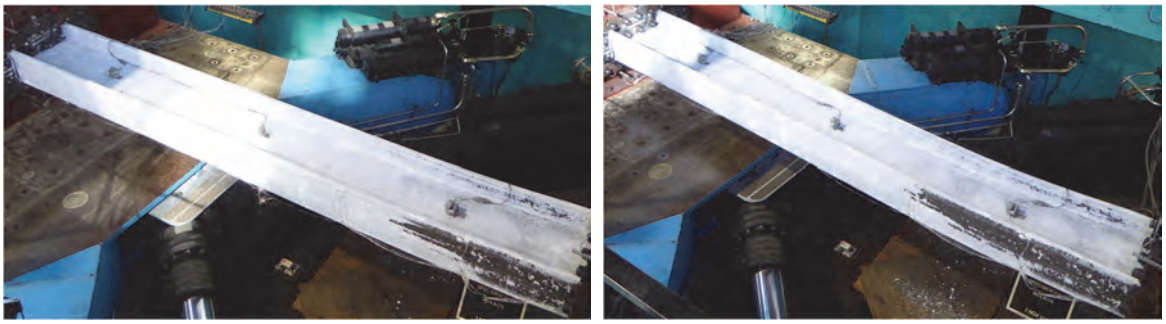

(c) *SDA* = 0.015 rad (d) *SDA* = 0.02 rad

Figure 5.11 Specimen 11H-BC: Overall Yielding and Buckling Progression

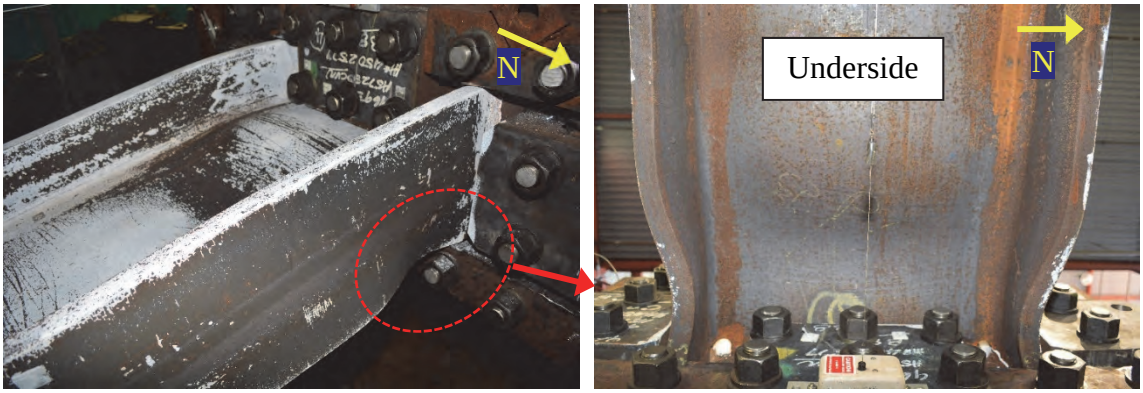

Figure 5.12 Specimen 11H-BC: LTB-Induced Flange Local Buckling at End of Test (West End)

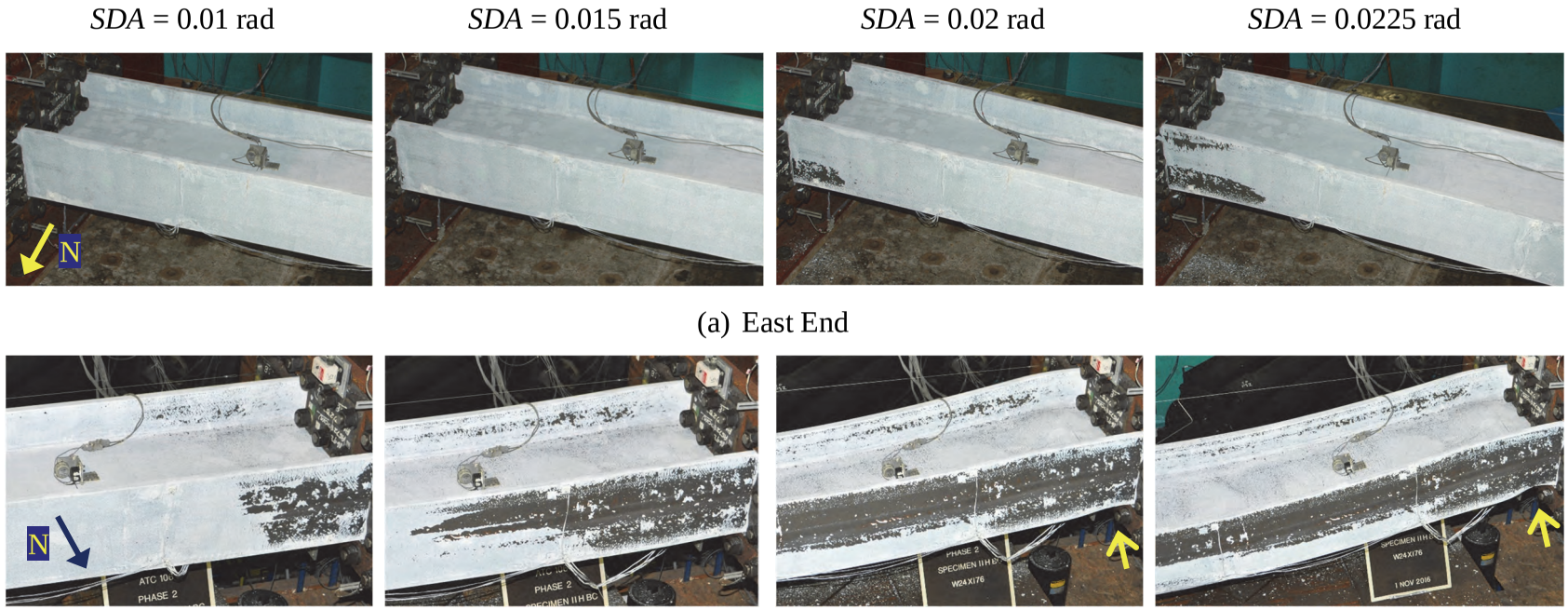

(a) East End

(b) West End

Figure 5.13 Specimen 11H-BC: Yielding and Buckling Progression at Member Ends

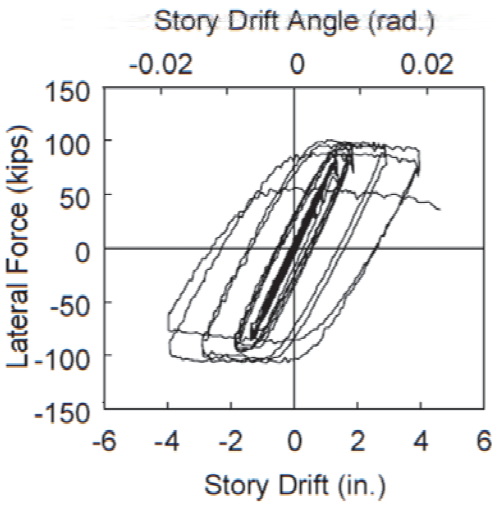

(a) Lateral Force vs. *SDA*

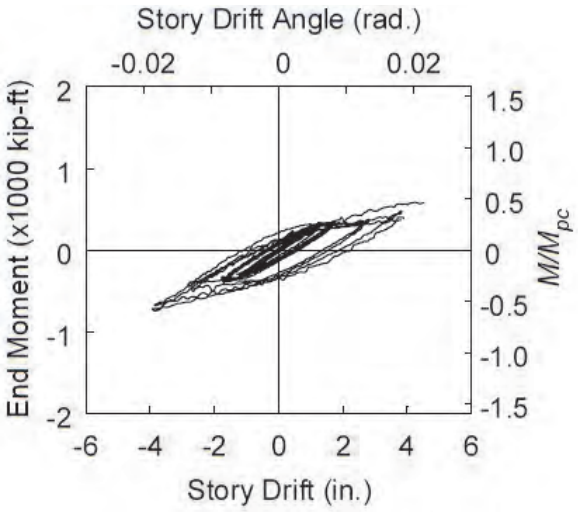

(b) East End Moment vs. *SDA*

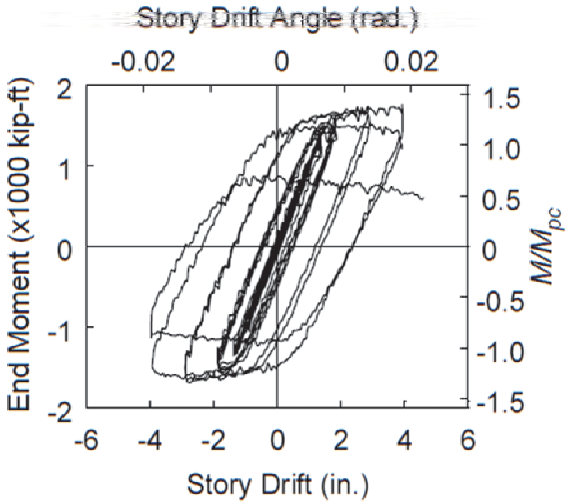

(c) West End Moment vs. *SDA*

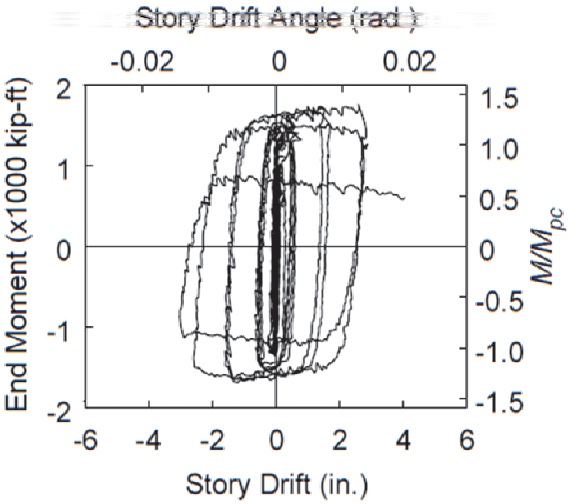

(d) West End Moment vs. Plastic *SDA*

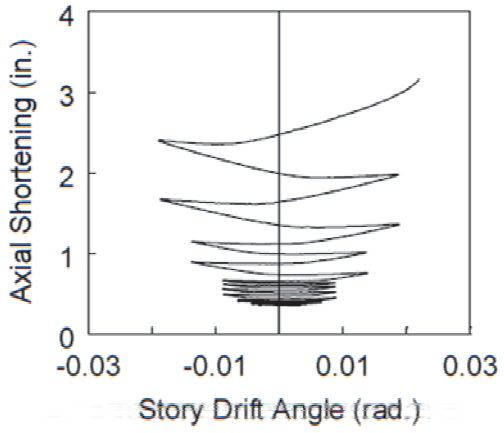

(e) Axial Shortening vs. *SDA*

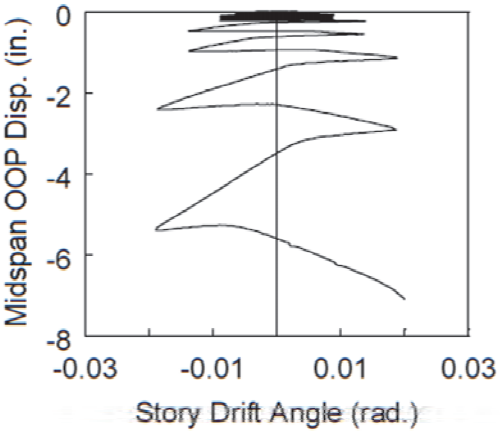

(f) Midspan OOP Disp. vs. *SDA*

Figure 5.14 Specimen 11H-BC: Global Responses

5.3 Group 12 Specimens: Section W30×261

5.3.1 General

Two W30×261 specimens were tested in Group 12; the width-thickness slenderness of this shape was very similar to that of W24×176 shape of Group 1 (and 11) specimens. The objective was to evaluate the effects of (1) section depth, and (2) loading type (cyclic vs. monotonic) on the buckling mode. Regarding the second objective, Specimen 12LM was subjected to the AISC loading protocol, while Specimen 12LM-P was loaded monotonically. Fixed-fixed boundary conditions were imposed on both specimens.

Group 12 specimens (W30×261) were the heaviest section tested in Phase 2A. The SRMD platen at its operational maximum capacity could only apply an axial load equal to 30 % of the member yield strength. Therefore, Specimens 12LM and 12LM-P were tested with C_a equal to 0.3 and named accordingly ("LM" indicated the average between the low- and medium-level axial compression).

5.3.2 Specimen 12LM

Specimen 12LM was initially subjected to 1,386 kips [6,165 kN] (C_a=0.4) axial compression. After completing 0.75 % drift cycles, the axial load was reduced to 1,040 kips [4,626 kN] (C_a=0.3) due to limitations of the shake table. Yielding and buckling progression is illustrated in Figure 5.15 and Figure 5.16. The sloped flaking pattern in the column flange, especially at the east end, was obvious at 1.5 % drift [see Figure 5.16(a)]. Web and flange local buckling were not obvious until 3 % drift was reached. A slight twisting motion in the specimen was also observed during the 2 % and 3 % drift cycles, indicating a tendency of LTB. The test was terminated after completing the 3 % drift cycles due to excessive web local buckling. At the end of the test, relatively limited yielding and the ALB pattern were observed at each column end.

Figure 5.17 shows the global responses. Flexural strength degraded slightly during the 3 % drift cycles corresponding to the development of local buckling in the plastic hinge regions. Axial shortening grew moderately during the 2 % drift cycles and drastically during the 3 % drift cycles as the amplitudes of local buckling increased.

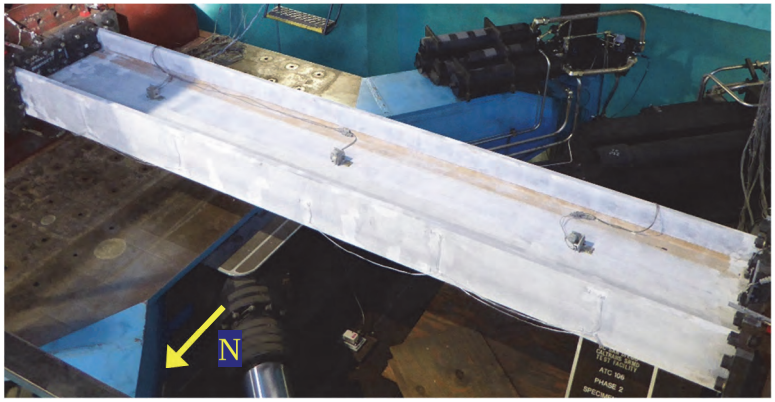

(a) *SDA* = 0.01 rad

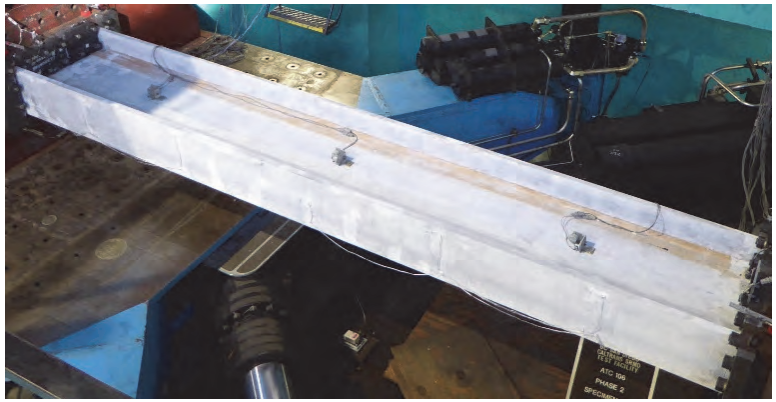

(b) *SDA* = 0.015 rad

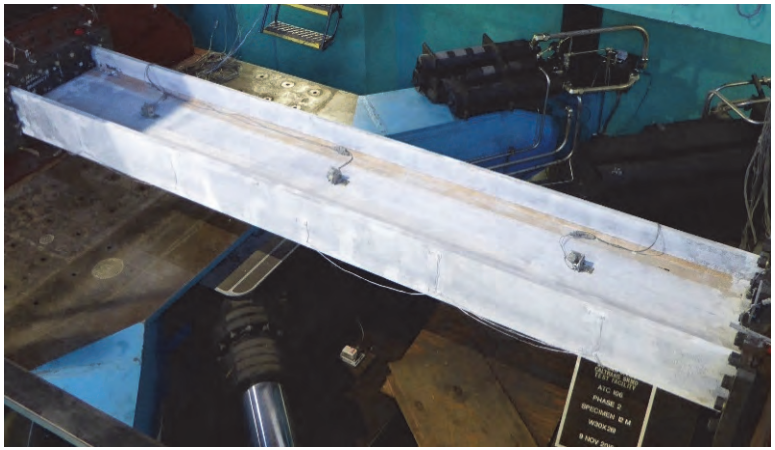

(c) *SDA* = 0.02 rad

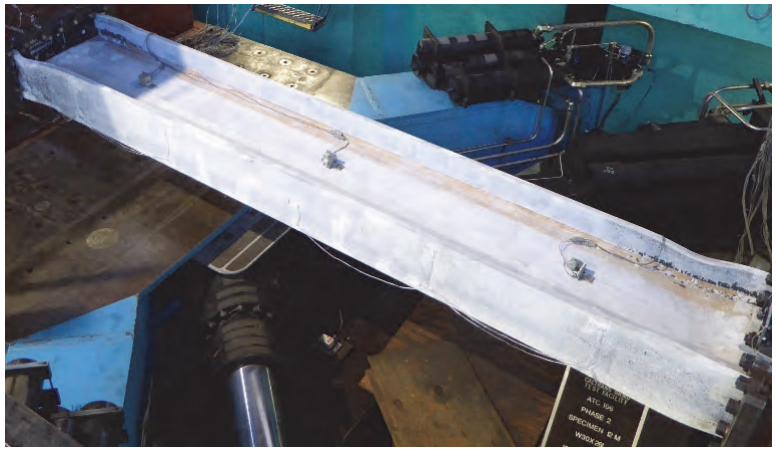

(d) *SDA* = 0.03 rad

Figure 5.15 Specimen 12LM: Overall Yielding and Buckling Progression

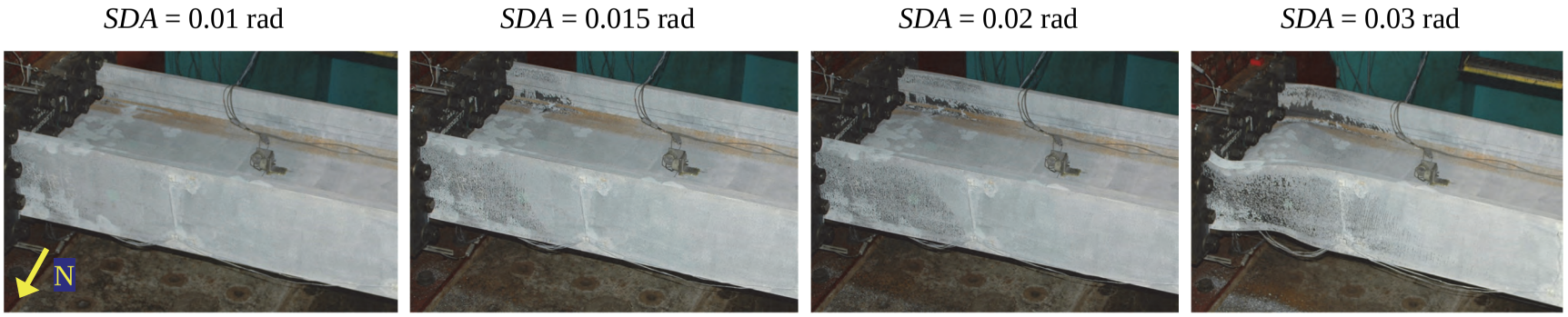

(a) East End

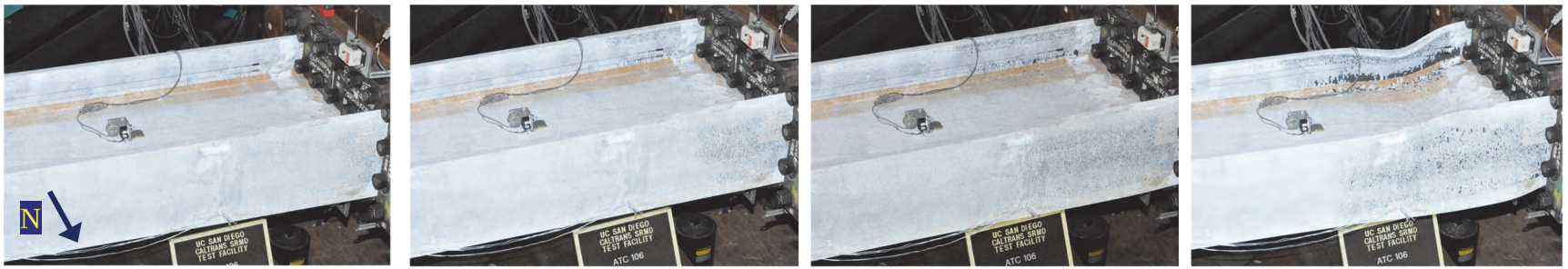

(b) West End

Figure 5.16 Specimen 12LM: Yielding and Buckling Progression at Member Ends

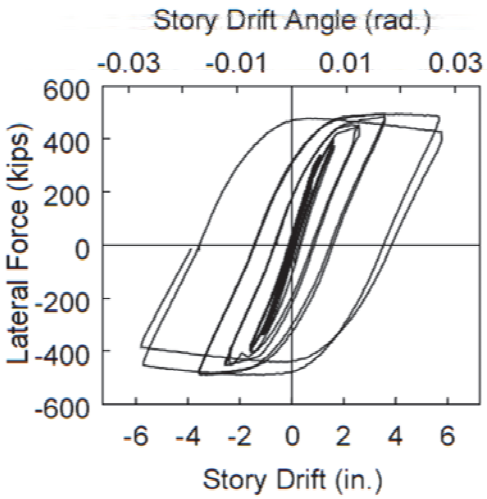

(a) Lateral Force vs. *SDA*

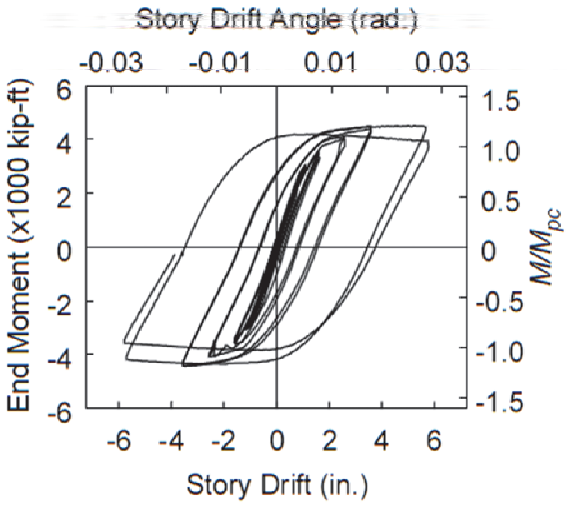

(b) End Moment vs. *SDA*

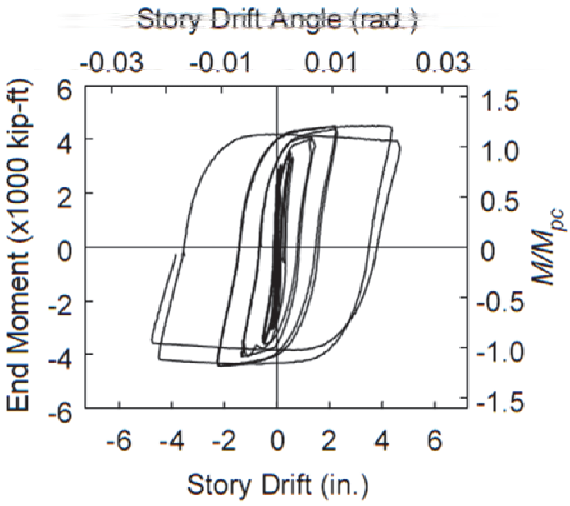

(c) End Moment vs. Plastic *SDA*

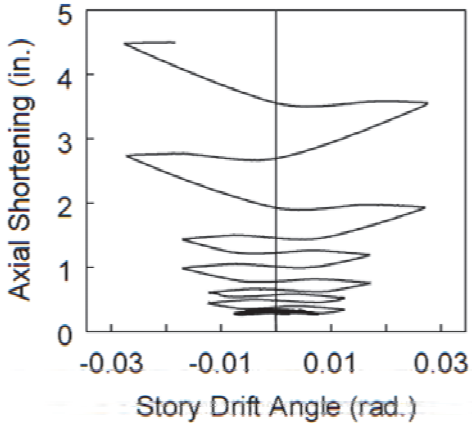

(d) Axial Shortening vs. *SDA*

Figure 5.17 Specimen 12LM: Global Responses

5.3.3 Specimen 12LM-P

This specimen was monotonically loaded to 11 % drift, at which point its flexural strength only degraded by 20 %. Figure 5.18 to Figure 5.20 illustrate yielding and buckling progression. At 6 % drift, web and flange local buckling were observed at both ends, which became obvious at 7 % drift. Only the flanges under compression buckled; tension flanges only yielded. In cyclic testing, web local buckling formed orthogonally to the longitudinal axis of the member with its apex at the mid-depth of the section. In contrast, web local buckling in this specimen exhibited an inclined shape with its apex toward the flange that buckled as shown in Figure 5.21.

Figure 5.22 shows the global responses. Flexural strength began to degrade after 6 % drift corresponding to the onset of local buckling. The axial shortening rate appeared to be relatively constant throughout the test.

5.3.4 Concluding Remarks

The deeper and stocky Specimen 12LM was predicted to experience CB under cyclic loading. Although tendency for such failure mode was evident from the sloped flaking pattern, ALB dominated later.

(a) *SDA* = 0.01 rad (b) *SDA* = 0.015 rad (c) *SDA* = 0.02 rad

(d) *SDA* = 0.03 rad (e) *SDA* = 0.04 rad (f) *SDA* = 0.05 rad

Figure 5.18 Specimen 12LM-P: Overall Yielding and Buckling Progression

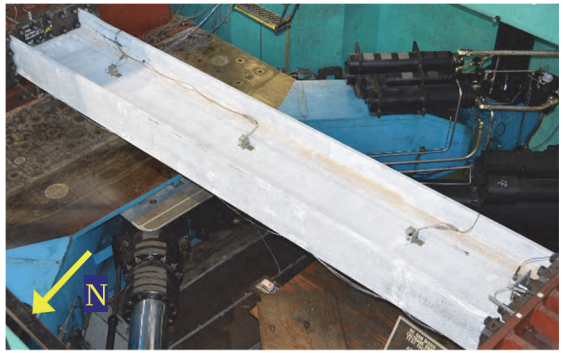

(g) *SDA* = 0.06 rad

(h) *SDA* = 0.07 rad

(i) *SDA* = 0.08 rad

(j) *SDA* = 0.09 rad

(k) *SDA* = 0.10 rad

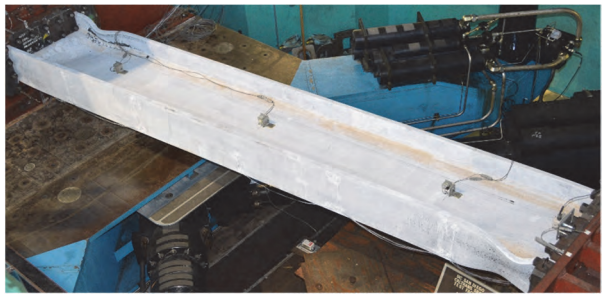

(l) *SDA* = 0.11 rad

Figure 5.18 Specimen 12LM-P: Overall Yielding and Buckling Progression (continued)

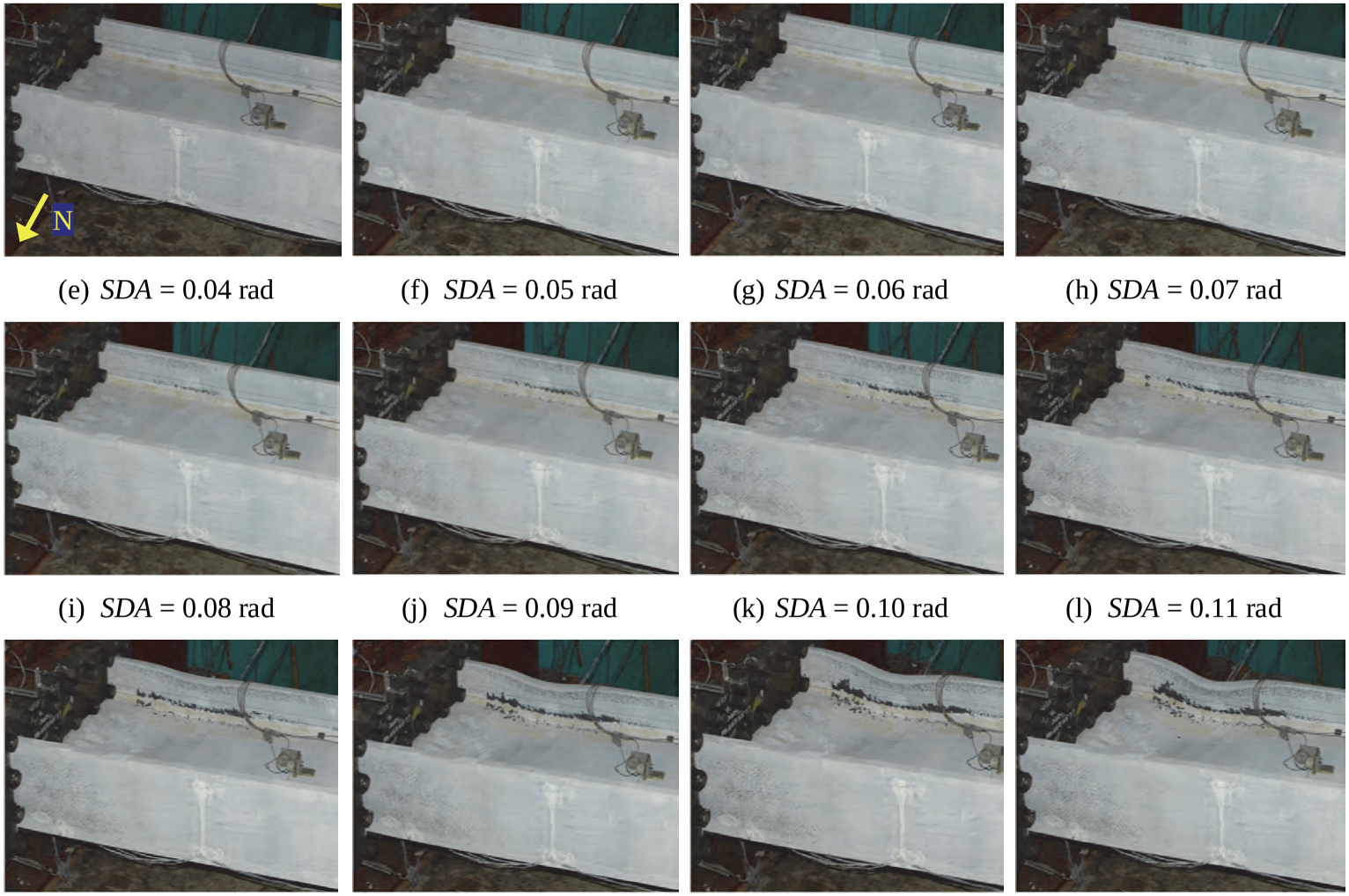

Figure 5.19 Specimen 12LM-P: Yielding and Buckling Progression at Member East End

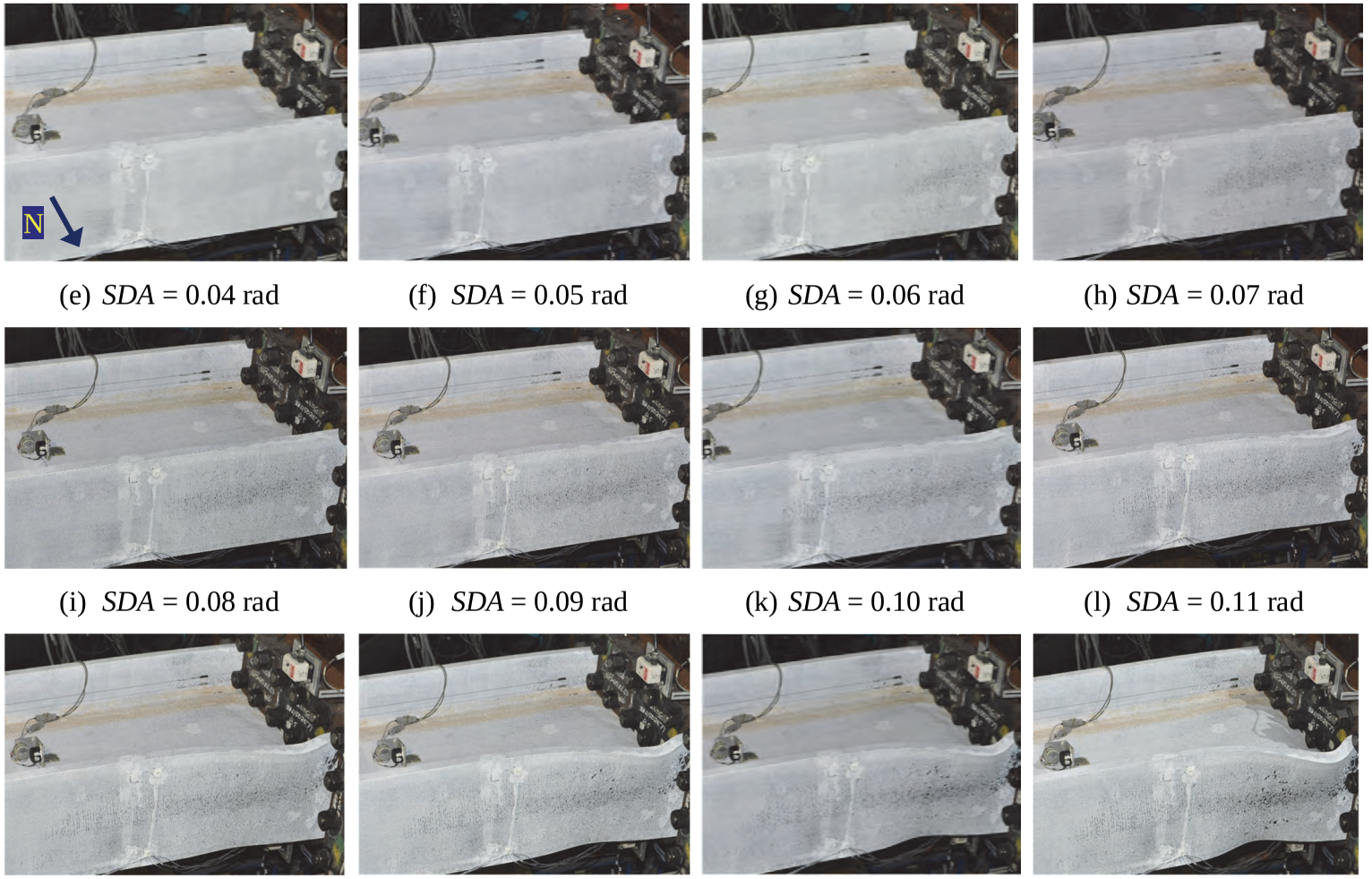

Figure 5.20 Specimen 12LM-P: Yielding and Buckling Progression at Member West End

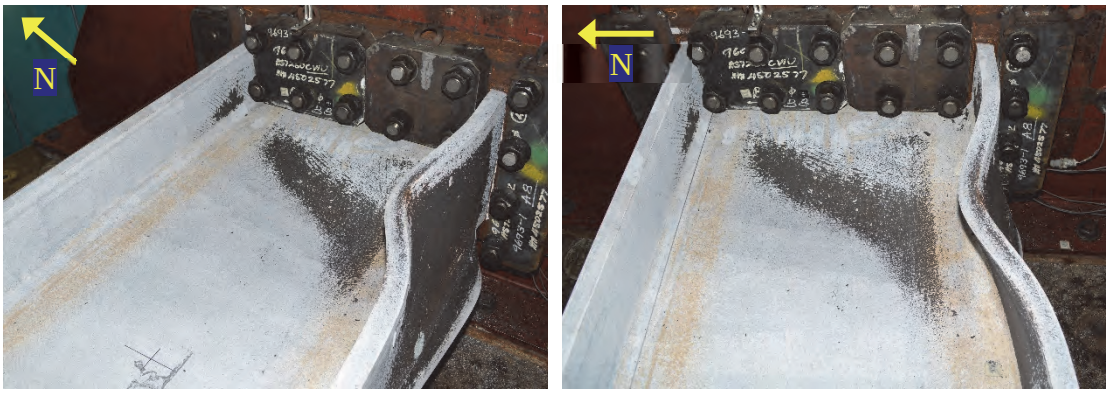

(a) East End

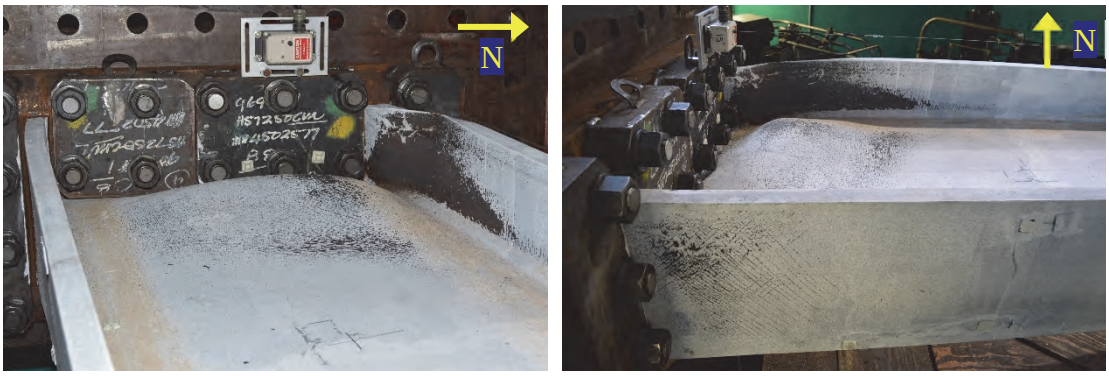

(b) West End

Figure 5.21 Specimen 12LM-P: Local Buckling at End of Test

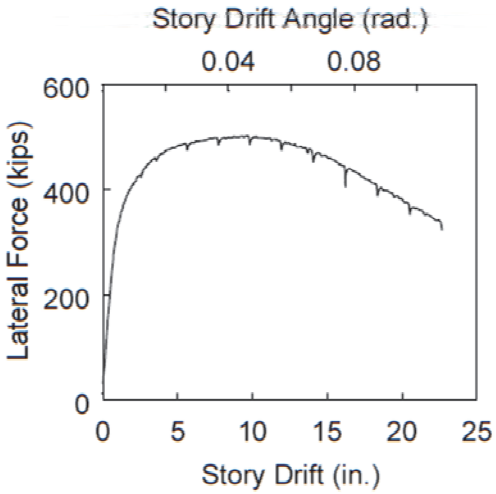

(a) Lateral Force vs. *SDA*

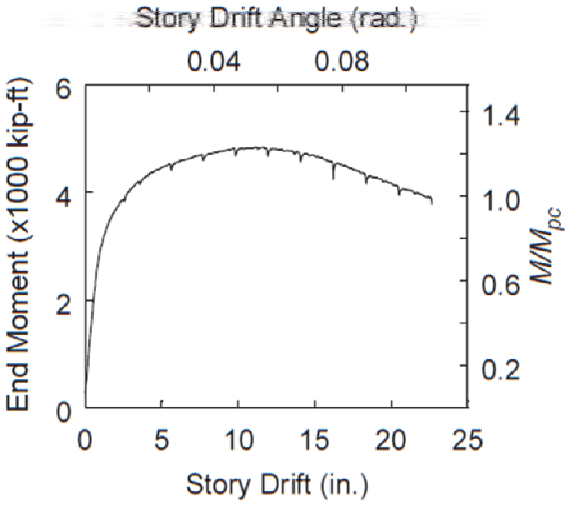

(b) End Moment vs. *SDA*

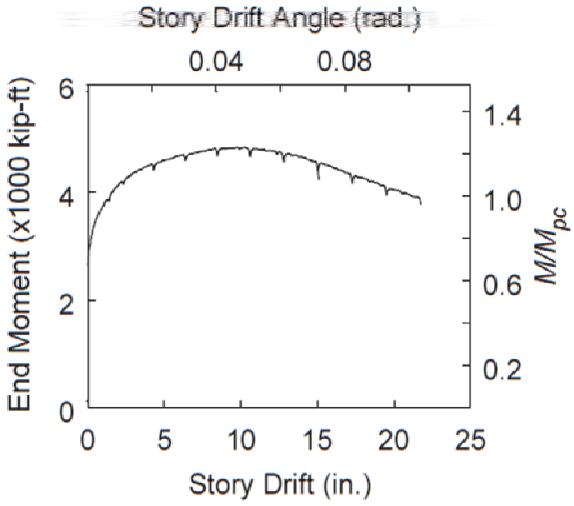

(c) End Moment vs. Plastic *SDA*

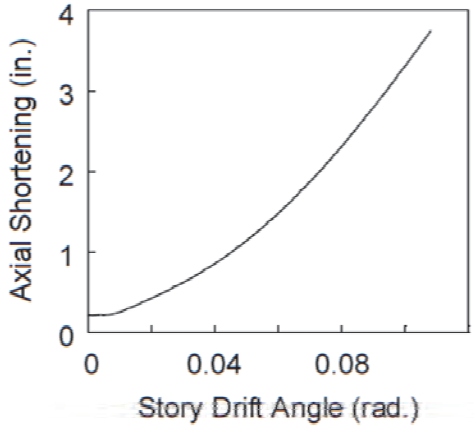

(d) Axial Shortening vs. *SDA*

Figure 5.22 Specimen 12LM-P: Global Responses

5.4 Group 13 Specimens: Section W30×173

5.4.1 General

Web and flange slenderness of Group 13 specimens was similar to that of Group 2 specimens with W24×131 section, which experienced the ALB failure mode. Test results from these groups were compared to study the effect of section depths on column inelastic cyclic responses involving in-plane plastic hinging. To investigate boundary condition effect, Specimens 13M and 13M-BC were subjected to fixed-fixed and fixed-rotating boundary conditions, respectively. Loading sequence of the latter boundary condition test was discussed in Section 4.5. Both specimens were subjected to constant axial compression with $C_a = 0.4$.

5.4.2 Specimen 13M

Specimen 13M exhibited the ALB failure mode; Figure 5.23 and Figure 5.24 depict yielding and buckling progression. Web and flange local buckling were first observed at both ends at 1 % drift. The buckled elements underwent larger deformation at 1.5 % drift, forming plastic hinges at the column ends. No out-of-plane, LTB-type motion was observed. Yield length was much shorter than that observed in testing of Group 11 specimens, which experienced the CB mode. Due to excessive web local buckling, the test was terminated after completing the positive excursion of the second 1.5 % drift cycle.

Figure 5.25 shows the global responses. Flexural strength degradation began during the 1 % drift cycles corresponding to the onset of web and flange local buckling. The specimen lost its flexural capacity rapidly, decreasing to 75 % of its maximum moment capacity after four cycles of 1 % drift. The onset of web and flange local buckling also triggered significant axial shortening, which continued to grow in proportion to the amplitudes of local buckling.

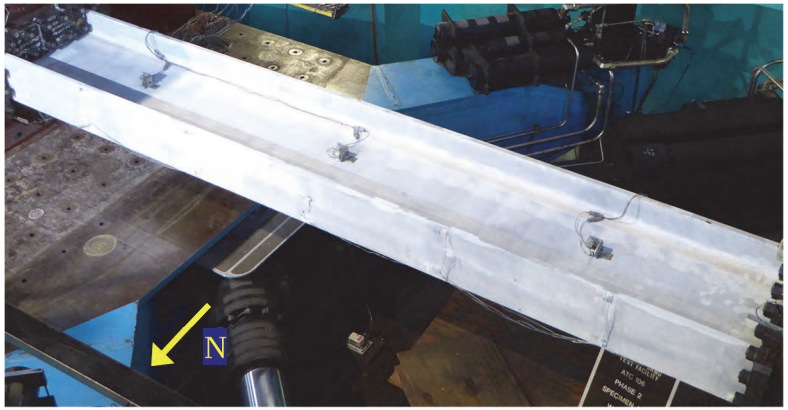

(a) *SDA* = 0.005 rad

(b) *SDA* = 0.0075 rad

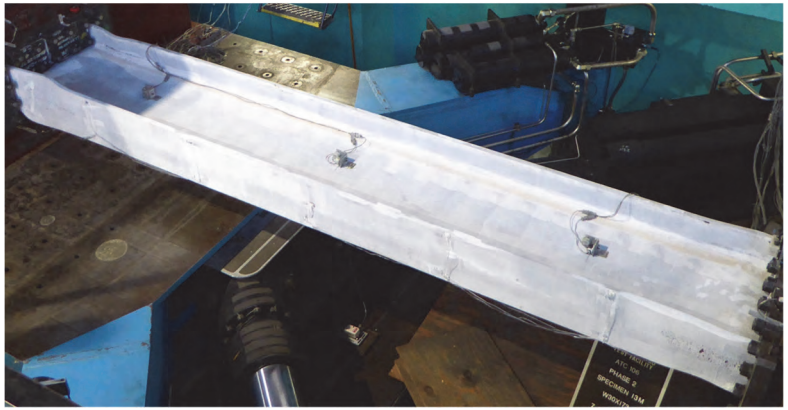

(c) *SDA* = 0.01 rad

(d) *SDA* = 0.015 rad

Figure 5.23 Specimen 13M: Overall Yielding and Buckling Progression

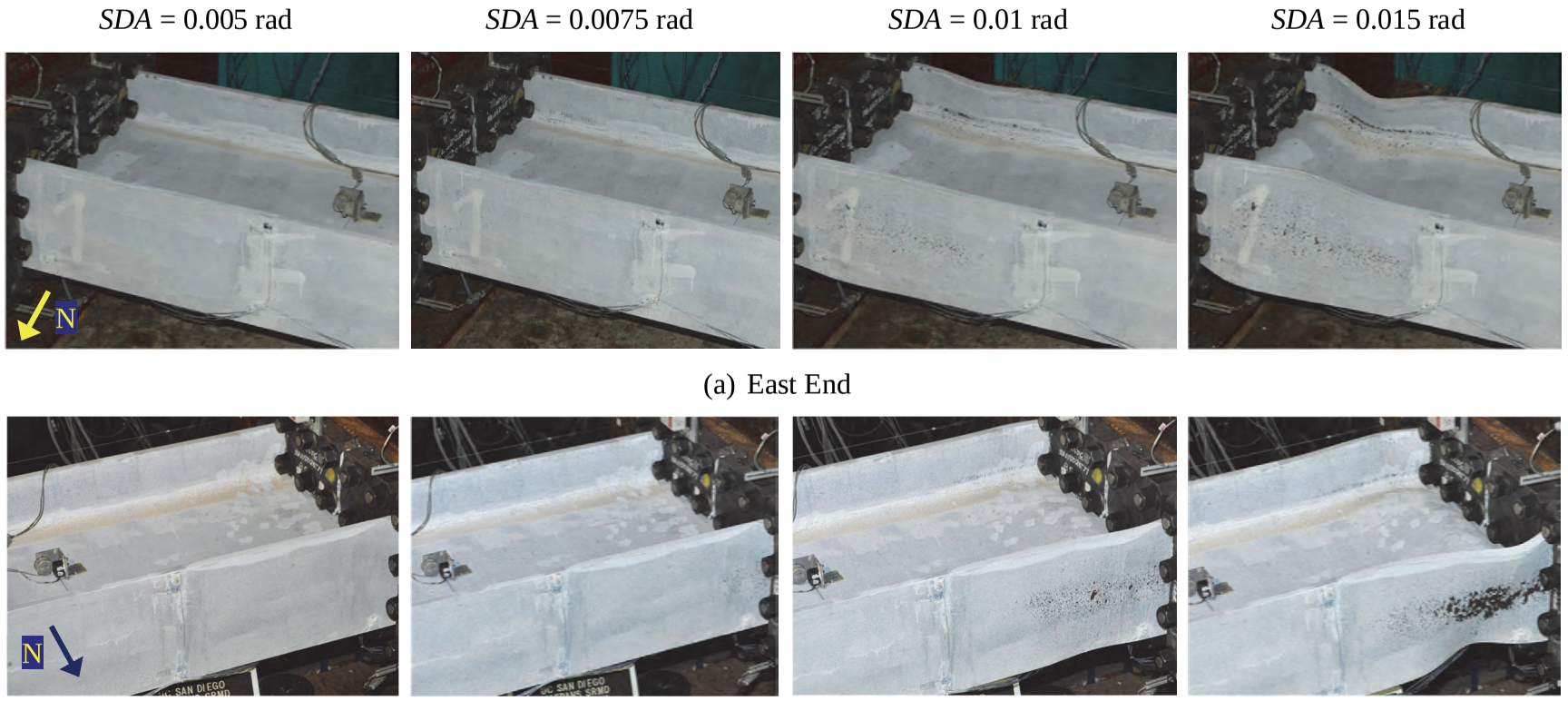

(a) East End

(b) West End

Figure 5.24 Specimen 13M: Yielding and Buckling Progression at Member Ends

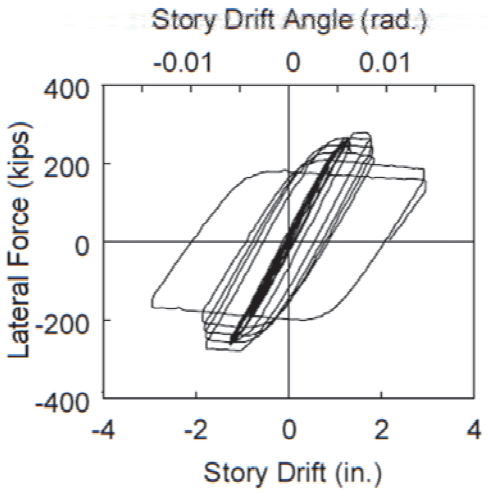

(a) Lateral Force vs. *SDA*

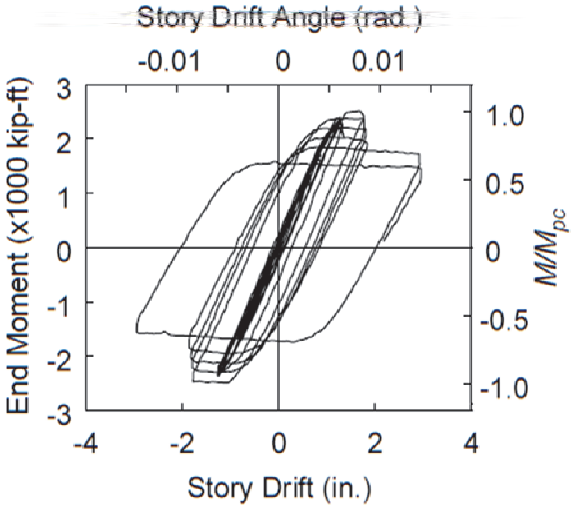

(b) End Moment vs. *SDA*

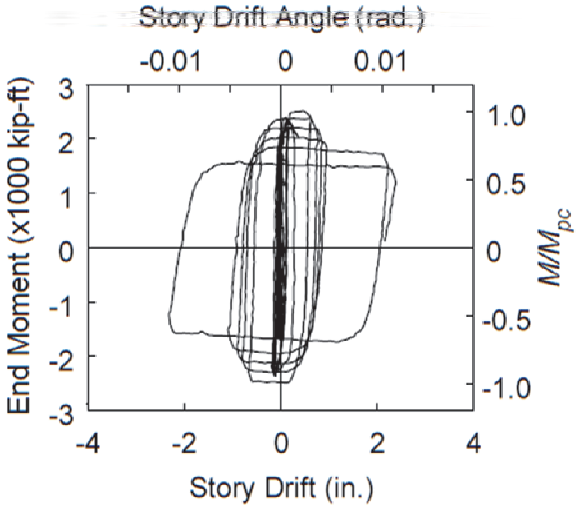

(c) End Moment vs. Plastic *SDA*

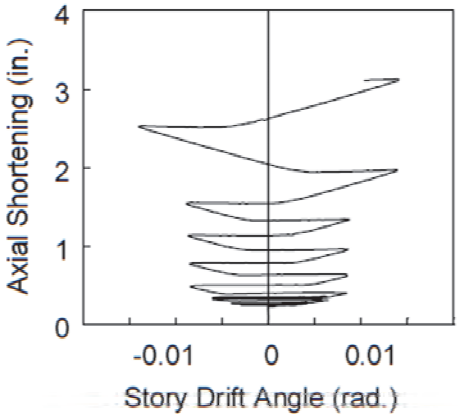

(d) Axial Shortening vs. *SDA*

Figure 5.25 Specimen 13M: Global Responses

5.4.3 Specimen 13M-BC

Like Specimen 13M, Specimen 13M-BC experienced the ALB failure mode. Neither plastic deformation nor local buckling occurred at the east (or rotating) end. In contrast, web and flange local buckling initiated at the west (or fixed) end at 1.5 % drift as demonstrated in Figure 5.26 and Figure 5.27; the ALB configuration was observed. LTB behavior of the specimen did not occur.

Figure 5.28 illustrates the global responses. Entering 1.5 % drift, flexural strength of the specimen began to degrade corresponding to the onset of local buckling at the west end; it reduced to 62 % of the maximum flexural strength after completing two cycles at 1.5 % drift. In addition, the formation of local buckles triggered a rapid increase in axial shortening during the 1.5 % drift cycles and beyond.

In comparison, Specimens 13M and 13M-BC experienced ALB at 1 % and 1.5 % drift, respectively. This demonstrated the effect of the fixed-rotating boundary conditions; the applied end rotation helped relieving some of the flexural demand that would have been produced with fixed-fixed boundary conditions at the same drift level. As a result, the specimen with fixed-rotating boundary conditions could withstand larger story drifts before it failed. Despite this difference, the global responses of Specimen 13M-BC had a similar characteristic to those of Specimen 13M.

5.4.4 Concluding Remarks

As predicted, ALB was the failure mode although the depth of this W30 section was larger than that of Group 2 specimens (W24) tested in Phase 1. Allowing one end of the column to rotate produced plastic hinging at one end (i.e., fixed end) only, but it did not alter the governing buckling mode.

(a) *SDA* = 0.0075 rad

(b) *SDA* = 0.01 rad

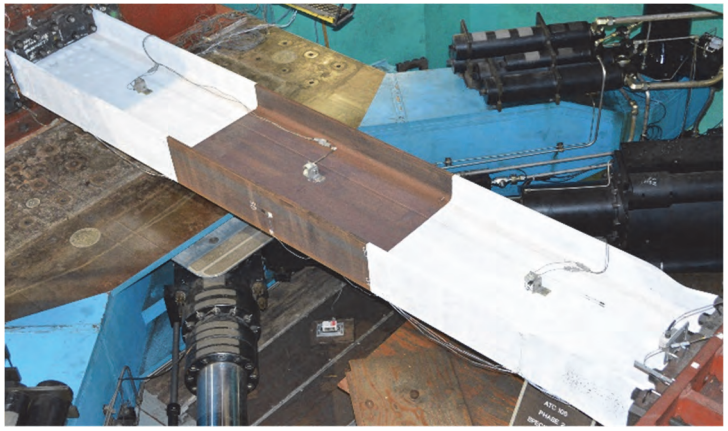

(c) *SDA* = 0.015 rad

(d) *SDA* = 0.02 rad

Figure 5.26 Specimen 13M-BC: Overall Yielding and Buckling Progression

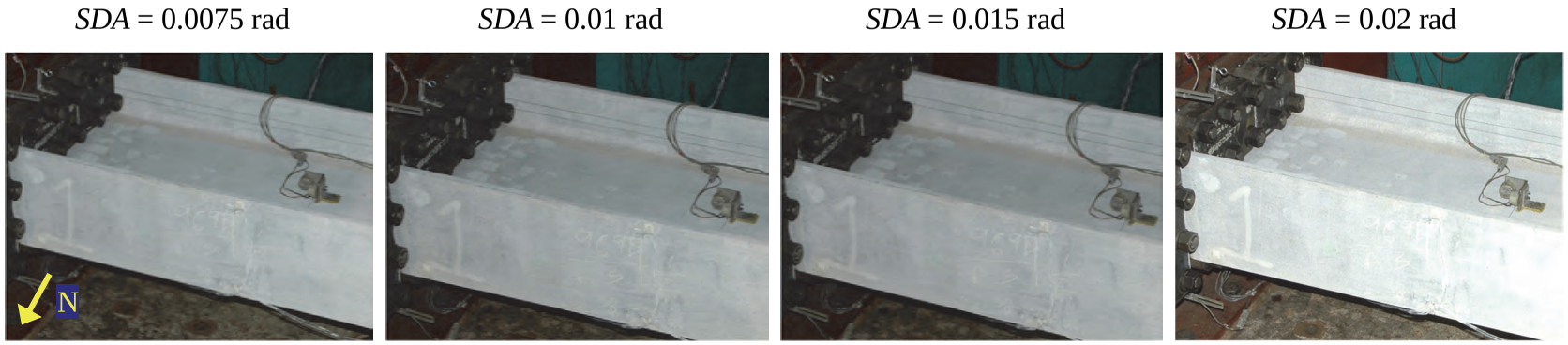

(a) East End

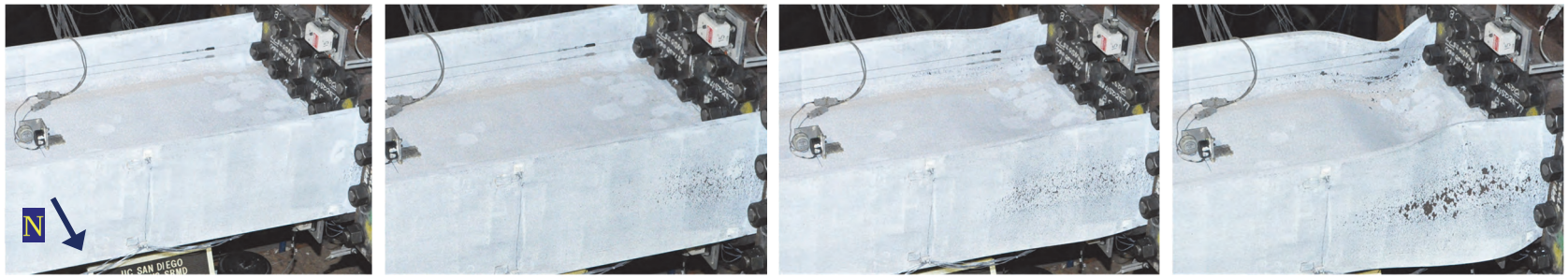

(b) West End

Figure 5.27 Specimen 13M-BC: Yielding and Buckling Progression at Member Ends

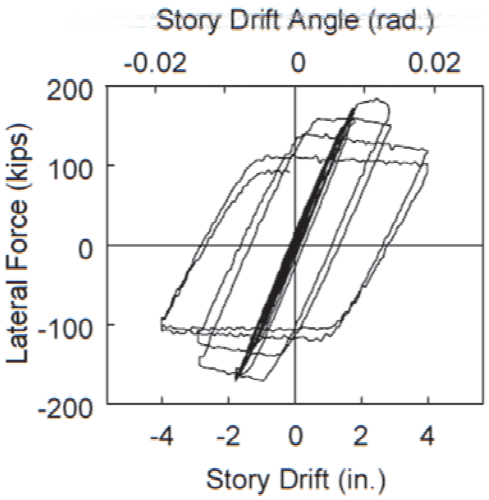

(a) Lateral Force vs. *SDA*

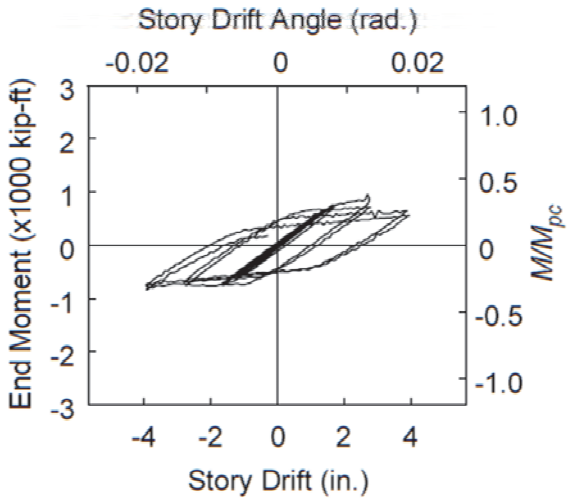

(b) East End Moment vs. *SDA*

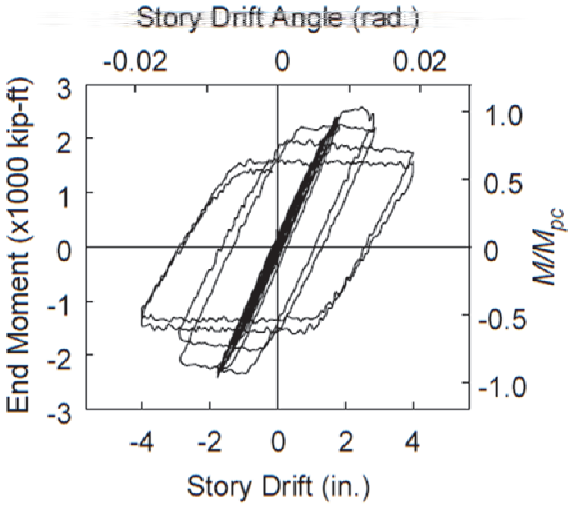

(c) West End Moment vs. *SDA*

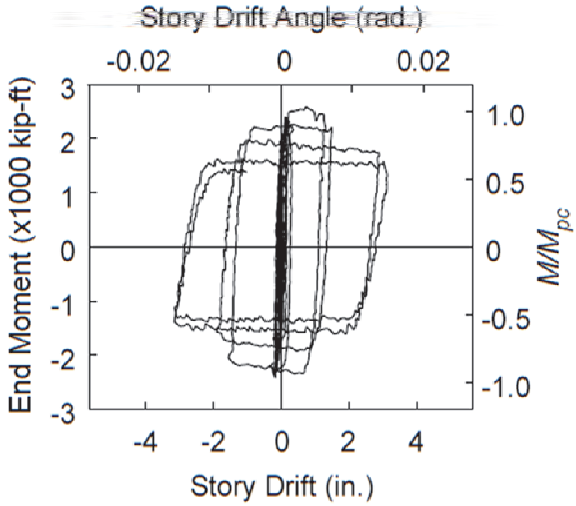

(d) West End Moment vs. Plastic *SDA*

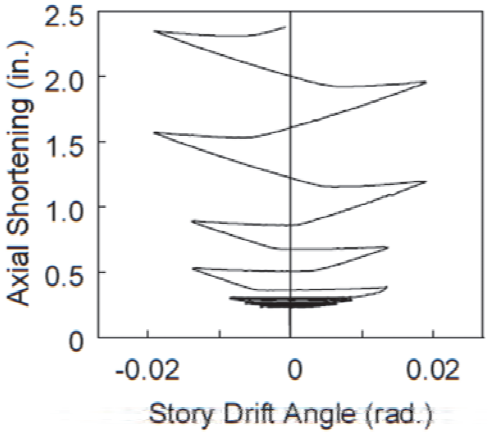

(e) Axial Shortening vs. *SDA*

Figure 5.28 Specimen 13M-BC: Global Responses

5.5 Group 14 Specimen: Section W30×90

5.5.1 General

In Phase 1 testing, all three Group 5 specimens with W24×55 section experienced elastic LTB due to their high member slenderness ($L/r_y = 161$). Thus, the plastic deformation capacity associated with their section slenderness properties (i.e., moderately ductile web and highly ductile flange) could not be evaluated. Group 14 specimen with W30×90 section had similar web slenderness but larger flange slenderness compared to those of Group 5 specimens (see Figure 2.4). L/r_y ratio ($= 101$) of the former was also much lower than that of Group 5 specimens, making it less prone to elastic LTB. Specimen 14L was subjected to constant axial compression with $C_a = 0.2$ and fixed-fixed boundary conditions.

5.5.2 Test Results

Specimen 14L exhibited the ALB failure mode; yielding and buckling progression is illustrated in Figure 5.29 and Figure 5.30. Web and flange local buckling developed at the east ends at 1 % drift but was not apparent at the west end until 1.5 % drift was reached. Local buckling at both ends showed the ALB pattern. An out-of-plane movement was not observed during the test. The test was terminated due to excessive local buckling in the plastic hinge regions after completing the 2 % drift cycles.

Figure 5.31 shows the global responses. Flexural strength degradation corresponding to the onset of web and flange local buckling was apparent during 1 % drift; the flexural strength reduced to 80 % of the maximum value after four cycles at 1 % drift were completed. Local buckling at both ends triggered significant axial shortening during the 1.5 % and 2 % drift cycles as shown in Figure 5.31(d).

5.5.3 Concluding Remarks

This specimen showed the predicted ALB mode. Compared to Group 5 specimens tested in Phase 1, reducing the L/r_y ratio from 161 to 101 was successful to preclude elastic LTB of this moderately ductile column that experienced in-plane hinging.

(a) *SDA* = 0.0075 rad

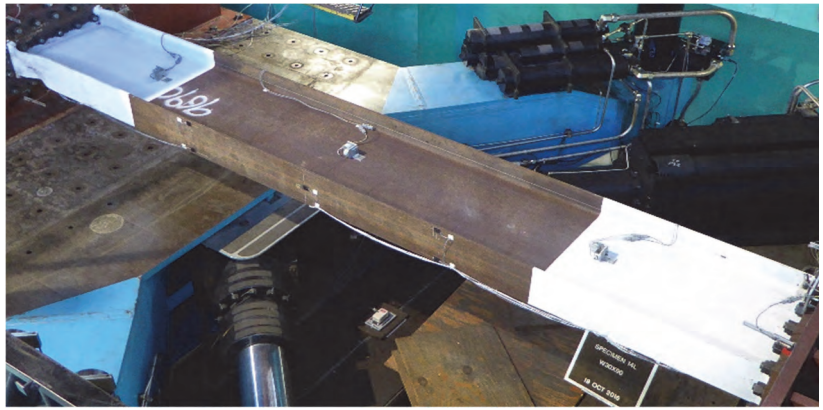

(b) *SDA* = 0.01 rad

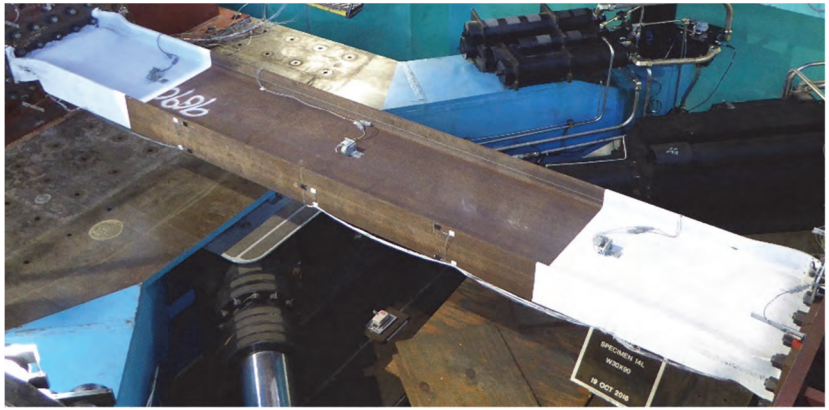

(c) *SDA* = 0.015 rad

(d) *SDA* = 0.02 rad

Figure 5.29 Specimen 14L: Overall Yielding and Buckling Progression

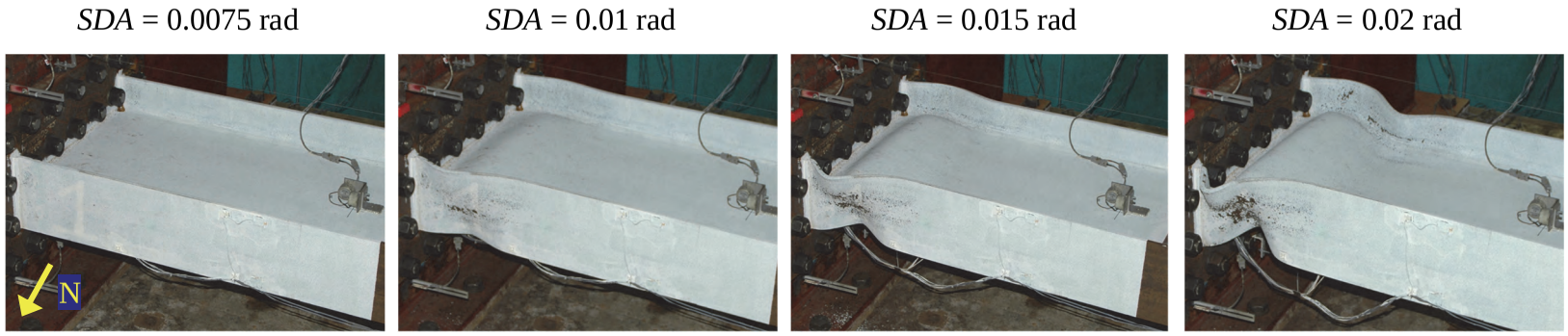

(a) East End

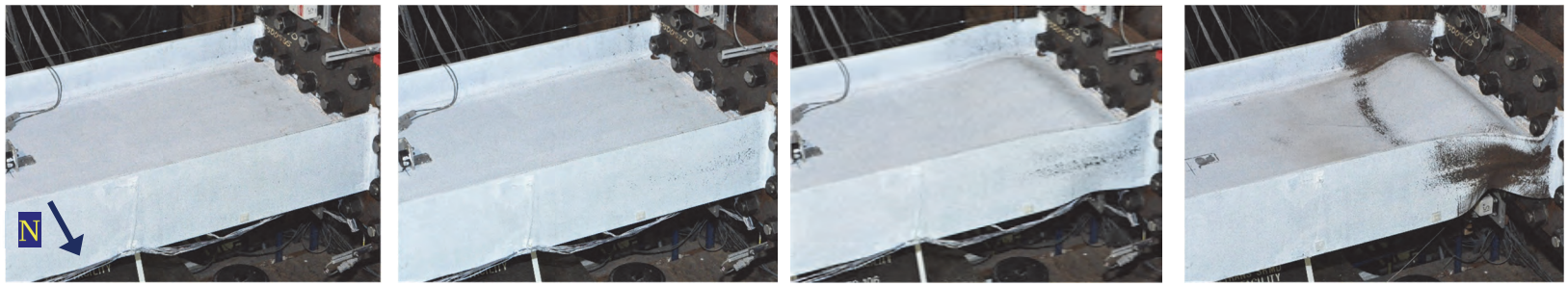

(b) West End

Figure 5.30 Specimen 14L: Yielding and Buckling Progression at Member Ends

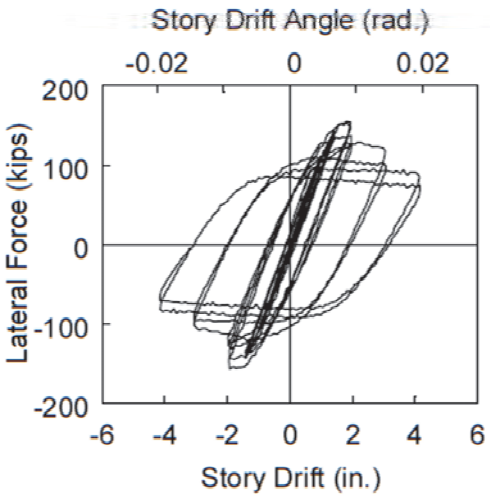

(a) Lateral Force vs. *SDA*

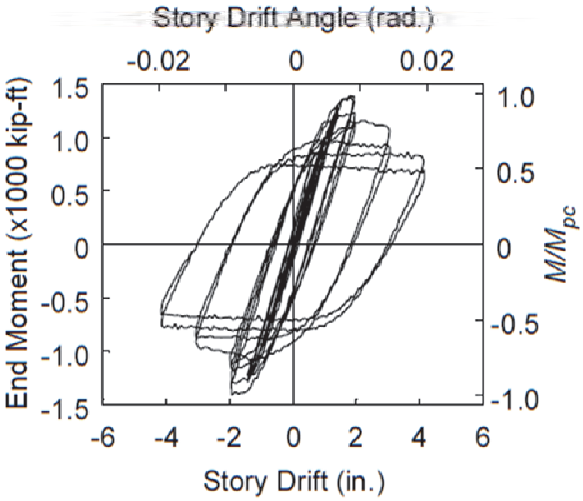

(b) End Moment vs. *SDA*

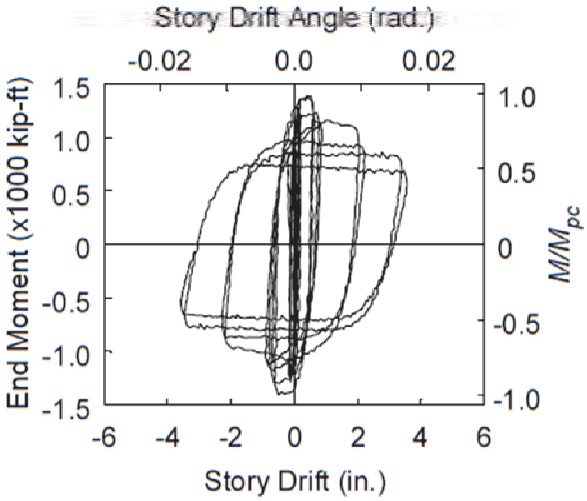

(c) End Moment vs. Plastic *SDA*

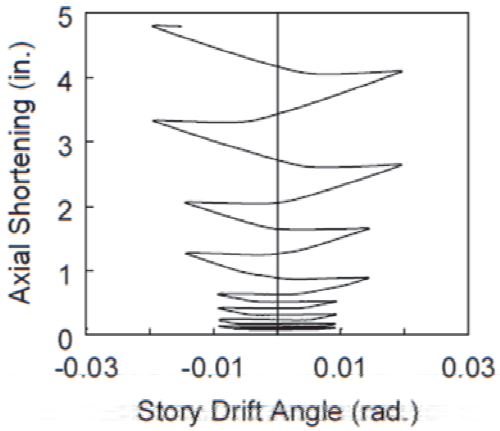

(d) Axial Shortening vs. *SDA*

Figure 5.31 Specimen 14L: Global Responses

5.6 Group 15 Specimen: Section W18×192

5.6.1 General

While Groups 12 to 14 were composed of deeper (W30) sections than those (W24) tested in Phase 1, Groups 15 to 17 were composed of shallower (W18) sections. Group 15 consisted of one W18×192 column (Specimen 15L) with the most compact web and flange elements among all groups (see Figure 2.4). The specimen sustained fixed-fixed boundary conditions and the AISC loading protocol.

5.6.2 Test Results

The governing failure mode of Specimen 15L is CB with the single-curvature out-of-plane buckling configuration; yielding and buckling development is depicted in Figure 5.32 and Figure 5.34. Initially, the specimen sustained 506 kips [2,250 kN] (C_a=0.2) axial compression. Yielding was significant at 3 % drift. At this drift level, prying actions at the end connections were also significant (large gaps between the column end plates and the reaction fixtures were observed). It was a concern that excessive elongation of the pretensioned rods due to the prying actions may lead to rupture of the rods. To mitigate this risk and expedite failure in the specimen, higher axial load ($C_a = 0.4$) was applied for the remaining drift cycles (4 % and 5 % drift cycles). LTB movements were apparent during the 4 % drift cycles and beyond. Local buckling was not observed before the onset of LTB. Since this column section is very stocky, only one LTB-induced flange local buckle was observed at the northwest flange as shown in Figure 5.33. The test was terminated due to the excessive downward displacement of the column during the first positive excursion to 5 % drift. At the end of the test, a CJP weld fracture was observed at the upper edge of both flanges at the west end as shown in Figure 5.33. The tensile stresses at the column flange CJP welds induced by the flanges bending about their strong axis as they moved out of plane contributed to these fractures.

Figure 5.35 shows the global responses. Flexural strength did not degrade significantly during the 4 % drift cycles although considerable LTB motions were observed; the flexural strength only reduced to 85 % of the maximum moment after completing two cycles at 4 % drift. The much compact web and flanges of this specimen helped moderating strength degradation until the end of the 4 % drift cycles. Drastic flexural strength reduction occurred during the 5 % drift positive excursion when the LTB

movements grew significantly. Axial shortening was minimal up to 3 % drift. Upon the onset of LTB at 4 % drift, the column began to shorten more drastically.

5.6.3 Concluding Remarks

The predicted and observed buckling modes (CB) were consistent, indicating that the buckling classification procedure outlined in Section 2.8 was not affected by the section depth.

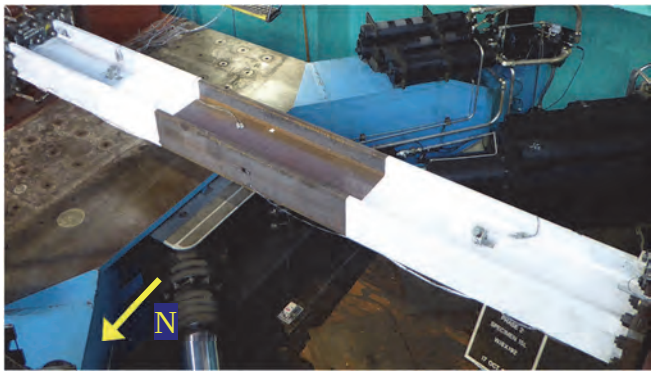

(a) *SDA* = 0.02 rad

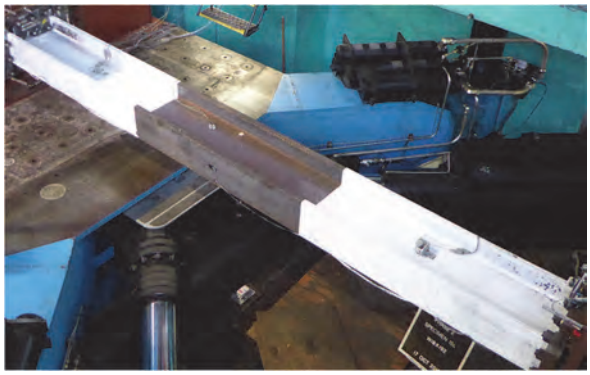

(b) *SDA* = 0.03 rad

(c) *SDA* = 0.04 rad

(d) *SDA* = 0.05 rad

Figure 5.32 Specimen 15L: Overall Yielding and Buckling Progression

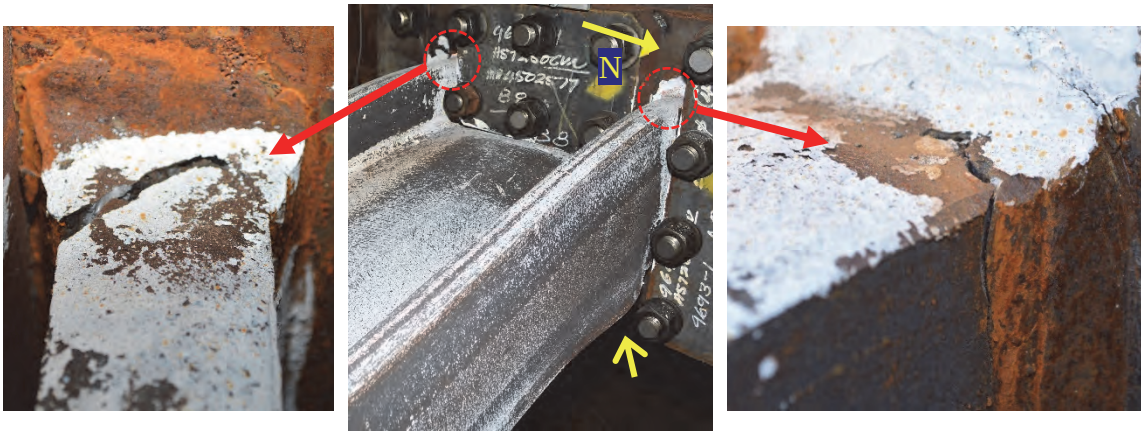

Figure 5.33 Specimen 15L: Column Flange CJP Weld Fracture and LTB-induced Flange Local Buckling at End of Test (West End)

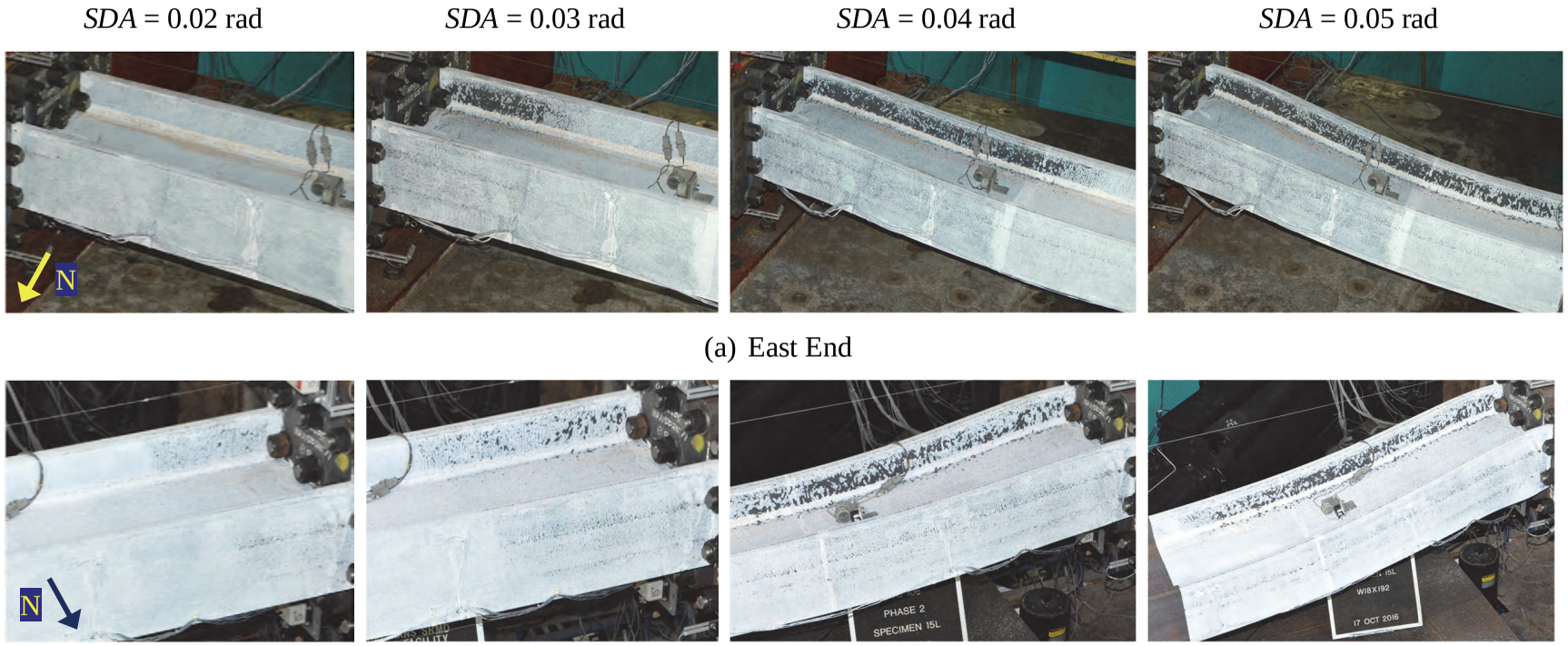

(a) East End

(b) West End

Figure 5.34 Specimen 15L: Yielding and Buckling Progression at Member Ends

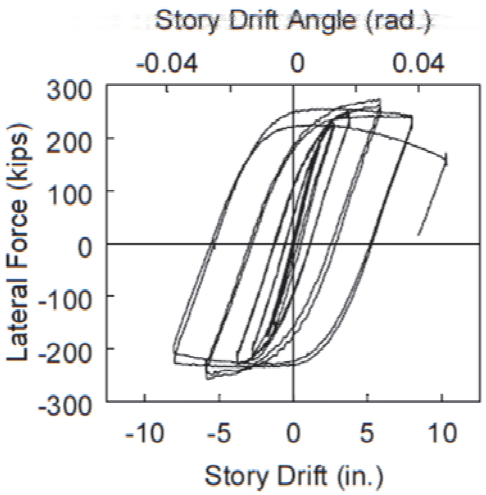

(a) Lateral Force vs. *SDA*

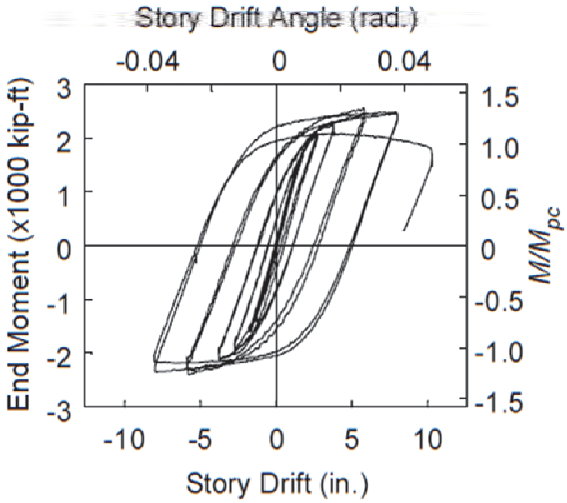

(b) End Moment vs. *SDA*

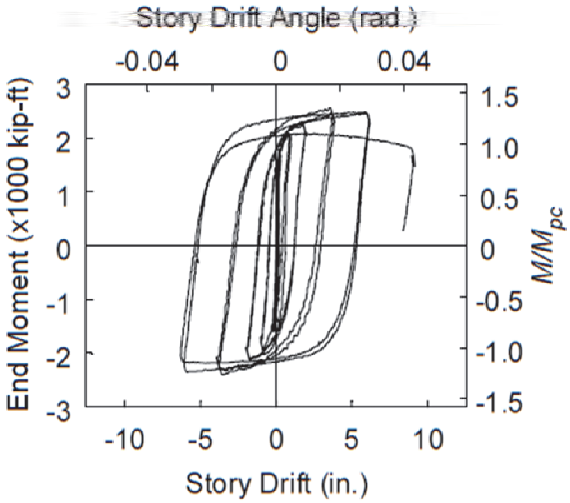

(c) End Moment vs. Plastic *SDA*

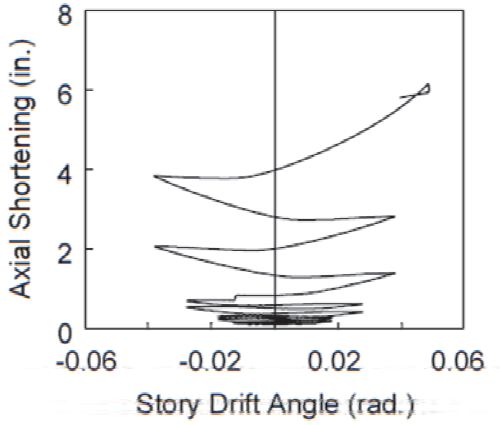

(d) Axial Shortening vs. *SDA*

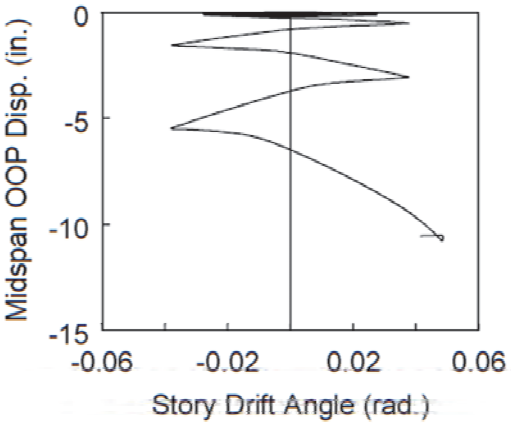

(e) Midspan OOP Disp. vs. *SDA*

Figure 5.35 Specimen 15L: Global Responses

5.7 Group 16 Specimens: Section W18×130

5.7.1 General

Two W18×130 specimens were tested in this group to study the boundary condition and section depth effects; the section had similar slenderness properties to those of Group 1 (and Group 11) specimens. Both specimens were subjected to the AISC loading protocol and constant axial compression with $C_a = 0.4$. For Specimen 16M-BC, the end rotation sequence discussed in Section 4.5 was also applied at the east (or moving) end to simulate rotation at the top end of a first-story column in an SMF. Additional testing of four more specimens with varying axial loads and different loading protocols was conducted in Phase 2B under Group 21; see Section 7.2.

5.7.2 Specimen 16M

The governing failure mode of Specimen 16M is CB with the single-curvature out-of-plane buckling configuration; yielding and buckling progression is shown in Figure 5.36 and Figure 5.37. The sloped flaking pattern was apparent at 1 % drift. At 2 % drift, LTB movements initiated; at 3 % drift, they exacerbated with compression flanges buckling out of plane more during each cycle. This led to a significant downward displacement at the column midspan. Corresponding to this out-of-plane curvature, an LTB-induced flange local buckle formed at each bottom half-width flange at each end (see the arrowed locations in Figure 5.37). The test was terminated due to the excessive downward displacement and significant flexural strength degradation in the specimen.

Figure 5.38 shows the global responses. Flexural strength was stable throughout the 2 % drift cycles even though LTB had initiated in some degree. After completing the first 3 % drift cycle, flexural strength reduced to 86 % of the maximum value despite considerable out-of-plane buckling in the specimen. Very significant flexural strength degradation was observed during the positive excursion of the second 3 % drift cycle, at which point the out-of-plane displacement increased rapidly. As shown in Figure 5.38(d) and Figure 5.38(e) respectively, the column axial shortening history and the out-of-plane displacement history were similar in shape.

(a) *SDA* = 0.01 rad

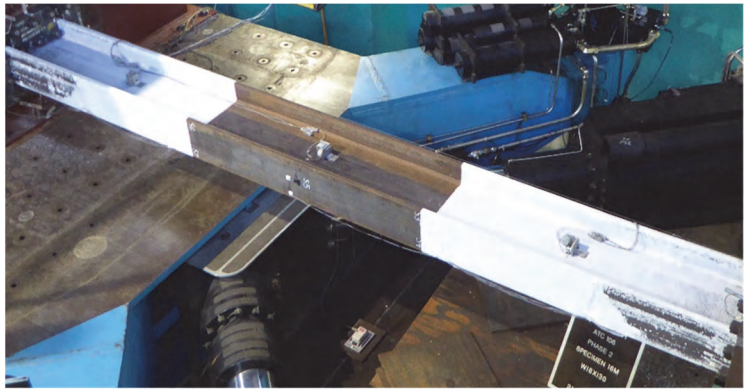

(b) *SDA* = 0.015 rad

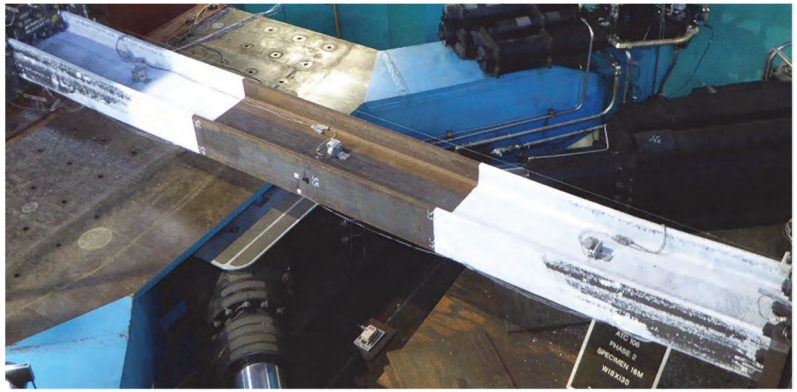

(c) *SDA* = 0.02 rad

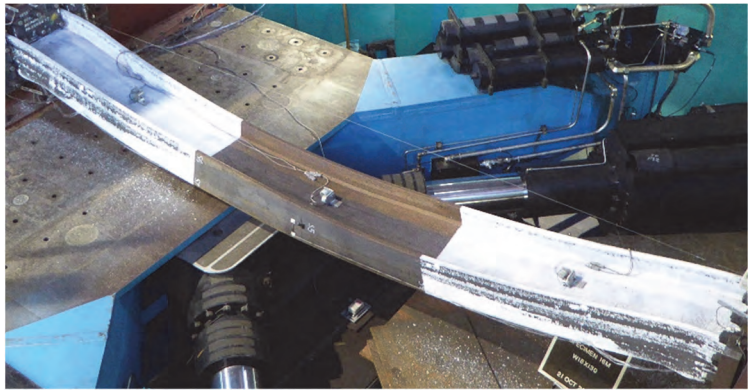

(d) *SDA* = 0.03 rad

Figure 5.36 Specimen 16M: Overall Yielding and Buckling Progression

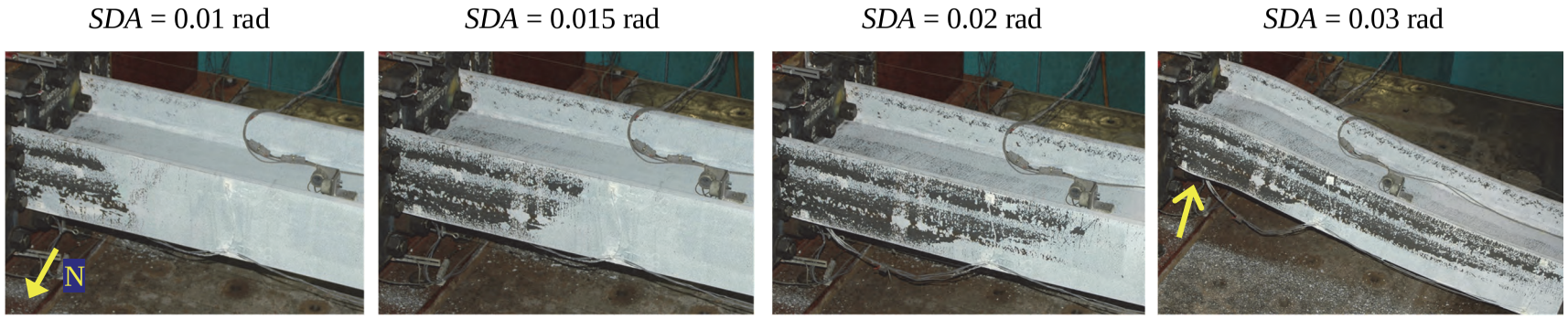

(a) East End

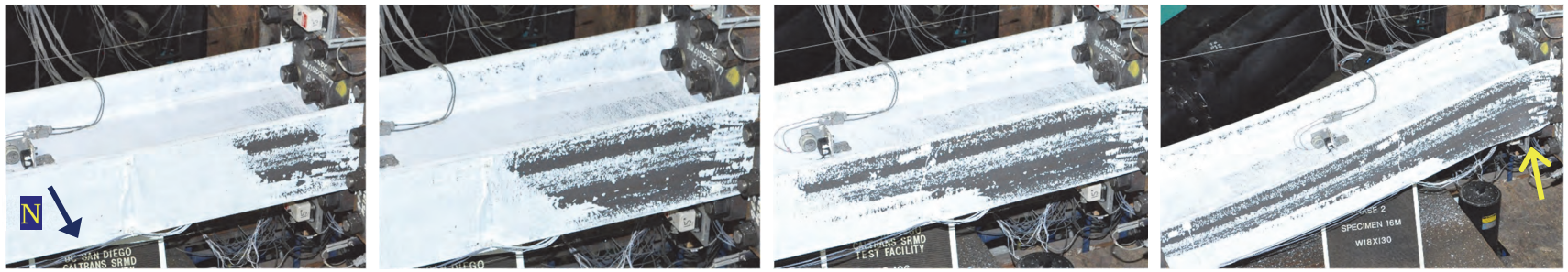

(b) West End

Figure 5.37 Specimen 16M: Yielding and Buckling Progression at Member Ends

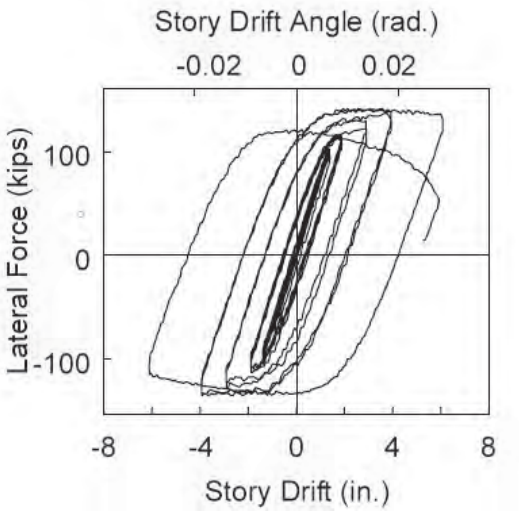

(a) Lateral Force vs. *SDA*

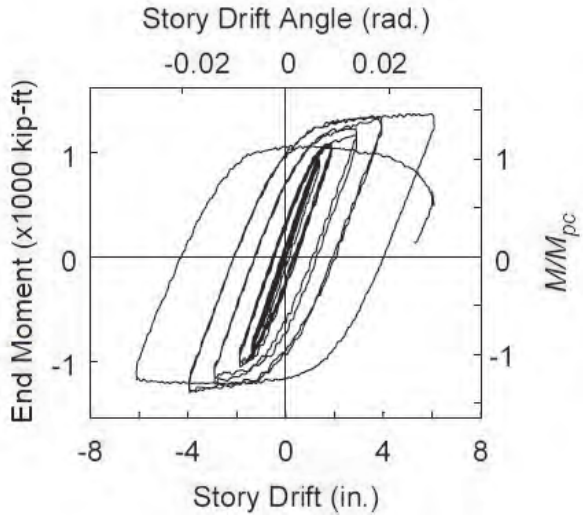

(b) End Moment vs. *SDA*

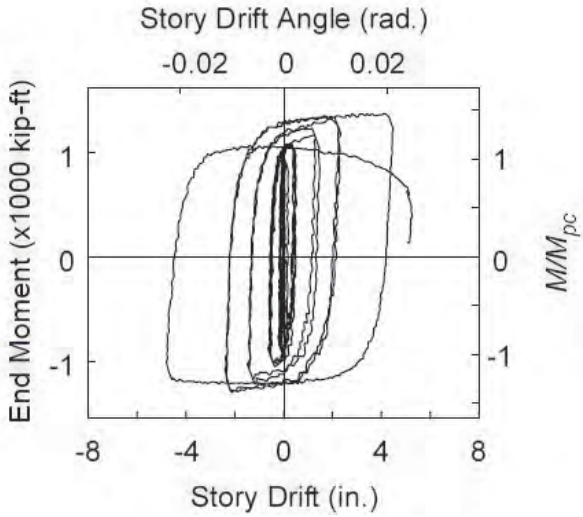

(c) End Moment vs. Plastic *SDA*

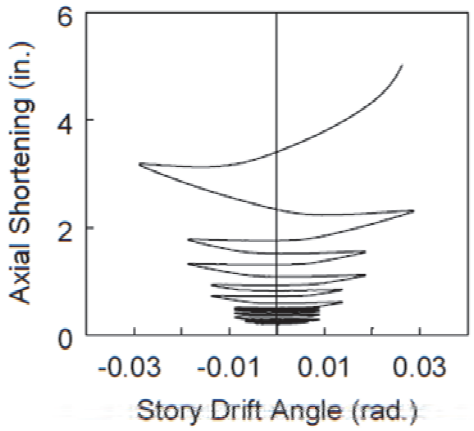

(d) Axial Shortening vs. *SDA*

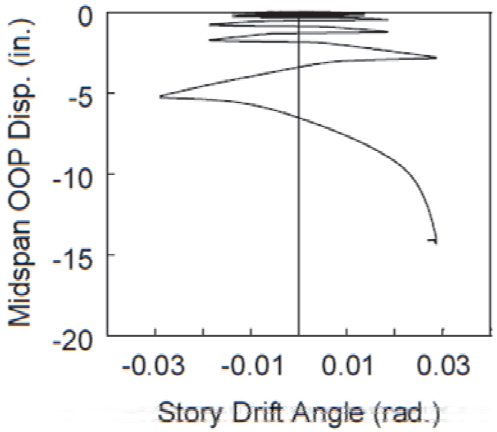

(e) Midspan OOP Disp. vs. *SDA*

Figure 5.38 Specimen 16M: Global Responses

5.7.3 Specimen 16M-BC

Like Specimen 16M, Specimen 16M-BC experienced the CB failure mode with the single-curvature out-of-plane buckling configuration; yielding and buckling progression is illustrated in Figure 5.39 and Figure 5.40. As expected in a boundary condition test, no significant deformation was observed at the east end; it remained mostly elastic and underwent some yielding toward the end of the test. At the west end, the sloped flaking pattern initiated at 2 % drift. Successively at 3 % drift, LTB of the specimen initiated and exacerbated at 4 % drift: the west flange under compression in positive drift and that in negative drift buckled upward out of plane more during the positive and negative excursions of each cycle, respectively. The exacerbated LTB movements caused a rapid increase in the column out-of-plane displacement, which concentrated near the west end. Corresponding to this out-of-plane curvature, an LTB-induced flange local buckle formed at each top half-width flange at the west end as shown in Figure 5.41. Significant flexural strength degradation in the specimen during the 4 % drift cycles prompted the termination of the test.

Figure 5.42 shows the global responses. Flexural strength remained stable during the 3 % drift cycles despite the considerable development of the out-of-plane buckling near the west end. Strength degradation prevailed at 4 % drift, corresponding to when the drastic out-of-plane movements occurred. Due to geometry of the deformed specimen, axial shortening aggravated proportionally to the amplitudes of the out-of-plane buckling. In comparison, Specimens 16M and 16M-BC reached their peak flexural strengths at 2 % and 3 % drift, respectively, and experienced strength degradation at 3 % and 4 % drift, respectively. This demonstrated the effect of the fixed-rotating boundary conditions; the applied end rotation helped relieving some of the flexural moment demand that would have been produced with fixed-fixed boundary conditions at the same drift level. As a result, the specimen with fixed-rotating boundary conditions could withstand larger story drifts before it failed. Despite this difference, the global responses of Specimen 16M-BC had a similar characteristic to those of Specimen 16M.

5.7.4 Concluding Remarks

As predicted, CB was the failure mode although the depth of this W18 section was shallower than that of Groups 1 and 11 specimens (W24). Allowing one end of the column to rotate did not alter the governing buckling mode.

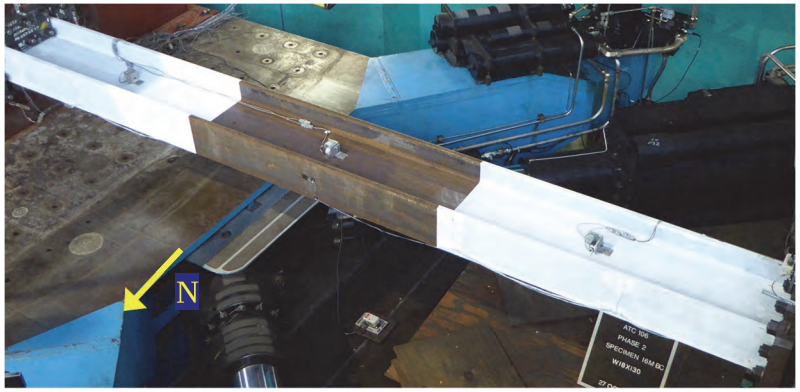

(a) *SDA* = 0.01 rad

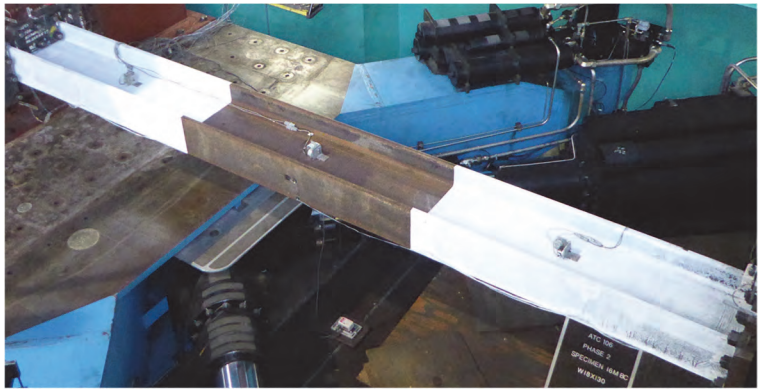

(b) *SDA* = 0.02 rad

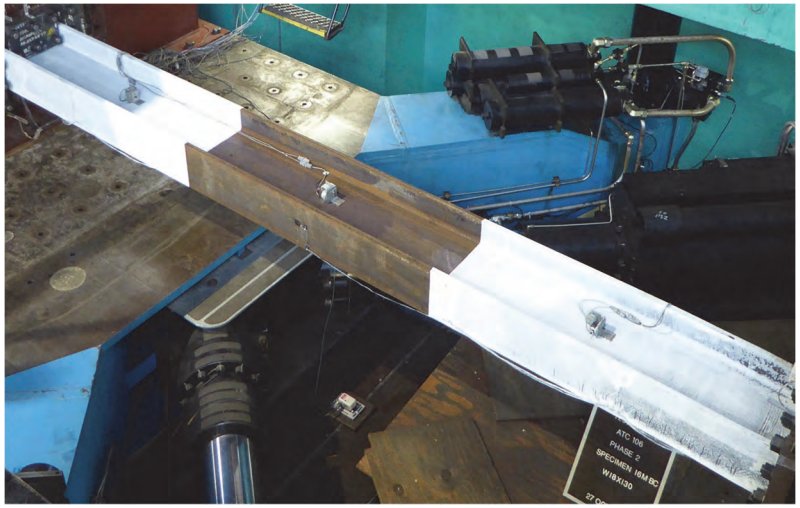

(c) *SDA* = 0.03 rad

(d) *SDA* = 0.04 rad

Figure 5.39 Specimen 16M-BC: Overall Yielding and Buckling Progression

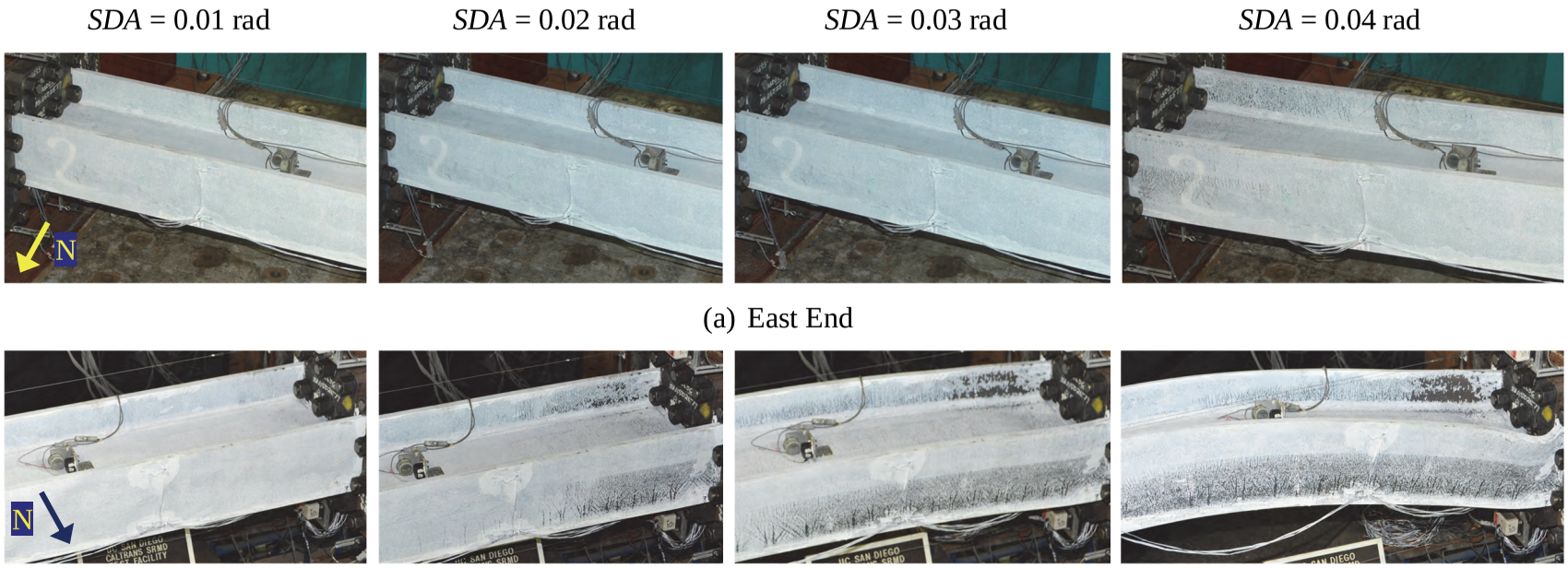

(a) East End

(b) West End

Figure 5.40 Specimen 16M-BC: Yielding and Buckling Progression at Member Ends

Figure 5.41 Specimen 16M-BC: LTB-Induced Flange Local Buckling at West End

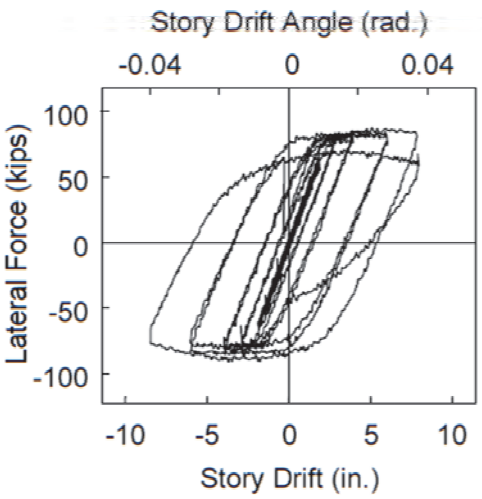

(a) Lateral Force vs. *SDA*

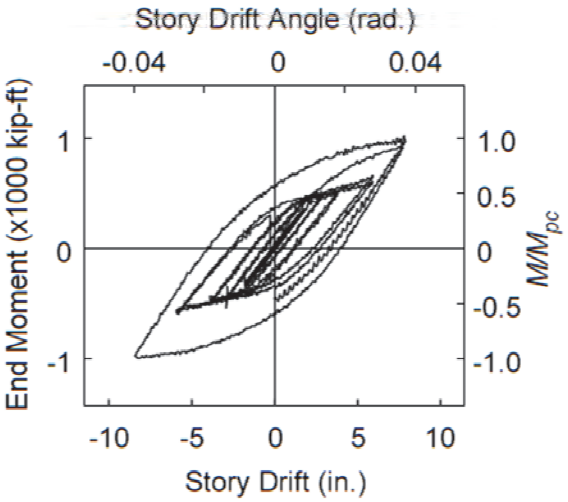

(b) East End Moment vs. *SDA*

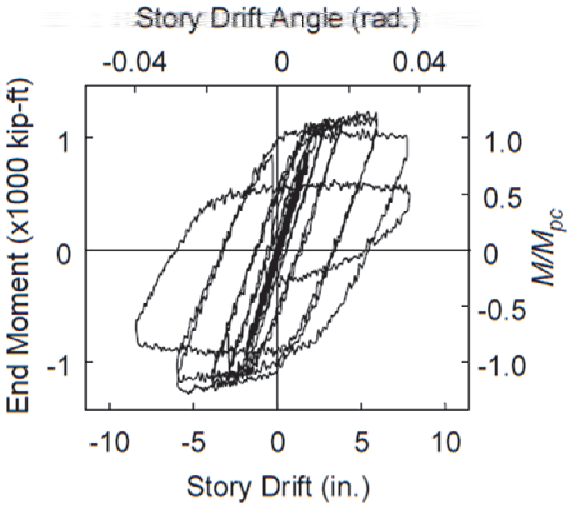

(c) West End Moment vs. *SDA*

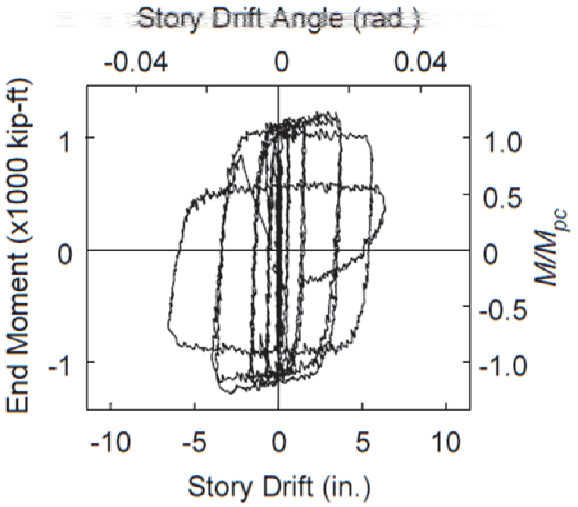

(d) West End Moment vs. Plastic *SDA*

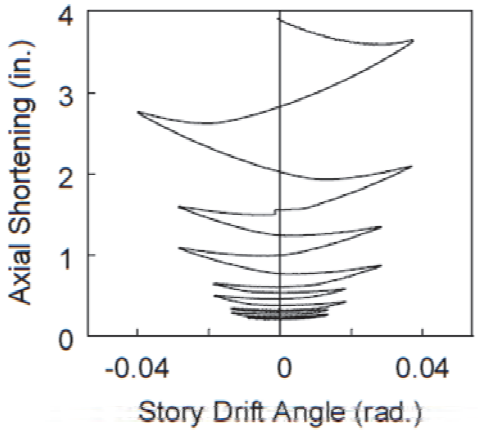

(e) Axial Shortening vs. *SDA*

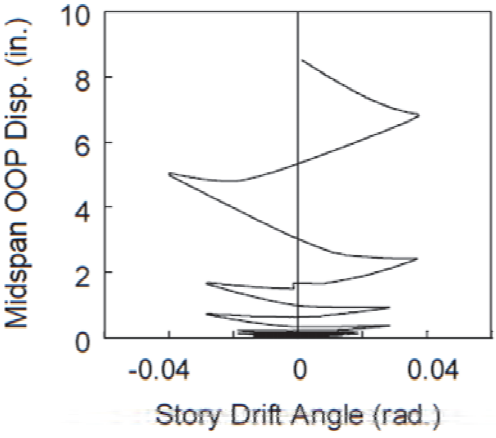

(f) Midspan OOP Disp. vs. *SDA*

Figure 5.42 Specimen 16M-BC: Global Responses

5.8 Group 17 Specimen: Section W18×76

5.8.1 General

Group 17 consisted of one W18×76 specimen; like Group 3 specimens, this specimen had a highly ductile web and moderately ductile flanges. The objective of Group 17 testing was to evaluate the section depth effect with respect to the ALB failure mode when the flanges are not highly ductile. Specimen 17L was subjected to fixed-fixed boundary conditions and constant axial compression with $C_a = 0.2$.

5.8.2 Test Results

Specimen 17L exhibited the ALB failure mode; yielding and buckling progression is illustrated in Figure 5.43 and Figure 5.44. The ALB sequence of this specimen initiated with one half-wave buckle set at 2 % drift. At 3 % drift, the ALB pattern became apparent. At 4 % and 5 % drifts, the specimen developed an additional half-wave buckle set, making a full-wave buckle set. This full-wave ALB configuration resulted in severely deformed column ends, which initiated an out-of-plane, rigid-body translation of the column portion between the buckled regions as demonstrated in downward displacement history in Figure 5.45(e). The test was terminated due to the excessive local buckling and significant flexural strength degradation.

Figure 5.45 shows the global responses. Flexural strength degradation initiated at 2 % drift, corresponding to the onset of ALB, which also triggered significant axial shortening in the column as its amplitudes increased.

5.8.3 Concluding Remarks

The failure mode of this column (ALB) was consistent with that of Group 3 specimens tested in Phase 1, although the depth of the former (W18) was shallower than that of the latter (W24).

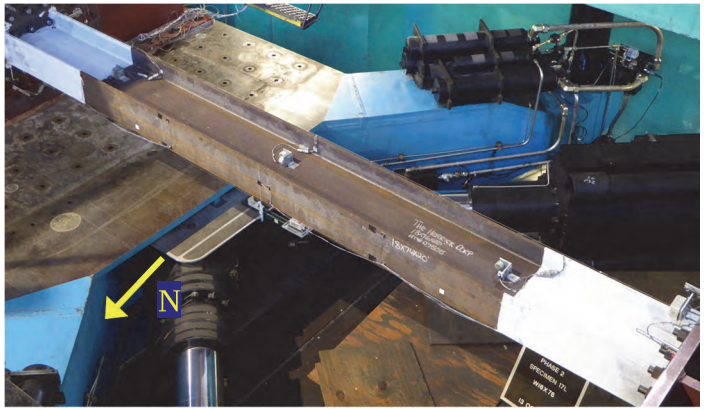

(a) *SDA* = 0.015 rad

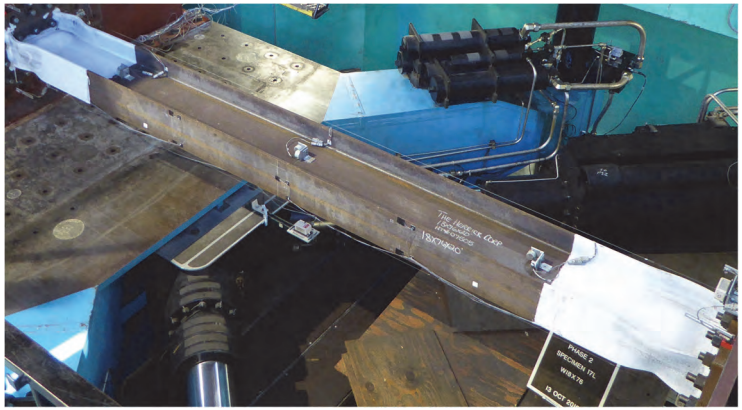

(b) *SDA* = 0.03 rad

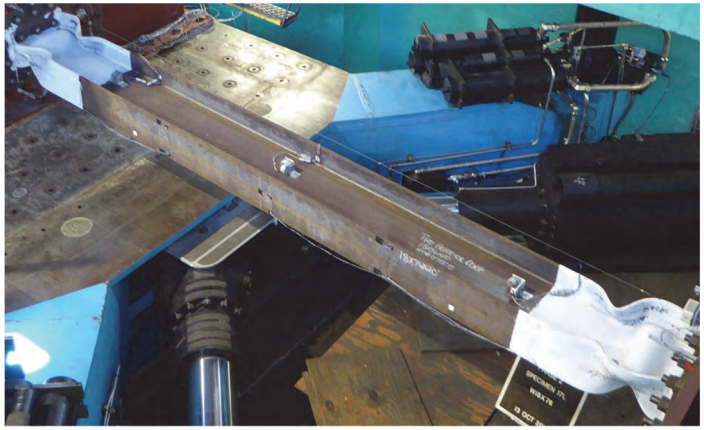

(c) *SDA* = 0.04 rad

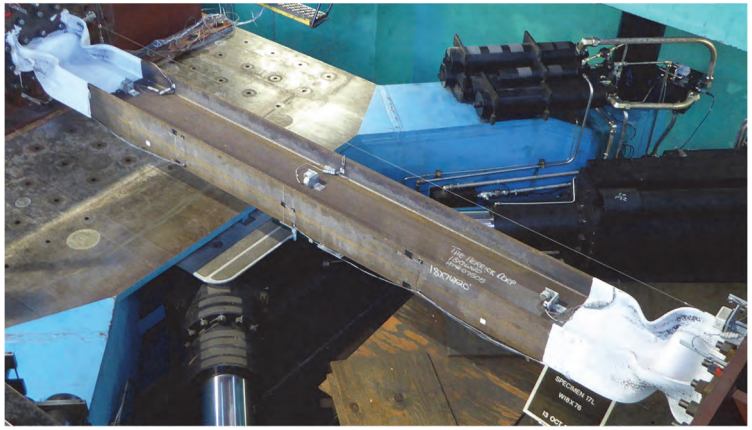

(d) *SDA* = 0.05 rad

Figure 5.43 Specimen 17L: Overall Yielding and Buckling Progression

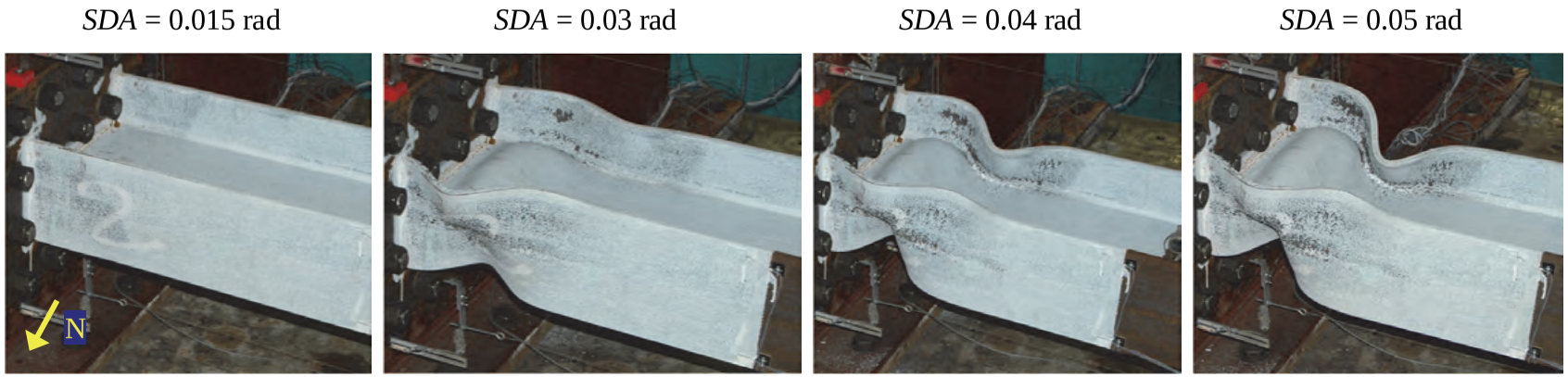

(a) East End

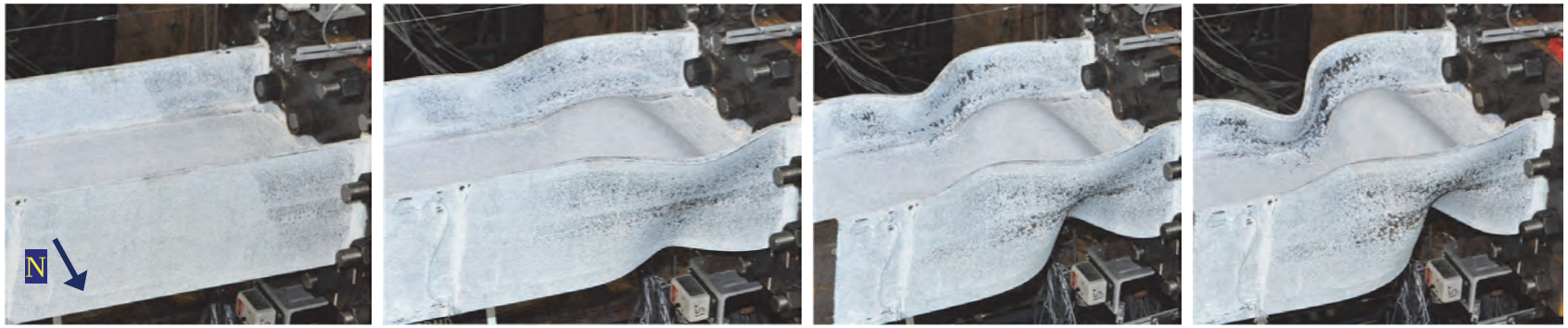

(b) West End

Figure 5.44 Specimen 17L: Yielding and Buckling Progression at Member Ends

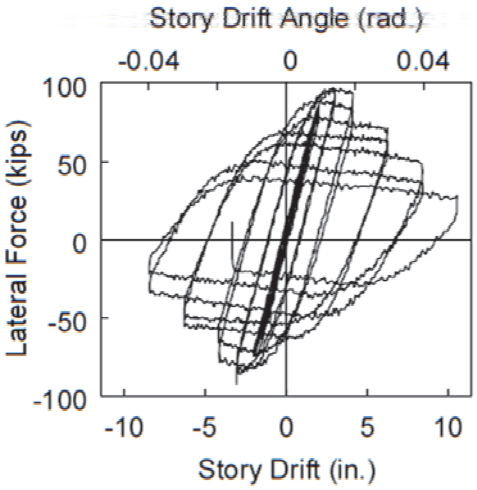

(a) Lateral Force vs. *SDA*

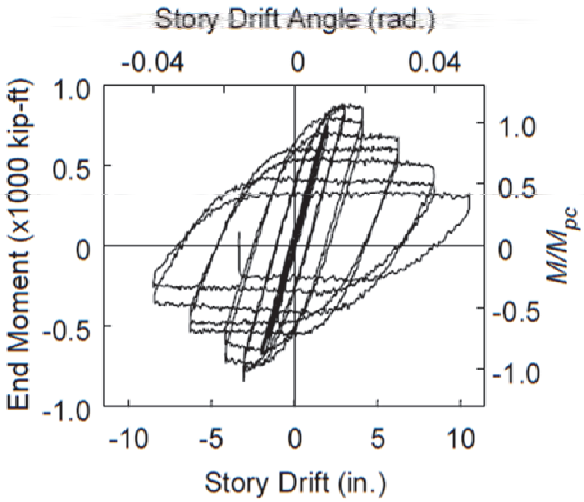

(b) End Moment vs. *SDA*

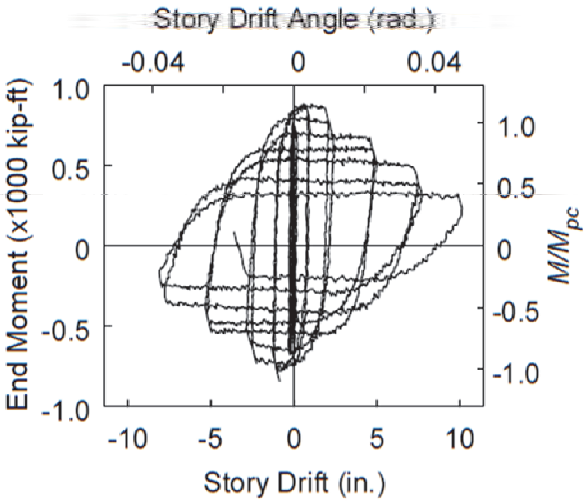

(c) End Moment vs. Plastic *SDA*

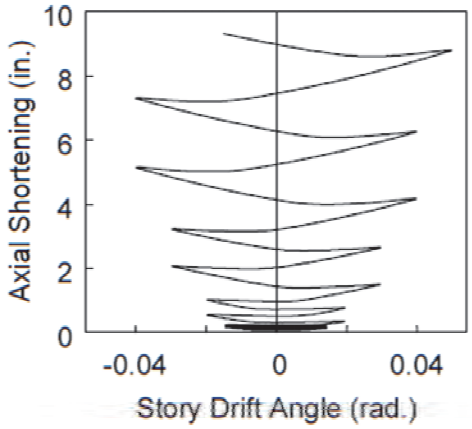

(d) Axial Shortening vs. *SDA*

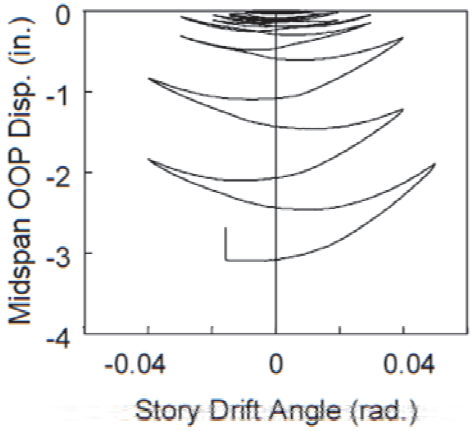

(e) Midspan OOP Disp. vs. *SDA*

Figure 5.45 Specimen 17L: Global Responses

6. TEST PROGRAM: PHASE 2B

6.1 Introduction

Eleven full-scale columns were tested in Phase 2B with similar test setup and loading protocols used in Phases 1 and 2A. Phase 2B test matrix shown in Table 6.1 includes both "deep" (e.g., W18, W24, and W30) and "shallow" (e.g., W14) sections. All specimens were subjected to strong-axis bending with the AISC loading protocol except for one (Specimen 21M-NF) which was subjected to a near-fault loading sequence. All were tested with the fixed-fixed boundary conditions except for Specimen 21M-VAU-BC that was tested with the fixed-rotating boundary conditions. In addition to testing with constant axial compression, four specimens underwent varying axial load sequences. Phase 2B testing was designed to further investigate Phase 2A objectives with additional emphases in (1) examining exterior column responses with respect to different axial load variations and amplitudes, (2) comparing "deep" versus "shallow" (W14) column responses and behaviors, and (3) investigating the effect of lateral drift loading sequences on the column response to include finding from the near-fault loading test.

6.2 Test Setup

Phase 2B testing was conducted in the Seismic Response Modification Device (SRMD) Test Facility at the University of California, San Diego. The setup of Phase 2B testing remained essentially the same as that used in Phases 1 and 2A (see Sections 2.2 and 4.2). Figure 6.1 and Figure 6.2 show the geometry and end details of the specimens with 18 ft and 14 ft clear length (i.e., excluded end plate thicknesses), respectively. As an exception, Group 21 specimens with W18×130 section was specified the same clear length of 17'-8" as that of Group 16 specimens tested in Phase 2A to facilitate a direct comparison. The geometry and end details of Group 21 specimens are shown in Figure 6.3.

6.3 Design of Test Specimens

Table 6.1 summarizes the slenderness ratios of each specimen as well as the axial load amplitudes and loading protocols used in testing. In Phase 2A, Group 16 specimens were tested with the AISC loading protocol under constant axial compression with $C_a = 0.4$. To study the boundary condition effect, the end rotation sequence was applied to

Specimen 16M-BC. In continuation of Phase 2A investigation, four specimens with the same section and geometry as Group 16 specimens were included in Phase 2B testing under Group 21. Three of them (Specimens 21M-VAU, 21M-VAM, and 21M-VAU-BC) were subjected to the AISC loading protocol and varying axial load sequences to study the response of exterior columns under different axial load variations caused by the overturning moment effect. In addition, the end rotation sequence was also applied to one of the three specimens (Specimen 21M-VAU-BC) to examine the combined effects of fixed-rotating boundary conditions and varying axial load. Details about the axial load sequences employed in Phase 2B testing are further discussed in Section 6.5. Lastly, the fourth specimen (Specimen 21M-NF) underwent constant axial compression and the near-fault loading protocol (see Section 6.5); the results were used to study how different lateral drift loading protocols influenced column responses.

All specimens in Phase 1 and 2A testing were considered "deep" columns with W18, W24, and W30 sections. To further examine the influence of section depths on column responses, three "shallow" sections—W14×82, W14×53, and W14×132—were assigned to Groups 24, 25, and 26, respectively, in addition to two new "deep" sections—W30×148 and W18×60—which were assigned to Groups 22 and 23, respectively. Furthermore, Group 26 also comprised two identical specimens. One was subjected to constant axial compression, while the other underwent a varying axial load sequence to examine the effect of varying axial load on the response of a "shallow" column. Lastly, testing of Group 27 specimen served as a repeat test of Specimen 4L from Phase 1 testing to confirm that the same CB failure mode could be reproduced.

6.4 Steel Material Properties

ASTM A992 was specified for all column specimens, and A572 Gr. 50 steel was specified for the end plates. Table 6.2 summarizes mechanical properties of the specimens; coupons were taken from both webs and flanges for material testing. The engineering stress versus engineering strain relationships are shown in Figure 6.4.

6.5 Testing Procedure and Loading Protocols

The AISC story drift angle loading protocol and the end rotation sequence remained the same as those used in Phase 2A testing [see Figure 4.4(a) and (c)]. Varying axial load

sequences used with Specimens 21M-VAU, 21M-VAM, 21M-VAU-BC, and 26LM-VAM are shown in Figure 6.5 with respect to the applied lateral drift (i.e., the AISC loading protocol).

In Phase 2A testing, the varying axial load sequence shown in Figure 4.4(b) was applied to Specimen 11H-VA. Note that the axial load fluctuation was in-phase with the applied story drift angle (dash lines at some peak drifts were provided in the figure to illustrate this characteristic). In Phase 2B testing, a similar axial load sequence was applied to Specimen 26LM-VAM [see Figure 6.5(d)] with a wider range of varying amplitudes: ΔC_a = 0.6 for Specimen 26LM-VAM compared to ΔC_a = 0.3 for Specimen 11H-VA. For testing of Group 21 specimens, it was realized that the axial load should reverse in direction at the same time step at which the lateral drift changed its direction as shown in Figure 6.5(b) and (c). This characteristic reflected a more accurate loading condition that exterior columns experienced during a seismic event. Therefore, the varying axial load sequences were modified as such for Specimens 21M-VAM, 21M-VAU, and 21M-VAU-BC. These three specimens experienced the same variation magnitude, ΔC_a, of 0.6. For the VAM specimen, C_a varied from 0.1 to 0.7, all in compression, with the mean value, $\overline{C_a}$, of 0.4. For the other two VAU specimens, the upper bound C_a value was set at 0.4 in compression, and the lower bound C_a value was set at -0.2 in tension. For all varying axial load sequences, the cyclic axial load amplitudes grew proportionally to the levels of lateral drift and was capped at the C_a limits (as discussed above) at 1 % drift and beyond. The reason for this loading characteristic was discussed in Section 4.5.

In addition to the AISC loading protocol, one specimen (Specimen 21M-NF) was tested with the near-fault loading protocol discussed in Section 2.5 [see Figure 2.10(d)].

6.6 Instrumentation

Phase 2B used the same instrumentation layouts as those of Phase 2A (see Section 4.6).

6.7 Data Reduction

See Section 2.7.

Table 6.1 Test Matrix for Phase 2B Testing

Group No.	Section	Specimen Designation	L (ft)	Slenderness			Column Axial Load		Parameter of Interest	Predicted Buckling Mode[a]
				$\frac{b_f}{2t_f}$	$\frac{h}{t_w}$	$\frac{L}{r_y}$	C_a	P_u (kips)		
21	W18×130	21M-VAU	17⅔	4.65	23.9	78.5	-0.2 to 0.4	-345 to 689	Varying Axial (VA) Load	Coupled Buckling
		21M-VAU-BC					-0.2 to 0.4	-345 to 689	VA with Boundary Condition	
		21M-NF					0.4	689	Loading Sequence	
		21M-VAM					0.1 to 0.7 ($\overline{C_a} = 0.4$)	172 to 1206	Varying Axial Load	
22	W30×148	22L	18	4.44	41.6	94.7	0.2	392	New $b_f/2t_f - h/t_w$ domain	Coupled Buckling
23	W18×60	23L	14	5.44	38.7	100.0	0.2	158	New $b_f/2t_f - h/t_w$ domain	Coupled Buckling
24	W14×82	24L	14	5.92	22.4	67.7	0.2	216	Shallow Section	In-Plane Hinging with ALB
25	W14×53	25L	14	6.11	30.9	87.5	0.2	140	Shallow Section	Coupled Buckling
26	W14×132	26LM	14	7.15	17.7	44.7	0.3	524	Shallow Section	SFB
		26LM-VAM					0 to 0.6 ($\overline{C_a} = 0.3$)	0 to 1048	Varying Axial Load	
27	W24×84	27L	18	5.86	45.9	110.8	0.2	222	4L Repeat	Coupled Buckling

[a] Per the prediction of Ozkula et al. (2017).

Table 6.2 Steel Mechanical Properties for Phase 2B Testing

Group No.	Section	Comp.	Yield Stress (ksi)	Tensile Strength (ksi)	Elong.[c] (%)	Heat No.
21	W18×130	Flange	54.8	70.9	39.1	471309
		Web	59.0	72.0	41.7	
22	W30×148	Flange	54.6	79.6	35.5	3G3357
		Web	66.2	83.3	34.5	
23	W18×60	Flange	49.4	68.1	37.3	59055727
		Web	55.4	69.0	35.6	
24	W14×82	Flange	51.6	68.4	38.7	59070575
		Web	54.4	69.5	36.9	
25	W14×53	Flange	54.8	70.4	35.9	438715
		Web	62.6	73.6	34.6	
26[a]	W14×132	Flange	51.5	70.8	38.4	456819
		Web	50.0	69.0	35.6	
26[b]		Flange	55.0	72.5	39.0	456821
		Web	55.7	71.6	39.0	
27	W24×84	Flange	54.1	80.8	35.2	36829
		Web	58.4	81.9	32.4	

[a] Specimen 26LM.

[b] Specimen 26LM-VAM.

[c] Elongations are based on a 2-in. gauge length.

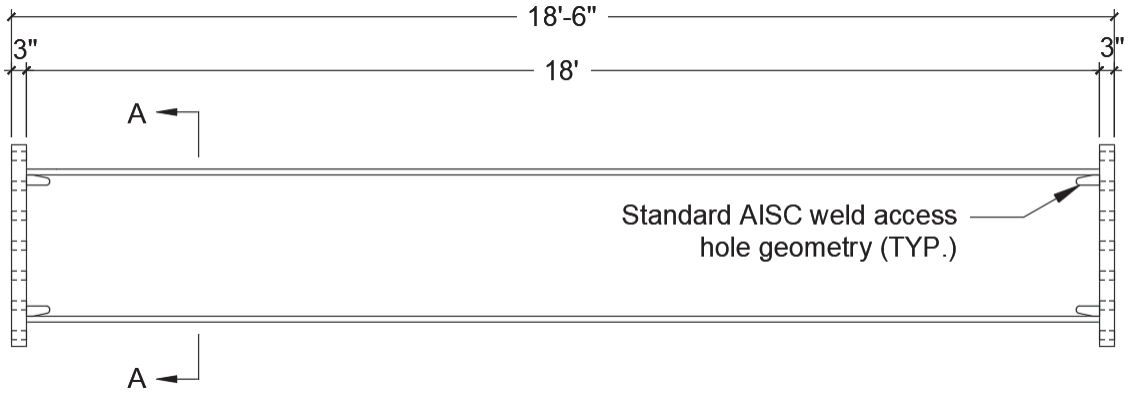

PLAN

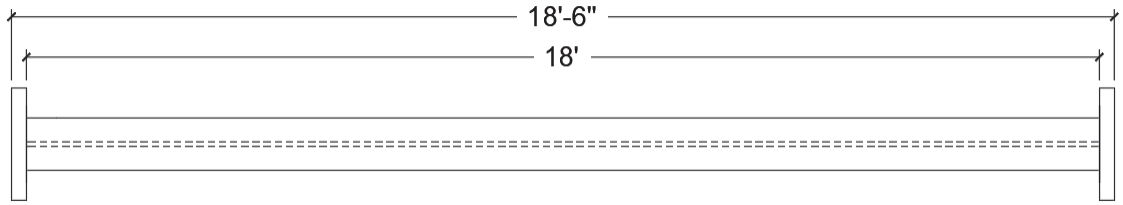

ELEVATION

(a) Overall Dimensions

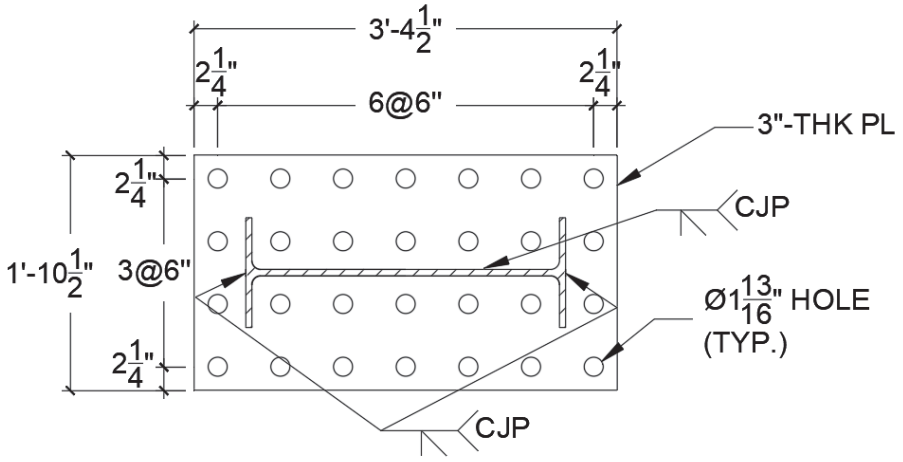

(b) Section A-A

Figure 6.1 Phase 2B Specimen Geometries and End Details (18-ft Column Length)

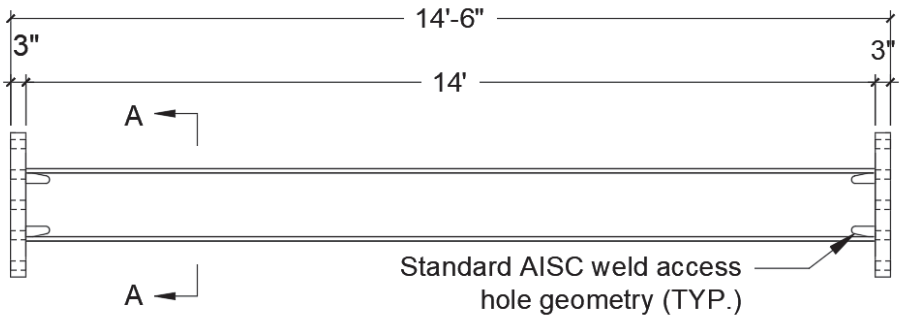

PLAN

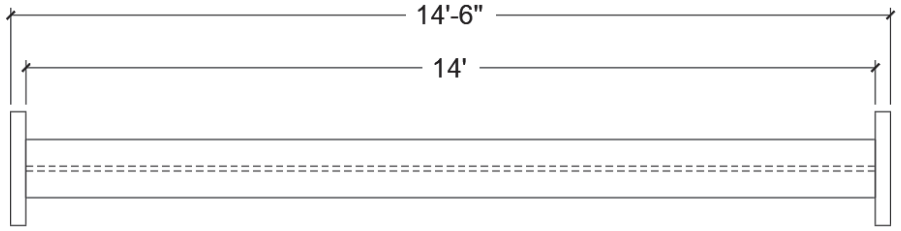

ELEVATION

(a) Overall Dimensions

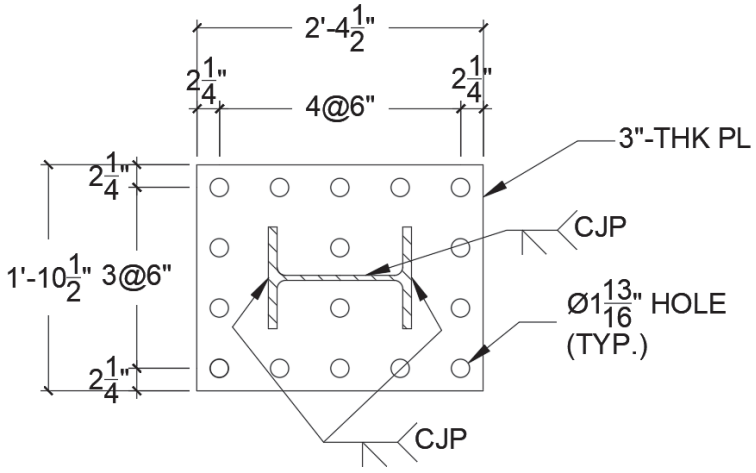

(b) Section A-A

Figure 6.2 Phase 2B Specimen Geometries and End Details (14-ft Column Length)

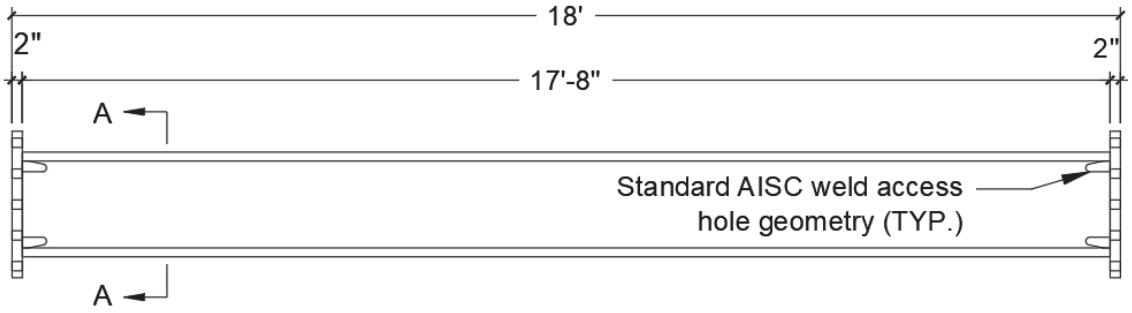

PLAN

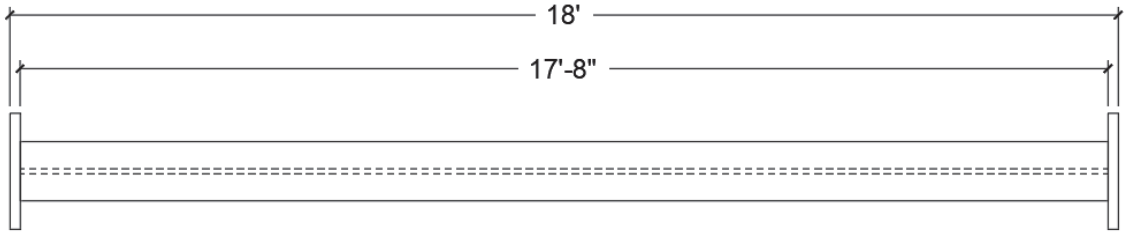

ELEVATION

(a) Overall Dimensions

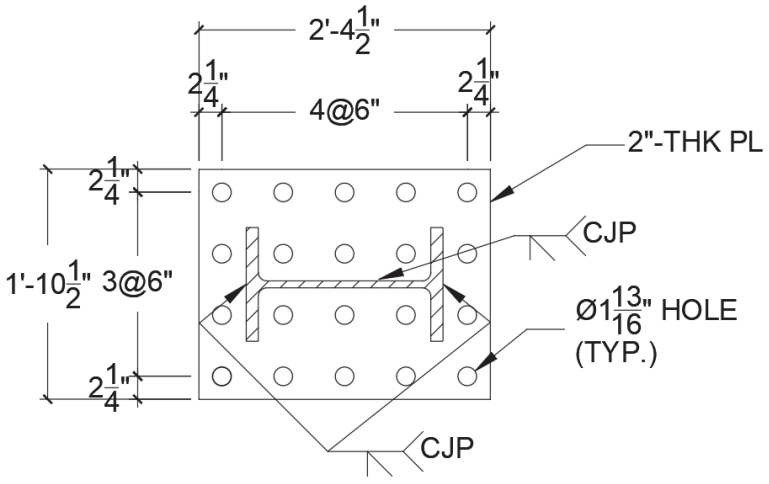

(b) Section A-A

Figure 6.3 Phase 2B Specimen Geometries and End Details (Group 21)

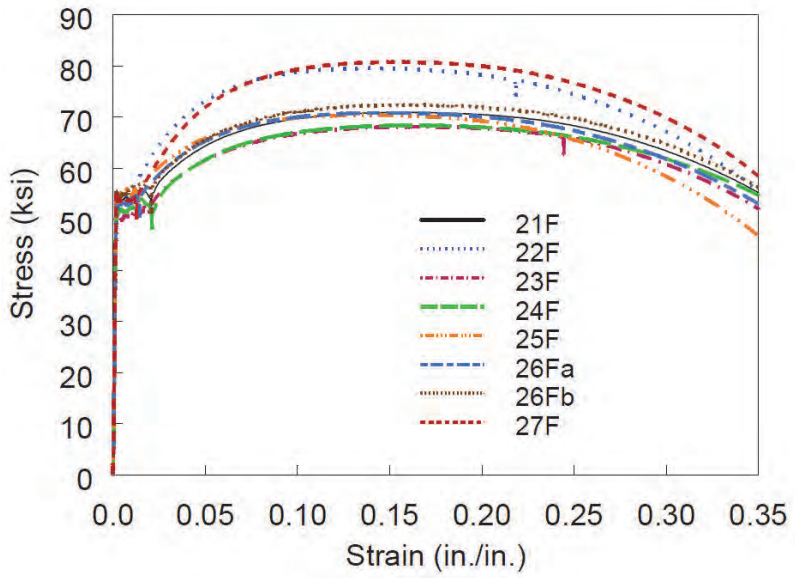

(a) Flange

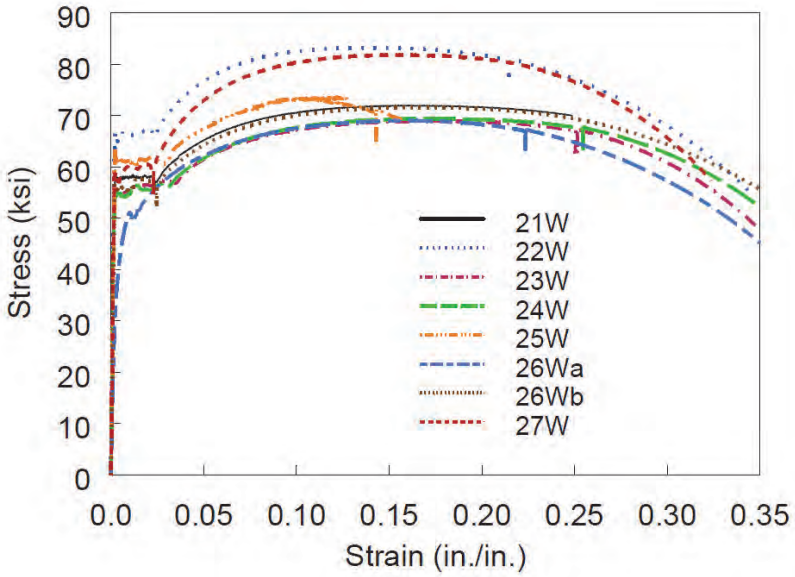

(b) Web

Figure 6.4 Phase 2B Engineering Strain versus Stress Curves

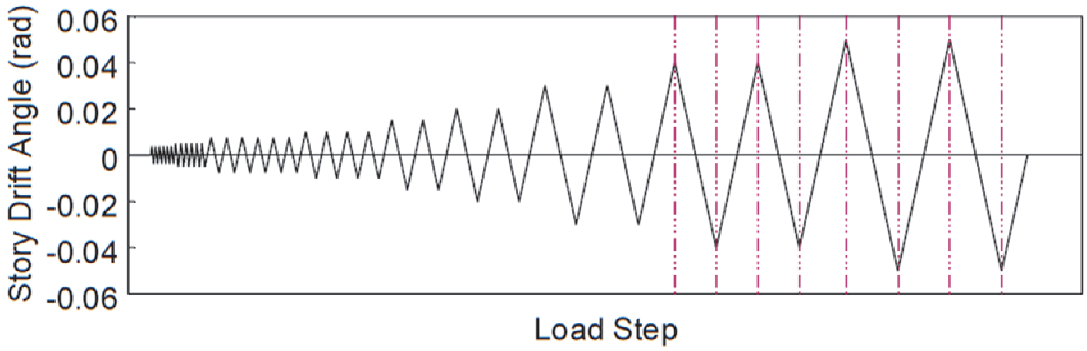

(a) AISC Stordy Drift Angle Loading Protocol

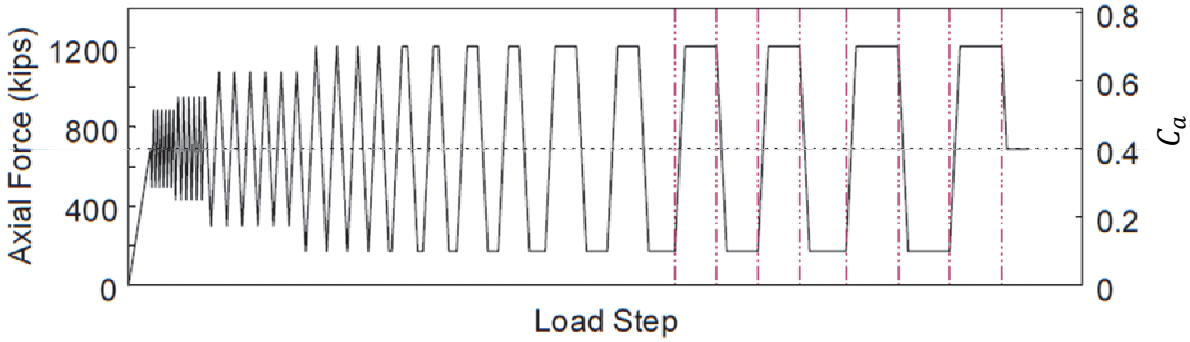

(b) Axial Load for Specimen 21M-VAM

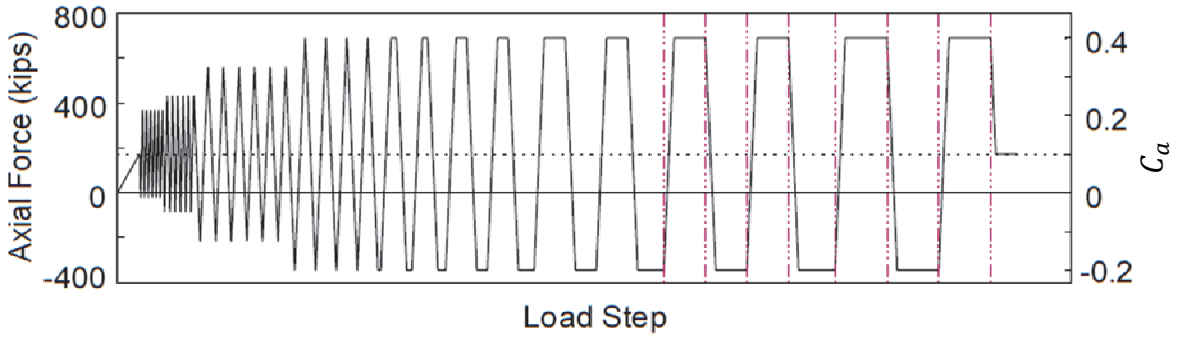

(c) Axial Load for Specimens 21M-VAU and 21M-VAU-BC

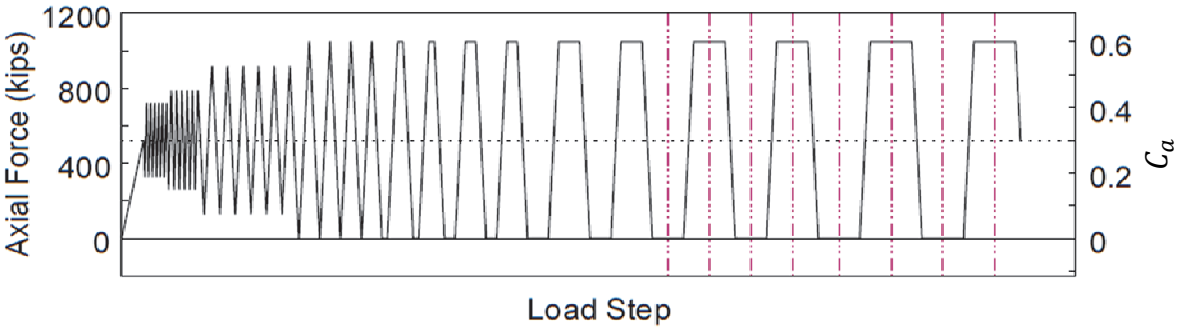

(d) Axial Load for Specimen 26LM-VAM

Figure 6.5 Phase 2B Story Drift Angle and Varying Axial Load Sequences

7. TEST RESULTS: PHASE 2B

7.1 Introduction

Measured responses and observed behavior of eleven specimens from Phase 2B testing are presented in this chapter. All specimens were subjected to strong-axis bending. Except for Specimen 21M-NF, which underwent the near-fault loading protocol, all specimens sustained the AISC loading protocol. For each specimen, figures are included to illustrate the progression of yielding, buckling, and the overall deformed configuration with respect to increasing story drift angle (*SDA*). Global responses of the specimens are presented in the form of lateral force (i.e., column shear), end moment, and axial shortening versus story drift plots.

In addition to uniaxial strain gauges and rosettes, Digital Image Correlation (DIC) was utilized to measure surface deformation at the column west end. To create visible features on the surfaces of the specimen that followed the column deformation (required for DIC), mill scale at the west end was removed via abrasive grinding; then, white rubber coating and black speckles were applied to the polished surface. Due to this preparation, flaking of the paint did not occur at the west end. Thus, yielding progression could only be observed at the east end.

7.2 Group 21 Specimens: Section W18×130

7.2.1 General

In Phase 2A, two W18×130 specimens—Specimens 16M and 16M-BC—were tested with constant axial compression ($C_a = 0.4$); Specimen 16M-BC was also subjected to the end rotation sequence in conjunction with the typical AISC loading protocol. In Phase 2B, four specimens (Group 21) with the same section and geometry as Group 16 specimens were tested with four different loading scenarios. Specimen 21M-VAM was subjected to varying compressive axial load with C_a ranging from 0.1 to 0.7, while Specimen 21M-VAU was subjected to varying tensile and compressive axial load with C_a ranging from -0.2 (tension) to 0.4 (compression). Note that the former axial load sequence had its *mean* C_a value equal to 0.4; in contrast, the C_a value of 0.4 represented the *upper bound* value in the latter axial load sequence. In both cases, the axial load range (ΔC_a) remained the same

(= 0.6). Specimen 21M-NF was tested with the near-fault loading protocol. Lastly, Specimen 21M-VAU-BC was subjected to both varying axial load and the end rotation sequence. Characteristics of all loading scenarios were discussed in Sections 4.5 and 6.5.

7.2.2 Specimen 21M-VAM

The governing failure mode of Specimen 21M-VAM is CB with the single-curvature out-of-plane buckling configuration; yielding and buckling progression is shown in Figure 7.1 and Figure 7.2. Local buckling was not observed before the sloped flaking pattern and LTB movements initiated at 1.5 % and 2 % drift, respectively. LTB movements were triggered in the first negative excursion at 2 % drift when axial compression increased to its highest amplitude ($C_a = 0.7$). They exacerbated at 3 % drift: during each cycle, compression flanges in the negative drift buckled out of plane more than those in positive drift since the former experienced higher combined axial and in-plane flexural compression than the latter. In addition, out-of-plane amplitudes of the former decreased (or recovered) somewhat in the positive excursions due to the progressive decrease in axial compression. Since axial shortening grew proportionally to the out-of-plane amplitudes, it also recovered somewhat in the positive excursions as shown in Figure 7.5(d).

Significant LTB movements induced flange local buckling at both column ends as shown in Figure 7.3. At the west end, the two half-wave buckles formed at the top half-width flanges; at the east end, they formed at the top and bottom half-width flanges of the northeast and southeast flanges, respectively. The former appeared to be triggered primarily by out-of-plane stresses, while the latter appeared to be induced primarily by warping stresses due to significant twisting at the east end as shown in Figure 7.4.

Influenced by web-flange interactions, the web at each end also buckled in the direction that conformed to the flange local buckling configurations. In summary, global buckling occurred first in this specimen, followed by local buckling. Figure 7.5 shows the global responses. The specimen exhibited higher plastic moment capacity in the positive excursions compared to that in the negative excursions since lower axial compression was applied in the former. A drastic flexural strength degradation occurred during the second negative excursion at 3 % drift as the applied axial load progressively returned to its highest amplitude. Axial shortening began to grow at an increasing rate at 2 % drift, corresponding to the onset of LTB movements.

(a) *SDA* = 0.01 rad

(b) *SDA* = 0.015 rad

(c) *SDA* = 0.02 rad

(d) *SDA* = 0.03 rad

Figure 7.1 Specimen 21M-VAM: Overall Yielding and Buckling Progression

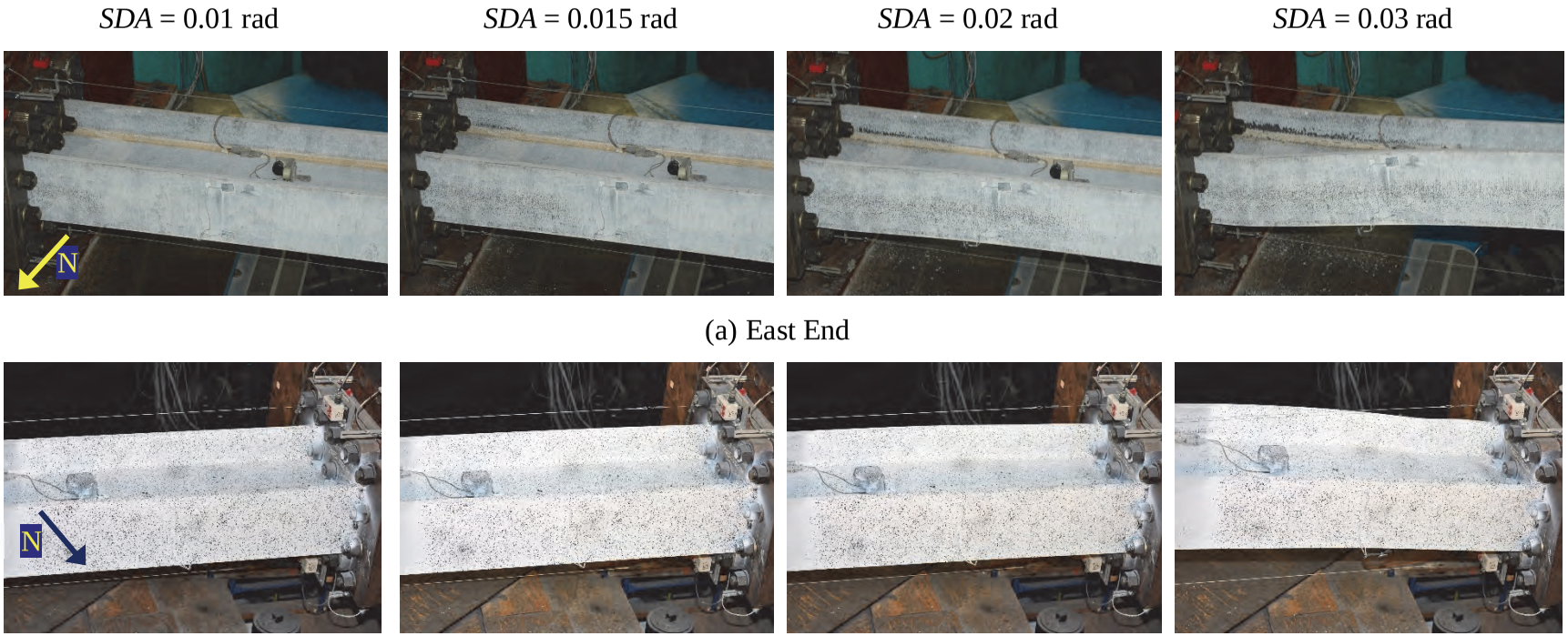

(a) East End

(b) West End

Figure 7.2 Specimen 21M-VAM: Yielding and Buckling Progression at Member Ends

(a) Southwest Flange

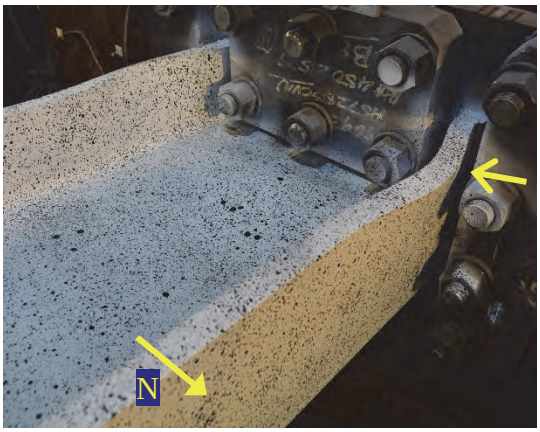

(b) Northwest Flange

(c) Web Local Buckling at West End

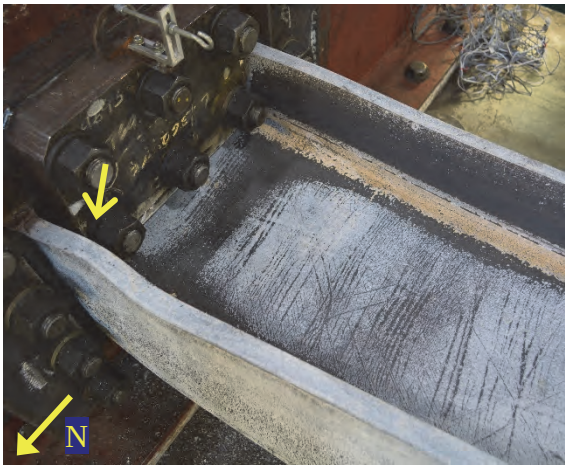

(d) Northeast Flange

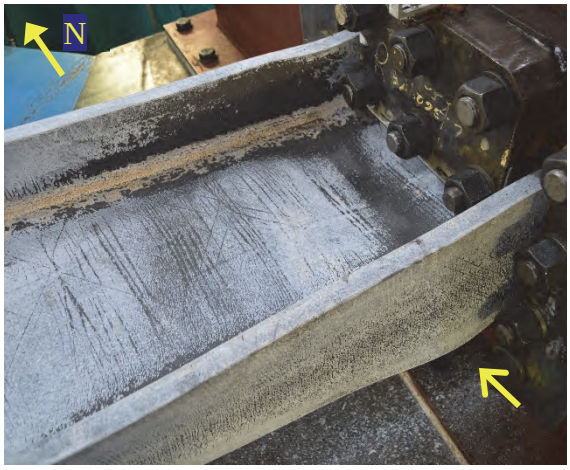

(e) Southeast Flange

Figure 7.3 Specimen 21M-VAM: LTB-Induced Local Buckling at End of Test

(a) Overall

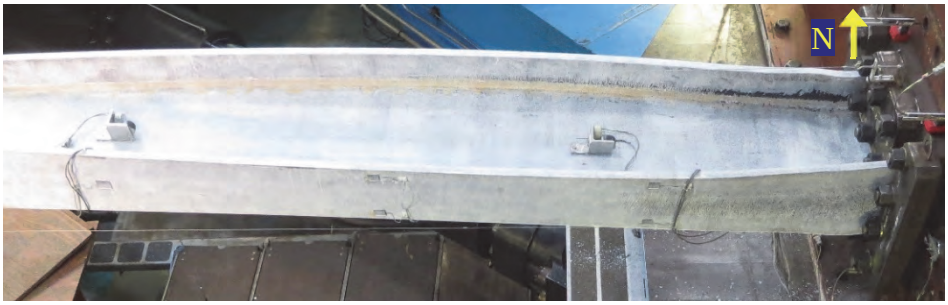

(b) East End

Figure 7.4 Specimen 21M-VAM: Significant Twisting at East End

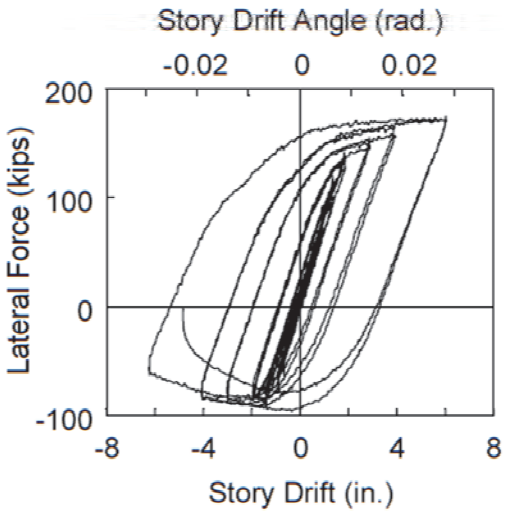

(a) Lateral Force vs. *SDA*

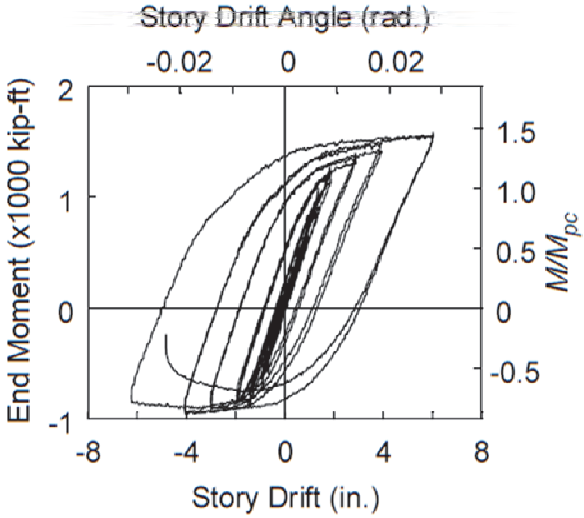

(b) End Moment vs. *SDA*

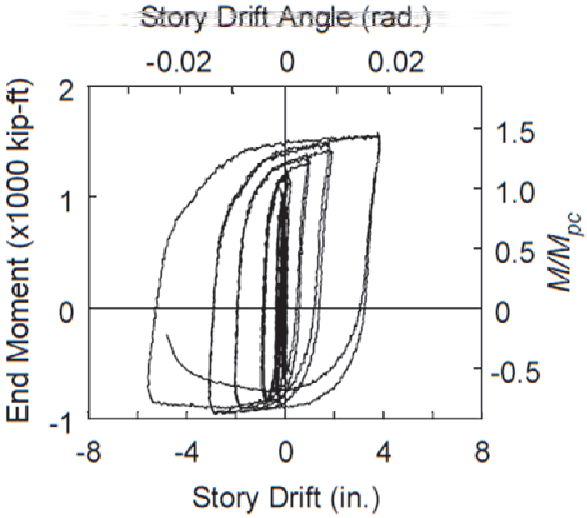

(c) End Moment vs. Plastic *SDA*

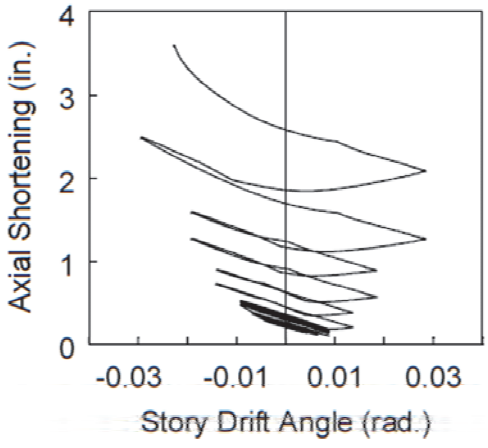

(d) Axial Shortening vs. *SDA*

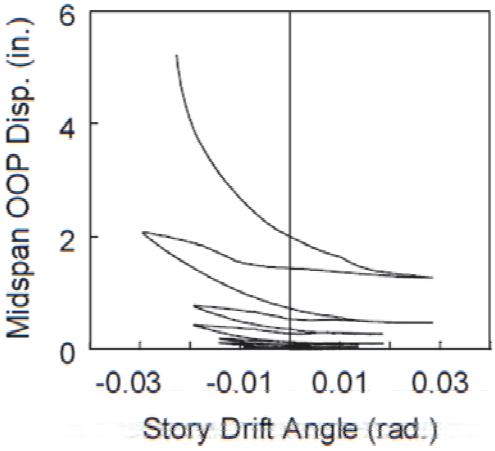

(e) Midspan OOP Disp. vs. *SDA*

Figure 7.5 Specimen 21M-VAM: Global Responses

7.2.3 Specimen 21M-VAU

Testing of Specimen 21M-VAM, which had an axial force coefficient C_a varied from 0.1 to 0.7 in compression, was stopped after completing two cycles at 3 % drift due to excessive global buckling and strength degradation. By varying C_a from -0.2 (tension) to 0.4 (compression), testing of Specimen 21M-VAU was stopped after completing one cycle at 5 % drift. The governing buckling mode of Specimen 21M-VAU is CB with the reverse-curvature out-of-plane buckling configuration; yielding and buckling progression is shown in Figure 7.6 and Figure 7.7.

LTB of the specimen was triggered during the 4 % and 5 % drift cycles only in the negative excursions with downward and upward amplitudes at the northeast and southwest flanges, respectively. In the positive excursions, the column sustained axial tension, which stretched it and mitigated the out-of-plane buckling amplitudes as shown in Figure 7.8; the column axial shortening also recovered corresponding to this phenomenon as shown in Figure 7.11(d).

Severe LTB movements were observed during the first negative excursion at 5 % drift, at which point the member flexural strength began to degrade considerably as shown in Figure 7.11(b). Out-of-plane and warping stresses associated with the LTB deformation contributed significant tension at the free edges of the column flange CJP welds. In an attempt to displace the specimen to +5 % drift with increasing tensile axial load for the second time, a rupture occurred at the northeast flange near the end plate as shown in Figure 7.9; the test was terminated. A partial fracture of a CJP weld was also observed at the top edge of the southwest flange (see Figure 7.10). Indeed, the combined effects of in-plane bending, LTB-type movements, and axial tension were detrimental to CJP welded joints. (It will be shown in the next section that a similar flange rupture was also observed in Specimen 21M-VAU-BC, which also experienced axial tension.) Unlike Specimen 21M-VAM that experienced considerable LTB-induced local buckling at the member ends, Specimen 21M-VAU did not experience local buckling although this latter specimen underwent higher drift levels. Partly, this was due to the axial compression applied to the latter (maximum C_a = 0.4) was lower than that applied to the former (maximum C_a = 0.7).

(a) *SDA* = 0.02 rad

(b) *SDA* = 0.03 rad

(c) *SDA* = 0.04 rad

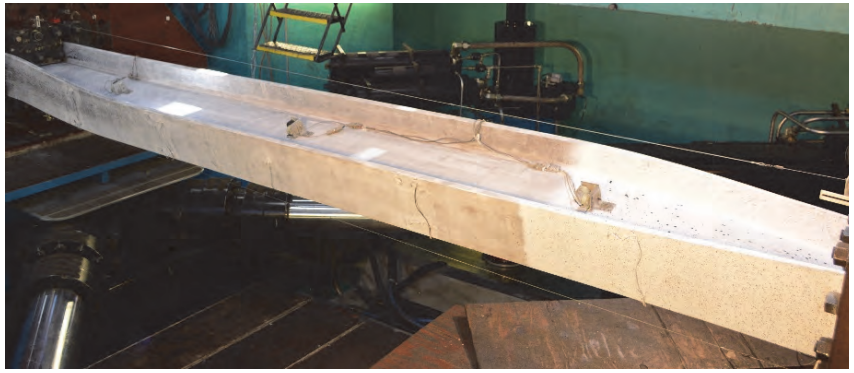

(d) *SDA* = 0.05 rad

Figure 7.6 Specimen 21M-VAU: Overall Yielding and Buckling Progression

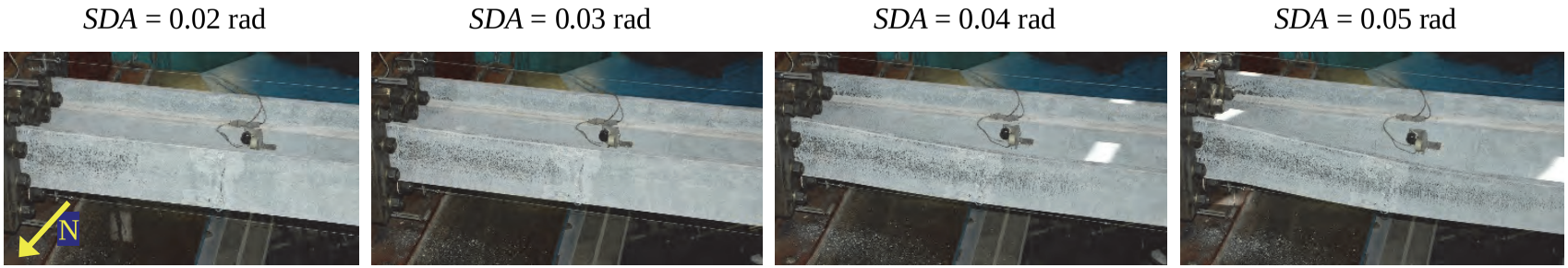

(a) East End

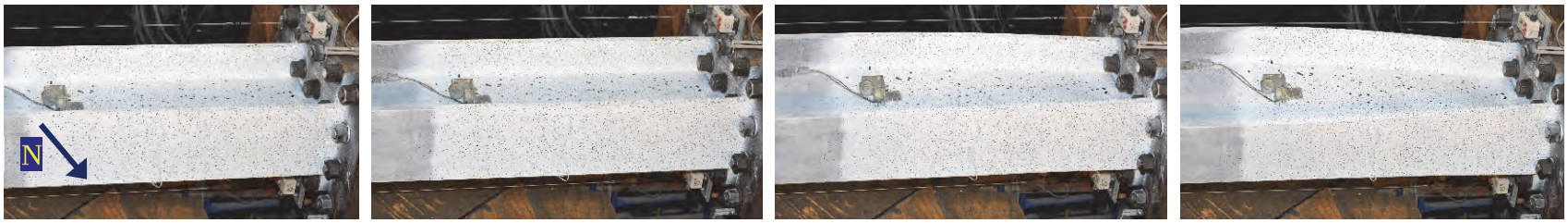

(b) West End

Figure 7.7 Specimen 21M-VAU: Yielding and Buckling Progression at Member Ends

SDA = -0.04 rad (1st Cycle) *SDA* = +0.04 *SDA* (2nd Cycle)

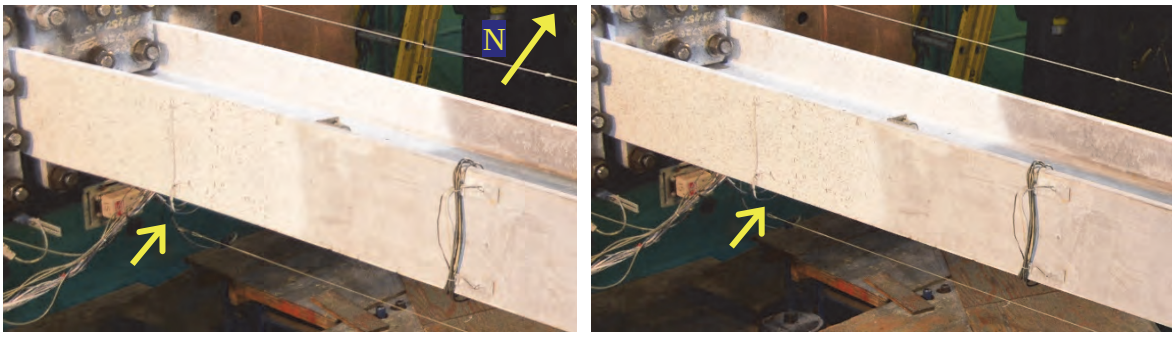

(a) Southwest Flange

(b) Northeast Flange

Figure 7.8 Specimen 21M-VAU: Tensile Axial Load Effect on Out-of-Plane Buckling

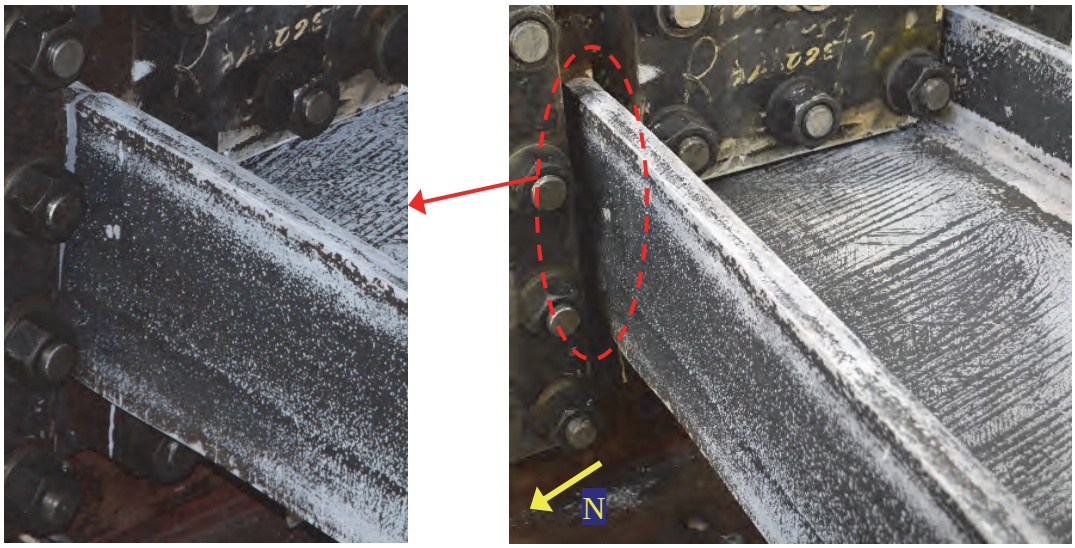

Figure 7.9 Specimen 21M-VAU: Rupture at Northeast Flange

(a) Northeast Flange

(b) Southwest Flange

Figure 7.10 Specimen 21M-VAU: Column Flange CJP Weld Fracture

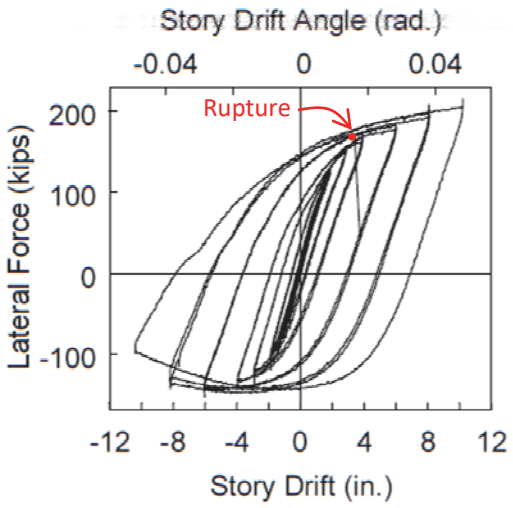

(a) Lateral Force vs. *SDA*

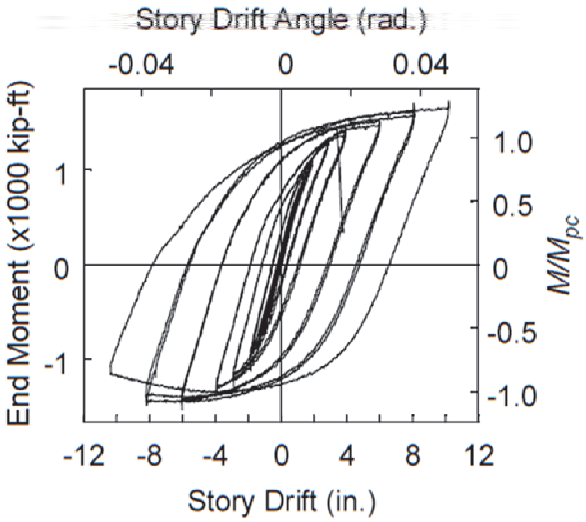

(b) End Moment vs. *SDA*

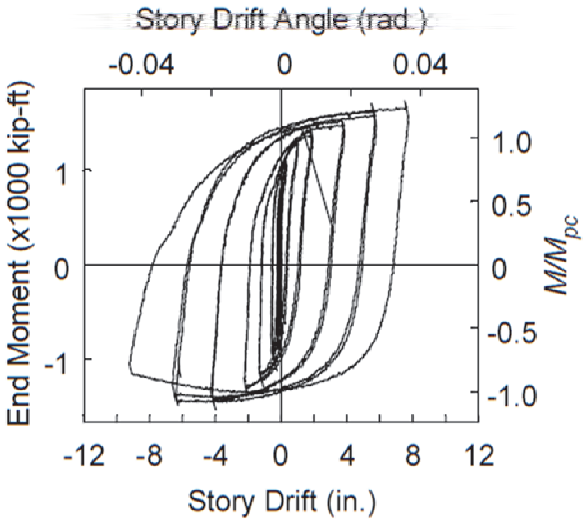

(c) End Moment vs. Plastic *SDA*

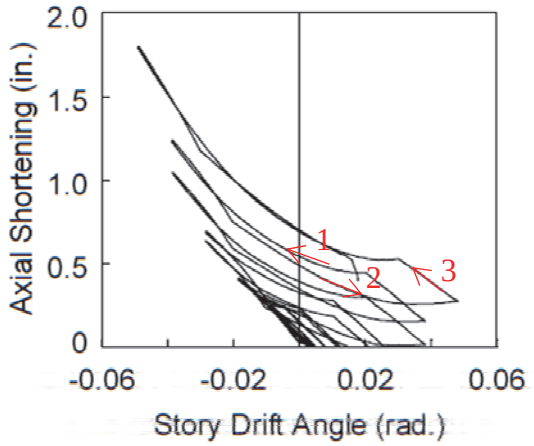

(d) Axial Shortening vs. *SDA*

Figure 7.11 Specimen 21M-VAU: Global Responses

7.2.4 Specimen 21M-VAU-BC

Section 4.5 discussed the end rotation sequence utilized in fixed-rotating boundary condition tests; it intended to apply a strong-axis end rotation at the east (or moving) end of the specimen with the same magnitude as the applied story drift angle (i.e., the AISC loading protocol). However, the SRMD platen could only apply approximately 0.035 rad rotation in both the clockwise and counterclockwise directions. Therefore, for 4 % and greater drift cycles, the rotation-to-drift ratio ξ defined in Section 4.5 became less than 1 for some portions of the test where the applied story drift angle exceeded 0.035 rad; ξ equaled 1 anywhere else. Figure 7.12(a) compares the story drift angle and end rotation histories of Specimen 21M-VAU-BC; two horizontal dashed lines indicates the maximum rotation the platen could accommodate during testing. It shows the load steps at which the applied story drift angle exceeded the applied end rotation. The corresponding global response portions are shown in dashed line in Figure 7.12(b); the solid line indicates the portions at which ξ is maintained at 1. The plot shows that lateral stiffness of the former is greater than that of the later when considering each loading and unloading branch of the 4 % and greater drift cycles separately; this demonstrated the effect of varying ξ.

With the imposed rotation at the east end, the specimen was able to displace further compared to Specimen 21M-VAU; it completed two cycles at 5 % drift and one cycle at 5.5 % drift (the platen setup at that time did not allow 6 % drift displacement) before the test was terminated. Specimen 21M-VAU only completed one cycle at 5 % drift before its northeast flange and CJP weld ruptured.

The governing buckling mode of Specimen 21M-VAU-BC is CB with the single-curvature out-of-plane buckling configuration; yielding and buckling progression is shown in Figure 7.13 and Figure 7.14. LTB behavior of this specimen was similar to that of Specimen 21M-VAU, except that (1) the east end remained essentially in the elastic range up to 3 % drift (see Figure 7.14) and did not exhibit obvious LTB movements until 5 % drift, and (2) CJP weld ruptured at the southwest flange as shown in Figure 7.15. A minor LTB-induced flange local buckling was observed at the top half-width southwest flange, which was accompanied by a minor web local buckling due to the influence of web-flange interactions as shown in Figure 7.16.

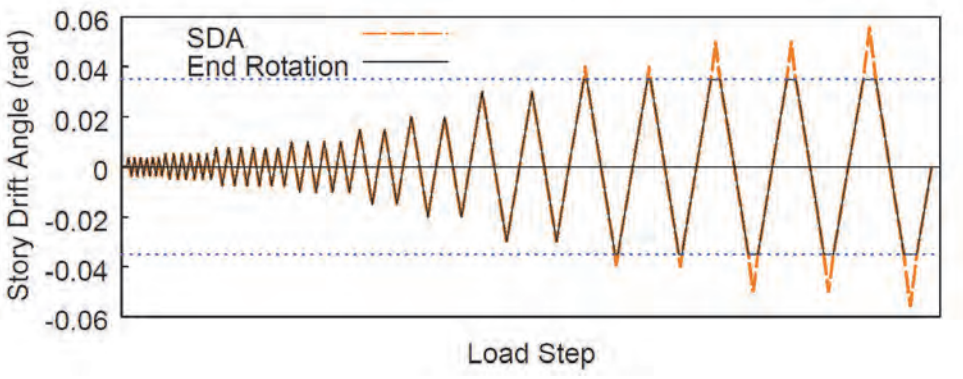

(a) Story Drift Angle and End Rotation (at Moving End) History Comparison

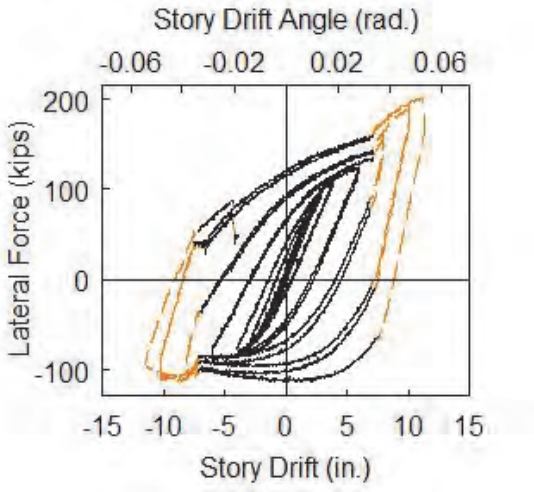

(b) Lateral Force vs. *SDA*

Figure 7.12 Specimen 21M-VAU-BC: End Rotation History and the Corresponding Global Response

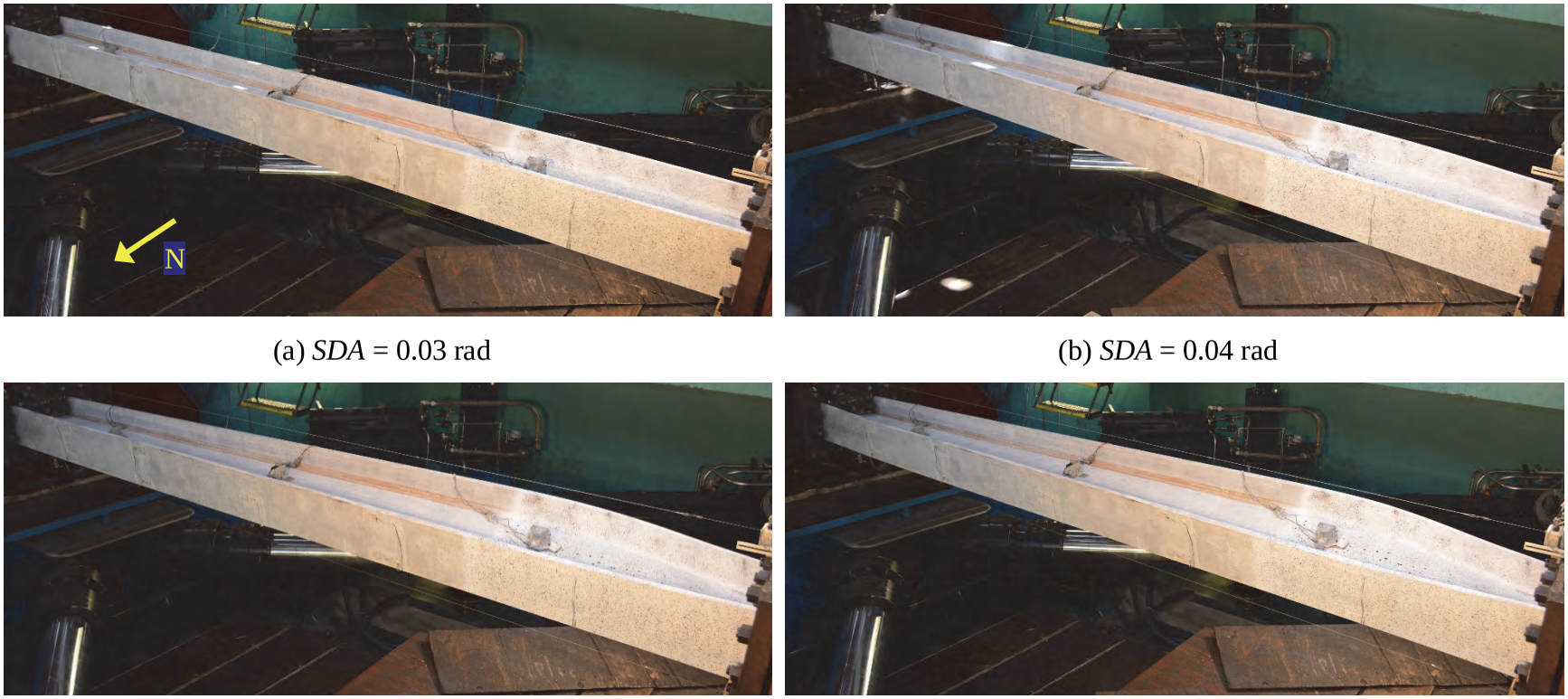

(a) *SDA* = 0.03 rad

(b) *SDA* = 0.04 rad

(c) *SDA* = 0.05 rad

(d) *SDA* = 0.055 rad

Figure 7.13 Specimen 21M-VAU-BC: Overall Yielding and Buckling Progression

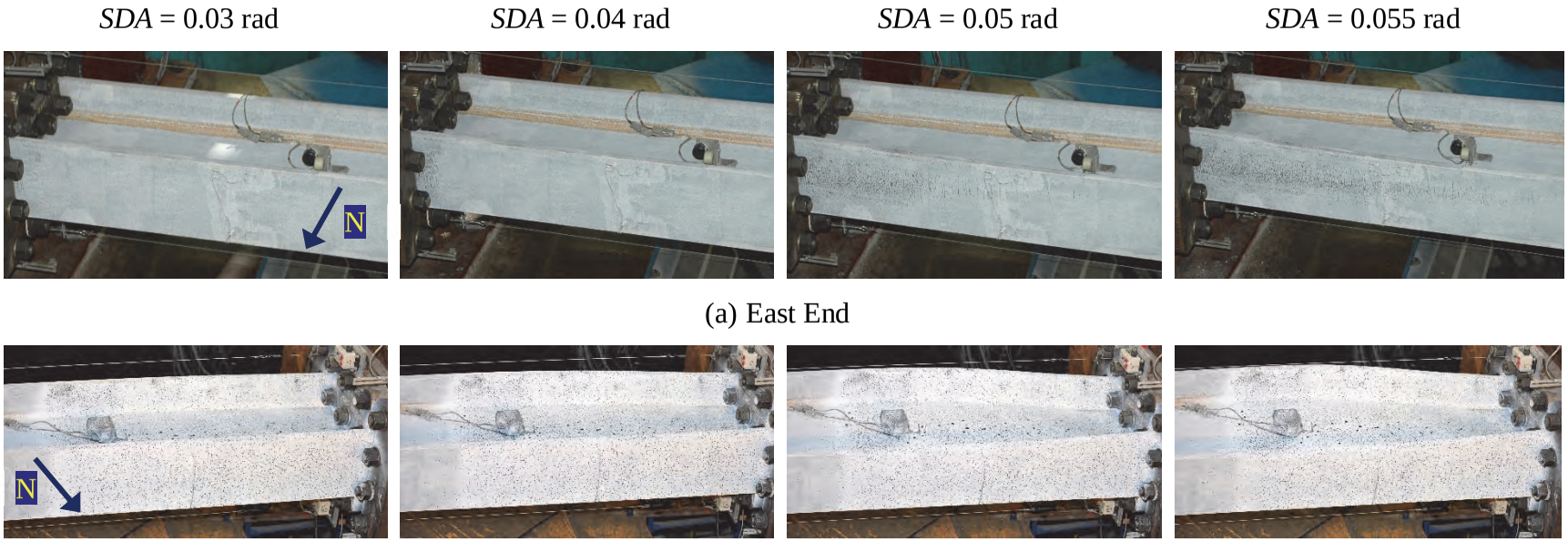

(a) East End

(b) West End

Figure 7.14 Specimen 21M-VAU-BC: Yielding and Buckling Progression at Member Ends

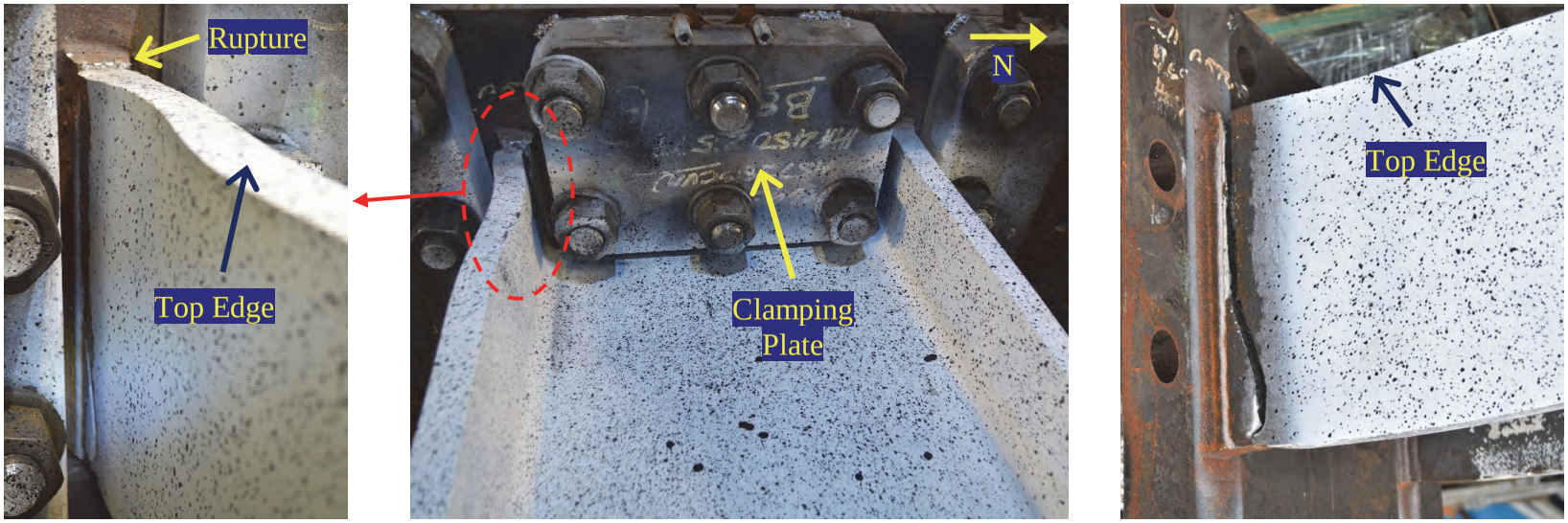

(a) *SDA* = 0.055 rad (b) Inspection after Test

Figure 7.15 Specimen 21M-VAU-BC: Rupture at Southwest Flange

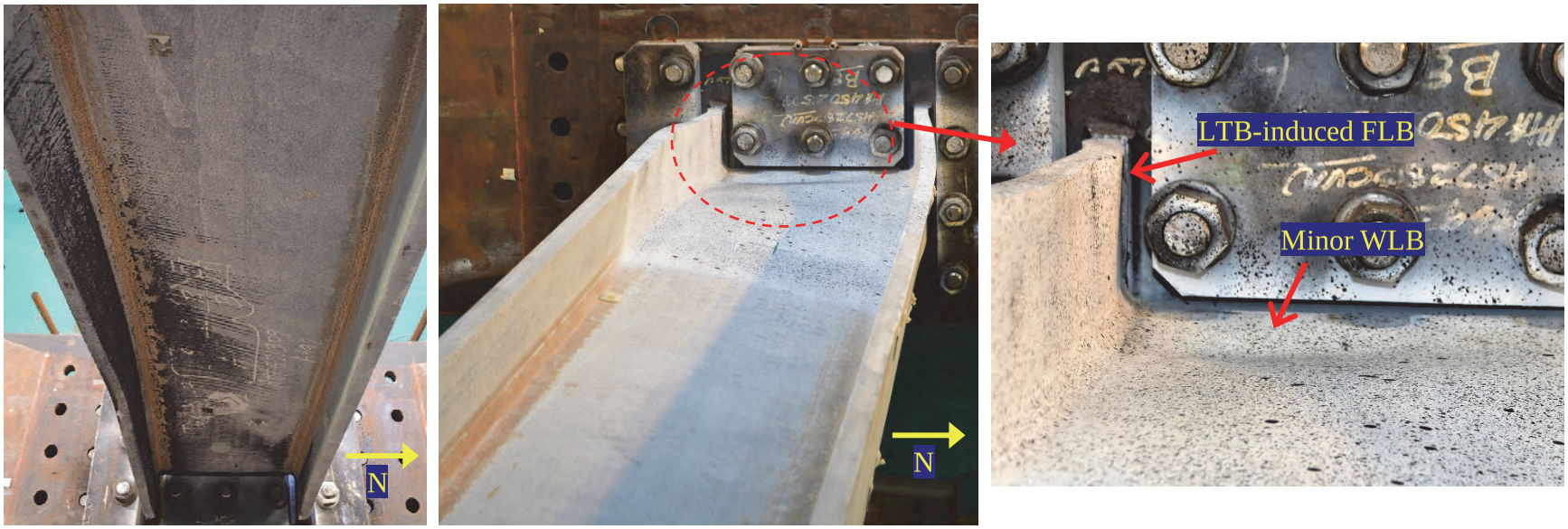

(a) Underside (b) Buckling Pattern (c) Detail

Figure 7.16 Specimen 21M-VAU-BC: Web Deformation at End of Test (West End)

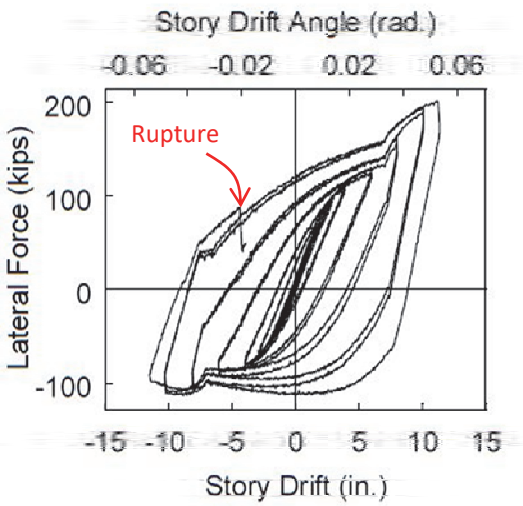

(a) Lateral Force vs. *SDA*

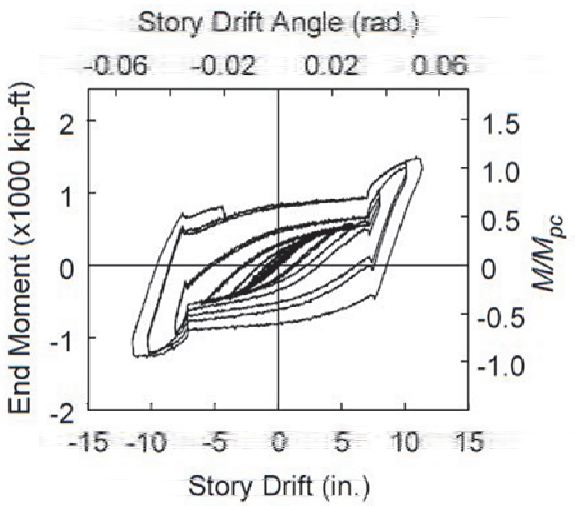

(b) East End Moment vs. *SDA*

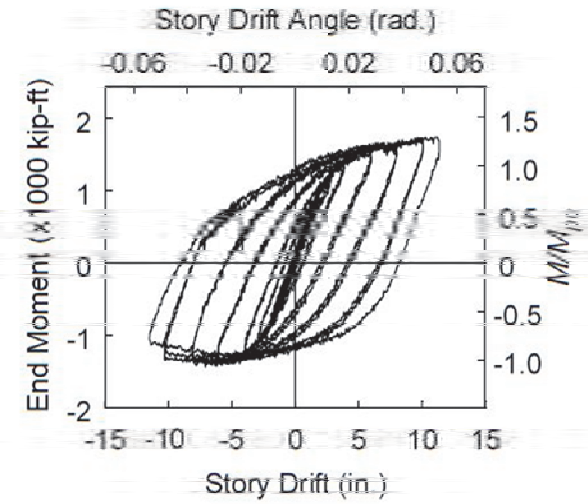

(c) West End Moment vs. *SDA*

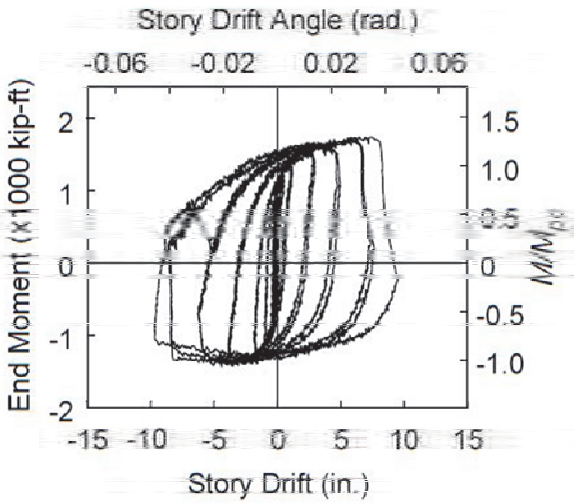

(d) West End Moment vs. Plastic *SDA*

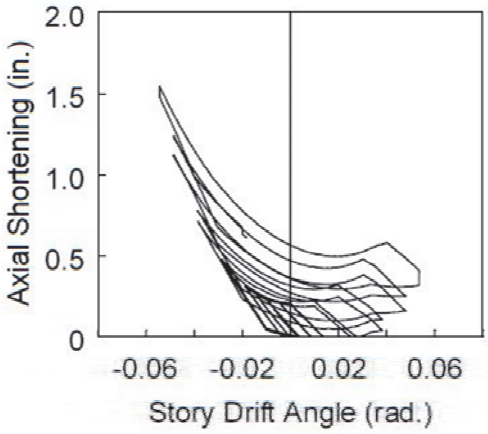

(e) Axial Shortening vs. *SDA*

Figure 7.17 Specimen 21M-VAU-BC: Global Responses

7.2.5 Specimen 21M-NF

Figure 7.18(a) shows the near-fault loading protocol, which is characterized by its large initial pulse and the following, smaller drift cycles that oscillate about a level of residual drift. The specimen underwent all these cycles but did not exhibit significant damage. Thus, after this "first run," the same loading protocol was applied from the 4 % residual drift as shown in Figure 7.18(b); the "second run" refers to this portion of the test. Although the specimen was subjected to a constant level of axial load, it underwent asymmetric lateral drift loading: except for the first negative drift peak in the combined near-fault loading protocol, all cycles were in a positive drift range.

Figure 7.19 illustrates the overall yielding and buckling progression. At the first -2 % drift, the specimen already experienced plastic deformation. In the following positive excursion to +6 % drift, LTB of the specimen initiated with upward and downward amplitudes at the northwest and southeast flanges (i.e., compression flanges in positive drift), respectively. Since plastic deformation had already established, the southwest and northeast flanges (i.e., compression flanges in negative drift) experienced in-plane flexural compression in the following negative excursion to +1 % drift, even though the specimen was not displaced into the negative drift range; Figure 7.20(a) shows the corresponding expansion of flaking. LTB of the specimen aggravated slightly but less aggressive than that observed during the former positive excursion. For the remaining first run cycles, LTB exacerbated more in the positive excursions than in the negative excursions, demonstrating the effect of the asymmetrical lateral drift loading. Figure 7.24(b) shows a slight flexural strength degradation in the positive excursions of the first run.

In the positive excursion to +10 % drift during the second run, LTB of the specimen aggravated drastically with significant out-of-plane amplitudes at the compression flanges in the positive drift as shown in Figure 7.19(b) and Figure 7.21. Together with the very large P-Δ moment, this led to a drastic flexural strength degradation as shown in Figure 7.24(b). Like the first run, LTB exacerbated in the positive excursions; unlike the first run, it appeared that LTB amplitudes recovered somewhat during the negative excursions. Since axial shortening grew proportionally to the out-of-plane amplitudes, it also recovered somewhat in the negative excursions as shown in Figure 7.24(d). Again, only the flexural strength in the positive excursions degraded while that in the negative excursions remained

relatively stable because of the asymmetrical lateral drift loading. The test was terminated due to excessive reduction in lateral force resistance.

LTB-induced flange local buckling configurations of this specimen were like those of Specimen 21M-VAM as shown in Figure 7.22; those at the west end appeared to be triggered primarily by out-of-plane stresses, while those at the east end later appeared to be induced primarily by warping stresses due to significant twisting at the east end as shown in Figure 7.23. Influenced by web-flange interactions, the web at each end also buckled locally in the direction that conformed to the flange local buckling configurations.

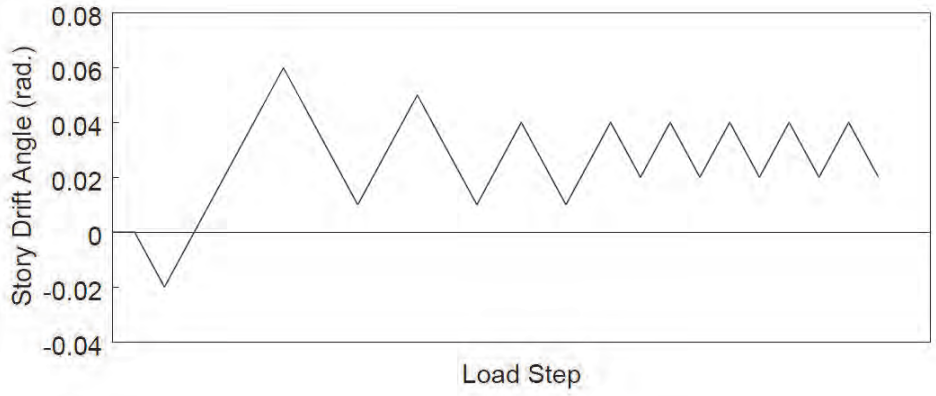

(a) Near-Fault Loading Protocol

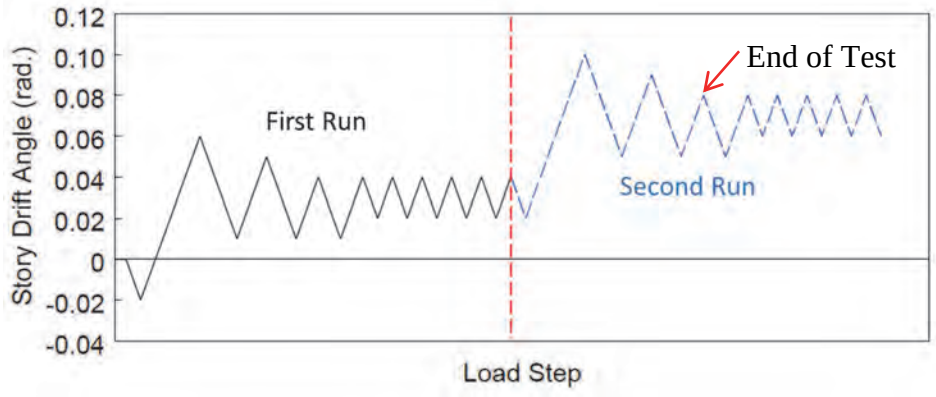

(b) Combined Near-Fault Loading Protocol

Figure 7.18 Specimen 21M-NF: Near-Fault Loading Protocols

SDA = -0.02 rad

SDA = +0.06 rad

SDA = +0.01 rad

SDA = +0.05 rad

(a) First Run

SDA = +0.02 rad

SDA = +0.10 rad

SDA = +0.05 rad

End of Test

(b) Second Run

Figure 7.19 Specimen 21M-NF: Overall Yielding and Buckling Progression

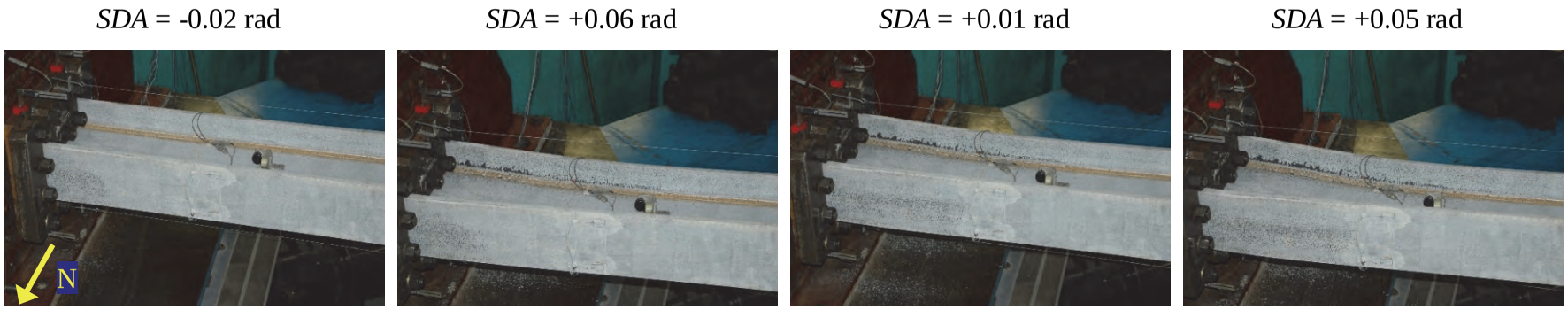

(a) East End

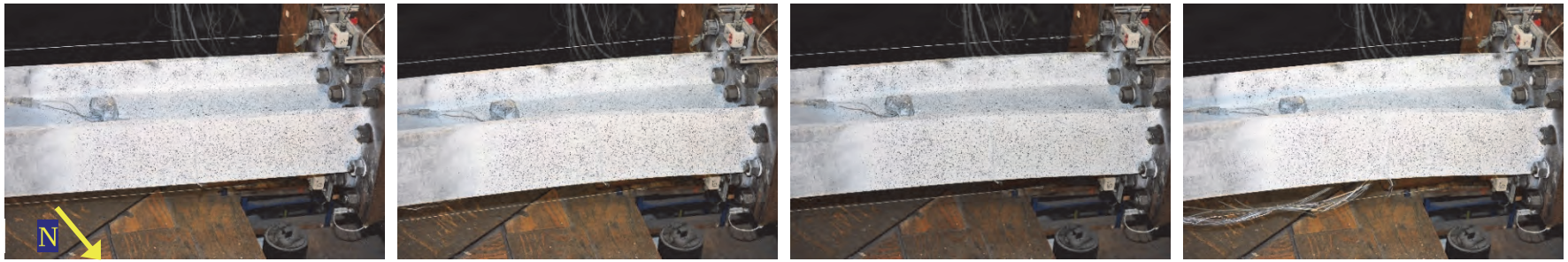

(b) West End

Figure 7.20 Specimen 21M-NF: Yielding and Buckling Progression at Member Ends (Fisrt Run)

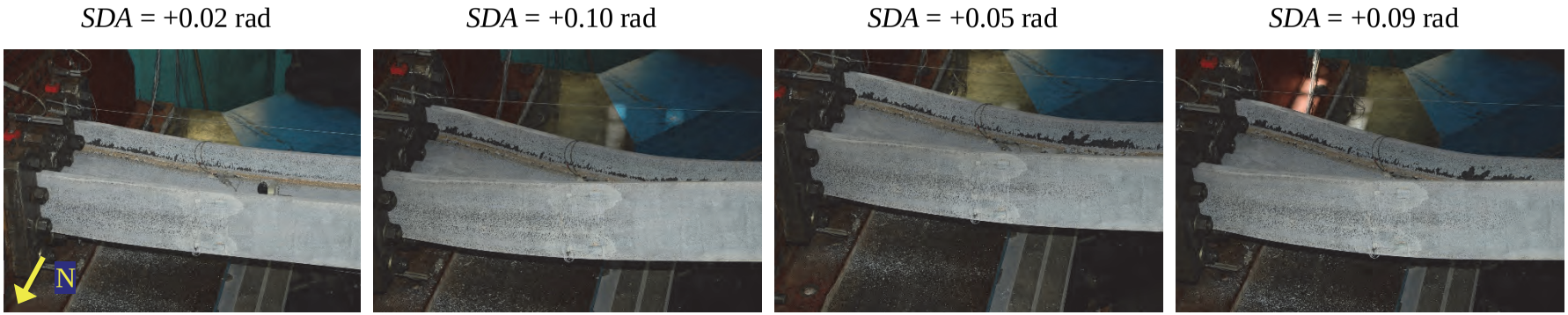

(a) East End

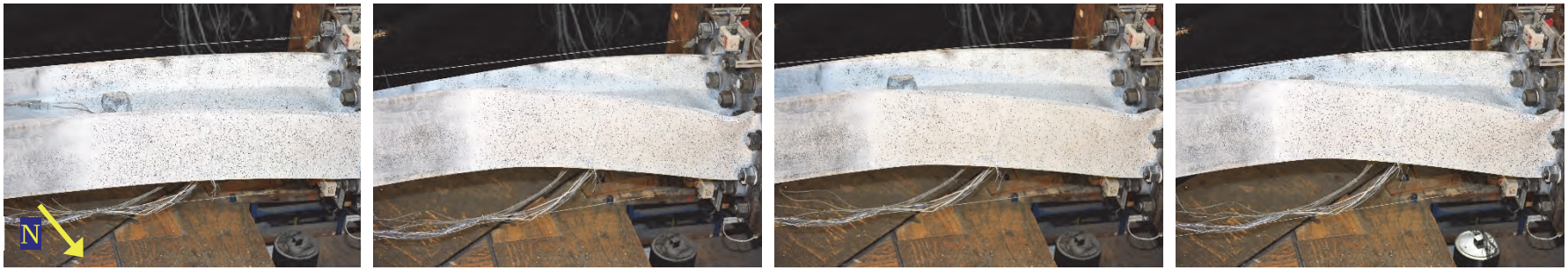

(b) West End

Figure 7.21 Specimen 21M-NF: Yielding and Buckling Progression at Member Ends (Second Run)

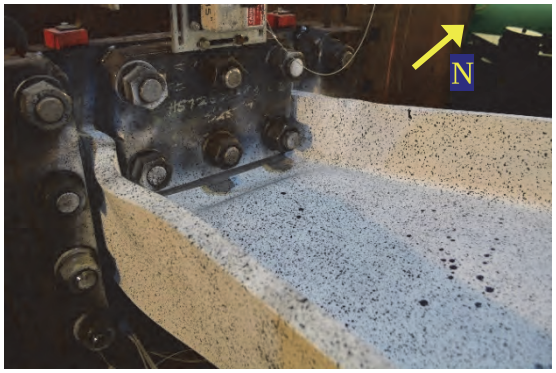

(a) Southwest Flange

(b) Northwest Flange

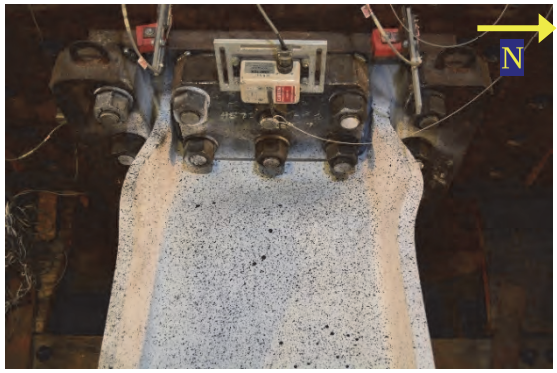

(c) West End (Top)

(d) Southeast Flange

(e) East End (Top)

(f) East End (Bottom)

Figure 7.22 Specimen 21M-NF: LTB-Induced Local Buckling at End of Test

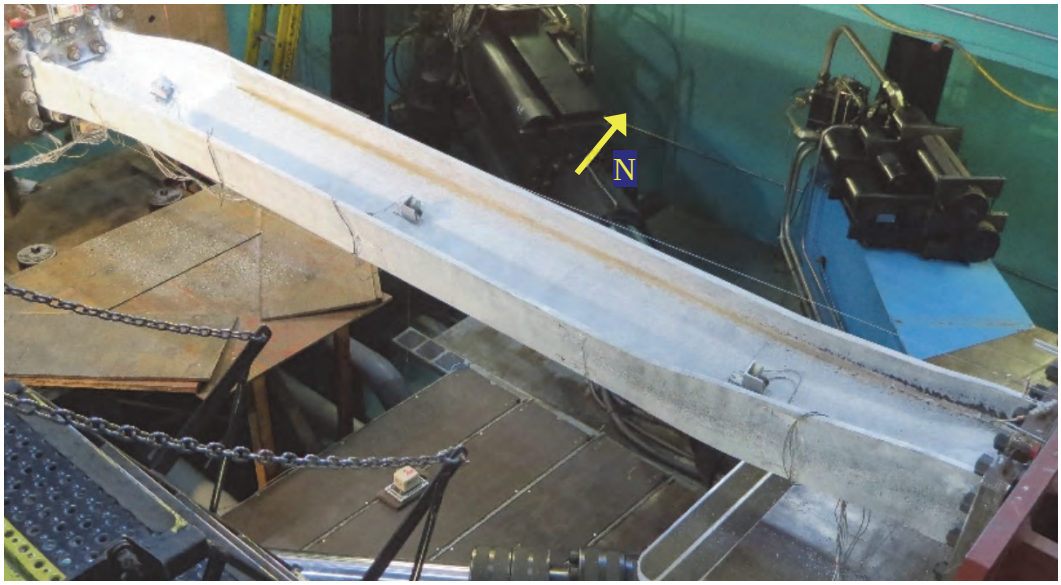

Figure 7.23 Specimen 21M-NF: Significant Twisting at East End

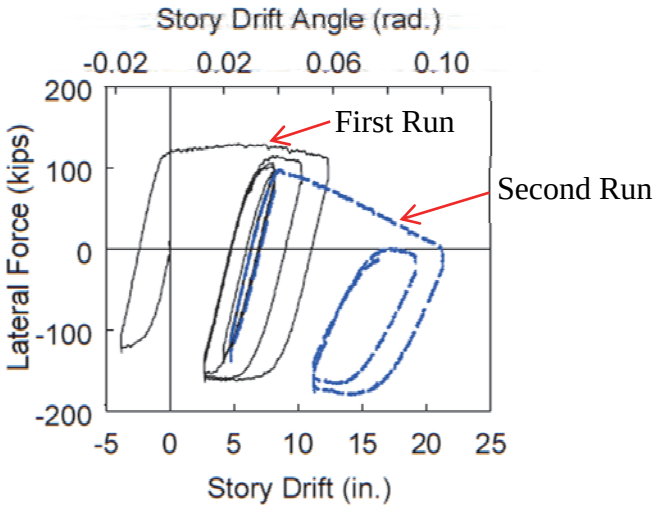

(a) Lateral Force vs. *SDA*

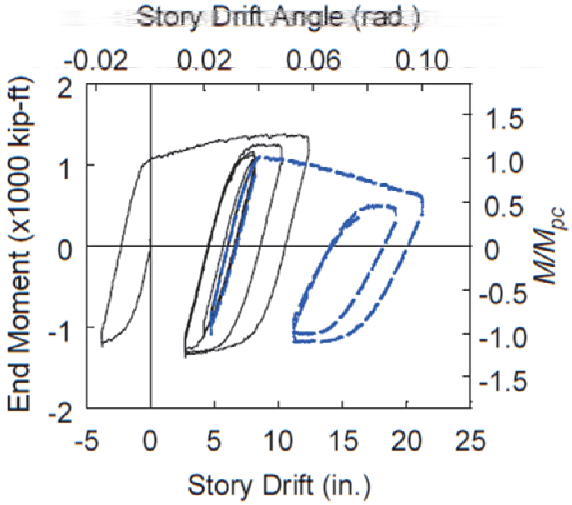

(b) End Moment vs. *SDA*

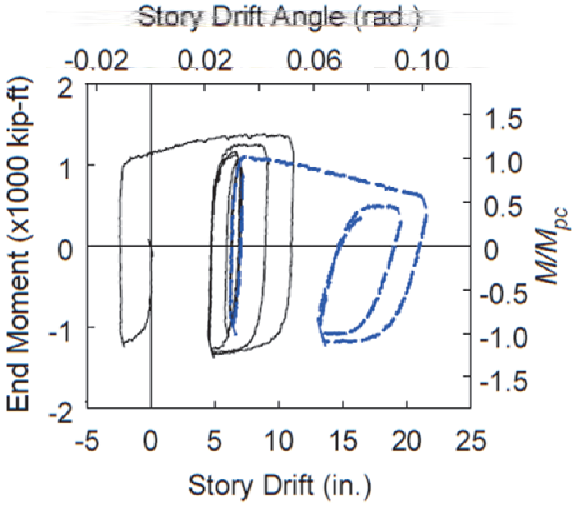

(c) End Moment vs. Plastic *SDA*

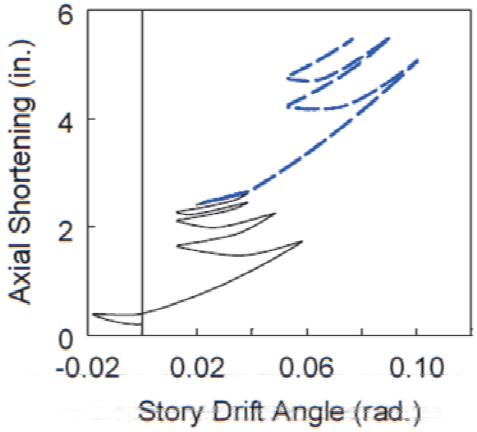

(d) Axial Shortening vs. *SDA*

Figure 7.24 Specimen 21M-NF: Global Responses

7.2.6 Concluding Remarks

Column end moment and axial shortening responses of all W18×130 specimens tested in Phases 2A and 2B are shown in Figure 7.25 and Figure 7.26, respectively. Comparisons can be made as follows:

(1) Flexural strengths of Specimens 16M and 16M-BC are similar in magnitude since the two specimens sustained the same level of axial compression ($C_a = 0.4$). Specimen 21M-VAM experienced varying axial compression with C_a ranging from 0.1 in the positive excursions to 0.7 in the negative excursions with a mean value of 0.4. This causes its end moment response to be asymmetrical with higher and lower flexural strength relative to those of the former specimens in the positive and negative excursions respectively.

(2) Compared to Specimen 21M-VAM, Specimens 21M-VAU and 21M-VAU-BC exhibit increased flexural and ductility capacities as their axial load range is offset from $C_a = 0.1 - 0.7$ to $C_a =$ -0.2 $-$ 0.4. Their end moment responses are also less asymmetrical compared to that of Specimen 21M-VAM because they sustained axial tension and compression that are relatively close in magnitude (0.2 and 0.4). For Specimen 21M-VAM, the magnitudes of the lowest and highest compression (0.1 and 0.7) are much more different.

(3) While flexural strength degradation is observed in both the positive and negative excursions for constant axial load tests, it is only observed in the negative excursions for varying axial load tests.

(4) Specimens 16M-BC and 21M-VAU-BC with fixed-rotating boundary conditions exhibit lower elastic flexural stiffness than that of their counterparts with fixed-fixed boundary conditions, i.e., Specimens 16M and 21M-VAU, respectively. The former also sustained a higher drift level than the latter before significant strength degradation or a column flange CJP weld rupture occurred.

(5) Specimen 21M-NF with the near-fault loading protocol exhibits a relatively stable end moment response compared to others despite being displaced to 6 % drift during the first run test (see Section 7.2.5).

(6) Specimens 16M, 16M-BC, and 21M-VAM experienced LTB movements at 2 %, 3 %, and 2 % drifts, respectively. Their axial shortening was relatively limited before the

onset of LTB. Such grew at an increasing rate proportional to the out-of-plane amplitude once LTB initiated. All three specimens exhibited similar out-of-plane amplitudes when their flexural strengths degraded significantly, prompting termination of the tests. As a result, they exhibited relatively similar level of axial shorting (roughly 4 to 5 in.) at the end of the tests.

(7) With a varying axial load that oscillated below the medium level (i.e., $C_a \leq 0.4$), Specimens 21M-VAU and 21M-VAU-BC exhibited significantly less axial shortening compared to others. This is because their LTB movements were not triggered until 4 % drift and did not exacerbate much before the specimens experienced column flange CJP weld ruptures.

(8) In constant axial compression tests, axial shortening remained constant and exacerbated during each in-plane flexural unloading and reloading branch, respectively. In contrast, that of varying axial load tests recovered (i.e., reduced in magnitude) in the positive excursions due to the simultaneous reduction of axial and in-plane flexural compression; it then aggravated in the negative excursions, corresponding to when axial load progressively returned to its highest compressive level.

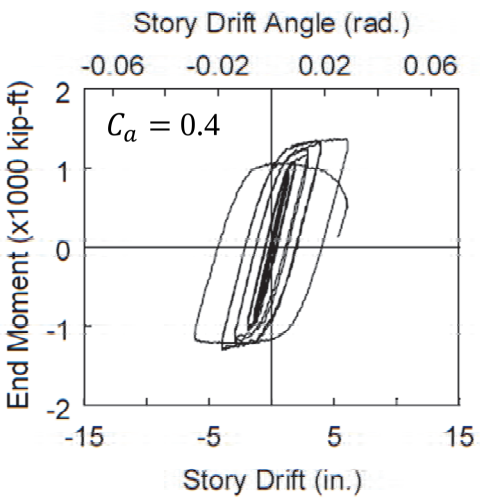

(a) Specimen 16M

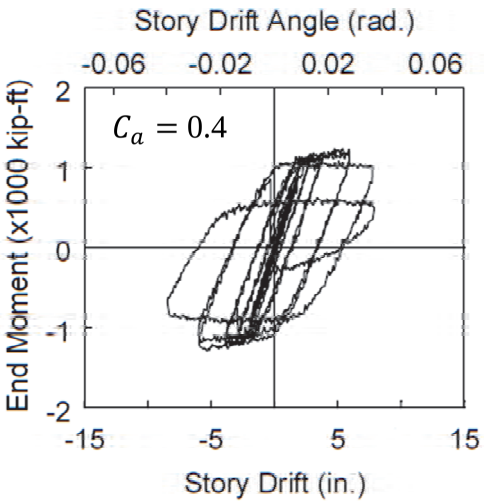

(b) Specimen 16M-BC

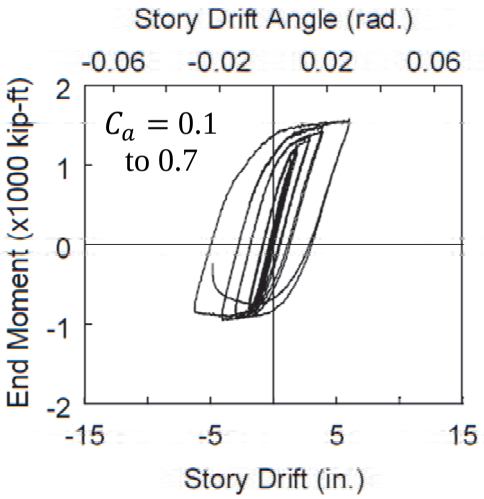

(c) Specimen 21M-VAM

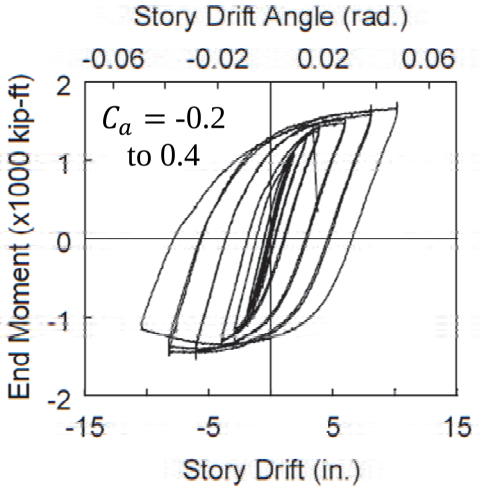

(d) Specimen 21M-VAU

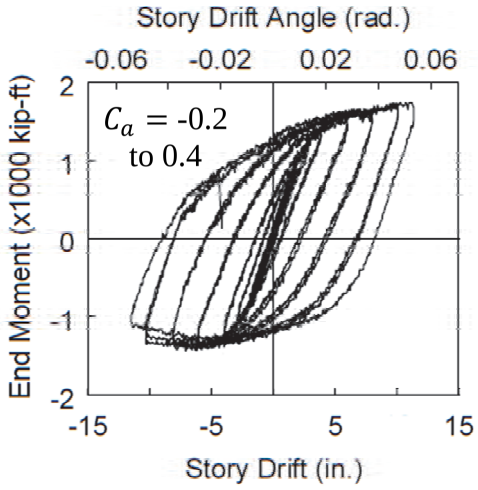

(e) Specimen 21M-VAU-BC

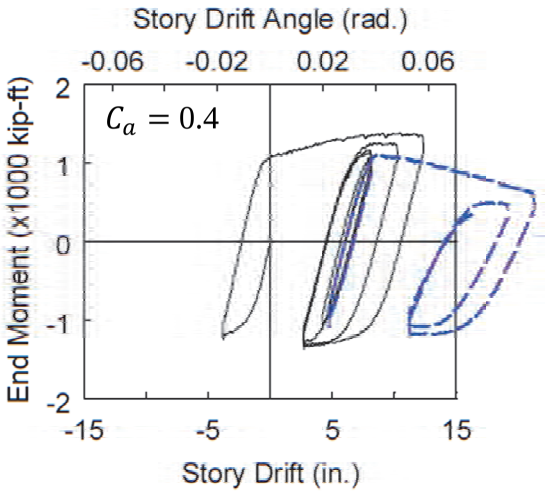

(f) Specimen 21M-NF

Figure 7.25 W18×130 Specimens (Groups 16 and 21): West End Moment Repsonse

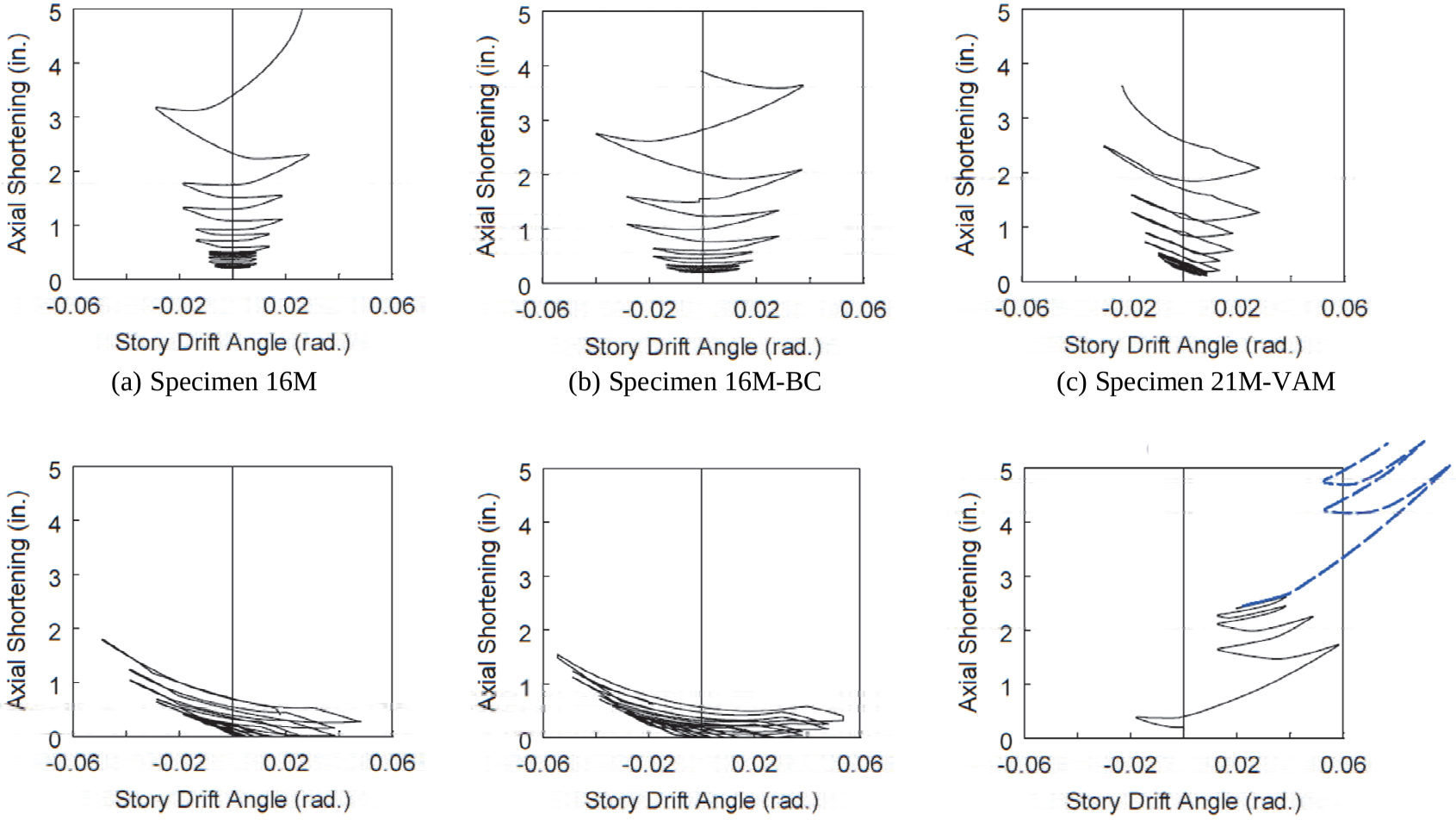

(a) Specimen 16M (b) Specimen 16M-BC (c) Specimen 21M-VAM

(d) Specimen 21M-VAU (e) Specimen 21M-VAU-BC (f) Specimen 21M-NF

Figure 7.26 W18×130 Specimens (Groups 16 and 21): Axial Shortening Repsonse

7.3 Group 22 Specimen: Section W30×148

7.3.1 General

Section W30×148 was assigned to Group 22 in addition to the three other W30 sections—W30×261, W30×173, and W30×90—that were assigned to Groups 12, 13, and 14 of Phase 2A testing, respectively. This section had a flange slenderness ratio similar to Group 12 specimens, but its web slenderness ratio was much larger. This section is classified as highly ductile per AISC 341, but it is classified as slender as a compression member per AISC 360. It also has a much larger L/r_y ratio (= 95.7) compared to Group 12 and 13 specimens (= 61.2 and 63.2). Specimen 22L was subjected to constant axial compression with C_a = 0.2.

7.3.2 Test Results

The governing failure mode of Specimen 22L is CB with the reverse-curvature out-of-plane buckling configuration; yielding and buckling progression is shown in Figure 7.27 and Figure 7.28. Local buckling at the member ends was not observed before the sloped flaking pattern and LTB movements initiated at 1.5 % and 2 % drift, respectively. LTB of the specimen exacerbated at 3 % and 4 % drifts: compression flanges in positive drift and those in negative drift buckled out of plane more during the positive and negative excursions of each cycle, respectively. These movements caused significant twisting motion in the specimen. East and west flanges buckled downward and upward, respectively, forming the reverse-curvature configuration.

Significant LTB movements induced flange local buckling at both ends, which formed in compliance with the out-of-plane curvatures of the flanges. Influenced by web-flange interactions, the web at each end also buckled locally in the direction that conformed to the flange local buckling configurations as shown in Figure 7.29. Although it may appear that a half-wave buckle could be observed at each top and bottom half-width flange of the same flange, assembling the ALB pattern, the amplitude of the LTB-induced half-wave buckle was clearly more significant than the another. It appeared, therefore, that the latter was a product of the former, forming through web-flange interactions.

Figure 7.30 shows the global responses. Flexural strength remained stable during the 2 % drift cycles even though some LTB movements had initiated. It degraded significantly

during the 3 % and 4 % drift cycles when LTB became severe. Due to geometry of the deformed specimen, axial shortening grew proportionally to the amplitudes of the out-of-plane buckling; it grew at an increasing rate at 3 % and 4 % drifts.

7.3.3 Concluding Remarks

The predicted and observed buckling modes (CB) were consistent, indicating that the buckling classification procedure outlined in Section 2.8 was not affected by the section depth.

(a) *SDA* = 0.015 rad

(b) *SDA* = 0.02 rad

(c) *SDA* = 0.03 rad

(d) *SDA* = 0.04 rad

Figure 7.27 Specimen 22L: Overall Yielding and Buckling Progression

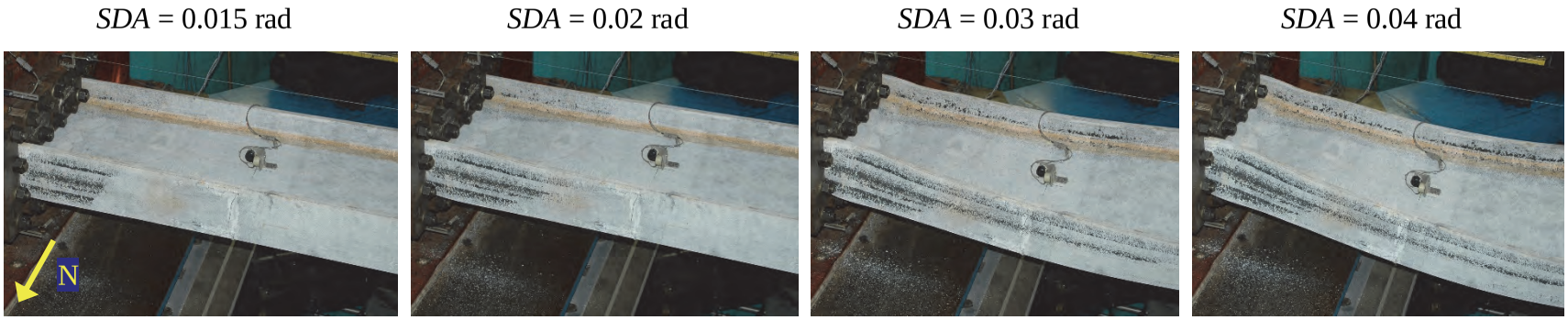

(a) East End

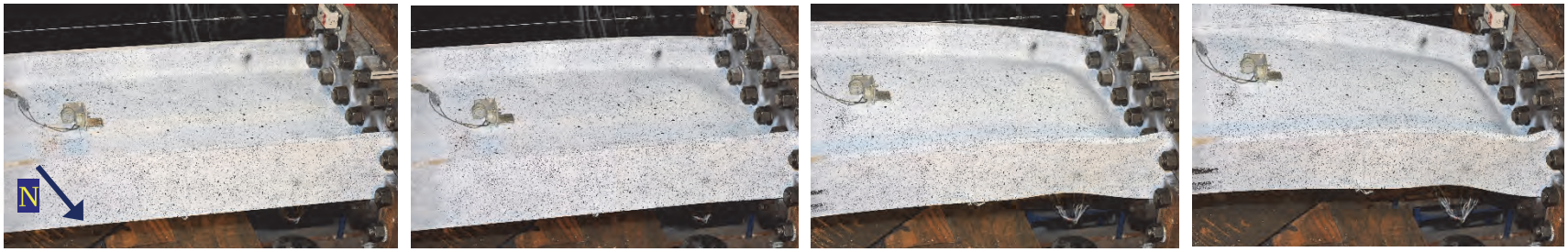

(b) West End

Figure 7.28 Specimen 22L: Yielding and Buckling Progression at Member Ends

(a) Southwest Flange

(b) Northwest Flange

(c) Northeast Flange

(d) East End (Top)

Figure 7.29 Specimen 22L: LTB-Induced Local Buckling at End of Test

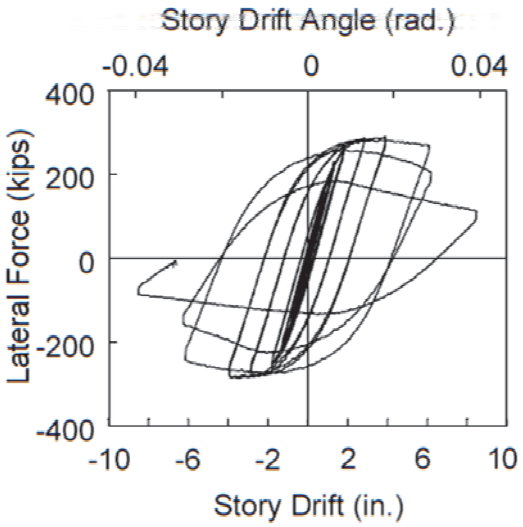

(a) Lateral Force vs. *SDA*

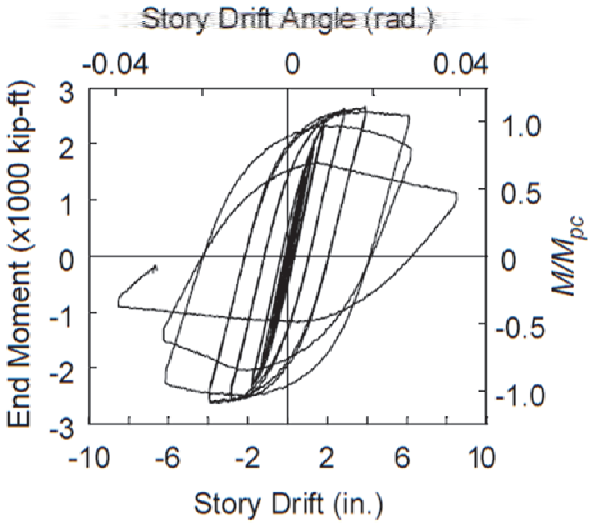

(b) End Moment vs. *SDA*

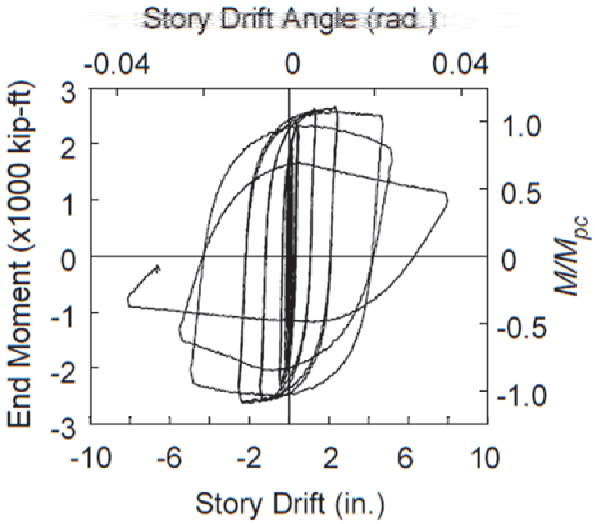

(c) End Moment vs. Plastic *SDA*

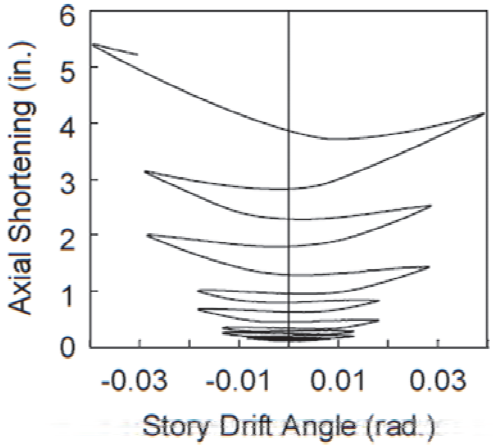

(d) Axial Shortening vs. *SDA*

Figure 7.30 Specimen 22L: Global Responses

7.4 Group 23 Specimen: Section W18×60

7.4.1 General

Group 23 was another group with a W18 section (W18×60) in addition to Groups 15, 16, 17, and 21. Its flange slenderness ratio was slightly greater than that of Group 16 specimens (W18×130), which failed in the CB mode. Its web slenderness ratio was similar to that of Group 17 specimens (W18×76), which experienced the ALB mode. Its L/r_y ratio (= 100) was slenderer than those of Groups 16 and 17 specimens. Specimen 23L was subjected to constant axial compression with C_a = 0.2.

7.4.2 Test Results

The column exhibited the ALB failure mode; yielding and buckling progression is illustrated in Figure 7.31. Similar to Specimen 17L, the ALB sequence of this specimen initiated with one half-wave buckle set at both column ends at 2 % drift. At 3 % drift, an additional half-wave buckle set developed at the east end, making a full-wave buckle set; this was not observed at the west end. The full-wave ALB configuration at the east end appeared to trigger an out-of-plane, rigid-body translation of the column portion between the buckled regions as demonstrated in Figure 7.32; the out-of-plane displacement history in Figure 7.34(e) confirmed that significant out-of-plane displacement initiated during the 3 % drift cycles. This phenomenon was not associated with LTB. The test was terminated due to the excessive local buckling and significant flexural strength degradation. Figure 7.33 shows local buckling configurations at the end of the test.

Figure 7.34 shows the global responses. Flexural strength degradation initiated at 2 % drift, corresponding to the onset of ALB, which also triggered significant axial shortening in the column as its amplitudes increased.

7.4.3 Concluding Remarks

This specimen was predicted to fail in the CB mode with the classifying parameter ζ of 8.1. Note that this value was close to the upper limit of the proposed ALB classification range ($4.25 \leq \zeta \leq 8$: Ozkula et al. 2017). Although tendency for CB mode showed early [see the sloped flaking pattern at 1 % drift in Figure 7.31(a)], ALB took over and governed the failure mode, mainly due to the high web slenderness.

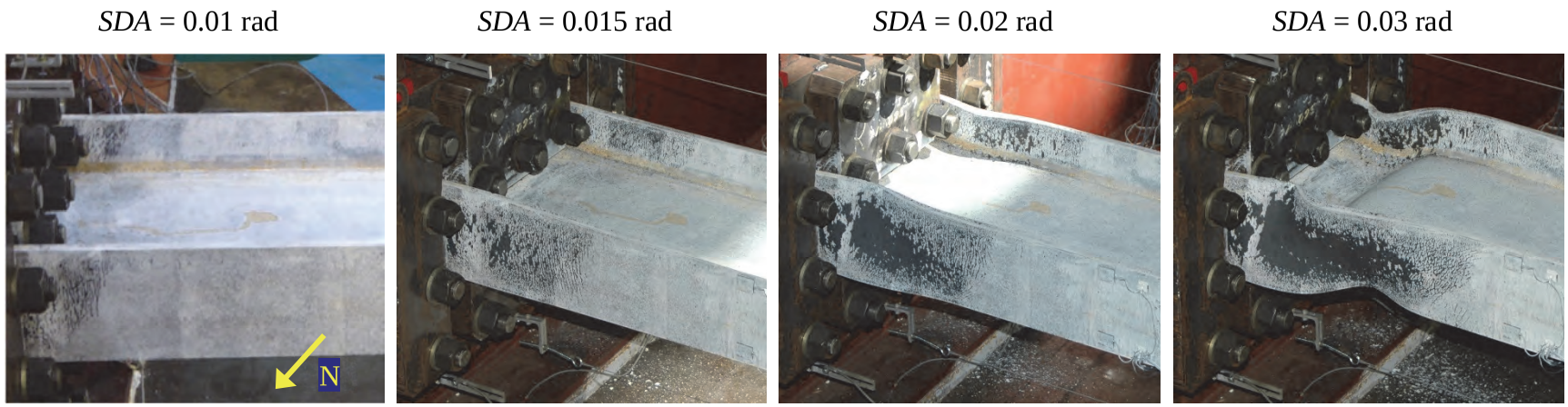

(a) East End

(b) West End

Figure 7.31 Specimen 23L: Yielding and Buckling Progression at Member Ends

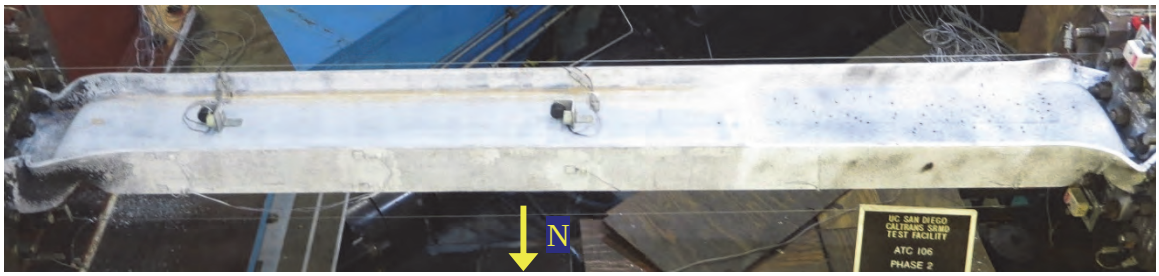

Figure 7.32 Specimen 23L: Global Out-of-Plane Movement

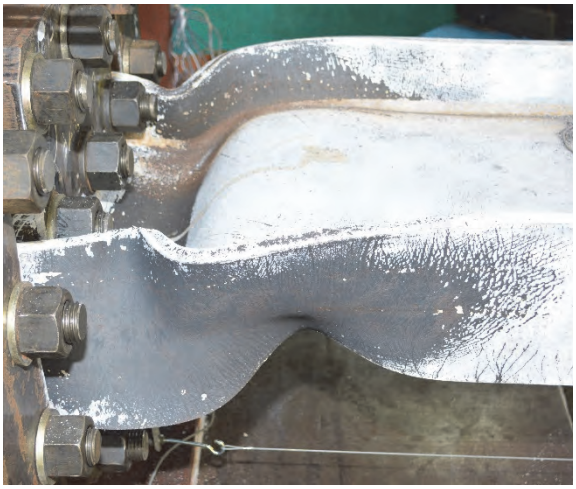

(a) Northeast Flange

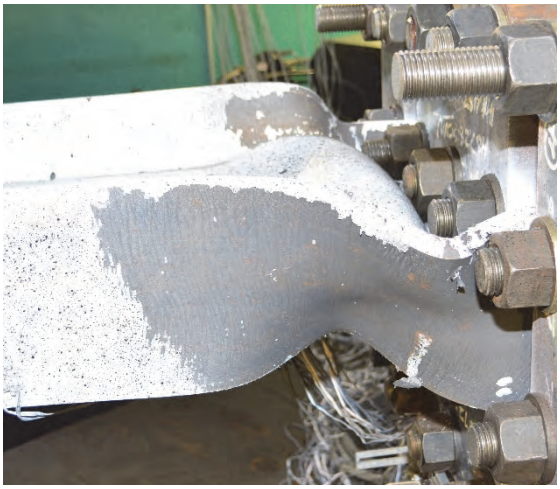

(b) Northwest Flange

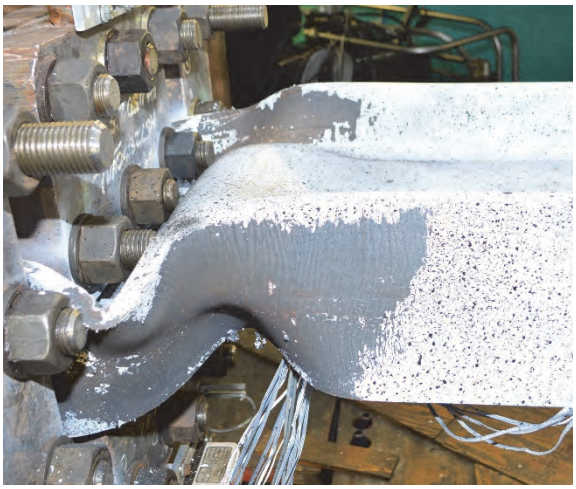

(c) Southwest Flange

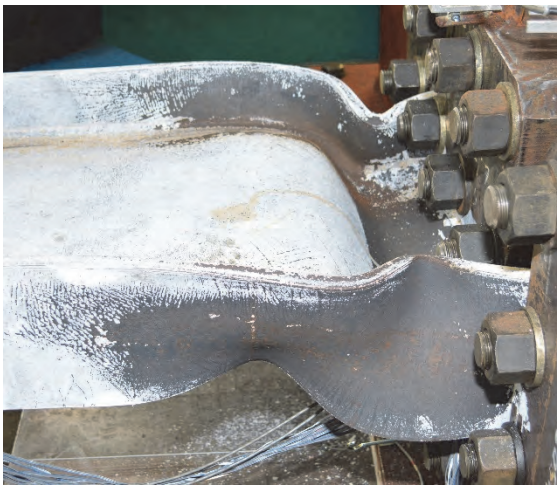

(d) Southeast Flange

Figure 7.33 Specimen 23L: Local Buckling at End of Test

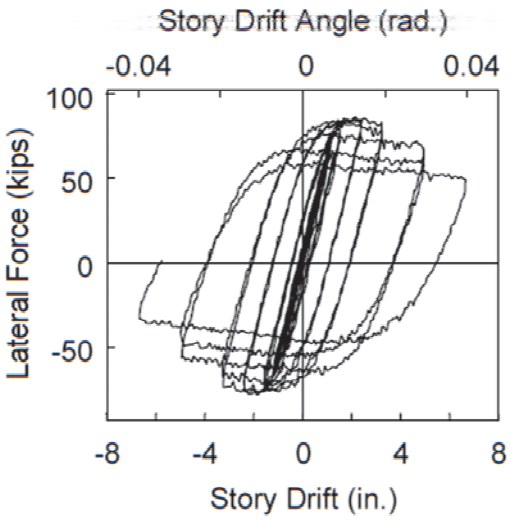

(a) Lateral Force vs. *SDA*

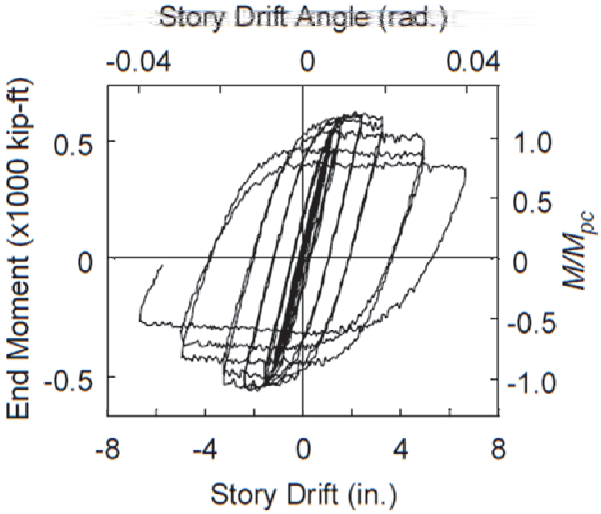

(b) End Moment vs. *SDA*

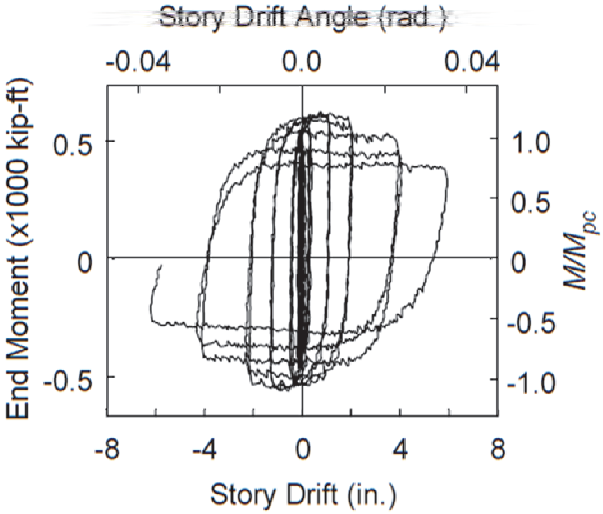

(c) End Moment vs. Plastic *SDA*

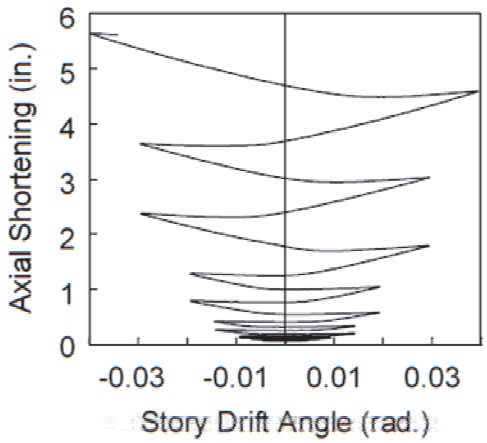

(d) Axial Shortening vs. *SDA*

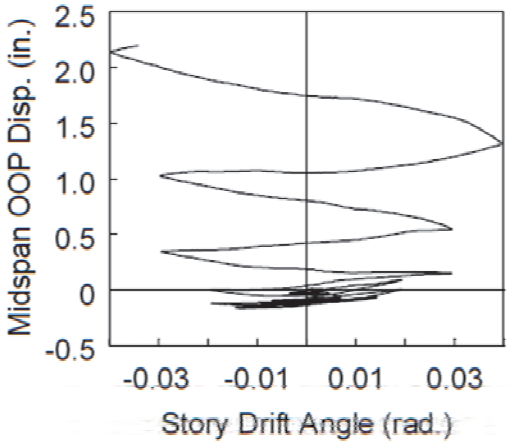

(e) Midspan OOP Disp. vs. *SDA*

Figure 7.34 Specimen 23L: Global Responses

7.5 Group 24 Specimen: Section W14×82

7.5.1 General

Group 24 was assigned with W14×82 section, which was one of the three W14 sections tested in Phase 2B. W14 sections were commonly referred to as “shallow” columns. Newell and Uang (2008) tested nine heavy W14 sections; all exhibited very stable cyclic responses. Due to their compact web slenderness, they experienced the SFB failure mode with minor or no web local buckling. To demonstrate that some “shallow” sections may also behave like “deep” sections with other types of buckling mode, lighter and slenderer W14 sections (W14×82 in this group and W14×53 in Group 25) were tested in this program. W14×132 was selected for Group 26 to repeat the test done by Newell and Uang. Among the lighter two W14 sections, W14×82 was more compact than W14×53 with respect to both the section and member slenderness. Specimen 24L was subjected to constant axial compression with C_a = 0.2.

7.5.2 Test Results

The specimen exhibited the ALB failure mode; yielding and buckling progression is illustrated in Figure 7.35. A sloped flaking pattern indicating the tendency for CB was visible up to 2 % drift. But such tendency was overtaken by the ALB mode at higher drift levels. At 3 % drift, minor flange local buckling was observed at both ends; web local buckling was less noticeable. At 4 % and 5 % drifts, local buckling aggravated: the amplitudes of the buckled web and flanges increased and became obvious, resembling the ALB pattern. The deformed configurations of the specimen at the end of test are shown in Figure 7.36.

Figure 7.37 shows the global responses. Flexural strength degradation began during the 4 % drift cycles when local buckling exacerbated, which also triggered significant axial shortening as shown in Figure 7.37(d).

7.5.3 Concluding Remarks

The specimen showed the predicted ALB mode, demonstrating that some shallow columns behave like deeper columns and experienced the same buckling phenomena observed in the latter.

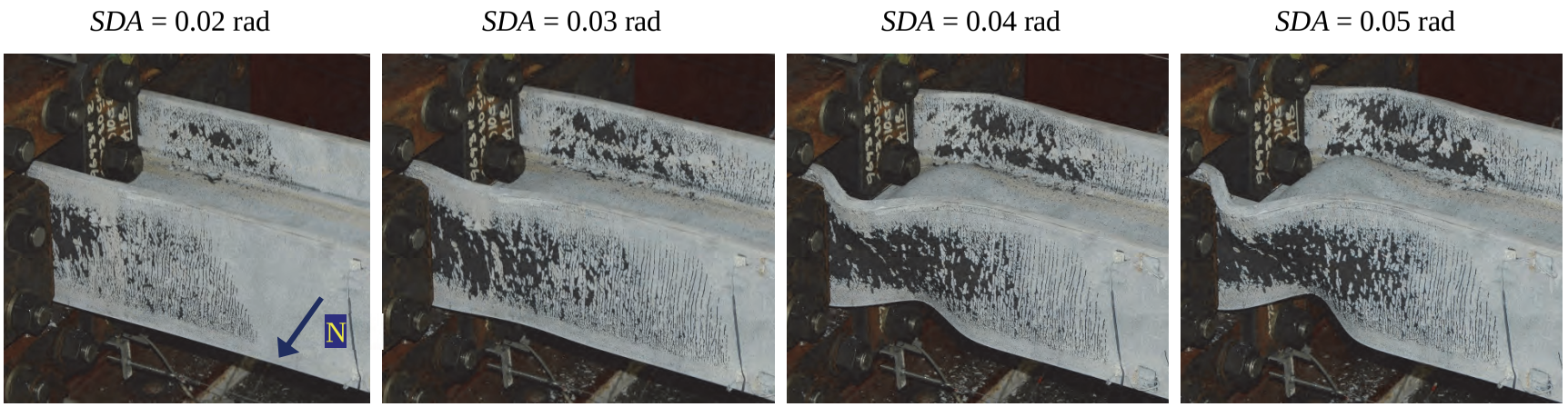

(a) East End

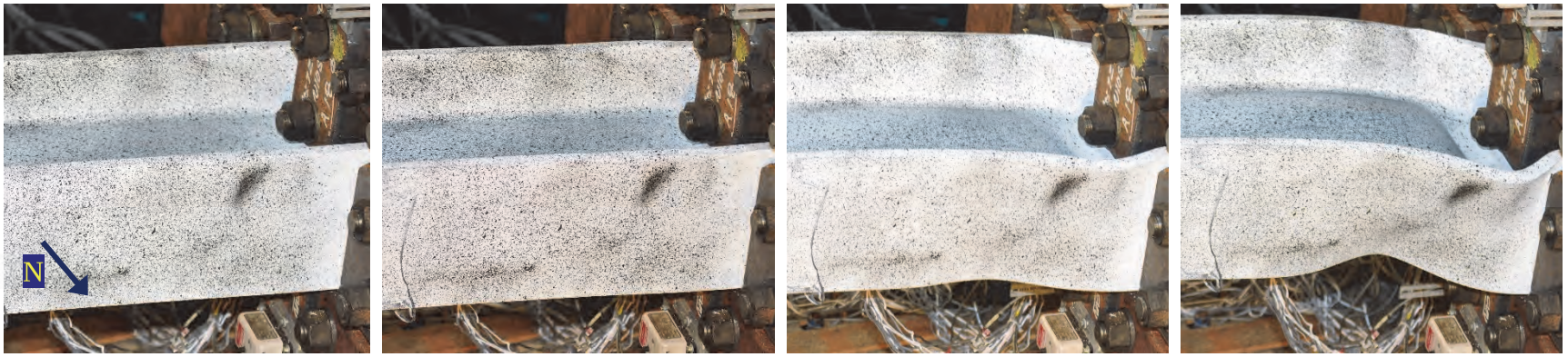

(b) West End

Figure 7.35 Specimen 24L: Yielding and Buckling Progression at Member Ends

(a) East End

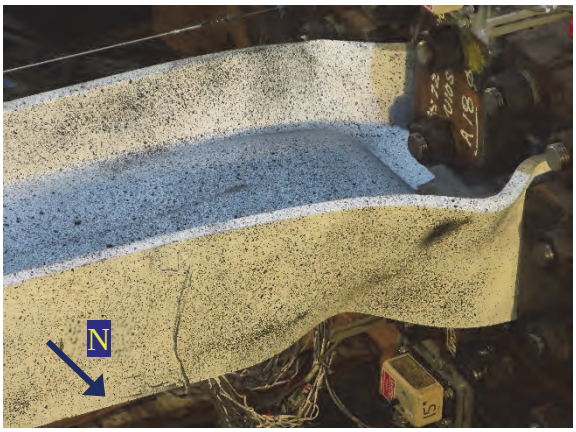

(b) West End

(c) Northeast Flange

(d) Northwest Flange

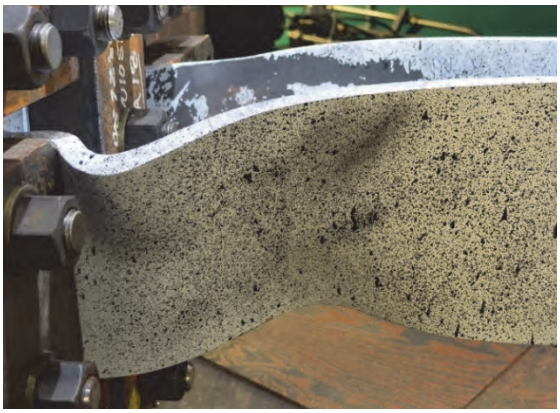

(e) Southwest Flange

(f) Southeast Flange

Figure 7.36 Specimen 24L: Local Buckling at End of Test

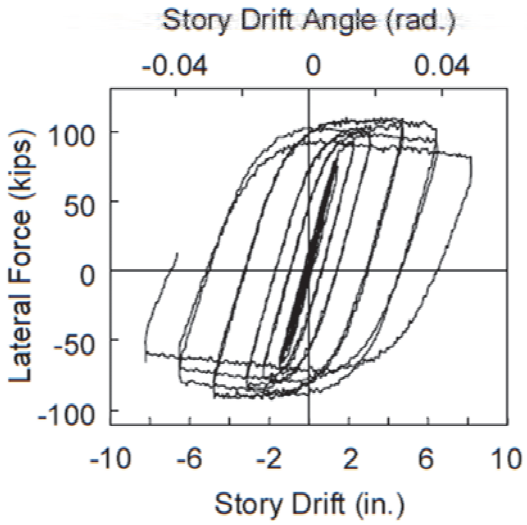

(a) Lateral Force vs. *SDA*

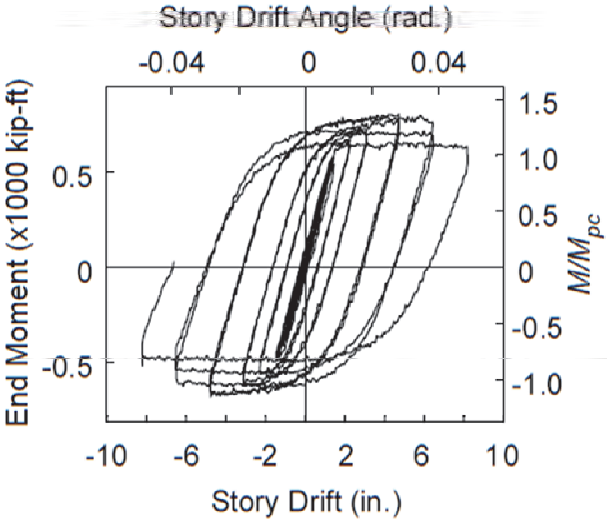

(b) End Moment vs. *SDA*

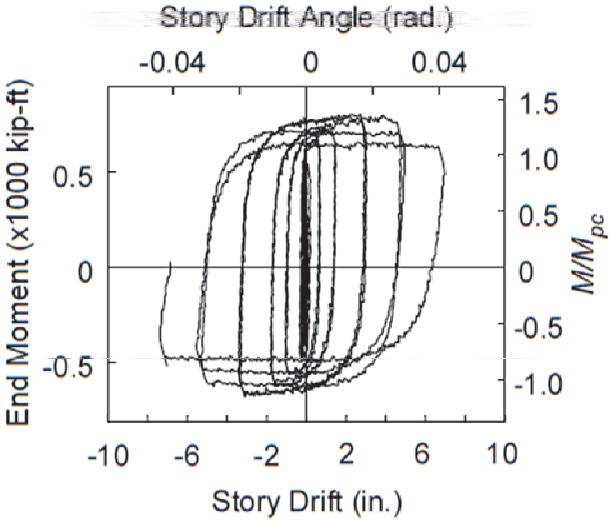

(c) End Moment vs. Plastic *SDA*

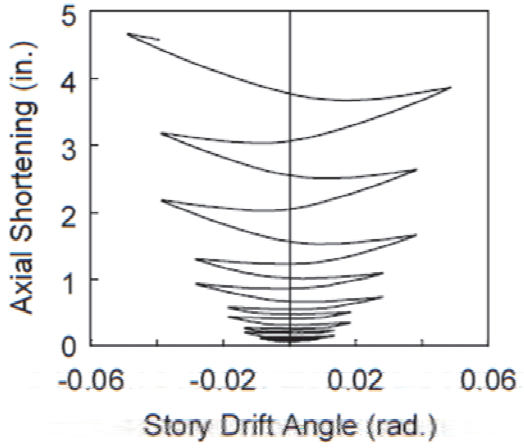

(d) Axial Shortening vs. *SDA*

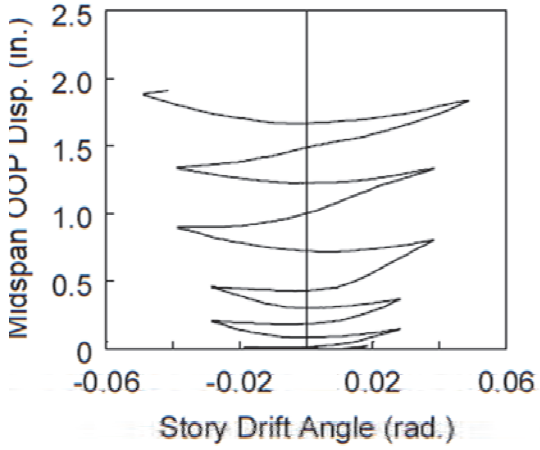

(e) Midspan OOP Disp. vs. *SDA*

Figure 7.37 Specimen 24L: Global Responses

7.6 Group 25 Specimen: Section W14×53

7.6.1 General

Group 25 specimen was the lightest W14 section tested in Phase 2B. Its flange slenderness ratio was comparable to that of Group 24, but its web slenderness and L/r_y ratios were the highest among the specimens with W14 sections. Specimen 25L was subjected to constant axial compression with $C_a = 0.2$.

7.6.2 Test Results

As discussed in Section 2.8, the CB failure mode usually involves both local buckling and LTB. This specimen had comparable strong- and weak-axis radii of gyration (= 5.89 in. and 1.92 in. [150 mm and 49 mm], respectively) and a small torsional constant *J* of 1.94 in.^{4} [807,000 mm^4] (the lowest among all but Group 5 specimens that experienced elastic LTB). Accordingly, it had the tendency to twist more than buckling out-of-plane. In testing, the specimen exhibited the CB mode, primarily involving torsion and local buckling; out-of-plane curvature was not observed. Yielding and buckling progression is illustrated in Figure 7.39 to Figure 7.42.

Response histories of the column axial shortening and twisting angle at the east end [see Figure 7.42(a) for the location of the measuring device] are shown in Figure 7.45(d) and Figure 7.45(e), respectively. During the 3 % drift cycles, initiation of local buckling at both ends in conjunction with the observed twisting movements triggered both quantities to grow at increasing rates. Since both local and global instabilities occurred simultaneously, local buckling configurations at both ends were influenced by the twisting motions as follows.

Figure 7.38 shows the normal stress due to warping of an I-shaped member twisting about its longitudinal axis: the flange tips diagonal to each other experience the same maximum warping stress (either compression or tension). Corresponding to the twisting motions in the specimen with the north flange moving downward, Figure 7.40 and Figure 7.41 illustrate the warping stresses inherent in each flange tip at the east and west ends, respectively ("C" for compression and "T" for tension). The influence of these warping stresses may not be obvious in the beginning stage of local buckling formation: it appeared that flange local buckles initiated first at the tips under warping compression.

The final local buckling configurations shown in Figure 7.43 and Figure 7.44 better demonstrated the twisting effect. In general, local buckles of the flange tips under warping compression formed in a very localized fashion next to each end plate; in contrast, those of the flange tips under warping tension formed relatively further away from each end plate. This resulted in a *skewed* ALB configuration. This deformed configuration was more obvious at the east end since it experienced more twisting than the west end as shown in Figure 7.42. Furthermore, some distinctive peak amplitudes also provided an evidence of the torsional effect: those at the compression tips of the north flange as shown in Figure 7.43(a) and Figure 7.44(a) for example. Note that web local buckling at the east end was inclined (i.e., did not form orthogonally to the longitudinal axis of the member).

Figure 7.45 shows the global responses. Flexural strength degradation initiated at 3 % drift, corresponding to the onset of local buckling and twisting in the specimen. These behaviors also triggered significant axial shortening in the column as they aggravated.

7.6.3 Concluding Remarks

The specimen showed the predicted CB mode, affirming that some shallow columns may also exhibit out-of-plane, global-type buckling like some deeper columns.

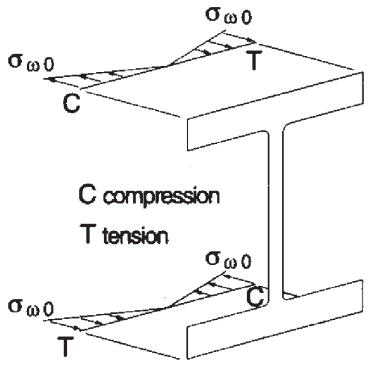

Figure 7.38 Specimen 25L: Normal Stress Due to Warping (Seaburg and Carter 1997)

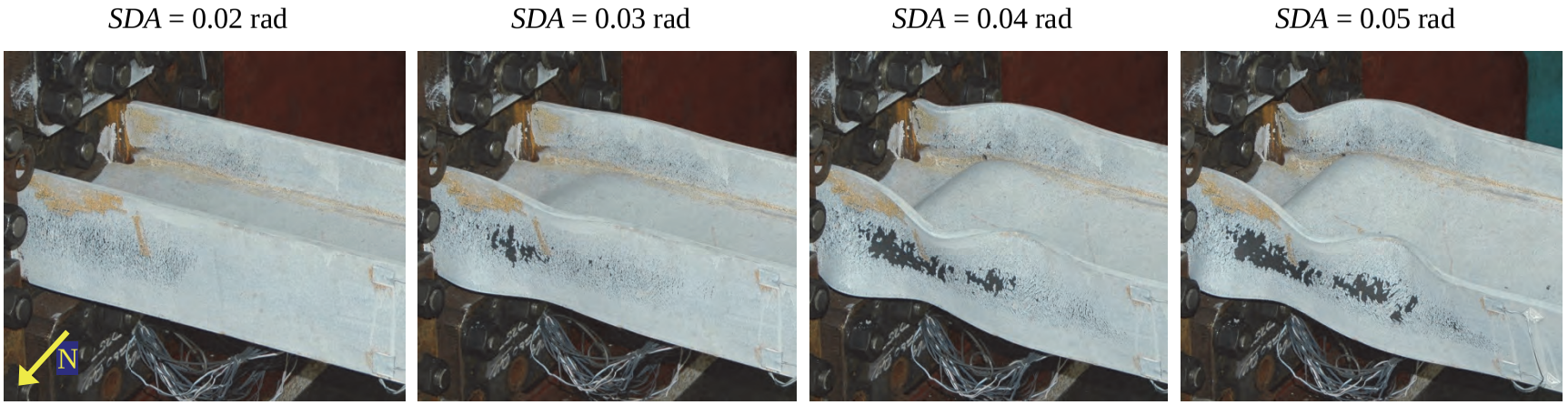

(a) East End

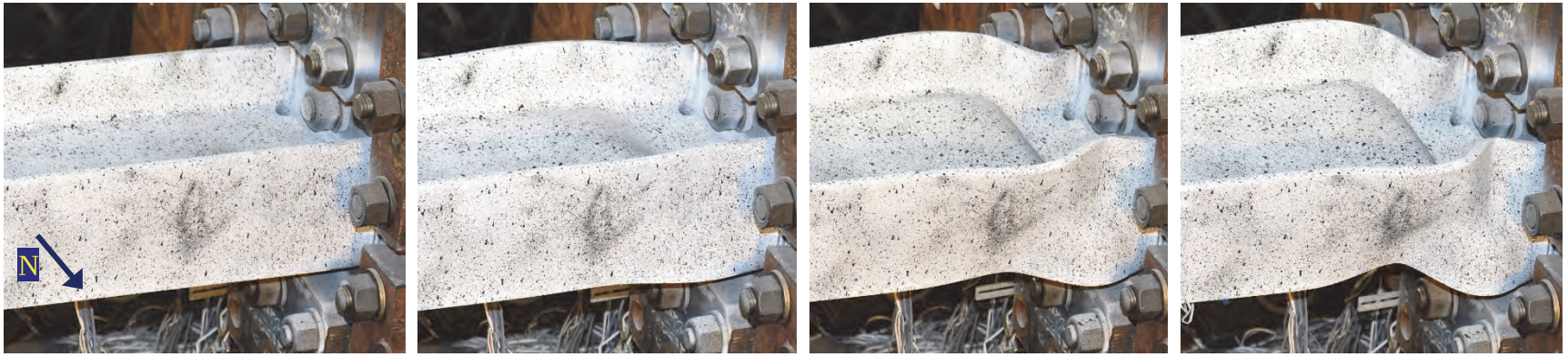

(b) West End

Figure 7.39 Specimen 25L: Yielding and Buckling Progression at Member Ends

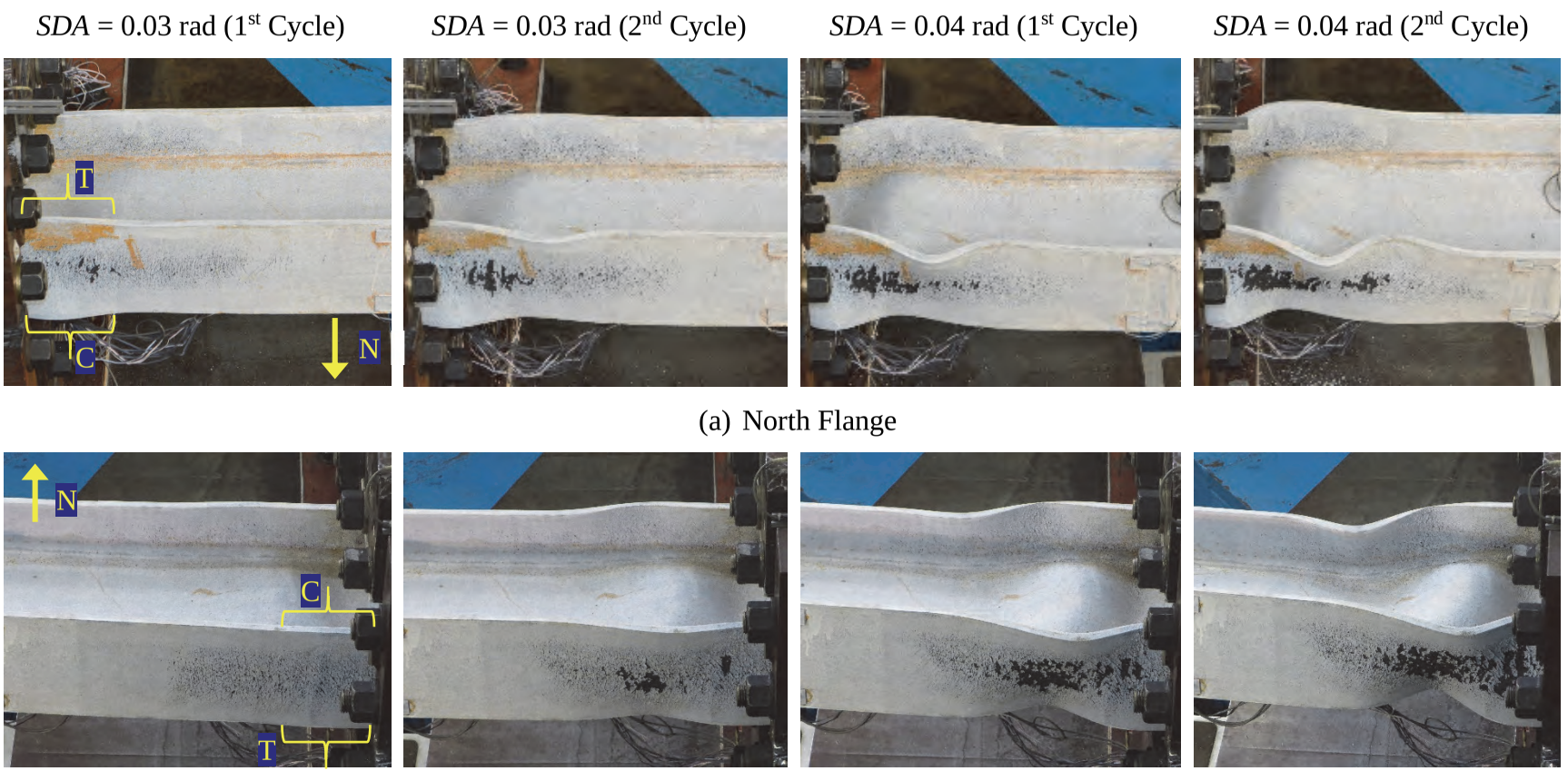

(a) North Flange

(b) South Flange

Figure 7.40 Specimen 25L: Yielding and Buckling Progression at East End

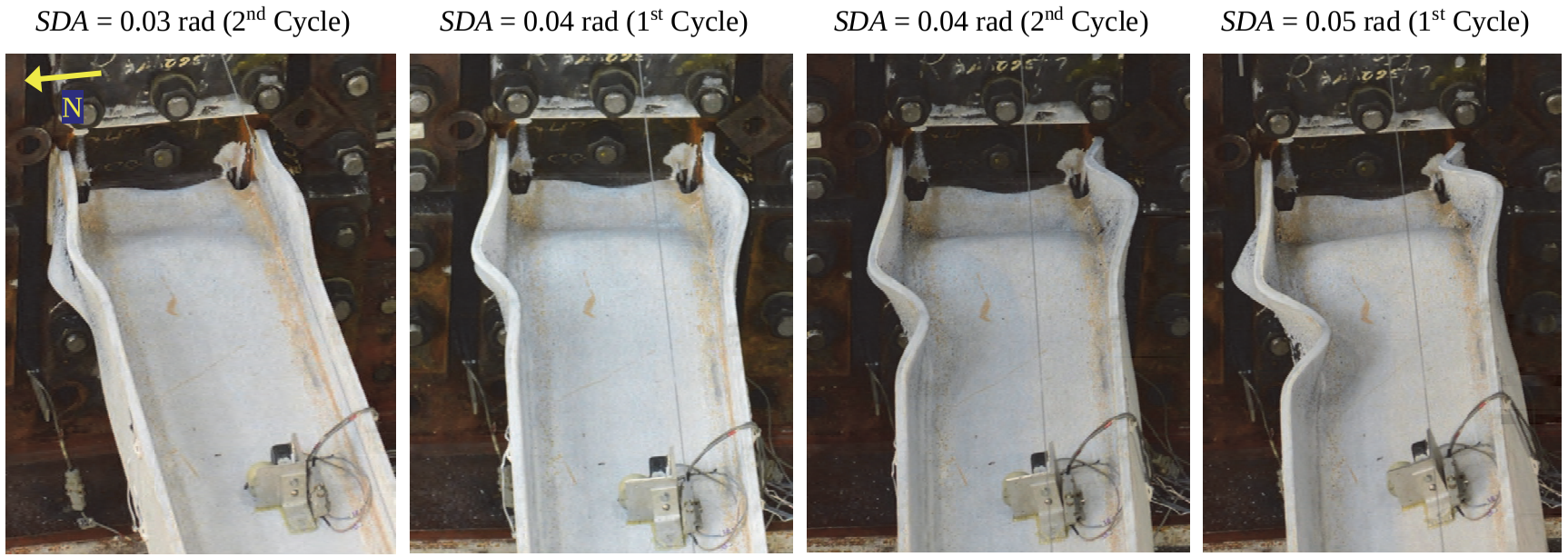

(c) Web

Figure 7.40 Specimen 25L: Yielding and Buckling Progression at East End (continued)

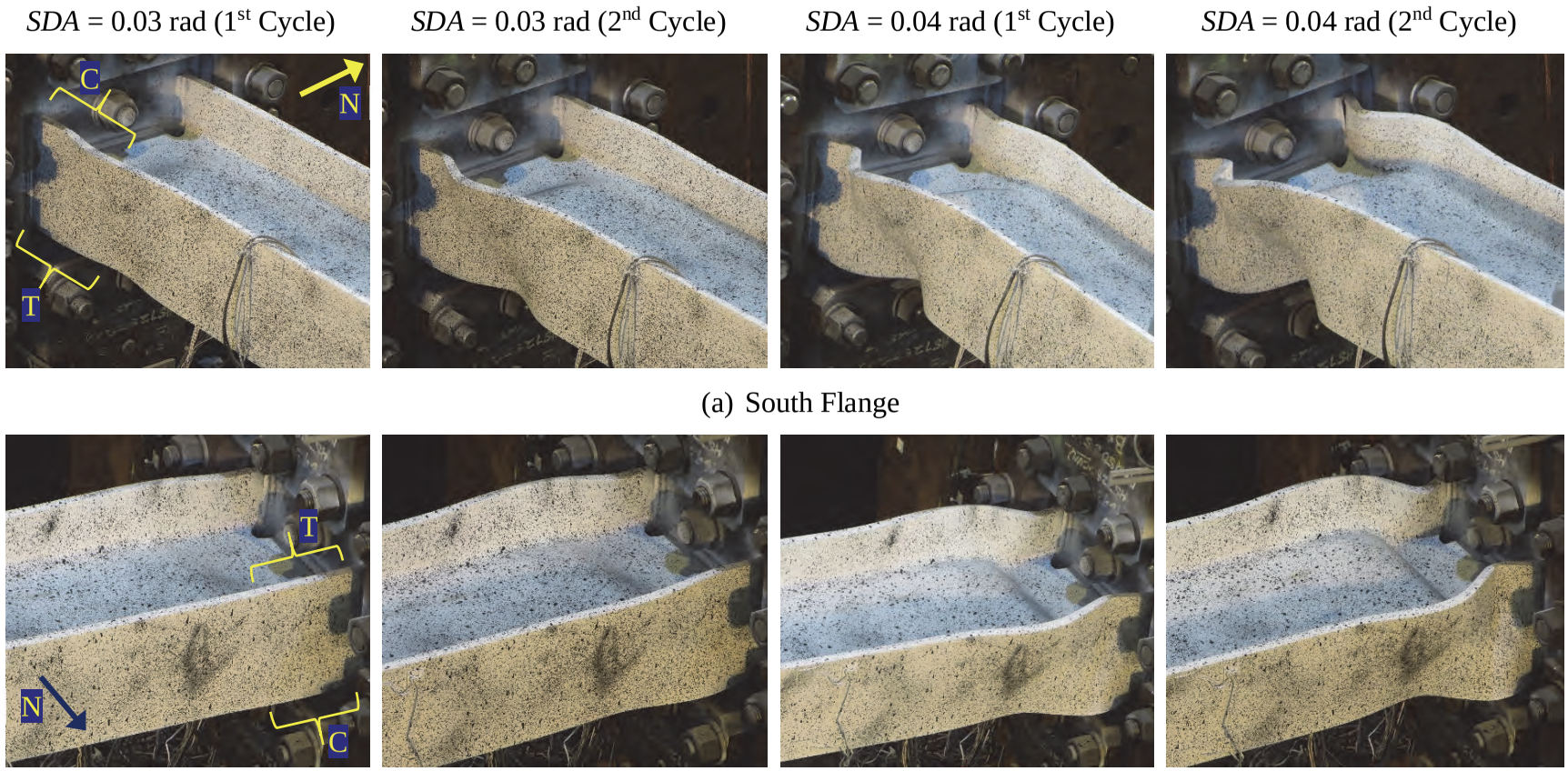

(a) South Flange

(b) North Flange

Figure 7.41 Specimen 25L: Yielding and Buckling Progression at West End

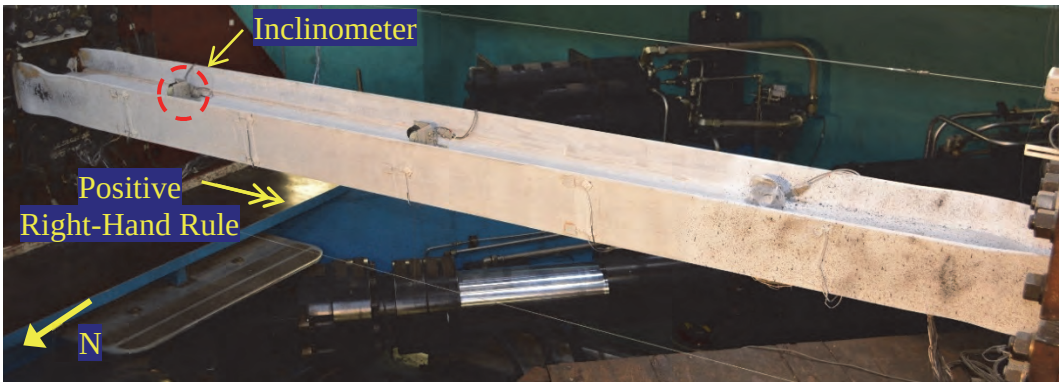

(a) *SDA* = 0.03 rad

(b) *SDA* = 0.04 rad

(c) *SDA* = 0.05 rad

Figure 7.42 Specimen 25L: Overall Yielding and Buckling Progression

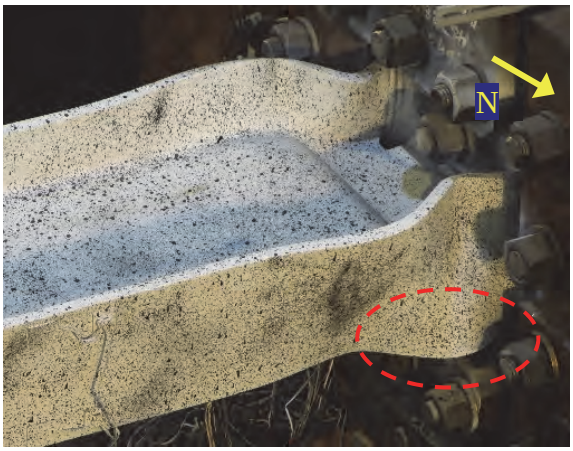

(a) North Flange

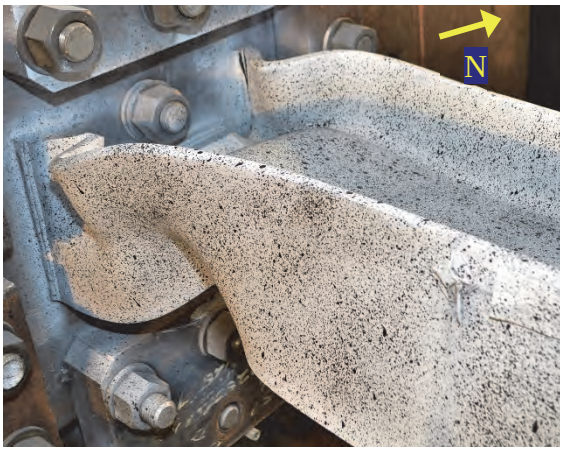

(b) South Flange

(c) Top View

(d) Bottom View

Figure 7.43 Specimen 25L: Local Buckling at End of Test (West End)

(a) North Flange (b) South Flange

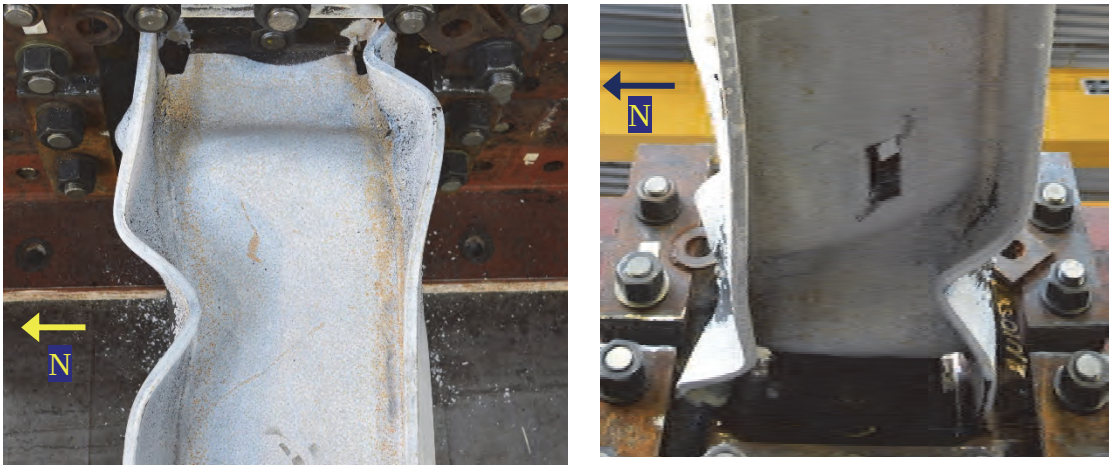

(c) Top View (d) Bottom View

Figure 7.44 Specimen 25L: Local Buckling at End of Test (East End)

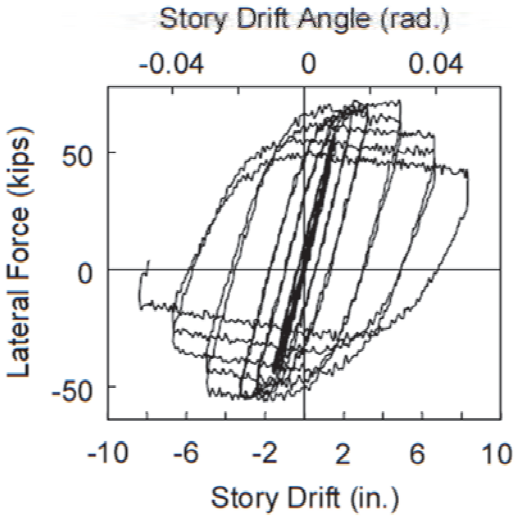

(a) Lateral Force vs. *SDA*

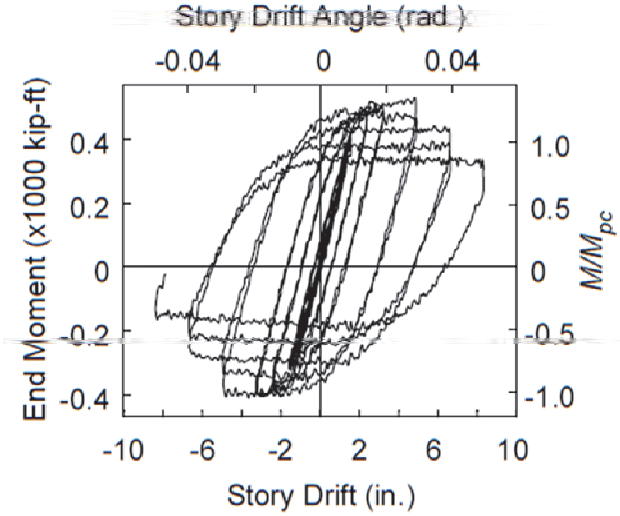

(b) End Moment vs. *SDA*

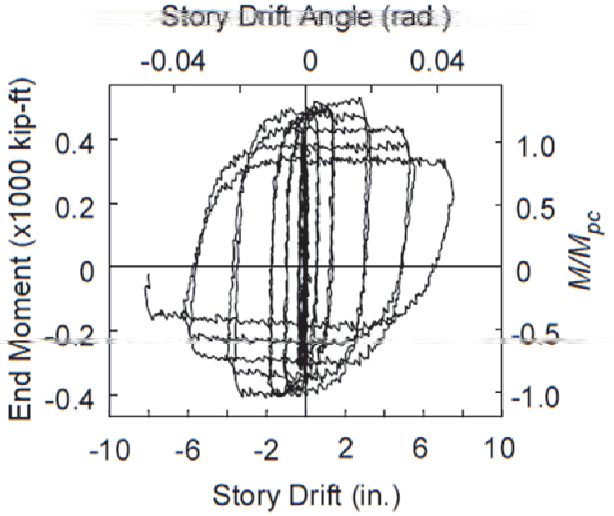

(c) End Moment vs. Plastic *SDA*

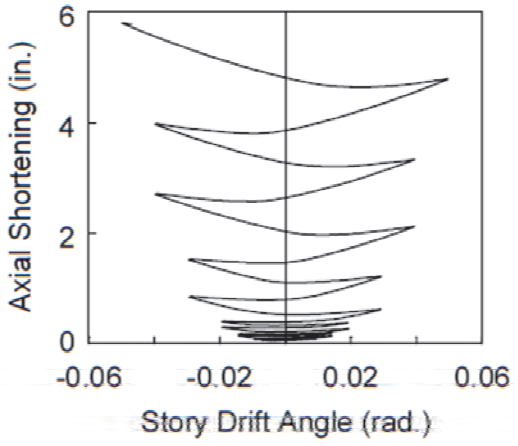

(d) Axial Shortening vs. *SDA*

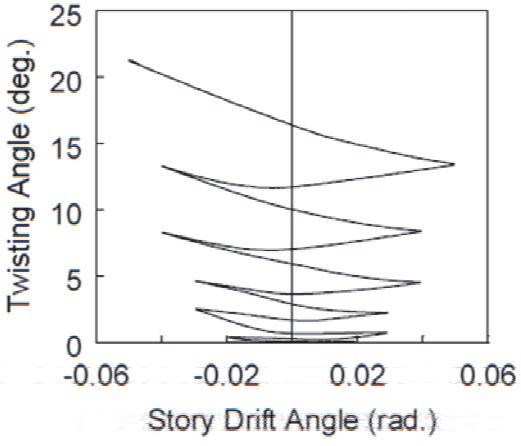

(e) Twisting Angle vs. *SDA*

Figure 7.45 Specimen 25L: Global Responses

7.7 Group 26 Specimens: Section W14×132

7.7.1 General

Group 26 specimens with W14×132 section had nearly the most compact web among all the specimens tested in the program (only slenderer than Specimen 15L with W18×192 section). Specimen 26LM was subjected to a constant axial load with C_a = 0.3, while Specimen 26LM-VAM was subjected to a varying axial load with C_a varying from 0 to 0.6 with a mean C_a value of 0.3.

7.7.2 Specimen 26LM

The specimen exhibited the SFB failure mode followed by the ALB mode; Figure 7.46 and Figure 7.47 illustrate yielding and local bucking progression at the east and west ends of the specimen, respectively. At 2 % drift, the SFB pattern initiated at the east end with a half-wave buckle at each half-width flange. It aggravated at 3 % drift and developed what appeared to be a full-wave buckle at the top half-width flanges; the web remained relatively flat at this point as shown in Figure 7.46(c). During the 4 % drift cycles, amplitudes of the flange local buckles increased, and the inward ones (i.e., the second half-wave buckles at the top half-width flanges) as well as the outward ones (i.e., the first half-wave buckles at the bottom half-width flanges) were accompanied by a downward web local buckling as the web tried to maintain perpendicular to them at the web-flange junction. By the end of the 4 % drift cycles, the overall local buckling configuration at the east end transitioned from the SFB to the ALB pattern, exhibiting obvious web and flange local buckling. The outward flange local buckles located closer to the end plate than the inward ones as shown in Figure 7.48.

At the west end, the SFB pattern was observed at the north flange at 3 % drift; the inclinometer response at the column midspan (see Figure 7.49) shown in Figure 7.51(e) also indicated that the specimen began to twist at this drift level with the south flange moving downward. Accordingly, the warping stresses due to the twisting motions influenced a local buckling configuration at the west end similarly to that occurred to Specimen 25L. Figure 7.47 illustrates the warping stresses inherent in each flange tip at the west ends (“C” for compression and “T” for tension). They influenced the skewed ALB configuration, which became obvious at 4 % drift. Local buckles of the flange tips under

warping compression were localized next to the end plate, while those of the flange tips under warping tension formed relatively further away. Although the flange local buckles at the northwest flange were both next to the end plate, the one under warping compression were more localized and severe with a larger amplitude than the another under warping tension as shown in Figure 7.50(b) and (c). Note that web local buckling at the west end was inclined (i.e., did not form orthogonally to the longitudinal axis of the member).

Figure 7.51 shows the global responses. Flexural strength degradation initiated at 4 % drift when local buckling became severe, which also caused axial shortening to grow at an increasing rate.

SDA = 0.02 rad | *SDA* = 0.03 rad | *SDA* = 0.04 rad | *SDA* = 0.05 rad

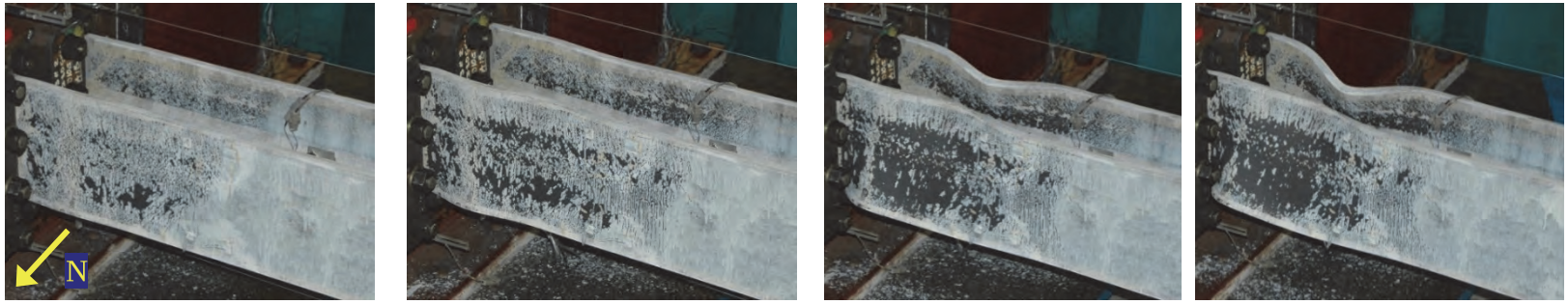

(a) North Flange

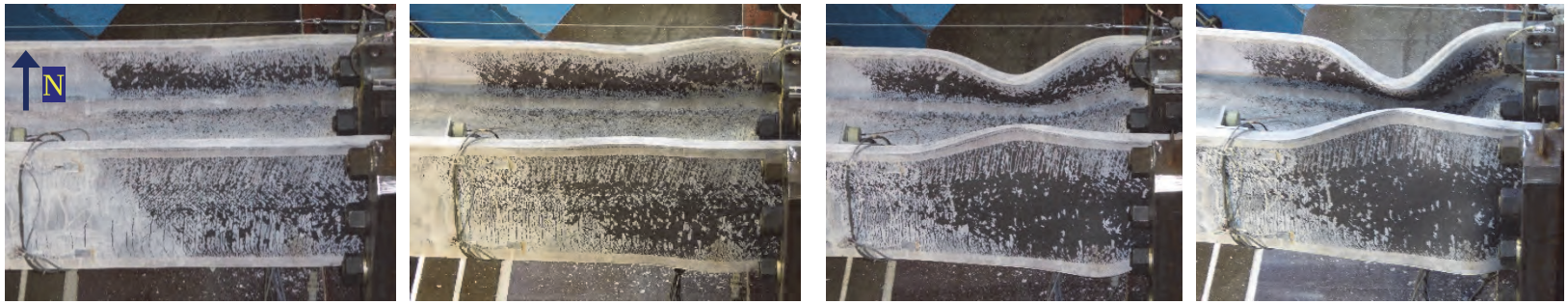

(b) South Flange

(c) Web

Figure 7.46 Specimen 26LM: Yielding and Buckling Progression at East End

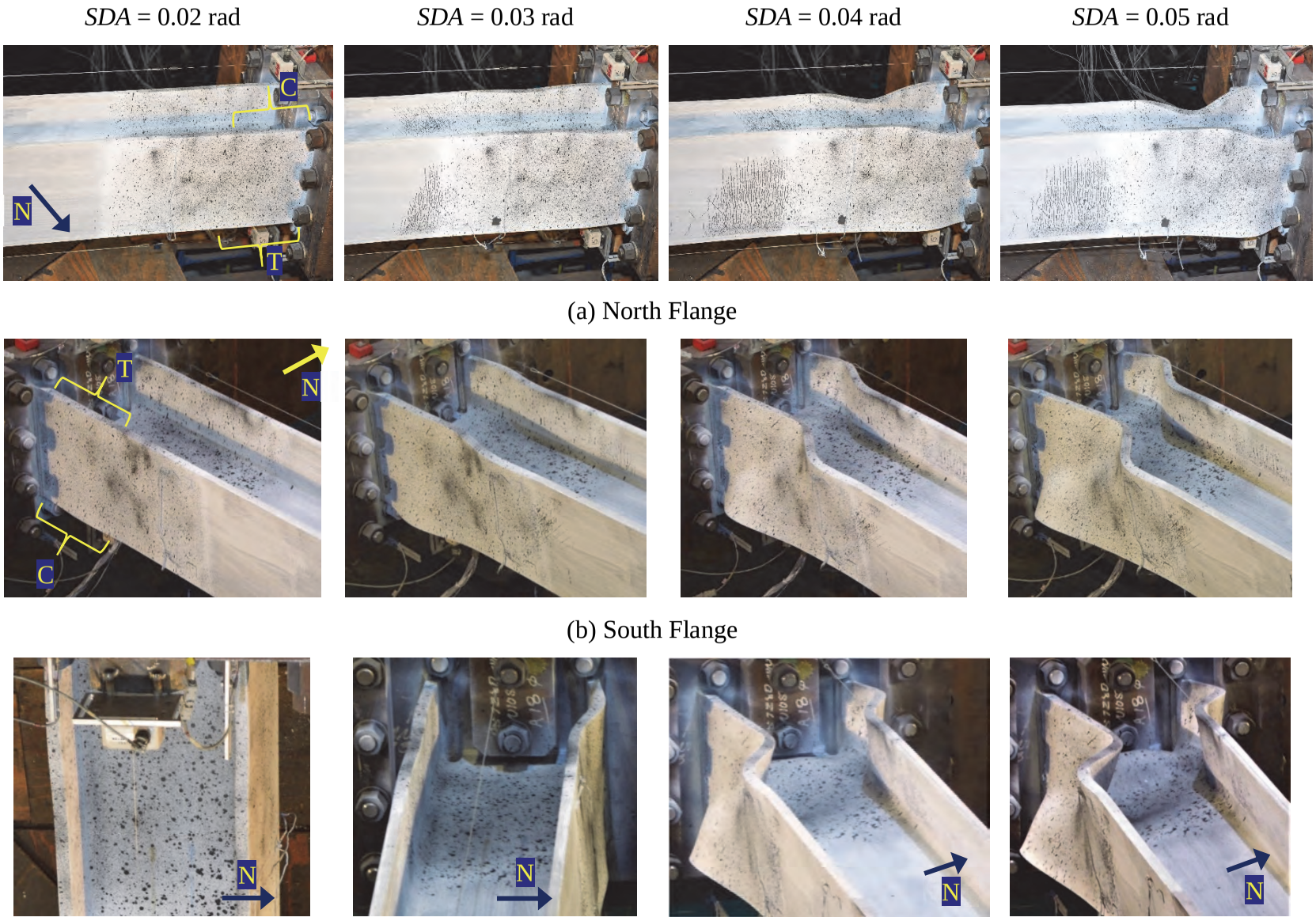

Figure 7.47 Specimen 26LM: Yielding and Buckling Progression at West End

(a) Overall (b) North Flange

(c) Top View (d) Bottom View

Figure 7.48 Specimen 26LM: Local Buckling at End of Test (East End)

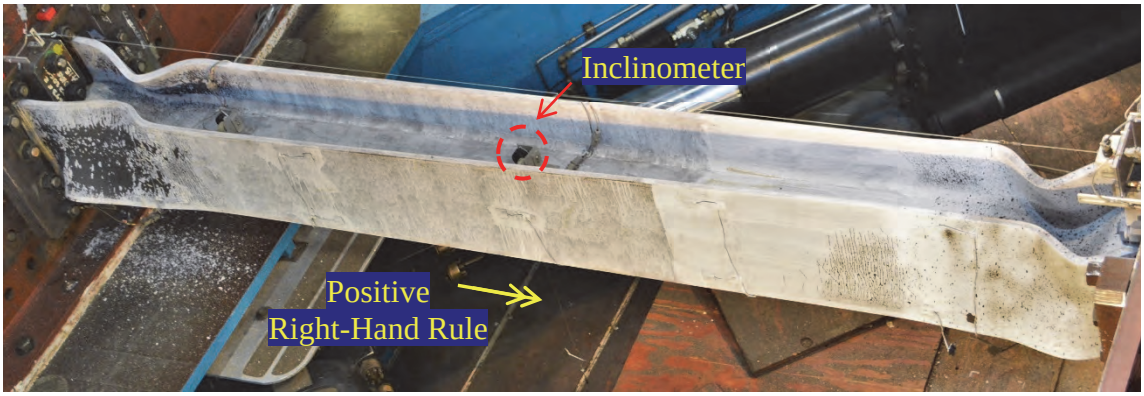

Figure 7.49 Specimen 26LM: Overall Yielding and Buckling (*SDA* = 0.05 rad)

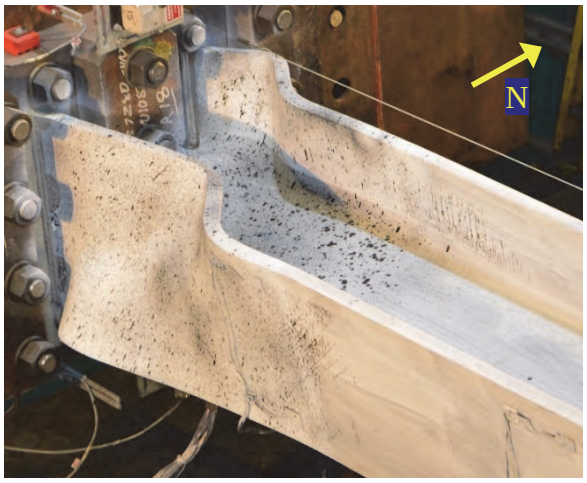

(a) South Flange

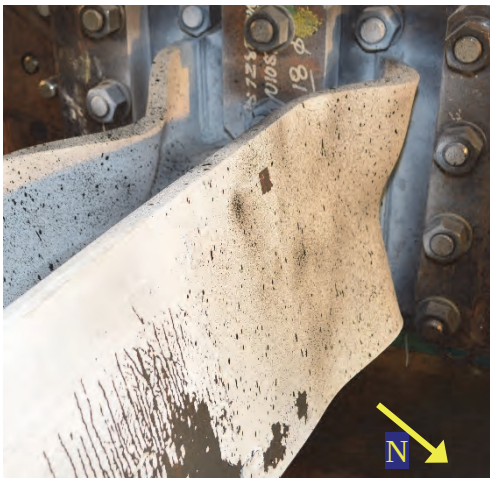

(b) North Flange

(c) Top View

(d) Bottom View

(e) Web Local Buckles

Figure 7.50 Specimen 26LM: Local Buckling at End of Test (West End)

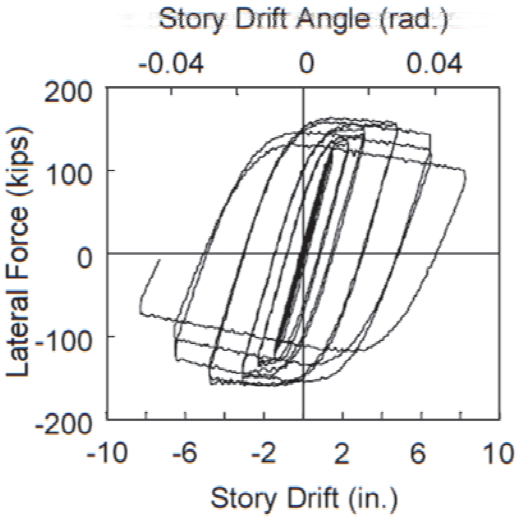

(a) Lateral Force vs. *SDA*

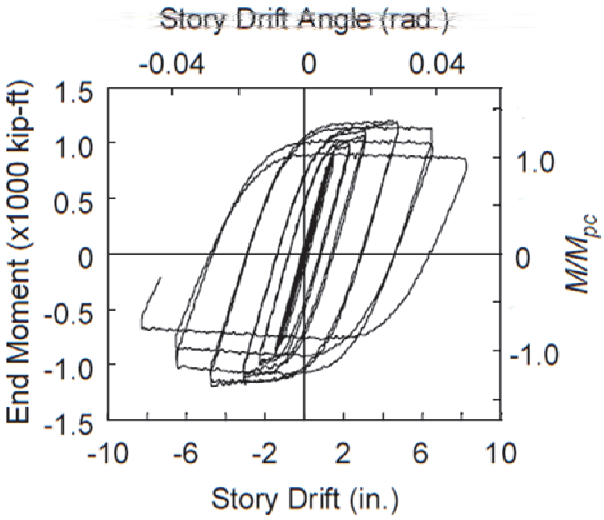

(b) End Moment vs. *SDA*

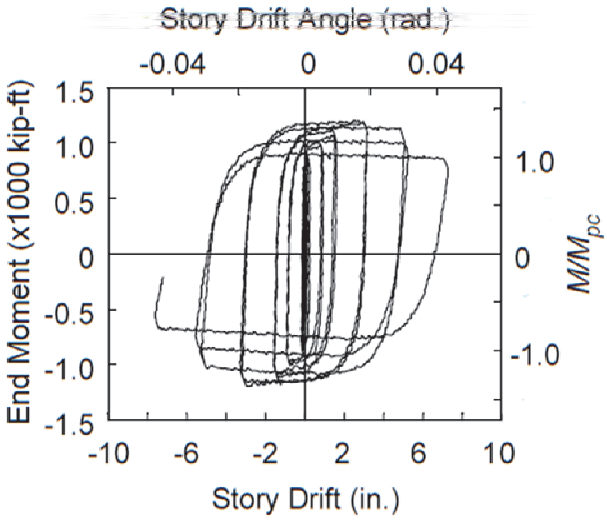

(c) End Moment vs. Plastic *SDA*

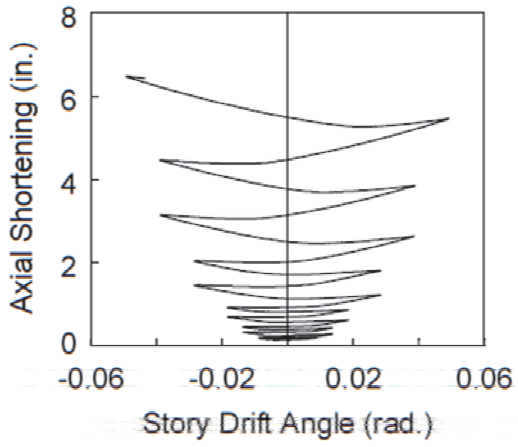

(d) Axial Shortening vs. *SDA*

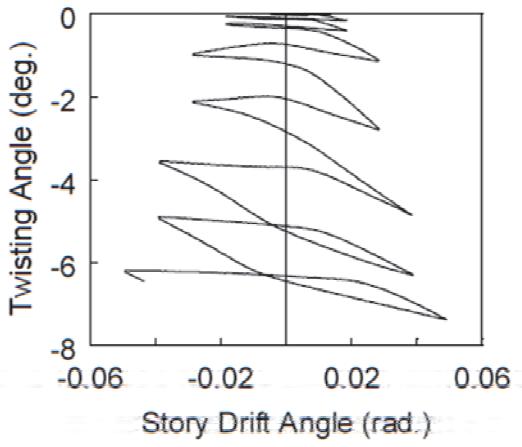

(e) Twisting Angle vs. *SDA*

Figure 7.51 Specimen 26LM: Global Responses

7.7.3 Specimen 26LM-VAM

The specimen exhibited the SFB failure mode followed by the ALB and CB mode; Figure 7.52 and Figure 7.53 illustrate yielding and bucking progression at the east and west ends of the specimen, respectively. At 3 % drift, the SFB pattern initiated at the east end with a half-wave buckle at each half-width flange; those at the north flange exhibited higher amplitudes than those at the south flange because the compression flanges in negative drift sustained higher combined axial and in-plane flexural compression than those in positive drift (due to the applied varying axial load). At this drift level, the inclinometer response at the column midspan (see Figure 7.54) shown in Figure 7.57(e) also indicated that the specimen began to twist with the south flange moving downward. Note that the twisting angle exacerbated and recovered in the negative and positive excursions, respectively. Accordingly, the warping stresses induced by the twisting motions influenced a local buckling configuration at the east end similarly to that occurred to Specimens 25L and 26LM. It became obvious at 5 % drift that the SFB pattern had transitioned into the skewed ALB configuration due to the influence of the warping stresses; the web local buckles at the east end were inclined (i.e., did not form orthogonally to the longitudinal axis of the member) as shown in Figure 7.55.

At 3 % drift, the sloped flaking pattern was obvious at the compression flanges in negative drift (i.e., southwest and northeast flanges), indicating the out-of-plane buckling tendency. In fact, a slight upward movement was observed near the east end as shown in Figure 7.54(b). At the west end, a half-wave flange local buckle was triggered at each bottom half-width flange next to the end plate at 3 % drift. They grew in amplitudes at 4 % drift, at which point additional half-wave flange local buckles began to form in the top half-width flanges with a distance about 2 ft way from the end plate. Both the former and the latter flange local buckles appeared to be triggered primarily under the influence of the out-of-plane curvature. As their amplitudes increased at 5 % drift, the specimen exhibited the reverse-curvature out-of-plane buckling configuration of the CB mode (minor upward and downward movements near the east and west ends, respectively) as shown in Figure 7.54(d). Web local buckling was not present at the west end as shown in Figure 7.56(c).

Figure 7.57 shows the global responses. The specimen exhibited higher plastic moment capacity in the positive excursions compared to that in the negative excursions

since lower axial compression was applied in the former. Flexural strength in the negative excursions began to degrade during the 4 % drift cycles, corresponding to when local buckling at the compression flanges in negative drift became severe. Similarly, flexural strength in the positive excursions began to degrade during the 5 % drift cycles, corresponding to when local buckling at the compression flanges in positive drift became severe. Axial shortening began to grow at an increasing rate at 3 % drift, corresponding to the onset of the SFB mode.

7.7.4 Concluding Remarks

The SFB mode was predicted for both Specimens 26LM and 26LM-VAM and was observed in the initial buckling stage of both tests. Although other buckling modes were triggered later in the tests, the columns exhibited relatively stable global responses, signifying the hysteretic feature of the SFB mode.

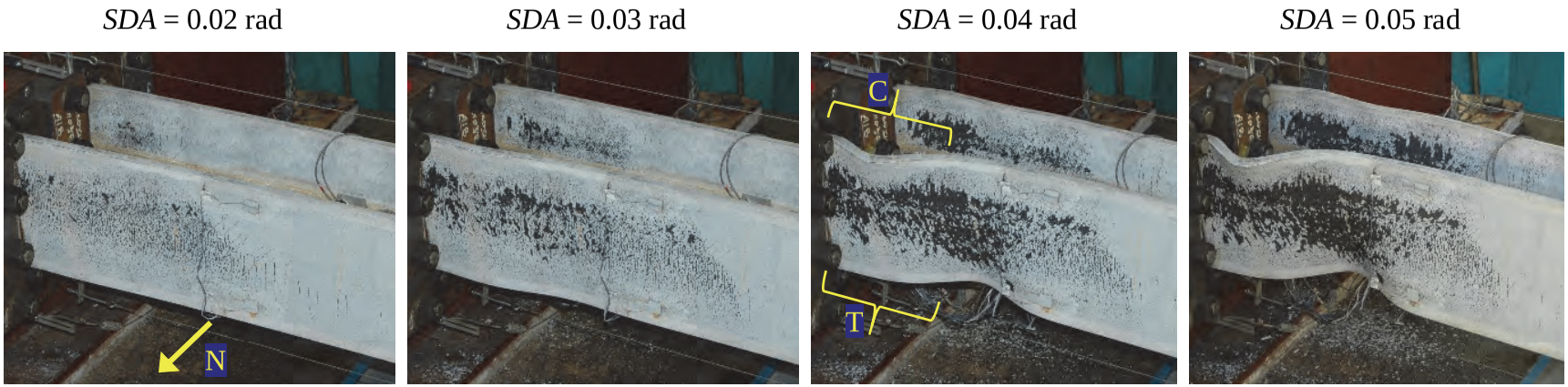

(a) North Flange

(b) South Flange

Figure 7.52 Specimen 26LM-VAM: Yielding and Buckling Progression at East End

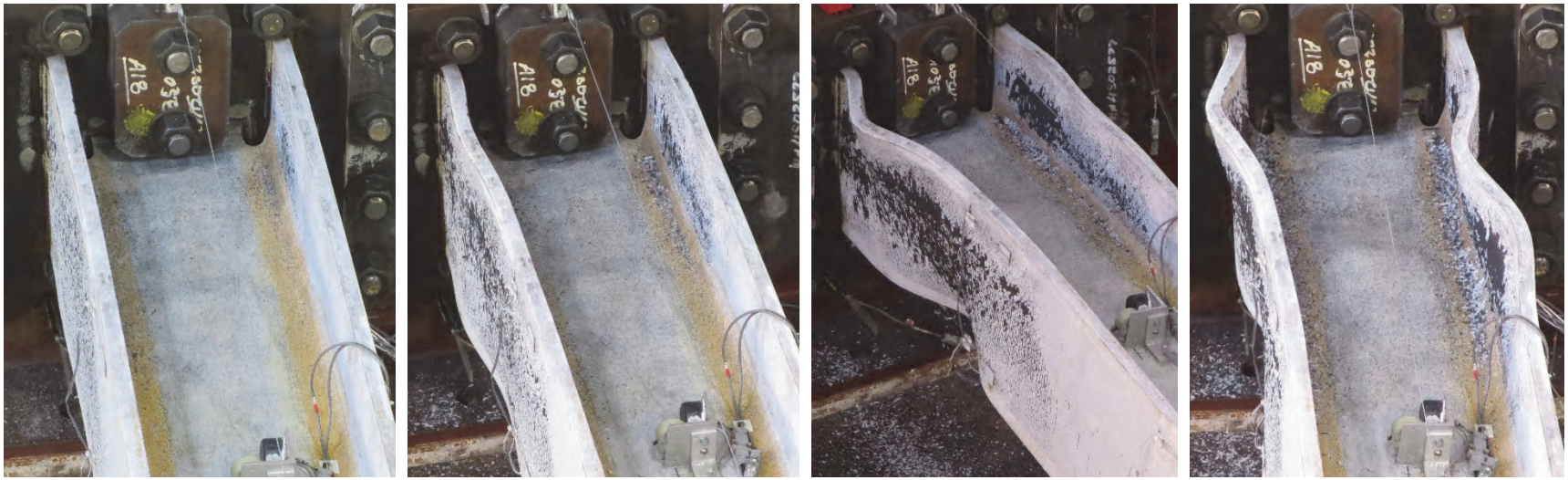

(c) Web

Figure 7.52 Specimen 26LM-VAM: Yielding and Buckling Progression at East End (continued)

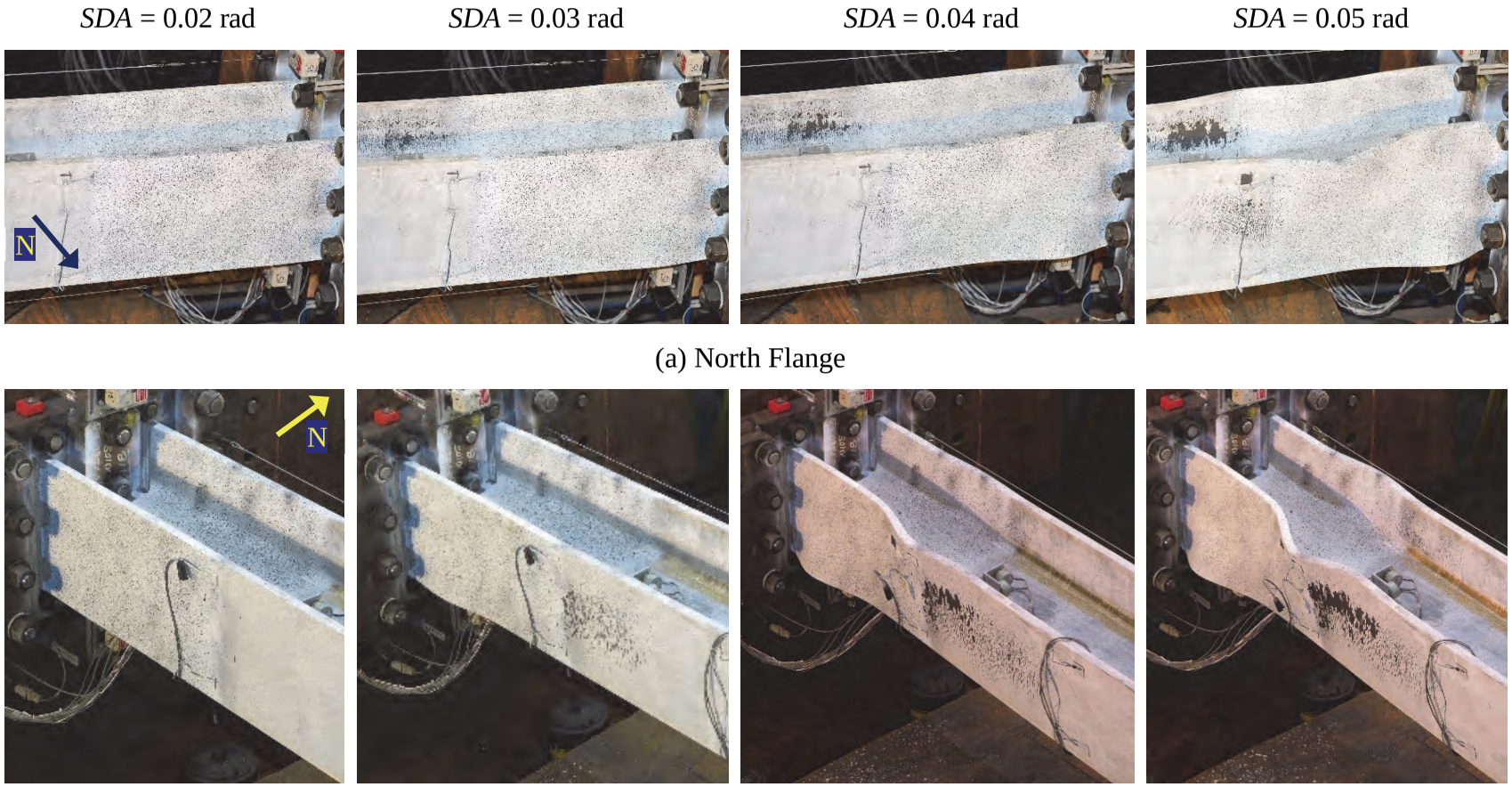

(a) North Flange

(b) South Flange

Figure 7.53 Specimen 26LM-VAM: Yielding and Buckling Progression at West End

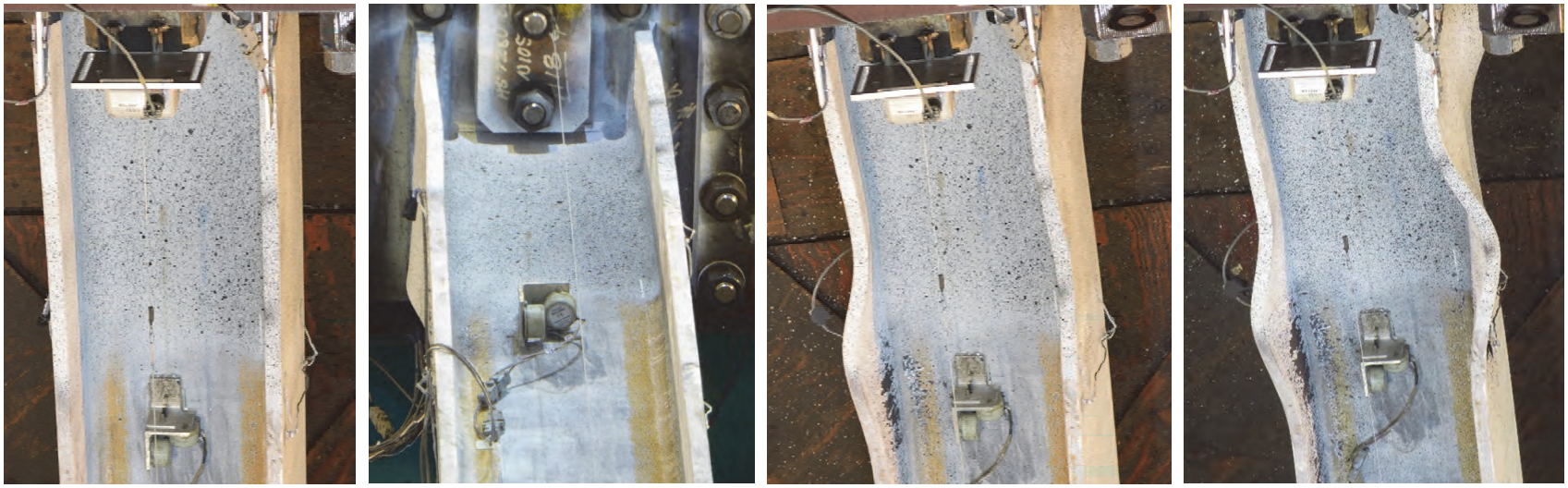

(c) Web

Figure 7.53 Specimen 26LM-VAM: Yielding and Buckling Progression at West End (continued)

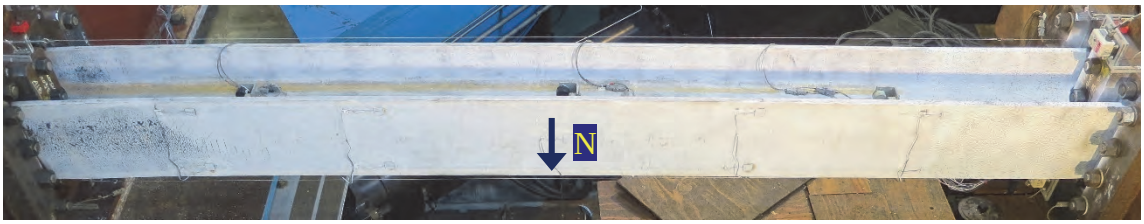

(a) *SDA* = 0.02 rad

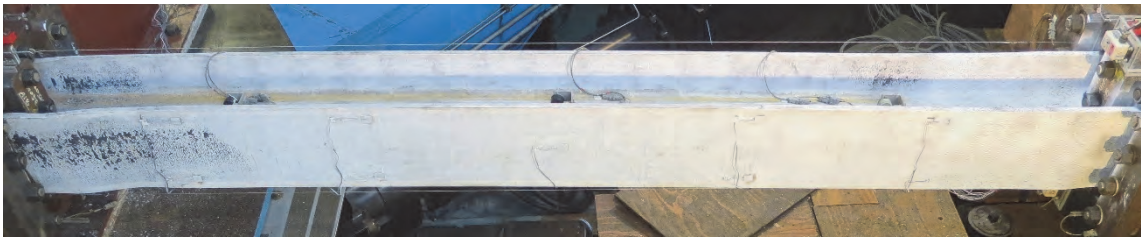

(b) *SDA* = 0.03 rad

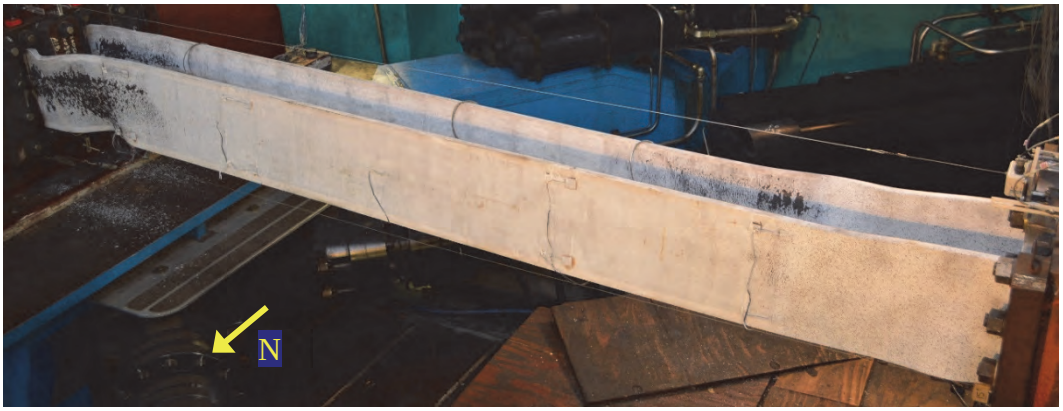

(c) *SDA* = 0.04 rad

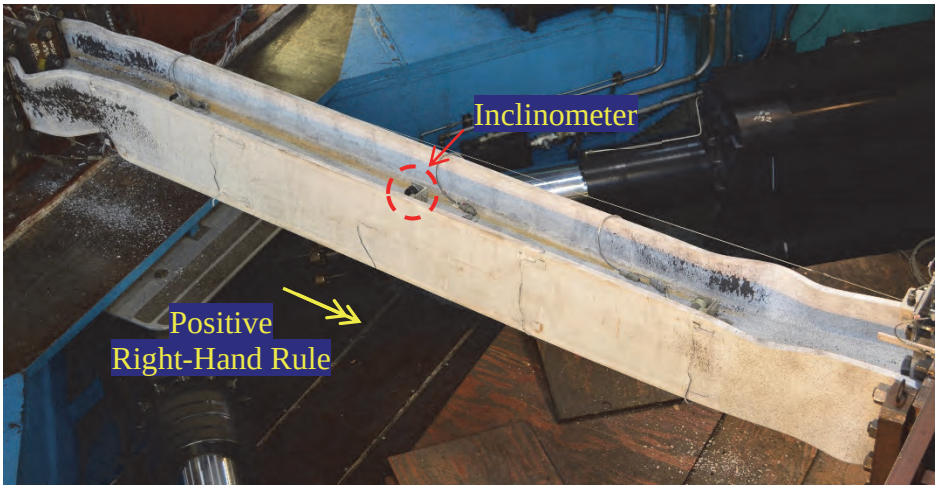

(d) *SDA* = 0.05 rad

Figure 7.54 Specimen 26LM-VAM: Overall Yielding and Buckling Progression

(a) North Flange

(b) South Flange

(c) Top View

(d) Bottom View

Figure 7.55 Specimen 26LM-VAM: Local Buckling at End of Test (East End)

(a) North Flange

(b) South Flange

(c) Top View

(d) Bottom View

Figure 7.56 Specimen 26LM-VAM: Local Buckling at End of Test (West End)

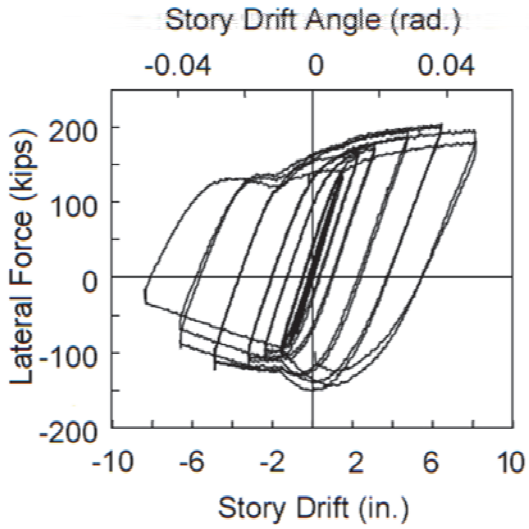

(a) Lateral Force vs. *SDA*

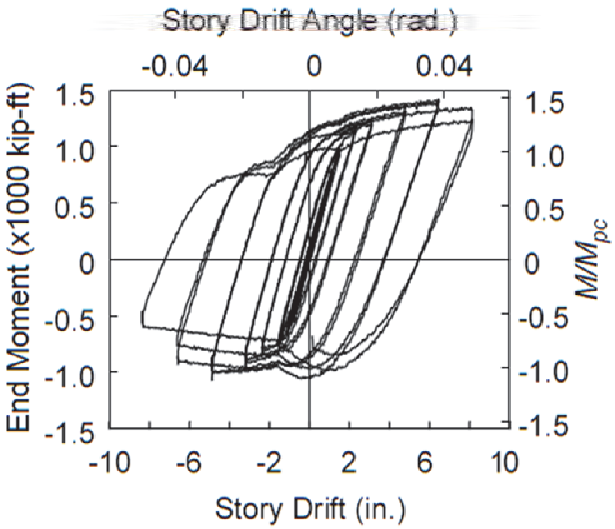

(b) End Moment vs. *SDA*

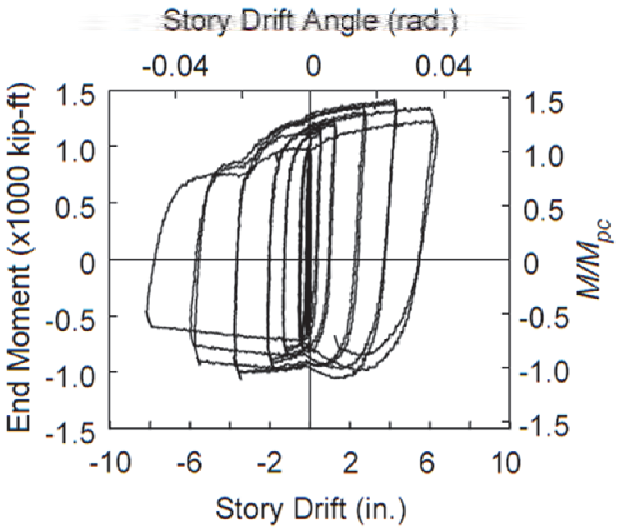

(c) End Moment vs. Plastic *SDA*

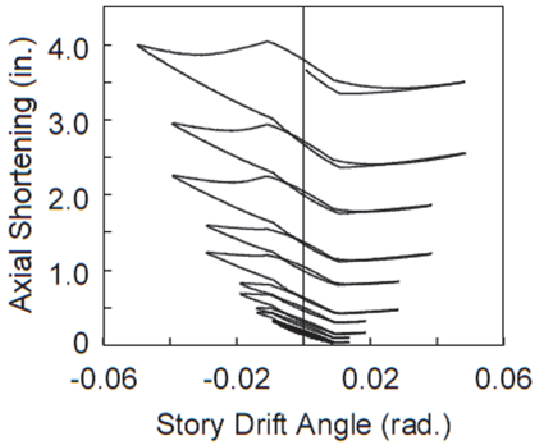

(d) Axial Shortening vs. *SDA*

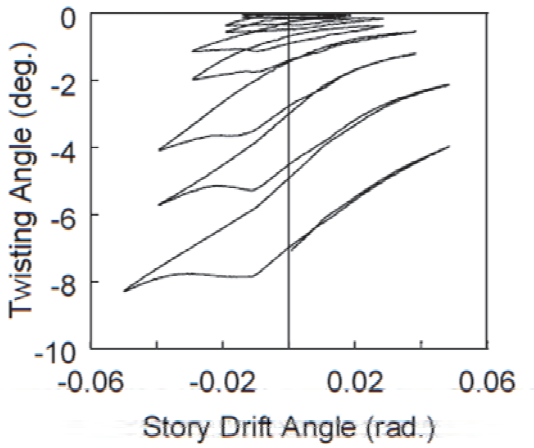

(e) Twisting Angle vs. *SDA*

Figure 7.57 Specimen 26LM-VAM: Global Responses

7.8 Group 27 Specimen: Section W24×84

7.8.1 General

Group 27 specimen had the same section and geometry as Group 4 specimens from Phase 1 study. Specimen 27L was subjected to constant axial compression with C_a = 0.2. It represented a repeat of Specimen 4L test. Coupled buckling was the predicted failure mode.

7.8.2 Test Results

The specimen exhibited the CB failure mode with the single-curvature out-of-plane buckling configuration; yielding and buckling progression at each member end is shown in Figure 7.58. Web and flange local buckling initiated at both ends at 2 % drift, exhibiting the ALB pattern. Obvious out-of-plane movements of compression flanges were observed at 3 % drift, which generated significant twisting motions in the entire column, as shown in Figure 7.59. The out-of-plane amplitude concentrated at the west end. In summary, the specimen first formed local buckles at the member ends with the ALB pattern and was followed by LTB behavior at higher drifts. Figure 7.60 shows local buckling configurations at the end of the test.

Figure 7.61 shows the global responses. A minor flexural strength degradation and axial shortening was observed during the 2 % drift cycles when local buckling initiated. Successively, the onset of LTB at 3 % drift triggered significant flexural strength degradation and axial shortening.

7.8.3 Concluding Remarks

This testing demonstrated that CB was the governing failure mode of W24×84 section, confirming Group 4 test results from Phase 1 program. The only difference is that Specimen 27L experienced the single-curvature CB mode, while Specimen 4L showed the double-curvature CB mode. The profile of the initial imperfections at both the member and section levels might have contributed to this difference.

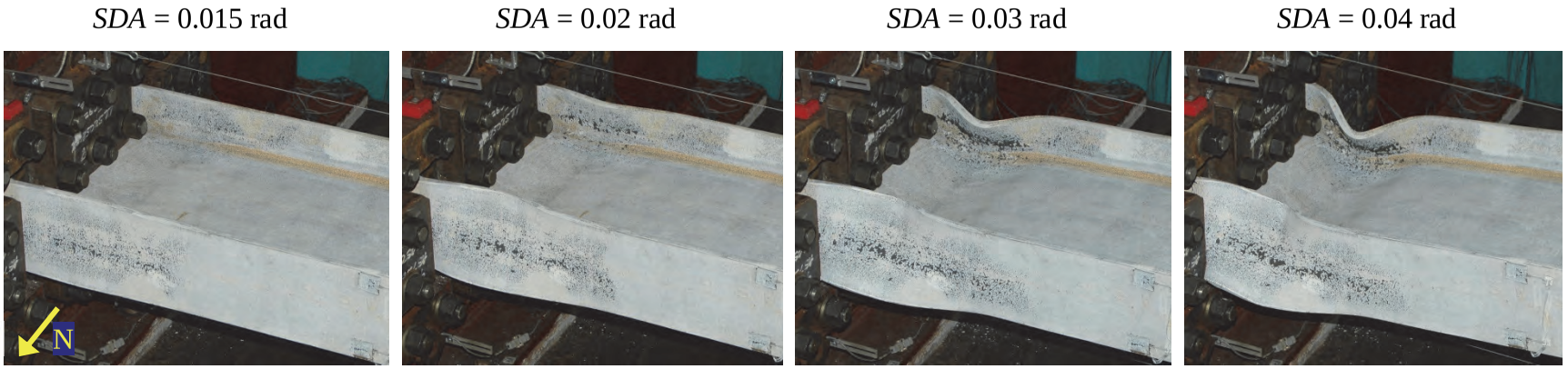

(a) East End

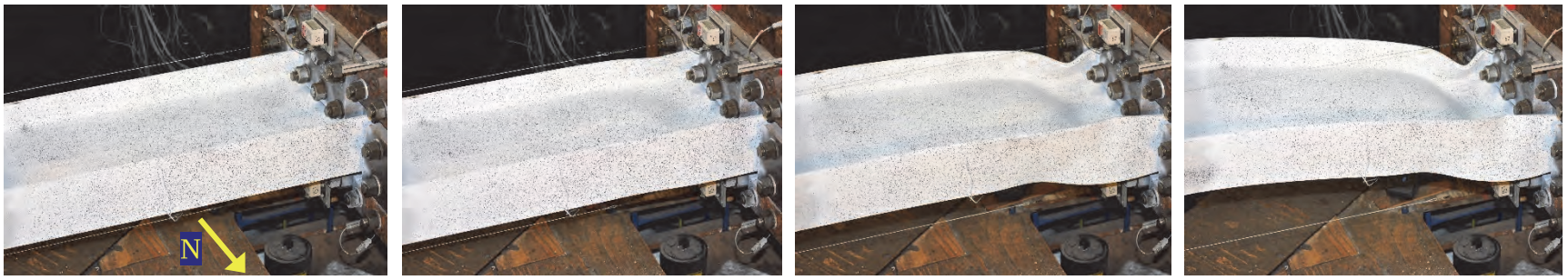

(b) West End

Figure 7.58 Specimen 27L: Yielding and Buckling Progression at Member Ends

(a) *SDA* = 0.02 rad

(b) *SDA* = 0.03 rad

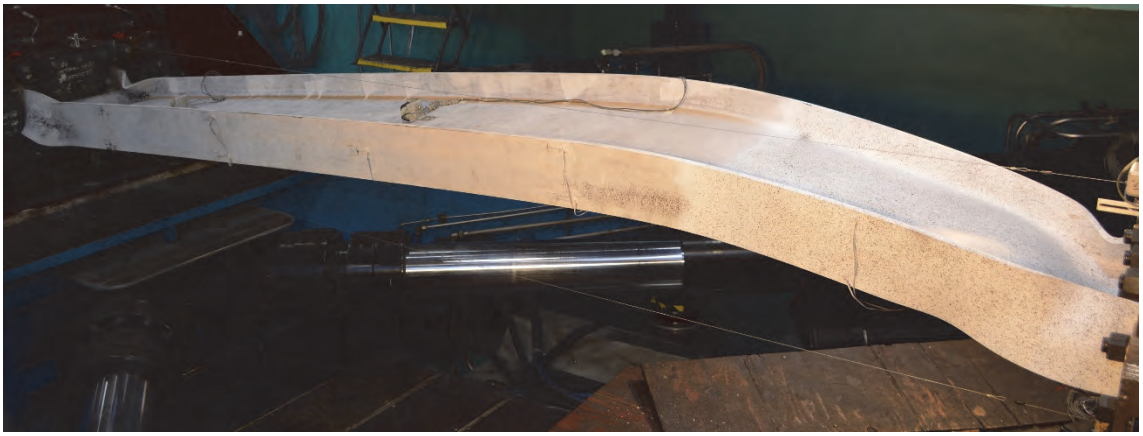

(c) *SDA* = 0.04 rad

Figure 7.59 Specimen 27L: Overall Yielding and Buckling Progression

(a) Southwest Flange

(b) Northwest Flange

(c) Southeast Flange

(d) Northeast Flange

Figure 7.60 Specimen 27L: Local Buckling at End of Test

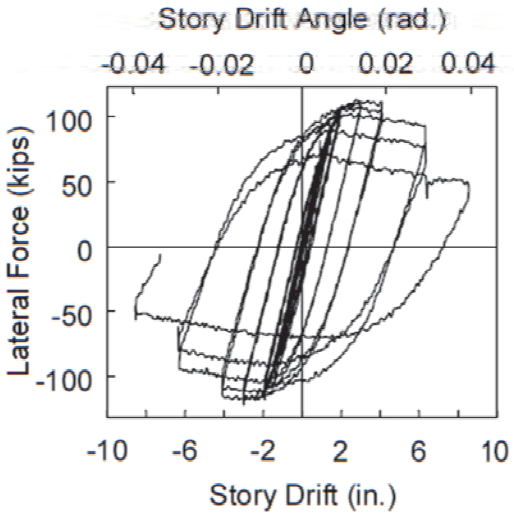

(a) Lateral Force vs. *SDA*

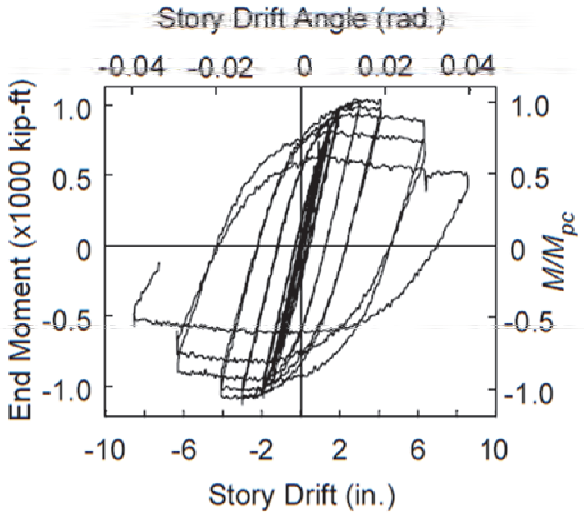

(b) End Moment vs. *SDA*

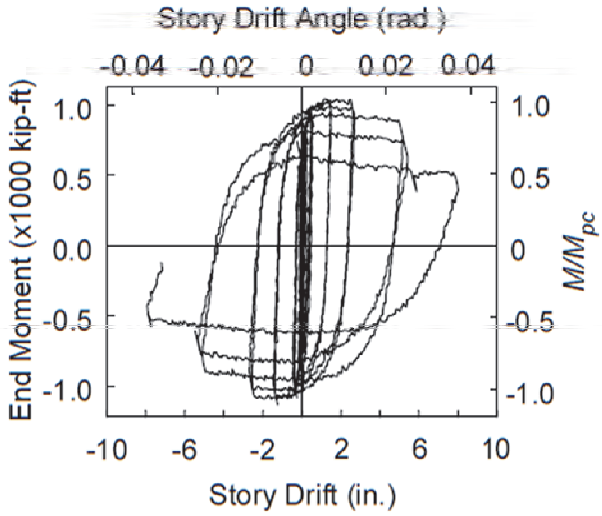

(c) End Moment vs. Plastic *SDA*

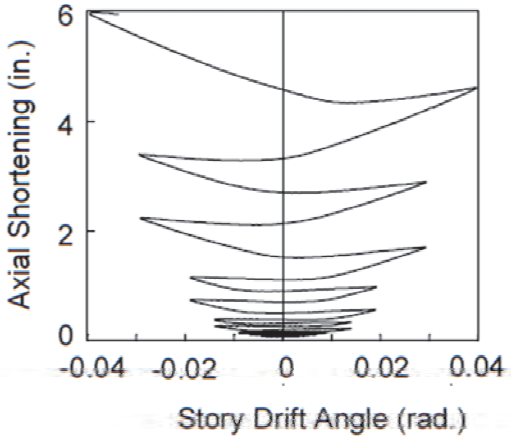

(d) Axial Shortening vs. *SDA*

Figure 7.61 Specimen 27L: Global Responses

8. SUMMARY AND CONCLUSIONS

8.1 Summary

Steel Special Moment Frame (SMF) is a preferred seismic force-resisting system for its architectural flexibility and high ductility. To meet the story drift limit specified in ASCE 7 (ASCE 2016), design engineers prefer to use deep columns for their high in-plane flexural stiffness about their strong axis. The design requirements in AISC 341 (AISC 2016a) intend to develop the high ductility of SMF through plastic hinge formation at not only beam ends but also column bases. While plastic hinging at the beam ends has been extensively researched (e.g., FEMA 2000), experimental research on deep columns with high axial load and cyclic bending, especially for large-size members, was very limited.

When deep columns (e.g., W24 to W36 columns) are used, local buckling is a concern because the width-thickness ratios for both flange local buckling (FLB) and web local buckling (WLB) are much larger. A deep column also has a smaller radius of gyration about the weak axis than that of a shallow column that has a similar strong-axis moment of inertia. Therefore, global-type member buckling, either lateral-torsional buckling (LTB) or flexural buckling (FB), may be a concern. To address the knowledge gap with deep, slender columns, the National Institute of Standards and Technology (NIST) developed a comprehensive research plan to study these columns at the member, subassemblage, and system levels (NIST 2011). Research at the member level, which started in 2013, was conducted at the University of California, San Diego (UCSD). The test program was conducted in two phases with a total of 44 full-scale columns tested. Hot-rolled W14 to W30 sections of A992 steel were considered. Twenty-one W24 columns were tested in Phase 1 to evaluate the behavior and response of deep columns for seismic application in SMF design. In Phase 2, twenty-three additional “shallow” (W14) and “deep” (W18, W24, and W30) columns were tested to further investigate Phase 1 objectives and examine the effects of section depths, fixed-rotating boundary conditions, and varying axial loads.

8.2 Conclusions

Phase 1 testing intended to investigate the effects of slenderness parameters, constant axial load levels, lateral drift loading protocols, and weak-axis bending on the column

response. See Table 2.1 for the test matrix. The following conclusions can be made from Phase 1 testing.

(1) The reference Group 2 specimens had the section (W24×131) classified as highly ductile per AISC 341. Under strong-axis bending, in-plane plastic hinges developed, and no out-of-plane buckling was observed. Test results showed that the hysteresis responses were sensitive to the level of axial load. Each plastic hinge was developed in the forms of FLB and WLB; these two buckling modes occurred interactively. Severe local buckling caused the columns to shorten by a significant amount. Group 3 specimens (W24×104) experienced the same failure mode.

(2) An "unexpected" failure mode, or the coupled buckling mode as defined in Ozkula et al. (2017), was observed from Group 1 specimens. The section (W24×176) was more compact than that of the reference Group 2 specimens, and the L/r_y ratio for LTB or FB was also smaller. Unlike Group 2 specimens, LTB developed after in-plane plastic hinges were formed. Group 4 specimens (W24×84) also experienced the similar failure mode.

(3) Group 5 specimens (W24×55) had the L/r_y ratio (= 161) that was 2.21 times that of the reference Group 2 specimens. Local buckling did not occur. Instead, LTB was the dominating failure mode, indicating that L/r_y needs to be limited.

(4) Group 6 specimens (W24×131) with weak-axis bending showed an excellent ductility capacity. Local buckling in the flanges would only occur at a very large story drift level or a high level of axial force. The AISC section compactness requirements do not distinguish between strong- or weak-axis bending. Such approach is very conservative.

(5) Compared to the AISC cyclic loading protocol, near-fault loading was found to be less damaging in terms of energy dissipation and column axial shortening. But the residual drift could be larger with this type of excitation.

The following conclusions can be made from Phase 2 testing.

(6) Ozkula et al. (2017) categorize buckling behaviors of wide-flange columns into three distinct modes—Symmetric Flange Local Buckling (SFB), Anti-symmetric Local Buckling (ALB), and Coupled Bucking (CB). A procedure is also proposed to predict

the governing buckling mode of a given column based on its section slenderness parameters. This procedure was implemented in Phase 2 testing to predict failure modes of selected specimens under cyclic loading (Table 4.1 and Table 6.1); the observed failure modes from Phase 2 testing confirmed the predictions.

(7) Wide-flange sections with similar web and flange slenderness performed similarly under cyclic loading regardless of their difference in nominal depths; they exhibited consistent failure modes and similar hysteretic attributes.

(8) Cyclic responses of interior columns and exterior columns are very different in terms of maximum flexural strength, post-buckling stiffness degradation, and axial shortening. The backbone curves associated with the interior and exterior columns need to be distinguished for seismic design applications.

(9) Elastic flexural stiffness of specimens subjected to fixed-rotating boundary conditions is lower than that of their nominally identical specimens with fixed-fixed ends. Failure mode did not change despite the change in boundary conditions. Allowing the column top end to rotate increased the story drift capacity.

(10) Testing of W14 specimens (Specimens 24L and 25L) in Phase 2 program has shown that not all shallow columns fail in the SFB mode (see Section 2.8) with stable hysteresis and high ductility. Some shallow columns with relatively slender web and flanges exhibited the deep column phenomena, failing in the ALB or CB modes.

This page intentionally left blank.

REFERENCES

(1) AISC. (2010a). “Seismic provisions for structural steel buildings.” *ANSI/AISC 341-10*, Chicago, IL.

(2) AISC. (2010b). “Code of Standard Practice for Structural Steel Buildings and Bridges.” *AISC 303-10*, Chicago, IL.

(3) AISC. (2016a). “Seismic provisions for structural steel buildings.” *ANSI/AISC 341-16*, Chicago, IL.

(4) AISC. (2016b). “Specification for structural steel buildings.” *ANSI/AISC 360-16*, Chicago, IL.

(5) ASCE. (2017). “Seismic evaluation and retrofit of existing buildings.” *ASCE/SEI 41-17*, Reston, VA.

(6) ASCE. (2016). “Minimum design loads and associated criteria for buildings and other Structures.” *ASCE/SEI 7*, Reston, VA.

(7) ASCE-WRC (Welding Research Council). (1971). “Plastic design in steel: A guide and commentary.” *Manual of Practice No. 41*, New York, NY.

(8) Benzoni, G. and Innamorato, D. (2017). SRMD2017-05: *SRMD System Calibration Conducted Jan.-Feb. 2017*. Charles Lee Powell Structural Research Laboratories, CALTRANS SRMD Test Facility, Department of Structural Engineering, University of California, San Diego (UCSD), La Jolla, CA. Electronic copy of the report can be obtained by contacting the Department of Structural Engineering at UCSD.

(9) Chansuk, P., Ozkula, G., and Uang, C.-M. (2019). “Application of Timoshenko beam-column theory in data correction for steel beam-column testing.” *J. Struct. Eng*. https://doi.org/10.1061/(ASCE)ST.1943-541X.0002533.

(10) Chugh, A. K. (1977). “Stiffness matrix for a beam element including transverse shear and axial force effects.” *Int. J. Numer. Methods Eng.* 11 (11): 1681–1697. https://doi.org/10.1002/nme.1620111105.

(11) FEMA. (2000). “NEHRP recommended provisions for seismic regulations for new buildings and other structures.” *Rep. No. FEMA-369*, Washington, DC.

(12) Harris, J. L., and Speicher, M. S. (2015). “Assessment of first generation performance-based seismic design methods for new steel buildings volume 1: Special moment frames.” *NIST TN 1863-1*, Gaithersburg, MD.

(13) Krawinkler, H., Gupta, A., Medina, R., and Luco, N. (2000). “Development of Loading histories for testing of steel beam-to-column assemblies.” *SAC Background Rep. No. SAC/BD-00/10*, SAC Joint Venture, Sacramento, CA.

(14) Newell, J. D., and Uang, C.-M. (2008). “Cyclic behavior of steel wide-flange columns subjected to large drift.” *J. Struct. Eng.*, 134(8), 1334-1342. https://doi.org/10.1061/(ASCE)0733-9445(2008)134:8(1334).

(15) NIST. (2011). “Research plan for the study of seismic behavior and design of deep, slender, wide-flange structural steel-beam-column members.” *NIST-GCR-11-917-13*, Gaithersburg, MD.

(16) Ozkula, G., Harris, J., and Uang, C.-M. (2017). “Classifying cyclic buckling modes of steel wide-flange columns under cyclic loading.” In *Proc.*, *Structures Congress*, ASCE, Reston, VA.

(17) Seaburg, P. A., and Carter, C. J. (1997). “Torsional analysis of structural steel members.” *Steel Design Guide Series 9*, AISC.

(18) Ziemian, R. D., ed. (2010). *Guide to stability design criteria for metal structures*, 6th Ed., Wiley, Hoboken, NJ.